Karlsruhe Institute of Technology

Institute of Fluid Mechanics

Convection Velocities of Passive Scalar and Velocity Fluctuations in Wall-Bounded Turbulence

Konvektionsgeschwindigkeiten von passiven Skalar- und Geschwindigkeitsfluktuationen in wandgebundener Turbulenz

Master Thesis of

Christian Erik Dederichs

At the Department of Mechanical Engineering,
Institute of Fluid Mechanics

Advisors: Prof. Dr.-Ing. Bettina Frohnapfel
Dr.-Ing. Davide Gatti
M.Sc. Jonathan Neuhauser

Duration: December 2024 – June 2025

I declare that I have developed and written the enclosed thesis completely by myself, and have not used sources or means without declaration in the text.

Karlsruhe, 02.06.2025

(**Christian Erik Dederichs**)

Abstract

Taylor's hypothesis of frozen turbulence is applied to many experimental use cases to convert time series into spatial field data. To do so, the concept of a convection velocity is needed, which characterises the velocity at which coherent turbulent structures move within the considered flow. This thesis uses a definition of convection velocity from the literature to analyse the convection behaviour of different quantities in wall-bounded turbulence. Therefore, a deeper understanding of the underlying physical mechanisms is gained, which can be used to apply Taylor's hypothesis more sophisticated. The considered quantities are structures of all three velocity components as well as passive scalar structures at three different Prandtl numbers. Direct numerical simulations of periodic channels at three different Reynolds numbers are conducted to generate data. To validate these data, typical turbulence statistics are retraced, which show good agreement with results from the literature. Next, a transport equation analysis is conducted, revealing where and why Taylor's hypothesis might not be applicable. The results of this analysis are in good agreement with data from the literature in the case of turbulent velocity structures. Therefore, trustworthy insights can be gained from the remaining analyses on the behaviour of passive scalar structures. In the following step, the convection velocities of all structures considered are inspected regarding their dependency on the wall distance. To validate these results, known statistics from the literature are used. In addition, new findings regarding the influence of the Prandtl and Reynolds numbers, different-sized structures, and physical driving mechanisms are made. Finally, a spectral analysis of the convection velocity distribution in the Fourier space is performed. The insights resulting from this provide fundamental information on the physical behaviour, which was shown by the previous analyses.

Zusammenfassung

Taylors Hypothese der eingefrorenen Turbulenz kommt in vielen experimentellen Anwendungsfällen zum Einsatz, um Informationen aus Zeitreihen in räumliche Felddaten zu überführen. Dazu wird das Konzept der Konvektionsgeschwindigkeit benötigt, mit welcher sich kohärente turbulente Strukturen durch die betrachtete Strömung bewegen. In dieser Arbeit wird eine in der Literatur bekannte Definition der Konvektionsgeschwindigkeit genutzt, anhand welcher das Konvektionsverhalten verschiedener Größen in wandgebundener Turbulenz analysiert wird. Damit wird ein tieferes Verständinis über die zugrundeligenden physikalischen Prozesse gewonnen, welches zur besseren Anwendung von Taylors hypothese genutzt werden kann. Es werden Geschwindigkeitsstrukturen aller drei Raumrichtungen sowie Strukturen von passiven Skalaren bei drei verschiedenen Prandtl-Zahlen betrachtet. Zur Datenerzeugung werden direkte numerische Simulationen von periodischen Kanalströmungen bei drei unterschiedlichen Reynolds-Zahlen durchgeführt. Zur Validierung werden zunächst typische Turbulenzstatistiken reproduziert, die in guter Übereinstimmung mit den Ergebnissen aus der Literatur stehen. Anschließend wird eine Transportgleichungsanalyse durchgeführt, die Aufschluss darüber gibt, wo und warum Taylors Hypothese möglicherweise nicht anzuwenden ist. Im Falle turbulenter Geschwindigkeitsstrukturen stimmen die Resultate dieser Analyse gut mit Ergebnissen aus der Literatur überein. Aus den weiteren Analysen lassen sich demnach vertrauenswürdige Rückschlüsse über das Verhalten von passiven Skalar-Strukturen ziehen. Anschließend werden die Konvektionsgeschwindigkeiten aller betrachteten Strukturen in Bezug auf ihre Wandabstandsabhängigkeit untersucht. Zur Validierung werden bekannte Statistiken aus der Literatur herangezogen. Außerdem werden neue Erkenntnisse bezüglich der Einflüsse von Reynolds- und Prandtl-Zahl sowie von Strukturen unterschiedlicher Größe und physikalischer Triebkräfte gewonnen. Abschließend wird eine spektrale Betrachtung der Konvektionsgeschwindigkeitsverteilung im Fourier-Raum durchgeführt. Die dadurch ermöglichten Einblicke geben grundlegenden Aufschluss über das physikalische Verhalten, das durch die vorangegangenen Analysen aufgezeigt wurde.

Acknowledgement

I want to thank everyone who supported me during this thesis. First, I would like to express my gratitude to my supervisors, Davide and Jonathan, who not only assisted me with topic-related problems but also helped me significantly improve my programming skill-set. Additionally, I want to thank Nora, Aron, Natalie, Annika, Karl, and Manu for proofreading my thesis in part or in whole. Lastly, I would like to emphasise what a great time I had working at the ISTM – thanks to all my friends, who kept me company at the institute.

Contents

Nomenclature

Greek symbols

α_0	Base wavenumber in k_1-"direction" (channel: streamwise)
β_0	Base wavenumber in k_3-"direction" (channel: spanwise)
$\dot{\boldsymbol{\gamma}}$	Shear rate
δ_ν	Viscous length-scale
θ	Passive scalar
θ_τ	Friction scalar
Θ_b	Bulk scalar
κ	Von Kármán constant
$\boldsymbol{\lambda}$, λ_i	Wavelength tensor
μ	Dynamic viscosity
ν	Kinematic viscosity
ρ	Density
$\boldsymbol{\tau}$	Viscous shear stress tensor
τ_tot	Total shear stress
τ_turb	Turbulent shear stress
τ_visc	Viscous shear stress
$\Phi_{\phi\phi}$	Wavenumber spectrum
$\tilde{\Phi}_{\phi\phi}$	Wavenumber-frequency spectrum
$\tilde{\Phi}^\mathrm{mod}_{\phi\phi}$	Modified wavenumber-frequency spectrum
ϕ, ψ	Arbitrary flow-properties
$\boldsymbol{\omega}$, ω_i	Vorticity tensor
ω	Frequency of Fourier-mode

Roman symbols

a	Scalar diffusivity
B	Log-law constant
C_1, C_2	Scalar log-law constants
c_p	Specific heat capacity at constant pressure
$E_{\phi\phi}$	One-dimensional energy spectrum
$\boldsymbol{f}$	Volume force density tensor
$\boldsymbol{H}$	Tensor containing the non-linear and forcing terms of the NSE
h	Channel half-width
i	Imaginary unit
$\mathcal{K}$	Wavenumber-space
$\boldsymbol{k}$, k_i	Wavenumber tensor
$\mathcal{L}$	Characteristic length-scale
L_1	Channel length
L_3	Channel depth
m_i	Number of Fourier-modes in k_i-"direction"
$\mathbb{N}$	Set of natural numbers
n_i	Number of collocation points in x_i-direction

p	Pressure
$\mathcal{P}_\phi$	Balance equation production-term
Q	Passive scalar source
q	Passive scalar flux
q_{molec}	Molecular passive scalar flux
q_{tot}	Total passive scalar flux
q_{turb}	Turbulent passive scalar flux
$\boldsymbol{q}_\phi$	Balance equation non-convective flux-term
$\boldsymbol{r}$, r_i	Spatial separation tensor
$R_{\phi\psi}$	Space-time covariance
$R_{\phi\phi}$	Space-time auto-covariance
$\mathcal{S}_\phi$	Balance equation supply-term
s	Spacing parameter
t	Time
$\boldsymbol{u}$, u_i	Velocity tensor
u	Streamwise velocity component
$\mathcal{U}$	Characteristic velocity-scale
U_{b}	Bulk velocity
u_{k_1}	Streamwise velocity component of k_1-waves
$\boldsymbol{u}_{\mathrm{c},\phi}$	Convection velocity tensor
$u_{\mathrm{c},\phi}$	Streamwise convection velocity (scale-dependent)
$U_{\mathrm{c},\phi}$	Overall streamwise convection velocity (*not* scale-dependent)
u_τ	Friction velocity
$\boldsymbol{x}$, x_i	Position tensor

Subscripts

$(\,\cdot\,)_0$	Initial
$(\,\cdot\,)_1$	x_1-component (channel: streamwise)
$(\,\cdot\,)_2$	x_2-component (channel: wall-normal)
$(\,\cdot\,)_3$	x_3-component (channel: spanwise)
$(\,\cdot\,)_{\mathrm{c}}$	Convection
$(\,\cdot\,)_{\mathrm{i}}$	Intersection
$(\,\cdot\,)_{\mathrm{p}}$	Peak
$(\,\cdot\,)_{\mathrm{w}}$	Wall

Superscripts

$\widehat{(\,\cdot\,)}$	Spatial Fourier-coefficient
$(\,\cdot\,)'$	Fluctuations
$(\,\cdot\,)^*$	Complex-conjugate
$(\,\cdot\,)^+$	Normalised by viscous units
$(\,\cdot\,)^\top$	Transposition

Other expressions

$CFL_{\max}$	Upper limit for the Courant-Friedrichs-Lewy number
$\exp(\,\cdot\,)$	Exponential function
$\mathrm{Flat}(\,\cdot\,)$	Flatness
$\mathfrak{I}(\,\cdot\,)$	Imaginary part
$\ln(\,\cdot\,)$	Natural logarithm
Pr	Prandtl number
Re	Reynolds number
Re_{b}	Bulk Reynolds number
Re_τ	Friction Reynolds number

$rms\,(\,\cdot\,)$	Root mean square
$\mathrm{Skew}\,(\,\cdot\,)$	Skewness
$\tanh\,(\,\cdot\,)$	Hyperbolic tangent
$\Re\,(\,\cdot\,)$	Real part
$\triangle\,(\,\cdot\,)$	Delay
$\Delta\,(\,\cdot\,)$	Laplace-operator
$\Delta^2\,(\,\cdot\,)$	Biharmonic operator
$\nabla\,(\,\cdot\,)$	Gradient-operator
$\nabla\cdot\,(\,\cdot\,)$	Divergence-operator
$\partial_{(\cdot)}$	Partial derivative
$\|\,\cdot\,\|$	Tensor-norm
$\langle\,\cdot\,\rangle$	Ensemble average
$\langle\,\cdot\,\rangle_{(\,\cdot\,)}$	Average over $(\,\cdot\,)$
$\otimes$	Dyadic product
①	Transport equation analysis streamwise convection term
②	Transport equation analysis time development term
③	Transport equation analysis diffusion/conduction term
④	Transport equation analysis non-linear term
⑤	Transport equation analysis convection velocity difference term
⑥	Transport equation analysis pressure term

Abbreviations

Conti	Continuity
DNS	Direct numerical simulation
FFT	Fast-Fourier-Transformation
ISTM	Institute of Fluid Mechanics
KIT	Karlsruhe Institute of Technology
m180	Main simulation at $Re_\tau \approx 180$
m500	Main simulation at $Re_\tau \approx 500$
m1000	Main simulation at $Re_\tau \approx 1000$
NSE	Navier-Stokes Equation
p180	Preliminary simulation at $Re_\tau \approx 180$
pre.	Preliminary
RANS	Reynolds averaged Navier-Stokes
Resp.	Respectively

1. Introduction

Wall-bounded turbulent flows are present in a wide range of technical applications, and their behaviour is thus of great interest to numerical and experimental research. Since gaining full-field data from experimental setups is particularly difficult, Taylor's hypothesis is often used to relate time series at a constant point in space to instantaneous snapshots of the physical domain using convection velocities. Therefore, suitable definitions of these convection velocities are important for the applicability of Taylor's hypothesis. Ever since Taylor 1938 formulated his hypothesis, many convection velocity definitions have been published in the literature (e.g. Wills 1964 and Hussain and Clark 1980), all focussing on slightly different aspects of the actual physical flow behaviour. In the scope of this thesis, the formulation introduced by Del Álamo and Jiménez 2009 is of special interest since it allows for an individual analysis of the convection of different turbulent scales and offers the possibility of a simple numerical implementation. Additionally, their definition considers the convection velocities' dependency on the transported quantities and the wall distance. In their publication, Del Álamo and Jiménez consider fluctuating velocity structures as the convected properties of interest. This thesis aims to extend their findings with respect to passive scalar structures at different Prandtl and Reynolds numbers. A better understanding of the physical behaviour of the convection velocities of these structures is gained from a detailed statistical analysis of turbulent plane channel flow simulated during this work.
Following this introduction, the basic concepts of turbulence, plane channel flow, and Taylor's hypothesis are introduced in chapter 2. Subsequently, in chapter 3, the code used for conducting the simulations is briefly explained. In addition, an overview of all simulated cases with their characterising parameters is given, and some selected aspects of the implementations used during post-processing are described. The results of these investigations are discussed in chapter 4. They are organised into basic channel flow statistics, used to validate the simulation and averaging setups; a transport equation analysis, used to categorise the results of this thesis in the overall context of Taylor's hypothesis; and, lastly, the statistics on the convection velocity behaviour themselves. In chapter 5, the results are summarised, a conclusion is drawn, and an outlook to further research is given.

2. Theory

2.1. Equations of turbulent flow

2.1.1. General description

The behaviour of fluids is mathematically described by balance equations (also called transport equations), as stated, for example, by Pope 2000, Ferziger et al. 2019 and Zierep and Bühler 2023. They also mention the need for initial and boundary conditions, as well as material models, to solve a fluid-mechanical problem. While the former are dependent on the flow geometry and external influences, the latter are inherent properties of the analysed fluid. In addition, specific flow properties can simplify the formulation of the most general mathematical problems.
Ferziger et al. 2019 mention the simplifications resulting from the analysis of the incompressible and isothermal flow of a Newtonian fluid, which will be the case considered in the scope of this thesis. A flow is called incompressible if the material derivative of the density ρ vanishes at every point of the analysed domain, as

$$\partial_t \rho + \boldsymbol{u} \cdot \nabla \rho = 0. \tag{2.1}$$

Here $\partial_{(\cdot)}$ denotes a partial derivative with respect to $(\,\cdot\,)$, and $\nabla\,(\,\cdot\,)$ is the gradient-operator. Equation 2.1 therefore consists of a partial derivative with respect to time t and the so-called "convective derivative", which is the scalar product of the density gradient $\nabla\rho$ with the velocity tensor $\boldsymbol{u}$. The material class of Newtonian fluids, as mentioned by Zierep and Bühler 2023, is defined by the viscous shear stress $\boldsymbol{\tau}$ being proportional to the shear rate $\dot{\boldsymbol{\gamma}}$, as

$$\boldsymbol{\tau} = \mu \dot{\boldsymbol{\gamma}}. \tag{2.2}$$

The proportionality factor μ is the fluid's dynamic viscosity, which is a property of the material itself. Note that the shear rate is defined as twice the symmetric velocity-gradient

$$\dot{\boldsymbol{\gamma}} \equiv \nabla \boldsymbol{u} + (\nabla \boldsymbol{u})^{\top}, \tag{2.3}$$

which will later lead to simplifications due to Equation 2.1. Here, $(\,\cdot\,)^{\top}$ denotes the transpose of a second-order tensor. What makes a flow isothermal is the fact that its properties, here the viscosity in particular, are independent of temperature and therefore constant, as mentioned by Ferziger et al. 2019.
Balance equations, which are generally postulated in an integral form, can be transformed into an equivalent differential form, as explained in detail, for example, by Liu 2002 and Hirsch 2007. They formulate the most general balance equation for an arbitrary flow-property $\phi\,(\boldsymbol{x}, t)$ as

$$\partial_t \phi + \nabla \cdot (\phi \boldsymbol{u}) = \mathcal{P}_\phi + \mathcal{S}_\phi + \nabla \cdot \boldsymbol{q}_\phi. \tag{2.4}$$

Here, $\nabla \cdot (\,\cdot\,)$ denotes the divergence-operator and ϕ is in general a function of the spatial position $\boldsymbol{x}$ and time t. $\mathcal{P}_\phi$, $\mathcal{S}_\phi$ and $\boldsymbol{q}_\phi$ are the production, supply, and non-convective flux terms, respectively. These terms are balanced with the temporal evolution and the

convective flux of ϕ, as seen on the left-hand side of Equation 2.4.
Since statistical tools are often applied to study the behaviour of turbulence, as stated by Pope 2000, the mean field balance equation, as well as the fluctuation field balance equation, are of additional interest. The former balance equation for $\langle\phi\rangle$ can be derived by taking the mean of Equation 2.4. In general, $\langle\ \cdot\ \rangle$ is the ensemble average of a given quantity, which can still be a function of space and time. The latter balance equation for ϕ' can be derived by subtracting the mean field balance equation from Equation 2.4. Here, $(\ \cdot\ )'$ denotes a value's fluctuation around its statistical mean. Pope 2000 derives this using the linearity of derivation and averaging. The balance equations of the mean and fluctuating fields of quantities, which are products of random variables, can be derived from the respective equations of the separate variables. Note that averages might also be taken over quantities other than an ensemble of values. The average $\langle\ \cdot\ \rangle_{(\,\cdot\,)}$ over an arbitrary quantity $(\ \cdot\ )$ is indicated by a subscript. Such arbitrary quantities could range from statistically homogeneous directions in space or time to combinations of these.

2.1.2. Balance equations

Pope 2000 and Ferziger et al. 2019 show that for an incompressible flow the mass balance, also called "continuity equation" or just "conti equation", degenerates to the condition for the velocity field to be divergence-free, as

$$\nabla \cdot \boldsymbol{u} = 0. \tag{2.5}$$

By taking the average of Equation 2.5, the mean conti equation is again given as a divergence-free condition, but this time for the mean velocity field, like

$$\nabla \cdot \langle\boldsymbol{u}\rangle = 0. \tag{2.6}$$

Something similar follows for the fluctuating velocity-field, since the Reynolds decomposition $\boldsymbol{u} = \langle\boldsymbol{u}\rangle + \boldsymbol{u}'$ holds. The fluctuating conti equation

$$\nabla \cdot \boldsymbol{u}' = 0, \tag{2.7}$$

is obtained by subtracting Equation 2.6 from Equation 2.5, as done by Pope 2000.
Ferziger et al. 2019 derive the momentum balance equation for an isothermal incompressible flow of a Newtonian fluid (and fulfilled mass balance) as

$$\partial_t \boldsymbol{u} + \boldsymbol{u} \cdot \nabla \boldsymbol{u} = -\frac{1}{\rho}\nabla p + \nu \Delta \boldsymbol{u} + \boldsymbol{f}, \tag{2.8}$$

with the Laplace-operator $\Delta\,(\ \cdot\ )$, the pressure-field p, the volume force density tensor $\boldsymbol{f}$ and the kinematic viscosity

$$\nu \equiv \frac{\mu}{\rho}. \tag{2.9}$$

Equation 2.8 is also referred to as the "Navier-Stokes equation" (NSE). As for the mean conti equation, Pope 2000 obtains the mean NSE by taking the statistical average of the original formulation, resulting in

$$\partial_t \langle\boldsymbol{u}\rangle + \langle\boldsymbol{u}\rangle \cdot \nabla \langle\boldsymbol{u}\rangle = -\frac{1}{\rho}\nabla\langle p\rangle + \nu\Delta\langle\boldsymbol{u}\rangle - \nabla \cdot \langle\boldsymbol{u}' \otimes \boldsymbol{u}'\rangle + \langle\boldsymbol{f}\rangle, \tag{2.10}$$

where $\otimes$ denotes the dyadic product. Equation 2.10 is called "Reynolds averaged Navier-Stokes equation" (RANS equation). Note that due to the non-linearity of the convective term in Equation 2.8, the RANS equation contains an additional term (third on the right-hand side of Equation 2.10), called the "Reynolds stresses". Pope 2000 points out

the importance of the Reynolds stresses for the analysis and modelling of turbulent flows. They naturally also appear in the balance equation for the momentum fluctuations

$$\partial_t \boldsymbol{u}' + \boldsymbol{u}' \cdot \nabla \boldsymbol{u}' + \langle \boldsymbol{u} \rangle \cdot \nabla \boldsymbol{u}' + \boldsymbol{u}' \cdot \nabla \langle \boldsymbol{u} \rangle = -\frac{1}{\rho} \nabla p' + \nu \Delta \boldsymbol{u}' + \nabla \cdot \langle \boldsymbol{u}' \otimes \boldsymbol{u}' \rangle + \boldsymbol{f}', \quad (2.11)$$

as well as other non-linear terms, containing the mean and fluctuating velocity fields.
A balance equation for a passive scalar θ is derived by Pope 2000 and Ferziger et al. 2019. If again, the mass balance is fulfilled and the flow is considered incompressible with constant material properties, as for the NSE, the passive scalar balance equation takes the form

$$\partial_t \theta + \boldsymbol{u} \cdot \nabla \theta = a \Delta \theta + Q, \quad (2.12)$$

with the scalar diffusivity a and the passive scalar source-term Q. Note that Q could also take negative values, in which case it would be understood as a sink term. Pope 2000 explains the designation "passive" to be contributed to the fact that θ has, by assumption, no effect on the material properties and, in extension, no influence on the flow itself. As mentioned by Ferziger et al. 2019, passive scalars can be all kinds of quantities, such as temperature distributions or concentrations of immersed particles. An important characteristic of Equation 2.12 is its similarity to Equation 2.8, as referred to by Pope 2000. The passive scalar balance equation obeys a similar behaviour as the NSE, only without the non-linear feedback effects due to the convection term and the redistributive behaviour of the pressure term. However, Equation 2.12 still contains a non-linear convection term, that again yields an additional term in the mean passive scalar balance equation

$$\partial_t \langle \theta \rangle + \langle \boldsymbol{u} \rangle \cdot \nabla \langle \theta \rangle = a \Delta \langle \theta \rangle - \nabla \cdot \langle \boldsymbol{u}' \theta' \rangle + \langle Q \rangle, \quad (2.13)$$

which Pope 2000 mentions to take an analogous role to the Reynolds stresses of the RANS equations. Like for Equation 2.11, the additional non-linear term from the mean passive scalar balance equation carries over to the balance equation for the passive scalar fluctuations

$$\partial_t \theta' + \boldsymbol{u}' \cdot \nabla \theta' + \langle \boldsymbol{u} \rangle \cdot \nabla \theta' + \boldsymbol{u}' \cdot \nabla \langle \theta \rangle = a \Delta \theta' + \nabla \cdot \langle \boldsymbol{u}' \theta' \rangle + Q', \quad (2.14)$$

in addition to the mixed terms, containing averaged and fluctuating values.
Pope 2000 and Ferziger et al. 2019 state the importance of the non-dimensionalised form of the balance equations. A balance equation can be non-dimensionalised by first expressing all of its quantities as products of a dimensionally afflicted constant and a dimensionless variable and then dividing every term of the equation by the dimensionally afflicted prefactor of one of its terms. When considering a flow without the volume forces density $\boldsymbol{f}$ and no relevant characteristic time, pressure or scalar source scale, as is done in the scope of this thesis, the dimensionless form of equations 2.5, 2.8 and 2.12 result in

$$\nabla \cdot \boldsymbol{u} = 0, \quad (2.15)$$

$$\partial_t \boldsymbol{u} + \boldsymbol{u} \cdot \nabla \boldsymbol{u} = -\frac{1}{\rho} \nabla p + \frac{1}{Re} \Delta \boldsymbol{u}, \quad (2.16)$$

$$\partial_t \theta + \boldsymbol{u} \cdot \nabla \theta = \frac{1}{Re\ Pr} \Delta \theta + Q. \quad (2.17)$$

As mentioned by Ferziger et al. 2019, the problem of a passive scalar being transported by a turbulent flow is then characterised by the two dimensionless numbers

$$Re \equiv \frac{\mathcal{U}\mathcal{L}}{\nu}, \quad (2.18)$$

$$Pr \equiv \frac{\nu}{a}, \tag{2.19}$$

which are the "Reynolds number" and "Prandtl number", respectively. $\mathcal{U}$ is the characteristic velocity scale and $\mathcal{L}$ is the characteristic length scale of the flow. Note that all quantities in equations 2.15, 2.16, and 2.17 are non-dimensionalised by suitable characteristic scales. However, for the sake of simplicity, the notation is kept the same as for their dimensionally afflicted counterparts. The dimensionless forms of the mean and fluctuating balance equations can be derived in a similar manner.

2.2. Plane channel flow

2.2.1. Geometry

Pope 2000 states that since the canonical plane channel flow is a fairly simple geometric configuration, it is often used to study the physics of turbulent flows. Its simplicity can be used in particular, since the near-wall behaviour of turbulence is known to be quite similar for all kinds of wall-bounded flows. For this reason, all direct numerical simulations (DNSs) performed during the term of this thesis were simulations of plane channel flow.
The geometry of an exemplary plane channel is sketched in Figure 2.1, with a length of L_1, a width of $2h$ and a depth of L_3. The Cartesian coordinate system is located in the middle of the lower wall, where x_1, x_2 and x_3 are the streamwise, wall-normal and spanwise components of the coordinate system, respectively. The two channel walls are therefore located at $x_2 = 0$ and $x_2 = 2h$, while the channel centreline is located at $x_2 = h$ and $x_3 = 0$. The main flow is directed parallel to the x_1-axis.

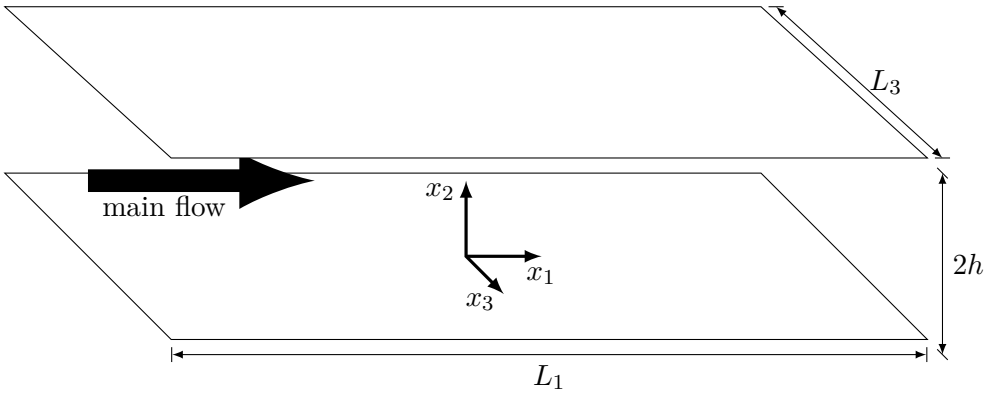

Figure 2.1.: Plane channel flow configuration

The channel is long and has a large aspect ratio, which Pope 2000 mathematically describes as $L_1/h \gg 1$ and $L_3/h \gg 1$, respectively. In the case of a simulation, such a geometry is realised by periodic boundary conditions in the streamwise and spanwise directions, as stated by Ferziger et al. 2019. In doing so, the channel would have an "infinite" length and depth. For the velocity field, the boundary conditions in the wall-normal direction are those of no-slip and impermeability. For the scalar field, another Dirichlet boundary condition is considered in the scope of this thesis, setting the value of the scalar to zero at the walls of the channel. Pope 2000 explains that therefore the mean values as well as the fluctuations of all velocity components are zero at the walls of the channel.
This geometry strongly impacts the properties of a turbulent flow contained within, as is described, for example, by Pope 2000, Schlichting and Gersten 2006, Durbin and Reif 2010, Spurk and Aksel 2019 and Aliabadi 2022. They conclude the following:

First, because of the geometric symmetry of the channel and its large aspect ratio, the contained flow must be statistically homogeneous in the spanwise direction. This can be expressed as all averaged quantities being independent of the homogeneous direction x_3, as

$$\partial_{x_3} \langle \cdot \rangle = 0. \tag{2.20}$$

Additionally, the mean velocity field experiences no cross-flows in the spanwise direction, resulting in its averaged x_3-component to be zero, as

$$\langle u_3 \rangle = 0. \tag{2.21}$$

Note that this is only true for either the channel geometry with "infinite" depth or, in real channels, for positions remote from the side walls.
Second, when neglecting the flow-development region, the flow must be statistically fully developed in the streamwise direction. This is mathematically equivalent to all velocity statistics being independent of x_1.
Third, in general, plane channel flows are considered to be statistically stationary, which is also true for all cases considered in the scope of this thesis. All mean quantities must, therefore, be independent of time, as

$$\partial_t \langle \cdot \rangle = 0. \tag{2.22}$$

Considering the mean continuity Equation 2.6 and the no-slip boundary condition yields the averaged wall-normal velocity-component to be zero, as

$$\langle u_2 \rangle = 0. \tag{2.23}$$

Pope 2000 notes that all velocity statistics are only dependent on the wall-normal coordinate x_2, and additionally, *all* statistics are symmetric about the channel mid-plane at $x_2 = h$.

2.2.2. Basic statistics

As mentioned in subsection 2.1.1, statistics are an important tool in the study of turbulent flows. Pope 2000 explains this to be the case since the statistics of turbulence are reproducible, while its instantaneous behaviour is chaotic and therefore strongly sensible to changes in initial and boundary conditions. For turbulent plane channel flow, the behaviour of some statistical quantities is known a priori from analytical consideration, as shown, for example, by Pope 2000, Schlichting and Gersten 2006 and Aliabadi 2022. By analysing the wall-normal RANS equation 2.10, they show the average axial pressure gradient

$$\partial_{x_1} \langle p \rangle = \partial_{x_1} p_\mathrm{w} \tag{2.24}$$

to be uniform across the flow and therefore equal to its respective value at the wall. Here $(\cdot)_\mathrm{w}$ denotes the value of a quantity at the channels coordinate $x_2 = 0$ (resp. $x_2 = 2h$). As demonstrated by Pope 2000, this results in the total shear stress

$$\tau_\mathrm{tot} \equiv \langle \tau_{12} \rangle = \mu \partial_{x_2} \langle u_1 \rangle - \rho \langle u_1' u_2' \rangle, \tag{2.25}$$

to be linear across the channel width when examining the axial RANS equation 2.10. Equation 2.25 also shows that the total shear is composed of two parts: On the one hand, the viscous stresses

$$\tau_\mathrm{visc} \equiv \mu \partial_{x_2} \langle u_1 \rangle, \tag{2.26}$$

containing the mean wall-normal velocity gradient, which would be the only part contributing to the stress profile of a laminar flow; on the other hand, the turbulent stresses

$$\tau_\mathrm{turb} \equiv -\rho \langle u_1' u_2' \rangle, \tag{2.27}$$

containing the off-diagonal component of the Reynolds stresses. Furthermore, Pope 2000 and Schlichting and Gersten 2006 refer to the analogy of shear stress with respect to the flux of a passive scalar q. They show the total scalar flux

$$q_{\mathrm{tot}} \equiv \rho a \partial_{x_2} \langle \theta \rangle - \rho \left\langle \theta' u_2' \right\rangle , \tag{2.28}$$

to be composed of two terms, similar to Equation 2.25. In general, a passive scalar flux can result from different phenomena. The first of these phenomena is the inhomogeneous distribution of the mean field, resulting in the molecular scalar flux

$$q_{\mathrm{molec}} \equiv \rho a \partial_{x_2} \langle \theta \rangle . \tag{2.29}$$

The second phenomenon is the flow rate due to the turbulent behaviour of the fluctuating velocity field, resulting in the turbulent scalar flux

$$q_{\mathrm{turb}} \equiv -\rho \left\langle \theta' u_2' \right\rangle . \tag{2.30}$$

Aliabadi 2022 points out that, since there are no velocity fluctuations at the wall due to the no-slip boundary condition, the wall shear stress

$$\tau_{\mathrm{w}} \equiv \mu \left(\partial_{x_2} \langle u_1 \rangle \right) \Big|_{\mathrm{w}} \tag{2.31}$$

is exclusively caused by the mean wall-normal velocity gradient. As a result of the same argument, the wall scalar flux

$$q_{\mathrm{w}} \equiv \rho a \left(\partial_{x_2} \langle \theta \rangle \right) \Big|_{\mathrm{w}} \tag{2.32}$$

is only contributed by the molecular scalar flux.
Another important statistical quantity, used for example in the study of turbulent plane channel flow by Kim et al. 1987, is the space-time covariance

$$R_{\phi\psi}(\boldsymbol{x}, \boldsymbol{r}, t, \triangle t) \equiv \left\langle \phi'(\boldsymbol{x}, t) \psi'(\boldsymbol{x} + \boldsymbol{r}, t + \triangle t) \right\rangle , \tag{2.33}$$

where $\boldsymbol{r}$ is the spatial separation from $\boldsymbol{x}$, $\triangle t$ is the time delay with respect to t and ψ is a second arbitrary flow property, just as ϕ. In the special case of $\phi = \psi$, Equation 2.33 is also referred to as the "space-time auto-covariance". The space-time covariance's connection to the behaviour of fluid motion becomes evident when considering its form for $\phi = u_i$, $\psi = u_j$ and vanishing spatial as well as temporal separations, as

$$R_{u_i u_j}(\boldsymbol{x}, \boldsymbol{r} = \boldsymbol{0}, t, \triangle t = 0) = \left\langle u_i'(\boldsymbol{x}, t) u_j'(\boldsymbol{x}, t) \right\rangle . \tag{2.34}$$

This expression is obviously another representation of the Reynolds stresses appearing in Equation 2.10, as stated by Pope 2000. For the case of plane channel flow, Pope further notes the typical behaviour of $\langle u_1' u_2' \rangle$ vanishing at the channel centre. In addition, $\langle u_1' u_3' \rangle$ and $\langle u_2' u_3' \rangle$ are zero throughout the whole channel, which can be attributed to the statistical symmetry with respect to u_3-fluctuations.
Wills 1964 demonstrates that Fourier-transforming the space-time auto-covariance in time and space yields the wavenumber-frequency spectrum

$$\tilde{\Phi}_{\phi\phi}(\boldsymbol{x}, \boldsymbol{k}, t, \omega) \equiv \frac{1}{(2\pi)^4} \int_{-\infty}^{\infty} \iiint_{-\infty}^{\infty} R_{\phi\phi}(\boldsymbol{x}, \boldsymbol{r}, t, \triangle t) \, \exp\left[-i \left(\boldsymbol{k} \cdot \boldsymbol{r} + \omega \triangle t \right) \right] \, \mathrm{d}\boldsymbol{r} \mathrm{d} \triangle t . \tag{2.35}$$

Here, $\exp(\,\cdot\,)$ is the exponential-function, i is the imaginary unit, $\boldsymbol{k}$ is the wavenumber tensor, and ω is the frequency of a given Fourier mode. Aliabadi 2022 shows similarly that

by only Fourier-transforming the space-time auto-covariance in space, while regarding the time delay to be zero, the wavenumber spectrum

$$\Phi_{\phi\phi}(\boldsymbol{x}, \boldsymbol{k}, t) \equiv \frac{1}{(2\pi)^3} \iiint_{-\infty}^{\infty} R_{\phi\phi}(\boldsymbol{x}, \boldsymbol{r}, t, \triangle t = 0) \, \exp\left[-i \left(\boldsymbol{k} \cdot \boldsymbol{r}\right)\right] \, \mathrm{d}\boldsymbol{r} \tag{2.36}$$

can be constructed. Note that the spatial directions in which Equation 2.35 and Equation 2.36 are transformed can vary depending on the flow configuration considered. In the case of plane channel flow, Kim et al. 1987 consider only spatial separations in the streamwise and spanwise directions since the insights resulting from the analysis of wall-normal correlations are limited by the influence of the channel walls. The simplifications introduced in subsection 2.2.1 further reduce the variables of Equation 2.33 and all its related quantities, resulting in their statistics being independent of x_1, x_3, t, r_2 and k_2. Pope 2000 introduces the one-dimensional energy spectra $E_{\phi\phi}$, which depend only on one wavenumber, for example k_1. In this case, the one-dimensional energy spectrum is defined as twice the Fourier-transformed space-time auto-covariance with respect to the "wanted" separation and vanishing "unwanted" separations, as

$$E_{\phi\phi}(\boldsymbol{x}, k_1, t) \equiv \frac{2}{2\pi} \int_{-\infty}^{\infty} R_{\phi\phi}(\boldsymbol{x}, r_1, r_2 = 0, r_3 = 0, t, \triangle t = 0) \, \exp\left[-i k_1 r_1\right] \, \mathrm{d}r_1. \tag{2.37}$$

One-dimensional energy spectra for spatial separations other than r_1 can be constructed in a similar manner. However, Kim et al. 1987 again show that only the energy spectra with respect to k_3 are of additional interest in the case of turbulent plane channel flow. As further shown by Pope 2000, the energy spectra defined via Equation 2.37 can also be calculated using the "full" wavenumber spectrum. This is done by calculating twice the integral over the "unwanted" wavenumbers, leaving a dependency on only the "wanted" wavenumber. The one-dimensional energy spectrum with respect to k_1 can, therefore, be calculated as

$$E_{\phi\phi}(\boldsymbol{x}, k_1, t) = 2 \iint_{-\infty}^{\infty} \Phi_{\phi\phi}(\boldsymbol{x}, \boldsymbol{k}, t) \, \mathrm{d}k_2 \mathrm{d}k_3. \tag{2.38}$$

2.2.3. Scaling

Aliabadi 2022 mentions the importance of wall shear stress τ_w, density ρ, and kinematic viscosity ν as parameters in the study of turbulent flows. The variables mentioned are especially useful for defining the so-called "viscous scales", as is done, for example, by Pope 2000, Schlichting and Gersten 2006 and Aliabadi 2022. These scales contain the friction velocity

$$u_\tau \equiv \sqrt{\frac{\tau_\mathrm{w}}{\rho}} \tag{2.39}$$

as a velocity-scale based on the wall shear stress, and the density and the viscous length-scale

$$\delta_\nu \equiv \frac{\nu}{u_\tau} \tag{2.40}$$

as a length-scale based on the kinematic viscosity and the newly defined friction velocity. Kader 1981 and Saha et al. 2014 further introduce the friction scalar

$$\theta_\tau \equiv \frac{q_\mathrm{w}}{\rho c_\mathrm{p} u_\tau} \tag{2.41}$$

as a passive scalar-scale based on the wall scalar flux, the density, the friction velocity and the specific heat capacity at constant pressure c_p. By using Equation 2.39 and the channel half-width h, the friction Reynolds number

$$Re_\tau \equiv \frac{u_\tau h}{\nu}, \tag{2.42}$$

can be defined. u_τ and δ_ν are the appropriate quantities for scaling the behaviour of the turbulent near-wall velocity field, as mentioned by Aliabadi 2022. Saha et al. 2014 note the difficulties of finding an appropriate scaling for the scalar field since its behaviour is not only dependent on the Reynolds number (as for the velocity field) but also on the Prandtl number. However, for the sake of simplicity in the scope of this thesis, equations 2.40 and 2.41 are used as "viscous scaling" for all scalar statistics if not mentioned otherwise. Values normalised by the viscous scales, are denoted by the superscript $(\,\cdot\,)^+$. Another way of scaling the variables of plane channel flow is by using the "outer scales", as is done, for example, by Pope 2000. These scales contain the bulk values of $\langle u_1 \rangle$ and $\langle \theta \rangle$

$$U_\mathrm{b} \equiv \frac{1}{2h} \int_0^{2h} \langle u_1 \rangle \, \mathrm{d}x_2 \tag{2.43}$$

$$\Theta_\mathrm{b} \equiv \frac{1}{2h} \int_0^{2h} \langle \theta \rangle \, \mathrm{d}x_2 \tag{2.44}$$

as the velocity and passive scalar scale, respectively. The channel half-width h is used as the length scale. The bulk Reynolds number

$$Re_\mathrm{b} \equiv \frac{U_\mathrm{b} 2h}{\nu} \tag{2.45}$$

follows as a natural definition from the outer scales. Results obtained by experiments or simulations can be nicely compared if they are scaled in viscous or outer units. This is done, for example, within the scope of this thesis (chapter 4), to validate new simulation results by comparison with existing data. The typical resulting mean profiles of one such simulation (p180 from Table 3.1) are shown in Figure 2.2 and Figure 2.3.

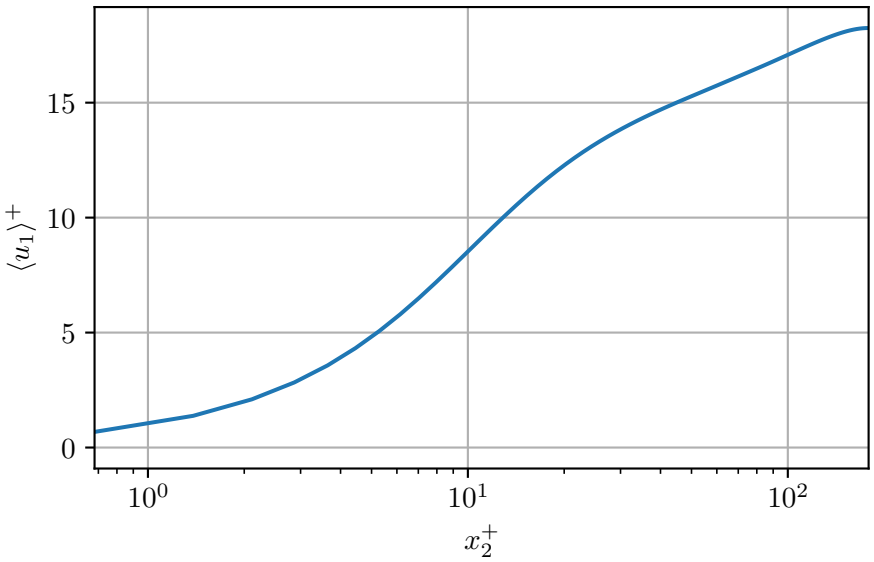

Figure 2.2.: Mean streamwise velocity profile of a turbulent channel flow ($Re_\tau = 180$)

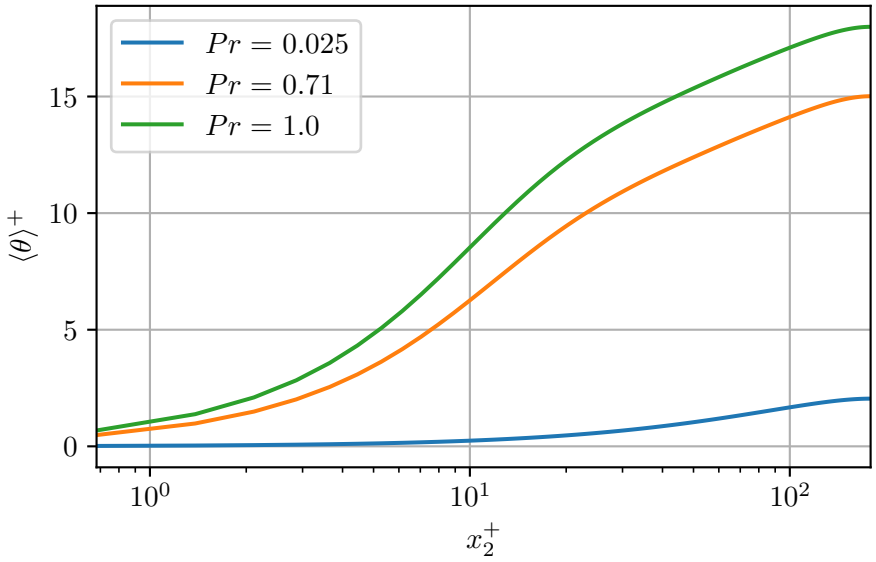

Figure 2.3.: Mean scalar profiles of a turbulent channel flow ($Re_\tau = 180$)

Figure 2.2 shows the mean streamwise velocity component normalised by the friction velocity $\langle u_1 \rangle^+ = \langle u_1 \rangle / u_\tau$ with respect to the wall distance normalised by the viscous length scale $x_2^+ = x_2/\delta_\nu$. Figure 2.3 shows the mean scalar profiles at different Prandtl numbers with respect to wall distance, again normalised by the viscous scales.
Another important characteristic of wall-bounded turbulence is the formation of distinct wall regions and layers (depending on the Reynolds number), as can be seen in part in Figure 2.2 for the velocity field and in Figure 2.3 for the scalar field. Pope 2000, Spurk and Aksel 2019 and Aliabadi 2022 mention the mean streamwise velocity growing linearly with respect to the wall-distance (in viscous units) as

$$\langle u_1 \rangle^+ = x_2^+ \tag{2.46}$$

within the so-called "viscous sublayer" closest to the wall. Near the channel centre, in the "log layer", the profile takes on a logarithmic shape as

$$\langle u_1 \rangle^+ = \frac{1}{\kappa} \ln\left(x_2^+\right) + B \tag{2.47}$$

called the log-law. Here, $\ln(\,\cdot\,)$ denotes the natural logarithm. The von Kármán constant κ, as well as the second constant B, are dependent on the flow physics. These two domains are connected via the "buffer layer". The locations and defining properties of these layers, as well as other regions of the velocity field in a plane channel flow, are explained in detail by Pope 2000. A brief overview of his explanations can be seen in Table 2.1.
Note that the locations of some domains in Table 2.1 are given with respect to x_2/h, while others are defined by means of x_2^+. This is relevant, since the viscous wall distance scales with the friction velocity. In other words, the relative size of some wall regions and layers with respect to others changes depending on the characteristics of the flow. To visualise this, Pope 2000 sketches the different regions, mentioned in Table 2.1, in dependence on the bulk Reynolds number. This dependency can also be seen in Figure 2.4, where the wall distance in outer units is plotted against the friction Reynolds number. Kader 1981, Saha et al. 2014 and Aliabadi 2022 explain that like the velocity field, the scalar field forms regions and layers with distinct defining properties. However, since the scalar field is dependent on the Prandtl number, the span of these regions and layers cannot simply be defined by the values x_2^+ and x_2/h. Traditionally, a four-layer structure results from the analysis of the mean scalar profile (Figure 2.3), as mentioned by Saha et al. 2014. The

Region	Location	Defining property
Outer layer	$x_2^+ > 50$	The direct effects of viscosity on $\langle u_1 \rangle$ are negligible.
Overlap region	$x_2^+ > 50$ and $x_2/h < 0.1$	The inner and outer layers are overlapping.
Log layer	$x_2^+ > 30$ and $x_2/h < 0.3$	The log-law holds.
Inner layer	$x_2/h < 0.1$	$\langle u_1 \rangle$ is determined by u_τ and x_2^+, independent of $\langle u_1 \rangle|_{x_2=h}$ and h.
Viscous wall region	$x_2^+ < 50$	The viscous contribution to the shear stress is significant.
Buffer layer	$5 < x_2^+ < 30$	Laying between the viscous sublayer and log layer.
Viscous sublayer	$x_2^+ < 5$	The turbulent stresses are negligible compared with the viscous stresses.

Table 2.1.: Defining properties of wall regions and layers in plane channel flow (Adapted from Pope 2000)

region closest to the wall is governed by the "molecular sublayer". Here, Kader 1981 finds the mean scalar profile in viscous units to be linearly dependent on the Prandtl number as

$$\langle \theta \rangle^+ = Pr \; x_2^+. \tag{2.48}$$

Like the mean streamwise velocity profile, the mean scalar field is a logarithmic function of the wall distance, in close vicinity of the channel centre. Considering viscous scaling,

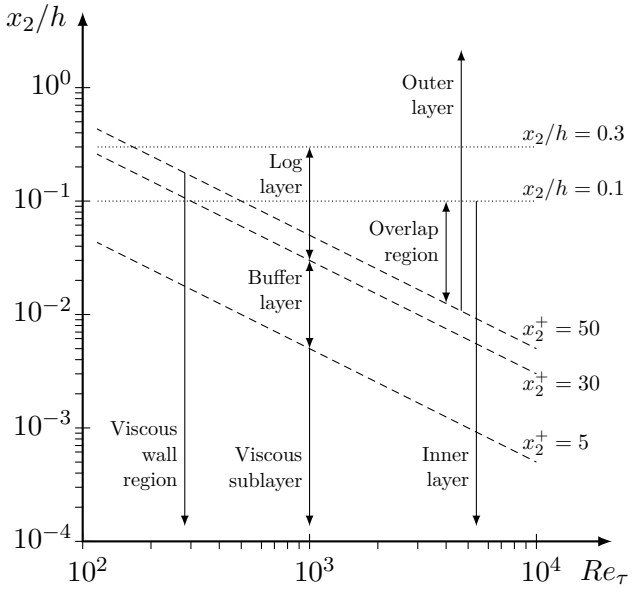

Figure 2.4.: Wall regions and layers in plane channel flow as functions of the friction Reynolds number (Adapted from Pope 2000)

Aliabadi 2022 describes this "scalar log layer" by

$$\langle\theta\rangle^+ = C_1 \ln\left(x_2^+\right) + C_2, \tag{2.49}$$

with the two flow specific constants C_1 and C_2. The last two layers considered by Saha et al. 2014 are the "scalar buffer layer", which connects the molecular sublayer and the scalar log layer, as well as the "outer scalar layer", which bridges the gap between the channel centreline and the other layers.

2.3. Taylor's hypothesis of frozen turbulence

2.3.1. Original formulation

As stated by Moin 2009, experimental measurements of turbulent flows have an inherent problem with the simultaneous resolution of spatial and temporal data. Most of the experimental methods used to analyse flows, many of which were explained in detail, for example, by Nitsche and Brunn 2006, can be divided into two general groups. The first type of methods are able to take velocity measurements in a large physical domain for discrete points in time (e.g. Particle-Image-Velocimetry), while the other type of methods can collect time series of the velocity at discrete points in space (e.g. Hot-Wire-Anemometry). While the temporal resolution of the former is limited by laser and/or camera technology, the spatial resolution of the latter is limited by the measuring probes themselves interfering with the flow field.
To bridge this problem, thereby introducing an approach to connect spatial and temporal flow behaviour, Taylor 1938 formulated his hypothesis of frozen turbulence. In his paper, Taylor considered the turbulent flow in a wind tunnel as a theoretical example, stating:

> "If the velocity of the air stream which carries the eddies is very much greater than the turbulent velocity, one may assume that the sequence of changes in u at the fixed point are simply due to the passage of an unchanging pattern of turbulent motion over the point [...]."

Where the streamwise velocity component u, which Taylor called turbulent velocity, is the transported quantity of interest. Taylor's hypothesis is, however, not limited to the description of u-transport, but can be applied to all kinds of flow-properties such as other velocity components (e.g. Quadrio and Luchini 2003 and Del Álamo and Jiménez 2009), pressure (e.g. Choi and Moin 1990), wall shear-stress (e.g. Jeon et al. 1999), enstrophy (e.g. Liu et al. 2023) or temperature (e.g. Hetsroni et al. 2004).
In general, Taylor's hypothesis can be used to link the real-time evolution of the arbitrary flow-property ϕ to the spatial evolution of the ϕ-field "frozen" in time as

$$\phi(\boldsymbol{x}, t) \approx \phi(\boldsymbol{x} - t\boldsymbol{u}_{\mathrm{c},\phi}, t_0), \tag{2.50}$$

by means of a suitable convection-velocity $\boldsymbol{u}_{\mathrm{c},\phi}$, as done by Del Álamo and Jiménez 2009. Where $\boldsymbol{x}$ is the spatial position and t is the time since t_0, when the field was "frozen".
Taylor 1938 already stated in his paper that Equation 2.50 is only certainly true in the limit case of $u/\|\boldsymbol{u}_{\mathrm{c},\phi}\| \to 0$. Here $\|\cdot\|$ is a tensor norm. This can again be generalised for an arbitrary flow property as the statement that Equation 2.50, and thereby Taylor's hypothesis, is certainly true if the "frozen" ϕ-field is convected infinitely faster through space than it can change in time, as expressed by Del Álamo and Jiménez 2009. However, in a general flow configuration, Equation 2.50 is only an estimate whose accuracy can vary. In flows containing high levels of shear, Lin 1953 found Taylor's hypothesis to be a

poor approximation, while Lee et al. 1992 evaluated the hypothesis to be applicable for vorticity-transport, even though they found it to be invalid for purely compressible motion. Geng et al. 2015 proposed an analytical/numerical approach to examine the applicability of Taylor's hypothesis by means of a transport equation analysis, which will be further discussed in section 4.2 for the flow configurations considered in the scope of this thesis.

2.3.2. Convection velocities

Even if Taylor's hypothesis is found to be applicable to a given fluid-mechanical problem, its accuracy is highly dependent on a suitable definition of the convection velocity ($\boldsymbol{u}_{\mathrm{c},\phi}$ in Equation 2.50), which is why Del Álamo and Jiménez 2009 mentioned regular warnings against the uncritical use of Taylor's hypothesis in the literature.
The original definition of the convection velocity is simply that of the local mean velocity

$$\boldsymbol{u}^{(1)}_{\mathrm{c},\phi}(\boldsymbol{x},t) \equiv \langle \boldsymbol{u}(\boldsymbol{x},t) \rangle, \tag{2.51}$$

as stated by Moin 2009. This is, however, an insufficient definition since it fails to represent the dependency of the convection velocity on material and flow properties. A suitable definition should certainly reflect these dependencies, since the convection velocity is found to be unlike for different transported quantities, as shown, for example, by Quadrio and Luchini 2003 and Del Álamo and Jiménez 2009. Hetsroni et al. 2004 showed its dependency on the Prandtl number in the case where the transported quantity is a passive scalar. The dependency of the convection velocity on the wavenumber tensor $\boldsymbol{k}$ and the frequency ω of different modes in turbulent flows is another important characteristic, which has therefore been researched for example by Wills 1964, Choi and Moin 1990 and Del Álamo and Jiménez 2009. And even though Equation 2.51 takes the effects of possible changes in Reynolds number or wall-distance somewhat into account, the convection velocity behaves differently than the mean velocity in these regards, which was shown for example by Wills 1964, Hetsroni et al. 2004, Del Álamo and Jiménez 2009 and Liu et al. 2023.
To take more of these dependencies into account when constructing a convection velocity, many definitions rely on the space-time auto-covariance $R_{\phi\phi}$ (Equation 2.33 with $\psi = \phi$) as mentioned by Hussain and Clark 1980 and Goldschmidt et al. 1981. In these papers, the most commonly used convection velocities, all based on isolines of the space-time auto-covariance, are presented.
Considering a plane channel flow, as described in section 2.2, and only evaluating the convection velocity in x_1-direction $u_{\mathrm{c},\phi}$, since flow-structures are mainly convected streamwise, the convection velocity for a given x_2-position can be calculated by different methods using isolines of $R_{\phi\phi}(x_2, r_1, \triangle t)$. Here, the space-time auto-covariance is only dependent on r_1 and $\triangle t$, since $r_2 = 0$ and $r_3 = 0$ for the evaluation of convection in x_1-direction. Where r_1, r_2 and r_3 are the spatial separations in x_1, x_2 and x_3-direction, respectively. For an exemplary isoline of this space-time auto-covariance, as sketched in Figure 2.5, the convection velocity in x_1-direction can be calculated as

$$u^{(2)}_{\mathrm{c},\phi}(x_2, r_1) \equiv \frac{r_1}{\triangle t_{\mathrm{p}}}, \tag{2.52}$$

where $\triangle t_{\mathrm{p}}$ is the corresponding time delay of the peak $R_{\phi\phi}$-value depending on r_1. Another common way of defining the convection velocity is by

$$u^{(3)}_{\mathrm{c},\phi}(x_2, \triangle t) \equiv \frac{r_{1,\mathrm{p}}}{\triangle t}, \tag{2.53}$$

with the corresponding spatial separation $r_{1,\mathrm{p}}$ of the peak $R_{\phi\phi}$-value depending on $\triangle t$. In the former definition $\triangle t_{\mathrm{p}}$ is chosen such that $\partial_{\triangle t} R_{\phi\phi}(x_2, r_1, \triangle t) = 0$ holds true, while in

the latter definition $r_{1,\mathrm{p}}$ is given as the parameter fulfilling $\partial_{r_1} R_{\phi\phi}(x_2, r_1, \triangle t) = 0$. The convection velocity can also be defined by

$$u_{\mathrm{c},\phi}^{(4)}(x_2, r_1, \triangle t) \equiv \frac{r_{1,\mathrm{i}}}{\triangle t_{\mathrm{i}}}, \tag{2.54}$$

with $(r_{1,\mathrm{i}}, \triangle t_{\mathrm{i}})$ being the point in the $(r_1, \triangle t)$-plane where the $R_{\phi\phi}$-isoline intersects its major axis. Other definitions include values of the derivative

$$u_{\mathrm{c},\phi}^{(5)}(x_2, r_1, \triangle t) \equiv \partial_{\triangle t} r_1 \tag{2.55}$$

on the $R_{\phi\phi}$-isoline at either the point, where Equation 2.52 is constructed, or the point, where Equation 2.53 is constructed. Some of the convection velocities listed by Hussain and Clark 1980 are depicted in Figure 2.5. A simplified example for a better interpretation of these definitions can be found in subsection A.1.
These definitions capture more of the mentioned dependencies. However, they still lack distinction between the different scales of turbulent structures, which is an especially important characteristic of turbulence. Hussain and Clark argued in their paper that convection velocities based on the space-time auto-covariance represent a weighted average of the velocities at which each turbulent scale is convected.

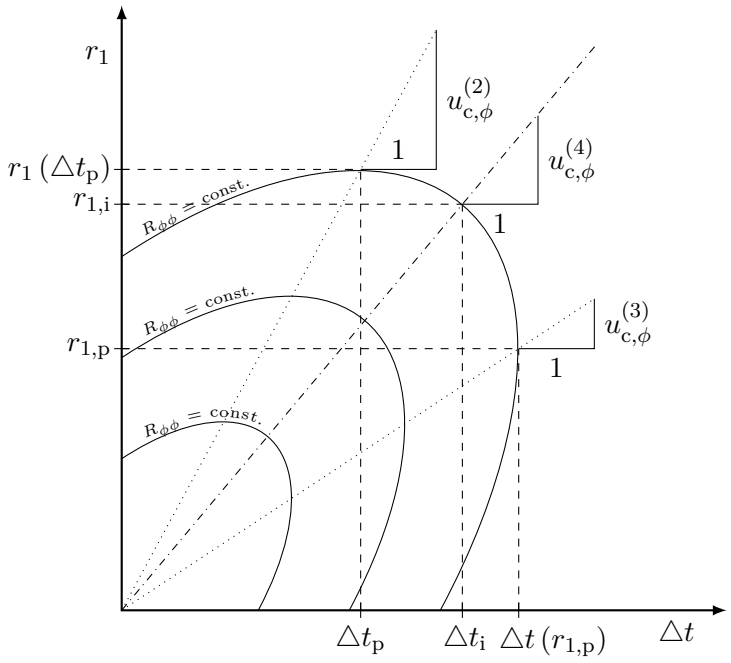

Figure 2.5.: Convection velocities and isolines of the space-time auto-covariance in a statistically steady and statistically homogeneous (x_1- and x_3-direction) channel flow with $r_2 = 0$, $r_3 = 0$ and at a constant x_2-position (Adapted from Hussain and Clark 1980)

Since larger scales tend to be long-lived in comparison to small ones, their behaviour has a greater influence on the calculated convection velocity with increasing time delay, thereby skewing the "real value".
To solve this problem, Wills 1964 introduced the idea of defining a convection velocity using the wavenumber-frequency spectrum $\tilde{\Phi}_{\phi\phi}$ (Equation 2.35). Wills argued that by supposing the flow-field to be a superposition of elemental waves, the frequency which these waves generate at a distinct spatial position can be expressed as

$$\omega = -k_1 u_{k_1}. \tag{2.56}$$

In this simplified case, each wave corresponds only to a wavenumber k_1 in x_1-direction. u_{k_1} is a range of velocities at which the waves of wavenumber k_1 move downstream. Substituting Equation 2.56 in Equation 2.35 and again considering the plane channel flow from section 2.2 yield a modified wavenumber-frequency spectrum

$$\tilde{\Phi}^{\mathrm{mod}}_{\phi\phi}(x_2, k_1, u_{k_1}) = \tilde{\Phi}_{\phi\phi}(x_2, k_1, -k_1 u_{k_1}) = \tilde{\Phi}_{\phi\phi}(x_2, k_1, \omega). \tag{2.57}$$

With this, the dominant convection velocity for a given wavenumber is defined as the velocity u_{k_1}, which maximizes the modified wavenumber-frequency spectrum as

$$\partial_{u_{k_1}} \tilde{\Phi}^{\mathrm{mod}}_{\phi\phi}(x_2, k_1, u_{k_1})\Big|_{u_{k_1} \equiv u^{(6)}_{\mathrm{c},\phi}(x_2, k_1)} = 0. \tag{2.58}$$

The convection velocity defined by Equation 2.58 fulfils the wanted requirements, especially regarding the desired turbulent scale-dependency. It can also be extended simply to take different wavenumbers k_3 in x_3-direction into account. However, its applicability is limited by the need for full spatial and temporal spectral information. Del Álamo and Jiménez 2009 addressed this problem by proposing a definition that is also based on the wavenumber-frequency spectrum, but only requires spectral information in either spatial or temporal direction while utilising local derivatives in the other. This is done by determining the convection velocity, not by the value maximising Equation 2.57, but by the position of the centre of gravity of the wavenumber-frequency spectrum for a given wavenumber. For the flow-configurations considered in their paper, they showed this definition to be in good agreement with the definition based on Equation 2.58. In the case of using spectral information for the spatial direction and local time derivatives, the convection velocity for the plane channel flow described in section 2.2 is defined as

$$u_{\mathrm{c},\phi}(x_2, k_1, k_3) \equiv -\frac{1}{k_1} \frac{\int_{-\infty}^{\infty} \omega \tilde{\Phi}_{\phi\phi}(x_2, k_1, k_3, \omega)\ \mathrm{d}\omega}{\int_{-\infty}^{\infty} \tilde{\Phi}_{\phi\phi}(x_2, k_1, k_3, \omega)\ \mathrm{d}\omega}. \tag{2.59}$$

Del Álamo and Jiménez further explained in their paper that by twice using Parseval's theorem

$$\left\langle \widehat{\phi'}^{*} \widehat{\phi'} \right\rangle_{(t)} = \int_{-\infty}^{\infty} \tilde{\Phi}_{\phi\phi}(x_2, k_1, k_3, \omega)\ \mathrm{d}\omega, \tag{2.60}$$

$$\left\langle \widehat{\phi'}^{*} \partial_t \widehat{\phi'} \right\rangle_{(t)} = i \int_{-\infty}^{\infty} \omega \tilde{\Phi}_{\phi\phi}(x_2, k_1, k_3, \omega)\ \mathrm{d}\omega, \tag{2.61}$$

where $\widehat{(\,\cdot\,)}$ is the spatial Fourier-coefficient with respect to the streamwise and spanwise directions, while $(\,\cdot\,)^*$ marks the complex-conjugate of a value, Equation 2.59 can be rewritten as

$$u_{\mathrm{c},\phi}(x_2, k_1, k_3) = -\frac{\Im\left[\left\langle \widehat{\phi'}^{*} \partial_t \widehat{\phi'} \right\rangle_{(t)}\right]}{k_1 \left\langle \widehat{\phi'}^{*} \widehat{\phi'} \right\rangle_{(t)}}, \tag{2.62}$$

with $\Im(\,\cdot\,)$ being the imaginary part of a complex number. This formulation clearly shows that, instead of spectral information in the temporal direction, only local time derivatives of $\widehat{\phi'}$ are needed to evaluate the convection velocity. Note that in contrast to the previous convection velocities, Equation 2.62 (resp. Equation 2.59) is not superscripted with a number. This is to simplify the notation, since Equation 2.62 is going to be the only definition of $u_{\mathrm{c},\phi}$ used further on.

Calculating a weighted average of these particular convection velocities yields a "natural" definition for the overall convection velocity

$$U_{\mathrm{c},\phi}(x_2) \equiv \frac{\int_{\mathcal{K}} u_{\mathrm{c},\phi}(x_2, k_1, k_3) k_1^2 \widehat{\phi'}^* \widehat{\phi'} \, \mathrm{d}k_1 \mathrm{d}k_3}{\int_{\mathcal{K}} k_1^2 \widehat{\phi'}^* \widehat{\phi'} \, \mathrm{d}k_1 \mathrm{d}k_3}, \tag{2.63}$$

as stated by Del Álamo and Jiménez. $\mathcal{K}$ is the space of wavenumbers that contributes to the overall convection velocity. Here, the wavenumber-dependent convection velocities are weighted by the energy contained within each respective scale. What makes this definition "natural" is the fact that it is equivalent to finding the overall convection velocity, which minimises the difference between the temporal evolutions of $\phi(x,t)$ and $\phi(x - tU_{\mathrm{c},\phi}, t_0)$, thereby best-approximating Taylor's hypothesis (Equation 2.50).

3. Simulations and post-processing

3.1. DNS solver

As mentioned in section 2.2, the behaviour of plane channel flow, analysed within this thesis, is simulated through DNSs. To do so, an in-house solver from the *Institute of Fluid Mechanics* (ISTM) of the *Karlsruhe Institute of Technology* (KIT) is used. The solver is based on the algorithms described by Luchini and Quadrio 2005. For the sake of computational efficiency, the velocity field is not calculated by solving the dimensionless mass balance (Equation 2.15) and the dimensionless NSE (Equation 2.16), but rather by solving two scalar equations. This equivalent formulation of a fluid mechanical problem was first introduced by Kim et al. 1987. The two scalar equations consist of a fourth-order equation for the wall-normal velocity component

$$\partial_t \Delta u_2 = -\partial_{x_2} \left(\partial_{x_1} H_1 + \partial_{x_3} H_3 \right) + \partial^2_{x_1 x_1} H_2 + \partial^2_{x_3 x_3} H_2 + \frac{1}{Re} \Delta^2 u_2, \tag{3.1}$$

as well as an additional second-order equation for the wall-normal vorticity component

$$\partial_t \omega_2 = \partial_{x_3} H_1 - \partial_{x_1} H_3 + \frac{1}{Re} \Delta \omega_2. \tag{3.2}$$

Here, $\Delta^2(\cdot)$ is the biharmonic operator and $\boldsymbol{H}$ is a tensor containing the non-linear convection and the forcing terms of the original formulation. The streamwise and the spanwise velocity components are recovered by solving a system of equations

$$-\partial_{x_2} u_2 = \partial_{x_1} u_1 + \partial_{x_3} u_3, \tag{3.3}$$

$$\omega_2 \equiv \partial_{x_3} u_1 - \partial_{x_1} u_3, \tag{3.4}$$

comprised of the continuity equation and the definition of the wall-normal vorticity component, respectively. As mentioned by Kim et al. 1987, pressure computation is not required during run-time, since no information from p is needed for time advancement. If needed, the pressure fields can be reconstructed from the velocity fields in any suitable way after the simulation has run.
Luchini and Quadrio 2005 explain the use of a spectral discretisation in the two statistically homogeneous directions. This is a natural choice, since periodic boundary conditions are employed in the streamwise and the spanwise directions, as mentioned in section 2.2. They further note the important advantage of Equation 3.3 and Equation 3.4 becoming an *algebraic* system of equations after being Fourier-transformed, as

$$-\partial_{x_2} \widehat{u}_2 = i k_1 \widehat{u}_1 + i k_3 \widehat{u}_3, \tag{3.5}$$

$$\widehat{\omega}_2 = i k_3 \widehat{u}_1 - i k_1 \widehat{u}_3. \tag{3.6}$$

The Fourier-representation of Equation 3.1, Equation 3.2 and the dimensionless transport equation of a passive scalar (Equation 2.17) are

$$\partial_t \left(-k_1^2 \widehat{u}_2 + \partial_{x_2 x_2}^2 \widehat{u}_2 - k_3^2 \widehat{u}_2 \right) = -\partial_{x_2} \left(i k_1 \widehat{H}_1 + i k_3 \widehat{H}_3 \right) - \left(k_1^2 + k_3^2 \right) \widehat{H}_2 + \frac{1}{Re} \left(k_1^4 \widehat{u}_2 - 2k_1^2 \partial_{x_2 x_2}^2 \widehat{u}_2 + \partial_{x_2 x_2 x_2 x_2}^4 \widehat{u}_2 - 2k_3^2 \partial_{x_2 x_2}^2 \widehat{u}_2 + 2k_1^2 k_3^2 \widehat{u}_2 + k_3^4 \widehat{u}_2 \right), \tag{3.7}$$

$$\partial_t \widehat{\omega}_2 = i k_3 \widehat{H}_1 - i k_1 \widehat{H}_3 + \frac{1}{Re} \left(-k_1^2 \widehat{\omega}_2 + \partial_{x_2 x_2}^2 \widehat{\omega}_2 - k_3^2 \widehat{\omega}_2 \right), \tag{3.8}$$

$$\partial_t \widehat{\theta} = -i k_1 \widehat{(u_1 \theta)} - \partial_{x_2} \widehat{(u_2 \theta)} - i k_3 \widehat{(u_3 \theta)} + \frac{1}{Re\, Pr} \left(-k_1^2 \widehat{\theta} + \partial_{x_2 x_2}^2 \widehat{\theta} - k_3^2 \widehat{\theta} \right) + \widehat{Q}, \tag{3.9}$$

respectively. Note that the Fourier coefficients of $\boldsymbol{H}$ in Equation 3.7 and Equation 3.8, as well as the Fourier coefficients of the non-linear terms contained within Equation 3.9, are calculated by inverse Fourier-transforming their parts into physical space, calculating the products there, and Fourier-transforming them back into wavenumber-space afterwards. This is done using Fast-Fourier-Transformation (FFT) algorithms, as mentioned by Luchini and Quadrio 2005. Luchini and Quadrio also explain that, by expanding the number of collocation points in physical space by a factor of 1.5 or more, the non-linear products are calculated with identical accuracy as if they were calculated in wavenumber-space. This expansion of the number of collocation points is called "de-aliasing". It is important to mention that the system of equations 3.5 to 3.8 becomes singular when considering the zero modes ($k_1 = k_3 = 0$), representative of the spatial mean values. Therefore, only non-zero modes are calculated by this procedure, while another set of equations is implemented for the averaged velocity components. These equations are analogous to the RANS equations, although the averages of Equation 2.10 are taken over the physical domain instead of an ensemble. This set of equations can then be solved since the non-linear terms of fluctuating values are known a priori from the solution of equations 3.5 to 3.8.
For discretisation of the wall-normal derivatives, Luchini and Quadrio 2005 employ a high-accuracy compact finite difference scheme, based on the formulation introduced by Lele 1992. However, because the third wall-normal derivative is absent in the governing equations, Luchini and Quadrio can explicitly determine the compact finite difference coefficients without solving a linear system of equations. In their implementation, they use a stencil of five adjacent grid points. This is adopted in the present work. An inhomogeneous grid is used for the spacing of the wall-normal collocation points. The position of each point (of index $j \in \mathbb{N} \cap [0, n_2]$) inside the channel, normalised by the channel half-width, is given by

$$\frac{x_2(j)}{h} = \frac{\tanh\left(s \left(\frac{2j}{n_2} - 1 \right) \right)}{\tanh(s)} + 1 \tag{3.10}$$

with the spacing parameter s and the number of wall-normal nodes n_2. Here, $\tanh(\,\cdot\,)$ denotes the hyperbolic tangent and $\mathbb{N}$ is the set of natural numbers. The grid is additionally extended by a plane of ghost-nodes "inside" each wall of the channel for better application of the wall-normal boundary conditions. The boundary conditions for $\widehat{u}_2$ and $\widehat{\omega}_2$ originate from the no-slip and impermeability conditions, introduced in subsection 2.2.1. By additionally considering the continuity equation as well as the definition of the wall-normal vorticity component, the boundary conditions for the flow field are given by

$$\widehat{u}_2 \Big|_{\mathrm{w}} = 0, \tag{3.11}$$

$$\partial_{x_2} \widehat{u}_2 \Big|_{\mathrm{w}} = 0, \tag{3.12}$$

$$\widehat{\omega}_2 \Big|_{\mathrm{w}} = 0. \tag{3.13}$$

Since the equations 3.11, 3.12 and 3.13 apply to both walls of the channel, they represent six individual conditions (for each non-zero Fourier-mode), thereby closing the system

of equations 3.5 to 3.8. The equations used to calculate the mean velocity components (zero modes) are closed directly by the no-slip and impermeability boundary conditions, mentioned in subsection 2.2.1. The boundary conditions for $\widehat{\theta}$ likewise originate from the conditions introduced in subsection 2.2.1. This results in the relationship

$$\widehat{\theta}\Big|_{\mathrm{w}} = 0, \tag{3.14}$$

for each Fourier-mode at both channel walls, closing Equation 3.9. Note that even though not *physically* needed, additional boundary conditions for the wall-normal vorticity component and the passive scalars are employed, due to these fields being enlarged by the planes of ghost-nodes as well. As additional conditions, the strongest possible constraints on the smoothness of the respective fields are chosen by forcing their fourth wall-normal derivatives to vanish at the wall, as

$$\partial^4_{x_2x_2x_2x_2}\widehat{\omega}_2\Big|_{\mathrm{w}} = 0, \tag{3.15}$$

$$\partial^4_{x_2x_2x_2x_2}\widehat{\theta}\Big|_{\mathrm{w}} = 0. \tag{3.16}$$

Luchini and Quadrio 2005 use a partially implicit memory-optimised method for time integration. This method consists of an explicit third-order low-storage Runge-Kutta method for discretising the non-linear and forcing terms combined with an implicit second-order Crank-Nicolson scheme for discretising the viscous terms. The governing equations are therefore integrated in time by two consecutive steps, as described by Luchini and Quadrio. First, the explicit terms on the right-hand side are assembled. This is done per wall-parallel plane, since Fourier-transformations of the non-linear terms need information of the whole (k_1-k_3)-space per wall-normal position x_2. Second, the viscous terms are implicitly time-integrated with the (at this point known) rest of the right-hand side. This is done per wall-normal line, since the finite differences discretisation of the wall-normal derivatives require information over all wall-normal positions x_2 for each wavenumber-pair of the (k_1-k_3)-space.

3.2. Simulation setups

In the scope of this thesis, four DNSs of turbulent plane channel flow are conducted. They can be classified into two groups. One "preliminary" (pre.) simulation and three "main" simulations at different Reynolds numbers. The latter are conducted after analysing the results of the former. This analysis is further described in section 4.1. Note that the Reynolds number for each simulation is set by choice of the dimensionless kinematic viscosity ν. In addition to solving for the velocity and pressure fields (p is reconstructed during post-processing, as mentioned in section 3.1), each simulation also evaluates the behaviour of three passive scalars of ranging Prandtl numbers. The resolution of the grid in x_2-direction (physical space) is controlled by the number of wall-normal nodes n_2. The spectral resolution in the statistically homogeneous directions (wavenumber-space) is set by the numbers m_1 and m_3 of modes in the k_1 and the k_3 "directions", respectively. Note that the numbers of modes, as stated here, also consider negative wavenumbers. The spacing of the wall-normal nodes is given by Equation 3.10, as explained in section 3.1, and is thereby controlled by the spacing parameter s. The last parameters characterising each simulation setup are the dimensions of the periodic box. When normalised by the channel half-width h, the channel width becomes 2 in all cases, trivially. The periodic lengths L_1 and L_3 of the respective streamwise and spanwise directions are however controlled by the

base wavenumbers α_0 and β_0, as

$$\frac{L_1}{h} = \frac{2\pi}{\alpha_0}, \tag{3.17}$$

$$\frac{L_3}{h} = \frac{2\pi}{\beta_0}. \tag{3.18}$$

The base wavenumbers additionally determine the spectral-bins governed by every discrete mode and their corresponding wavenumbers. Note that the latter are mirrored at zero, so that the wavenumber-ranges are $k_1 \in [-\alpha_0(m_1-1)/2, \alpha_0(m_1-1)/2]$ and $k_3 \in [-\beta_0(m_3-1)/2, \beta_0(m_3-1)/2]$, respectively.
A summary of all simulations and their characterising parameters is shown in Table 3.1. Forcing of the flow is controlled by adjusting the bulk velocity after each time step to equal unity. This is important to note, since by this approach, the friction velocity u_τ is *not* forced to a specific value at each time step. As a result, the desired friction Reynolds numbers (seen in Table 3.1) might only be reached approximately. The passive scalars are forced similarly by setting their bulk value to unity after each time step. The forcing is thereby already integrated into the respective field values, and no volume force or scalar source term is present, respectively. However, this has a negligible impact on the resulting data, since the forcing is about four orders of magnitude smaller than the respective field values in every case considered.

Case	Type	Re_τ	Re_b	Pr	n_2	m_1	m_3	s	L_1/h	L_3/h
p180	pre.	180	5600	[0.025, 0.71, 1]	161	191	193	1.5	4π	2π
m180	main	180	5600	[0.025, 0.4, 1]	161	383	193	1.5	8π	2π
m500	main	500	18170	[0.025, 0.4, 1]	251	1023	257	1.66	8π	2π
m1000	main	1000	40000	[0.025, 0.4, 1]	501	2047	1025	1.66	8π	2π

Table 3.1.: Simulation cases and variable parameters

Other parameters used in the simulations are the (dimensionless) density $\rho = 1$, the (dimensionless) specific heat capacity at constant pressure $c_\mathrm{p} = 1$ and the upper limit for the Courant-Friedrichs-Lewy number $CFL_\mathrm{max} = 1$. The latter dynamically adjusts the time-step size to maintain numerical stability during the simulation run-time. In contrast to most parameters in Table 3.1, these values are set once and remain unchanged throughout all simulations.

3.3. Selected aspects of implementation

There are important aspects to consider when working with discretely distributed values, as is done in the simulations and post-processing conducted throughout this thesis.
This is of particular relevance when integrating with respect to the wall-normal direction, since the wall-normal nodes are *not* distributed homogeneously along the channel width. For these integrals, which are used, for example, when calculating the bulk values Equation 2.43 and Equation 2.44, a quadrature scheme based on the Simpson rule is implemented.
In addition to the discrete distribution of the wall-normal nodes, the "spacing" of the Fourier modes must be considered. This is the case since the spectral solver exactly evaluates the energy contained within each wavenumber-bin. However, since the sizes of

these bins are controlled by the values of α_0 and β_0, their energy is also dependent on this spectral resolution. It is, therefore, useful to calculate the respective energy density of each wavenumber-bin by dividing its energy by the respective base wavenumber. The resulting energy density of each mode, represented by the wavenumber spectrum (Equation 2.36), is a quantity independent of the spectral resolution employed in the solver.
Since the analysis of turbulence requires the averages of quantities to be computed, as mentioned in subsection 2.1.1, these calculations need to be evaluated on discrete data as well. There are three general averaging operators applied in the following evaluations. First, arithmetic averaging in time, where the mean of each data point in the discrete (x_1-x_2-x_3)-space is calculated via all its corresponding values per time step, or at least over those fields saved for post-processing, as

$$\langle\phi\rangle_{(t)}(x_1, x_2, x_3) \equiv \frac{1}{n_{\mathrm{ts}}} \sum_{n=1}^{n_{\mathrm{ts}}} \phi(x_1, x_2, x_3, t(n)), \tag{3.19}$$

where n_{ts} is the number of time steps considered. The second and third averaging operators are the arithmetic means in the statistically homogeneous directions. If a flow variable is considered in the physical (x_1-x_2-x_3)-space, spatial means of each point in this domain are calculated via all their corresponding points in the streamwise or spanwise directions, as

$$\langle\phi\rangle_{(x_1)}(x_2, x_3, t) \equiv \frac{1}{n_1} \sum_{n=1}^{n_1} \phi(x_1(n), x_2, x_3, t), \tag{3.20}$$

$$\langle\phi\rangle_{(x_3)}(x_1, x_2, t) \equiv \frac{1}{n_3} \sum_{n=1}^{n_3} \phi(x_1, x_2, x_3(n), t), \tag{3.21}$$

respectively. Here, n_1 and n_3 are the corresponding numbers of collocation points in the statistically homogeneous directions of the physical space. Note that Equation 3.20 and Equation 3.21 do not necessarily have to be evaluated in physical space. A spatial average in, for example, the x_1-direction can also be "calculated" by only considering the respective modes corresponding to $k_1 = 0$. A similar approach is possible for spatial means in the x_3-direction. In addition to these three general operators, other symmetries in the data might be used for averaging. However, these depend on the individual quantity considered and will be introduced when applied. It is also possible to average in more than one way simultaneously.
As mentioned in section 3.1, the pressure field is not calculated during run-time but a posteriori, when it is needed for post-processing. In that case, p is calculated by solving the pressure Poisson equation using the saved velocity fields. This is done using an in-house code which utilises the same spectral (k_1 and k_3) and spatial (x_2) resolutions, as well as the same derivation schemes, as the main DNS solver. Since the wall-normal pressure gradient is needed as well during post-processing, it is also calculated by solving a Poisson equation, this time for $\partial_{x_2} p$ directly. Note that this is done to avoid deriving the pressure field in the wall-normal direction for reasons of computational precision, as explained in detail in subsection A.2.
To implement the previously selected convection velocity definition, an approximation of the local time derivative, present in the numerator of Equation 2.62, is needed. Del Álamo and Jiménez 2009 state that every appropriate approximation is valid. They further recommend reconstructing the time derivative terms of each quantity from the respective equation of motion. This approach is used in the scope of this thesis. Therefore, to calculate the convection velocity of turbulent u_1-structures, the first component of Equation 2.11 is considered. This equation is then Fourier-transformed, multiplied by $\widehat{u_1'}^*$ and averaged in time. Some of the non-linear terms still present in Equation 2.11 vanish due to the linearity of Fourier-transforming and averaging. Due to the setup, explained in section 3.2, the

volume force term vanishes as well (which is also the case for the other velocity components and the passive scalars). Taking the negative imaginary part of the resulting equation and dividing by the denominator of Equation 2.62 then yields the convection velocity

$$
\begin{aligned}
u_{\mathrm{c},u_1}(x_2,k_1,k_3) = \langle u_1\rangle_{(t,x_1,x_3)} &+ \frac{k_1\Re\left[\frac{1}{\rho}\left\langle \widehat{u_1'}^{*}\widehat{p'}\right\rangle_{(t,x_1,x_3)} + \left\langle \widehat{u_1'}^{*}\widehat{(u_1'u_1')}\right\rangle_{(t,x_1,x_3)}\right]}{k_1\left\langle \widehat{u_1'}^{*}\widehat{u_1'}\right\rangle_{(t,x_1,x_3)}} \\
&+ \frac{k_3\Re\left[\left\langle \widehat{u_1'}^{*}\widehat{(u_1'u_3')}\right\rangle_{(t,x_1,x_3)}\right] + \Im\left[\left\langle \widehat{u_1'}^{*}\widehat{u_2'}\right\rangle_{(t,x_1,x_3)}\partial_{x_2}\langle u_1\rangle_{(t,x_1,x_3)}\right]}{k_1\left\langle \widehat{u_1'}^{*}\widehat{u_1'}\right\rangle_{(t,x_1,x_3)}} \\
&+ \frac{\Im\left[-\nu\left\langle \widehat{u_1'}^{*}\partial^2_{x_2x_2}\widehat{u_1'}\right\rangle_{(t,x_1,x_3)} + \left\langle \widehat{u_1'}^{*}\partial_{x_2}\widehat{(u_1'u_2')}\right\rangle_{(t,x_1,x_3)}\right]}{k_1\left\langle \widehat{u_1'}^{*}\widehat{u_1'}\right\rangle_{(t,x_1,x_3)}},
\end{aligned}
\tag{3.22}
$$

as it is implemented in the post-processing script used throughout this thesis. Here, $\Re(\,\cdot\,)$ is the real part of a complex number. A Reynolds decomposition is applied, isolating the mean streamwise velocity profile (first term on the right-hand side of Equation 3.22). A similar procedure is used to derive the implemented convection velocity of turbulent u_2-structures

$$
\begin{aligned}
u_{\mathrm{c},u_2}(x_2,k_1,k_3) = \langle u_1\rangle_{(t,x_1,x_3)} &+ \frac{k_1\Re\left[\left\langle \widehat{u_2'}^{*}\widehat{(u_2'u_1')}\right\rangle_{(t,x_1,x_3)}\right] + k_3\Re\left[\left\langle \widehat{u_2'}^{*}\widehat{(u_2'u_3')}\right\rangle_{(t,x_1,x_3)}\right]}{k_1\left\langle \widehat{u_2'}^{*}\widehat{u_2'}\right\rangle_{(t,x_1,x_3)}} \\
&+ \frac{\Im\left[\frac{1}{\rho}\left\langle \widehat{u_2'}^{*}\partial_{x_2}\widehat{p'}\right\rangle_{(t,x_1,x_3)} - \nu\left\langle \widehat{u_2'}^{*}\partial^2_{x_2x_2}\widehat{u_2'}\right\rangle_{(t,x_1,x_3)}\right]}{k_1\left\langle \widehat{u_2'}^{*}\widehat{u_2'}\right\rangle_{(t,x_1,x_3)}} \\
&+ \frac{\Im\left[\left\langle \widehat{u_2'}^{*}\partial_{x_2}\widehat{(u_2'u_2')}\right\rangle_{(t,x_1,x_3)}\right]}{k_1\left\langle \widehat{u_2'}^{*}\widehat{u_2'}\right\rangle_{(t,x_1,x_3)}}.
\end{aligned}
\tag{3.23}
$$

Note that, in contrast to Equation 3.22, Equation 3.23 contains no wall-normal gradient of the mean field, since only the streamwise velocity component has a non-vanishing contribution to the averaged flow field of turbulent plane channel flow, as stated by Del Álamo and Jiménez 2009. However, Equation 3.23 also contains the mean streamwise velocity profile, resulting from the applied Reynolds decomposition. The convection velocity of turbulent u_3-structures, as it is implemented in the scope of this thesis, takes the form

$$
\begin{aligned}
u_{\mathrm{c},u_3}(x_2,k_1,k_3) = \langle u_1\rangle_{(t,x_1,x_3)} &+ \frac{k_1\Re\left[\left\langle \widehat{u_3'}^{*}\widehat{(u_3'u_1')}\right\rangle_{(t,x_1,x_3)}\right] + k_3\Re\left[\frac{1}{\rho}\left\langle \widehat{u_3'}^{*}\widehat{p'}\right\rangle_{(t,x_1,x_3)}\right]}{k_1\left\langle \widehat{u_3'}^{*}\widehat{u_3'}\right\rangle_{(t,x_1,x_3)}} \\
&+ \frac{k_3\Re\left[\left\langle \widehat{u_3'}^{*}\widehat{(u_3'u_3')}\right\rangle_{(t,x_1,x_3)}\right] + \Im\left[-\nu\left\langle \widehat{u_3'}^{*}\partial^2_{x_2x_2}\widehat{u_3'}\right\rangle_{(t,x_1,x_3)}\right]}{k_1\left\langle \widehat{u_3'}^{*}\widehat{u_3'}\right\rangle_{(t,x_1,x_3)}} \\
&+ \frac{\Im\left[\left\langle \widehat{u_3'}^{*}\partial_{x_2}\widehat{(u_3'u_2')}\right\rangle_{(t,x_1,x_3)}\right]}{k_1\left\langle \widehat{u_3'}^{*}\widehat{u_3'}\right\rangle_{(t,x_1,x_3)}}.
\end{aligned}
\tag{3.24}
$$

As it is the case for Equation 3.23, there is again no mean wall-normal gradient term in Equation 3.24. Nevertheless, because of the Reynolds decomposition, there is once again a contribution of the mean streamwise velocity profile. The implemented equation for the convection velocity of turbulent θ-structures

$$\begin{aligned} u_{\mathrm{c},\theta}(x_2,k_1,k_3) = \langle u_1\rangle_{(t,x_1,x_3)} &+ \frac{k_1\Re\left[\left\langle\widehat{\theta'}^{*}\widehat{(\theta' u_1')}\right\rangle_{(t,x_1,x_3)}\right] + k_3\Re\left[\left\langle\widehat{\theta'}^{*}\widehat{(\theta' u_3')}\right\rangle_{(t,x_1,x_3)}\right]}{k_1\left\langle\widehat{\theta'}^{*}\widehat{\theta'}\right\rangle_{(t,x_1,x_3)}} \\ &+ \frac{\Im\left[\left\langle\widehat{\theta'}^{*}\widehat{u_2'}\right\rangle_{(t,x_1,x_3)}\partial_{x_2}\langle\theta\rangle_{(t,x_1,x_3)} - a\left\langle\widehat{\theta'}^{*}\partial^2_{x_2x_2}\widehat{\theta'}\right\rangle_{(t,x_1,x_3)}\right]}{k_1\left\langle\widehat{\theta'}^{*}\widehat{\theta'}\right\rangle_{(t,x_1,x_3)}} \\ &+ \frac{\Im\left[\left\langle\widehat{\theta'}^{*}\partial_{x_2}\widehat{(\theta' u_2')}\right\rangle_{(t,x_1,x_3)}\right]}{k_1\left\langle\widehat{\theta'}^{*}\widehat{\theta'}\right\rangle_{(t,x_1,x_3)}}, \end{aligned} \tag{3.25}$$

shows some resemblances to Equation 3.22, due to the similarity of passive scalar and streamwise momentum transport. Since the mean passive scalar field does not vanish for turbulent plane channel flow, Equation 3.25 contains a mean wall-normal gradient term, as it is also the case for Equation 3.22. However, the convection velocity implementation of passive scalar structures differs from the equations 3.22 to 3.24 in terms of the pressure term. It is absent in the former since the pressure field has no direct influence on the transport of a passive scalar. Like for the convection velocities of velocity-structures, Equation 3.25 contains the mean streamwise velocity component. This emphasises again that the considered convection velocities are all oriented in the streamwise direction. Note the importance of this, when working with equations 3.22 to 3.24, since these are streamwise convection velocities of turbulent structures characterised by the components of the velocity tensor and *not* individual components of a "convection velocity tensor". Implementing the convection velocities using the respective equations of motion has the additional advantage of allowing for selective interpretations of individual terms contributing to the convection velocities, as mentioned by Del Álamo and Jiménez 2009. A detailed analysis of this is conducted in section 4.3. However, equations 3.22 to 3.25 already show the influence of pressure, convection and diffusion/conduction to a certain extent. This analysis is made possible by individually calculating every average seen in the convection velocity equations and summing them up afterwards. To do so, the individual fields are taken from the DNS time steps, which were saved for post-processing, and assembled into the terms of equations 3.22 to 3.25 in wavenumber-space. Only the Fourier-coefficients of the non-linear terms are calculated by inverse Fourier-transforming their parts, calculating the products in physical space and Fourier-transforming their products back into wavenumber-space. This is done using FFT algorithms, like in the DNS-solver itself, as is described in section 3.1.

4. Results

4.1. Preliminary investigation and validation

The preliminary simulation "p180" is carried out as a first step of data generation. The parameters characterising p180 are listed in Table 3.1. The purpose of a preliminary investigation, based on the data obtained from p180, is to analyse whether certain simulation parameters need to be adjusted before running the main simulations "m180", "m500", and "m1000" (also listed in Table 3.1). This is done by evaluating typical statistics of turbulent plane channel flow, presented, for example, by Kim et al. 1987, Kim and Moin 1990, Kawamura et al. 1998, Kong et al. 2000, Piller 2005, Ould-Rouiss et al. 2013 and Pirozzoli et al. 2016. In addition to the information taken from the statistics, comparisons to literature data are used for further validation. This validation is later repeated for the data obtained from m180, m500 and m1000. However, in this chapter, only the validation of p180 is discussed in detail since the procedure is equivalent for all simulations. The typical statistics of turbulent plane channel flow for the three main simulations are depicted in section B. All time averages (Equation 3.19) applied throughout this thesis are taken over a number of $n_{\mathrm{ts}} = 100$ fields, unless otherwise specified.
Figure 4.1 shows the mean profiles of the velocity components (4.1a) and passive scalars (4.1b) over the wall distance in viscous units. Only half of the channel width is represented, as the statistics are symmetric with respect to the channel mid-plane, as mentioned by Kim et al. 1987 and Kim and Moin 1990. The data show the typical behaviour expected from the analytical considerations of turbulent plane channel flow, introduced in subsection 2.2.1 and subsection 2.2.3. The mean wall-normal and mean spanwise velocity components vanish over the whole channel width, while the mean streamwise velocity component exhibits the characteristic separation into different wall layers. In the case of the log-law (Equation 2.47), a dashed grey line with $\kappa = 0.4$ and $B = 5.6$ is also plotted in Figure 4.1a. For comparison, the mean streamwise velocity profile of a similar simulation, executed by Abe et al. 2004, is additionally shown. This curve is in good agreement with the data obtained from p180, even though the actual friction Reynolds numbers of both simulations are not a perfect match due to the type of forcing employed in this thesis, as explained in section 3.2. The mean scalar fields follow the expected analytical behaviour as well. For all Prandtl numbers, a linear trend is seen in the respective molecular sublayer. The two scalars with $Pr = 0.71$ and $Pr = 1$ also show a scalar log layer close to the centre of the channel. Two logarithmic curves (defined by Equation 2.49) are plotted for comparison with $(C_1, C_2) = (2.46, 2.8)$ and $(C_1, C_2) = (2.5, 5.6)$ for the medium and large Prandtl numbers, respectively. For the mean passive scalar field with $Pr = 0.71$, literature data is used for further validation. The dotted line in Figure 4.1b shows the results of a simulation conducted by Horiuti 1992. Both curves are in good agreement with each other. The slight divergence between the literature data and the results obtained from p180 near the channel centre could be attributed to the fact that Horiuti 1992 simulated a passive scalar with $Pr = 0.7$, which is slightly less than the Prandtl number considered in the present case.
Figure 4.2 depicts the independent components of the Reynolds stress tensor over the wall distance in viscous units. Again, only half the channel width is plotted due to the present symmetry, mentioned by Kim et al. 1987. The data shown depict the expected behaviour. Especially $\langle u_1' u_2' \rangle$ exhibiting a zero crossing in the centre of the channel, as well as $\langle u_1' u_3' \rangle$

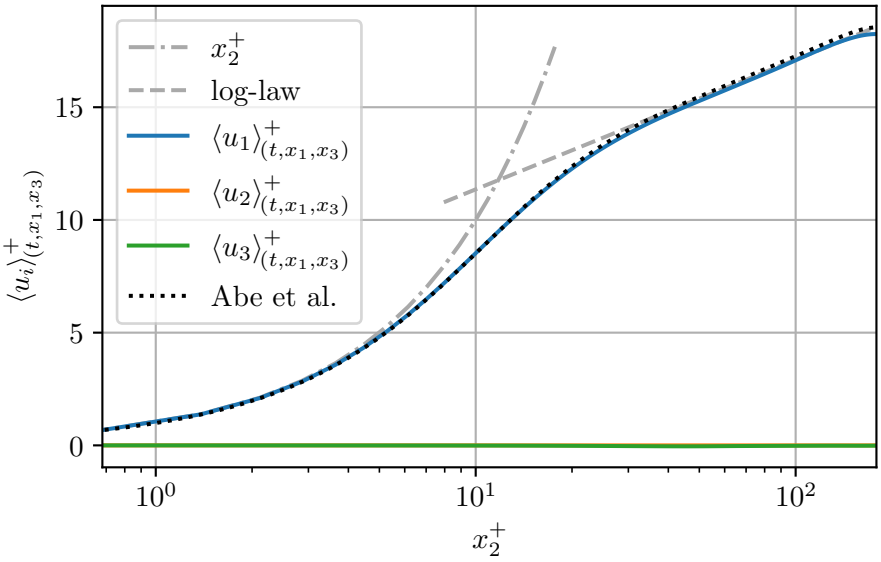

(a) Mean velocity profiles

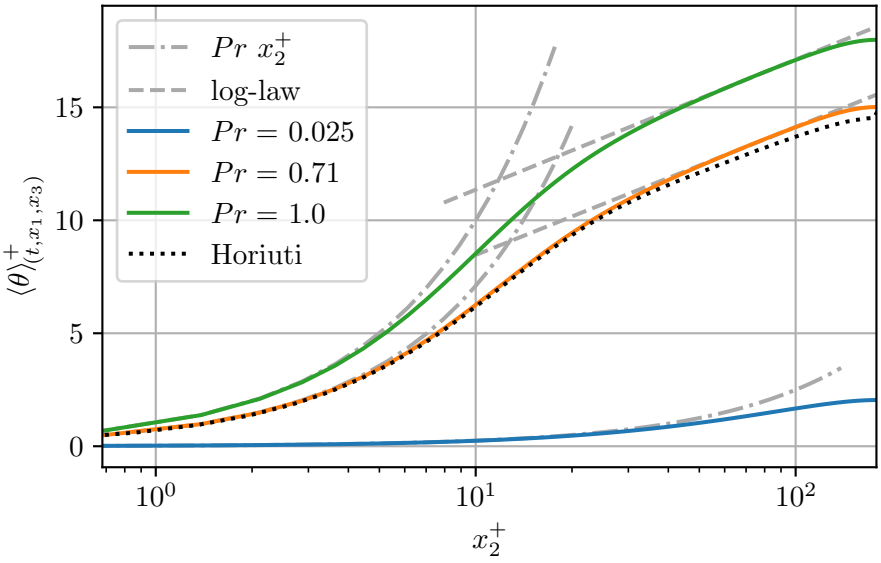

(b) Mean scalar profiles

Figure 4.1.: Mean quantities in turbulent plane channel flow (case p180)

and $\langle u_2' u_3' \rangle$ vanishing altogether, agree well with the theory introduced in subsection 2.2.2. The results of Abe et al. 2004 are again used for comparison. The literature data are in good agreement with the results obtained from p180, as it is the case for the mean streamwise velocity field. The minimal differences in the curves, plotted in Figure 4.2, might result from slightly different friction Reynolds numbers, as mentioned before. In Figure 4.3, one-point correlations of the scalar fields with themselves as well as the velocity components are shown for each Prandtl number individually. The respective values are plotted with respect to the wall distance in viscous units. Therefore, these quantities are somewhat analogous to the Reynolds stresses shown in Figure 4.2. When comparing the graphs for $Pr = 0.025$, $Pr = 0.71$ and $Pr = 1$ in Figure 4.3a, 4.3b and 4.3c, respectively, it is evident that larger Prandtl numbers correspond to larger correlation values. This is also shown by Kim and Moin 1990. Additionally, the peak of all non-zero components moves closer to the channel wall with increasing Pr, which is mentioned by Kim and Moin 1990 as well. The Reynolds analogy of momentum and scalar transport can be observed in the

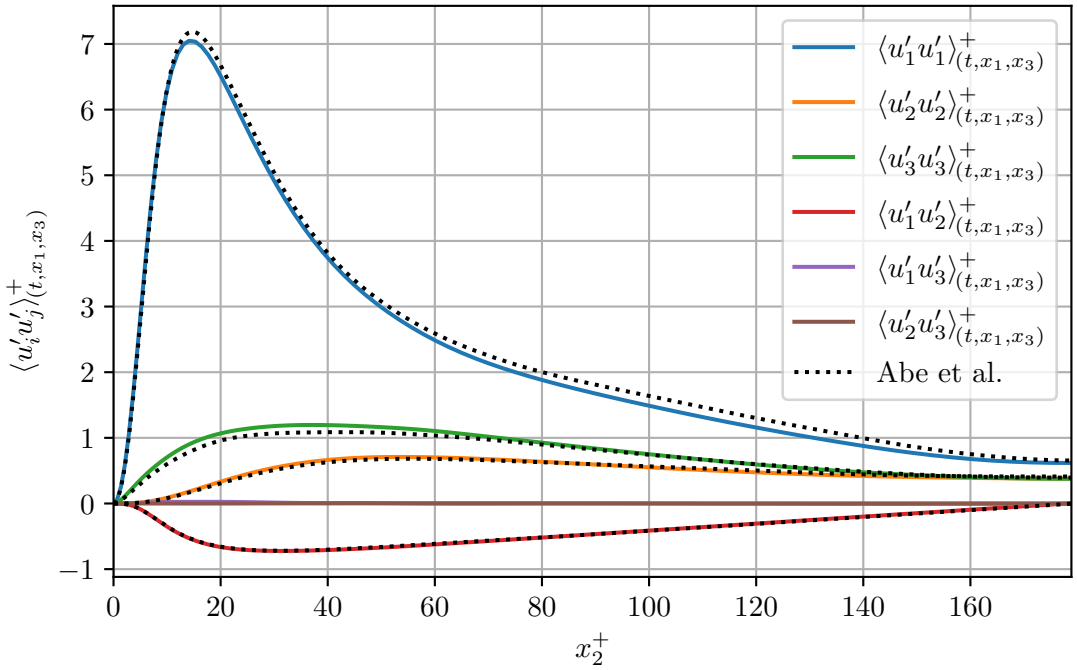

Figure 4.2.: Reynolds stress profiles (case p180)

similarity of Figure 4.3 and Figure 4.2, especially in the case of $Pr = 1$. Regarding this, it is interesting to note that for the medium and lower Prandtl numbers, $\langle \theta' u_1' \rangle$ shows the highest peak value of all components. Only for the largest Prandtl number, $\langle \theta' \theta' \rangle$ is the component of most influence. The simulation of a passive scalar with $Pr = 0.7$ by Horiuti 1992 was again considered for comparison. Close similarities between these data and the results obtained from p180 can be seen in Figure 4.3b. The small differences between the respective curves can again be attributed to the difference in the Prandtl numbers of both cases.

The good agreement of Figure 4.1, Figure 4.2 and Figure 4.3 with analytical derivations, as well as data from the literature, indicate that the simulation and averaging setups used are capable of reproducing low-order turbulence statistics.

Figure 4.4 shows the mean total, viscous and turbulent shear stresses, as defined by Equation 2.25, 2.26 and 2.27, respectively. The shear stress contributions are plotted with respect to the wall distance, normalised by the channel half-width. The stresses themselves are normalised by the wall shear stress (Equation 2.31) at $x_2 = 0$. The averages entailed within the definitions 2.25, 2.26 and 2.27 are only taken with respect to the statistically homogeneous spatial directions and *not* with respect to time. As a result, the curves, seen in Figure 4.4, still exhibit a significant amount of statistical noise. This is especially visible when considering $x_2/h = 2$, where $\tau/\tau_w = -1$ should hold, due to the geometric symmetry of the channel, mentioned by Kim et al. 1987 and Kim and Moin 1990. However, the reason for considering only one time step at once is to determine whether the flow field is statistically fully developed, in the way it is explained, for example, by Straub et al. 2019. As mentioned in subsection 2.2.2, analytical consideration of a statistically fully developed turbulent plane channel flow leads to the mean total shear stress being linear across the channel. This behaviour is approximately reached at the time step depicted in Figure 4.4. Therefore, the time step shown is considered statistically fully developed and thus chosen as a "starting point" for all time averages taken in the statistical analysis of the quantities obtained from p180. In analogy to the figure of the shear stress contributions, Figure 4.5 depicts the mean total, molecular and turbulent fluxes of each passive scalar, individually. The flux values, defined by Equation 2.28, 2.29 and 2.30, are normalised

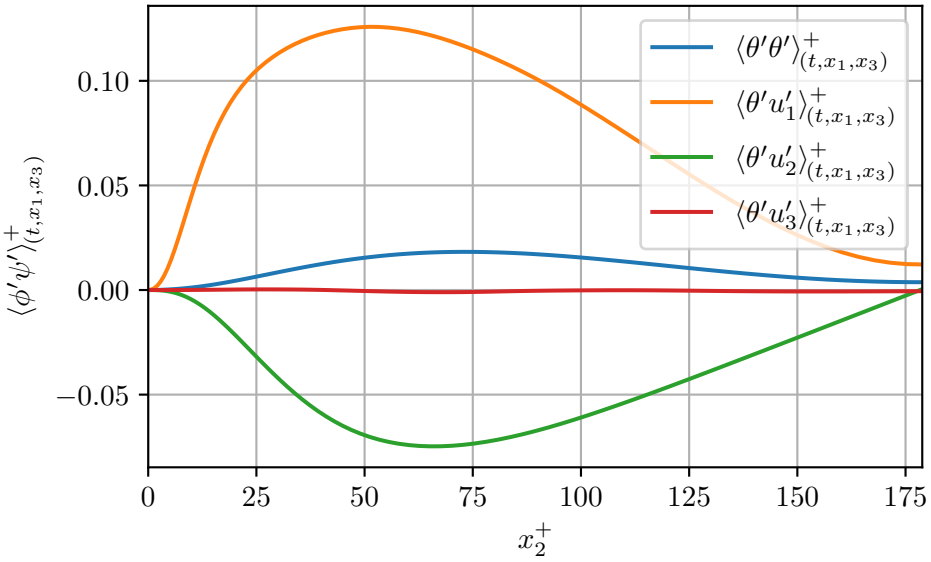

(a) Correlations of passive scalar with $Pr = 0.025$

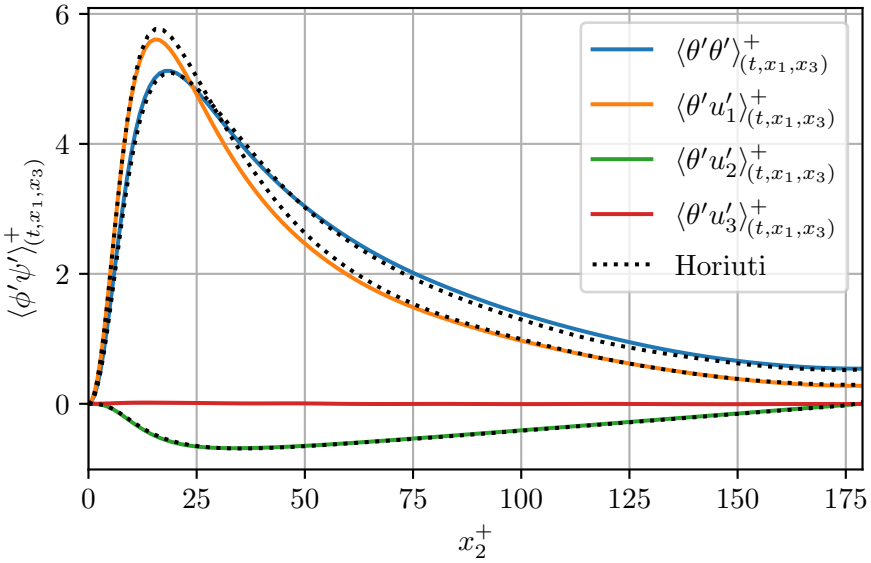

(b) Correlations of passive scalar with $Pr = 0.71$

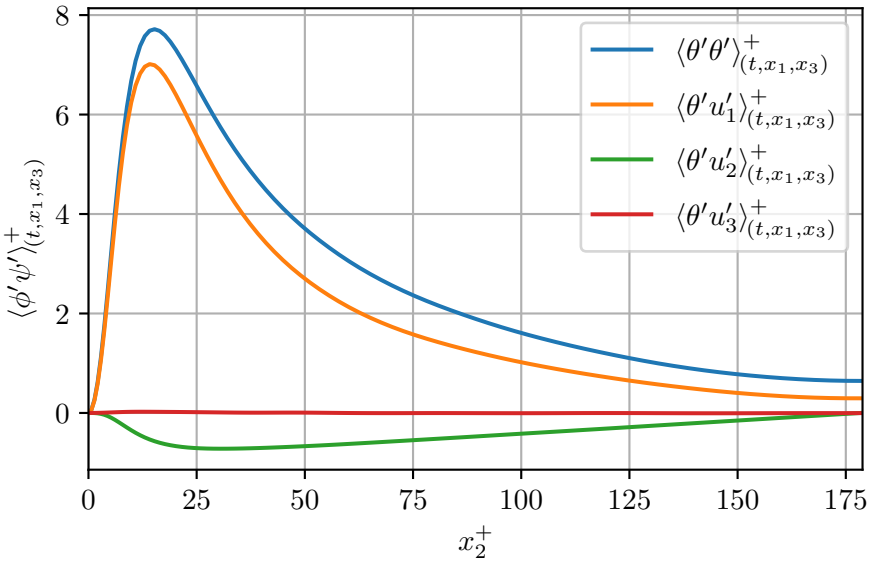

(c) Correlations of passive scalar with $Pr = 1$

Figure 4.3.: One-point correlations of passive scalars (case p180)

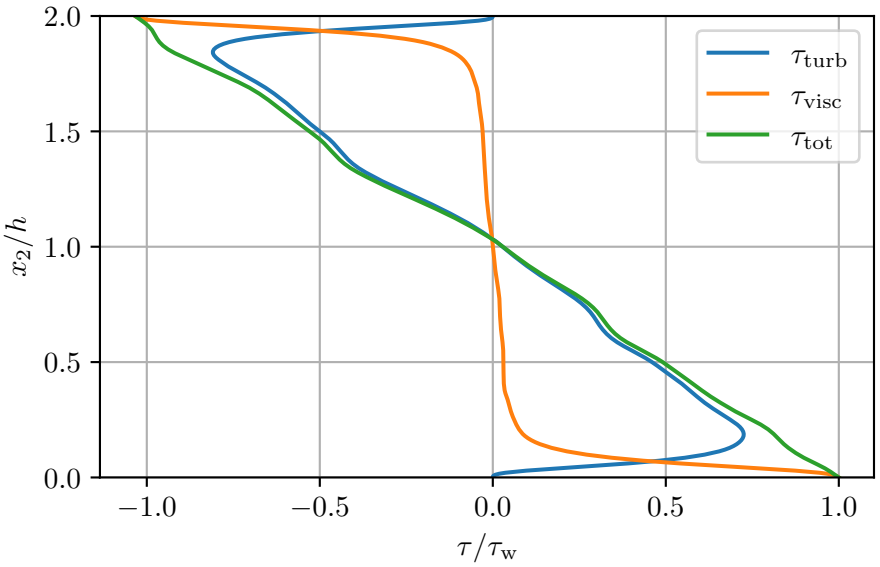

Figure 4.4.: Shear stress contributions (case p180)

by the respective wall scalar fluxes (Equation 2.32) at $x_2 = 0$. The wall distance, over which the individual flux contributions are plotted, is normalised by the channel half-width. Again, all quantities are only averaged in space, while just one single time step is considered. This is done to analyse whether the scalar fields are statistically fully developed as well. The time step depicted is the same as for the velocity field. Figure 4.5a, Figure 4.5b, and Figure 4.5c show close to linear behaviour in their mean total passive scalar fluxes. The scalar fields can therefore be considered statistically fully developed from this point out as well. Note that the contributions of the passive scalar flux for $Pr = 0.025$ in Figure 4.5a show no visible statistical noise. This can be attributed to the fact that the transport of low Prandtl number scalars exhibits "laminar-like" behaviour and therefore less turbulent fluctuations in general, as indicated by Kawamura et al. 1998. This is also apparent when considering the absolute values of q_{turb} for the case with the lowest Prandtl number. The contribution of the turbulent flux to the mean total flux is significantly smaller than in the cases with higher Prandtl numbers. Another interesting behaviour is evident when comparing Figure 4.5b and Figure 4.5c. The statistics of the scalars with $Pr = 0.71$ and $Pr = 1$ are nearly equal.

Figure 4.6 shows the streamwise (space-time) auto-covariance of the velocity components as well as the passive scalars in 4.6a and 4.6b, respectively. The values of $R_{\phi\phi}$, defined by Equation 2.33, are plotted with respect to the streamwise separation, normalised by the channel half-width, r_1/h. The streamwise auto-covariances are normalised by their respective values at vanishing separations $r_1 = 0$. Note that the *auto*-covariance is a special case of the general space-time covariance, where the correlation of a quantity with itself is analysed. According to this, no summation is applied with respect to the index α in Figure 4.6a, as is conventionally the case for Greek indices. The average within the definition of the auto-covariance is taken with respect to both statistically homogeneous spatial directions as well as with respect to time (over 100 statistically fully developed time steps), in these cases. By analysing the behaviour of auto-covariances, it is possible to determine if the periodic box sizes used are large enough to capture the largest scales of turbulent motion, as it is done by Kim et al. 1987 and Piller 2005. In that case, the value of $R_{\phi\phi}$ would approach zero at a separation of half the channel box size, indicating that no structures larger than the total channel box size are present in the flow. Due to the periodic boundary conditions, the auto-covariance is symmetrical with respect to half the streamwise periodic box size, which is why a maximum streamwise separation of only

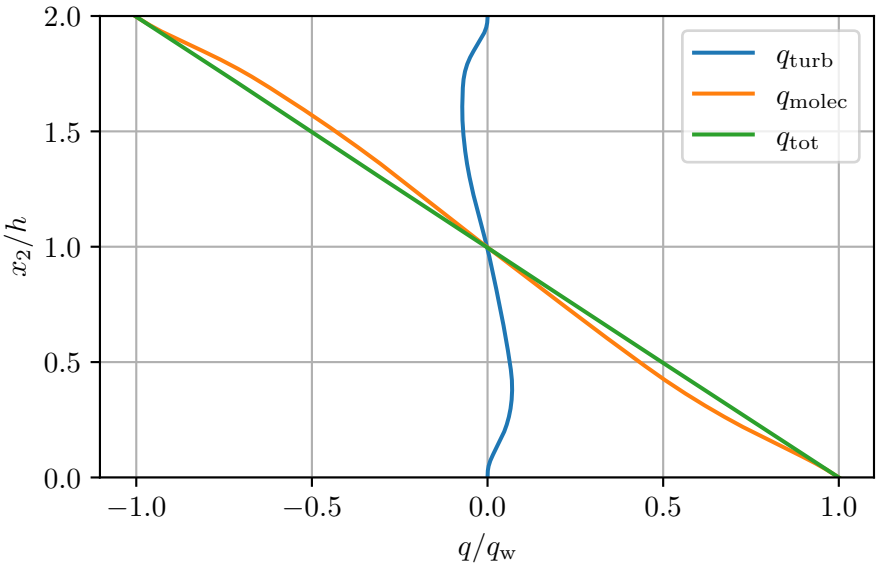

(a) Flux of passive scalar with $Pr = 0.025$

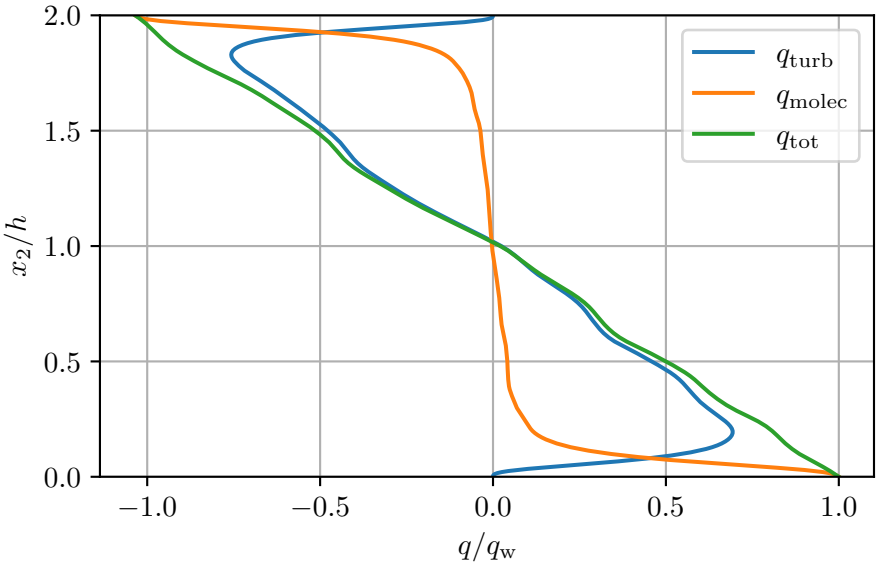

(b) Flux of passive scalar with $Pr = 0.71$

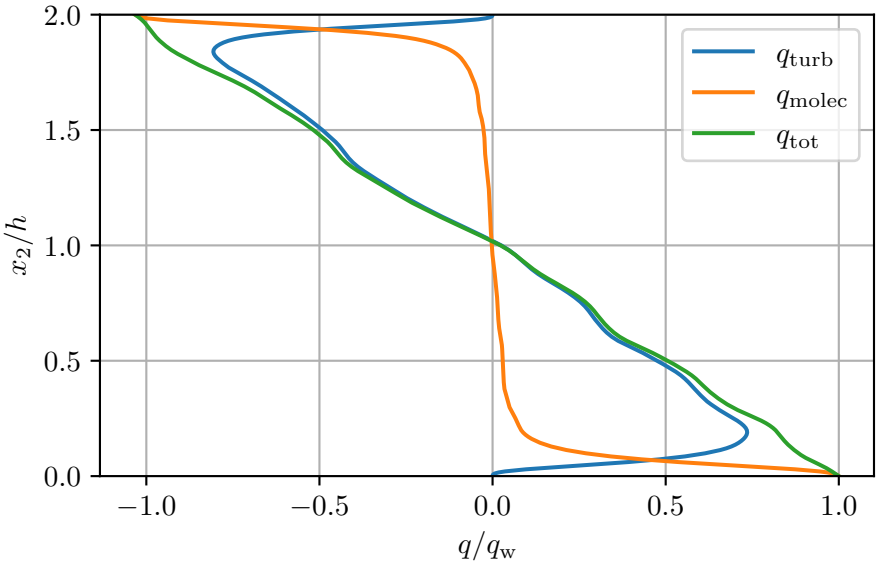

(c) Flux of passive scalar with $Pr = 1$

Figure 4.5.: Passive scalar flux contributions (case p180)

$L_1/2h$ is depicted, like in the case of Kim et al. 1987. All auto-covariances depicted in the following figures are evaluated in the channel centre ($x_2^+ \approx 180$), since the largest turbulent structures are expected to form far away from the channel walls, as mentioned by Jiménez and Simens 2001. The idea is that if no scales are curtailed at the centre line, no scales are cut off at all in the channel. Considering $R_{u_2u_2}$ and $R_{u_3u_3}$ in Figure 4.6a, it is obvious that the streamwise expansion of turbulent u_2-structures as well as turbulent u_3-structures are fully captured by the chosen size of the periodic box since their auto-covariance values vanish for large spatial separations. However, no such behaviour is evident when considering $R_{u_1u_1}$. Similar results are shown by the literature data, taken from Moser et al. 1999, also depicted in Figure 4.6a. Moser et al. also simulated turbulent plane channel flow at $Re_\tau \approx 180$. However, the statistics of their results are not as well-converged as in the present case, which is why the lines obtained from p180 do not match exactly with the data taken from the literature. In the case of the passive scalars, Figure 4.6b shows the auto-covariances of θ for the medium and high Prandtl numbers to vanish at half the channels periodic box size. Note that a similar statistical behaviour of these two scalars

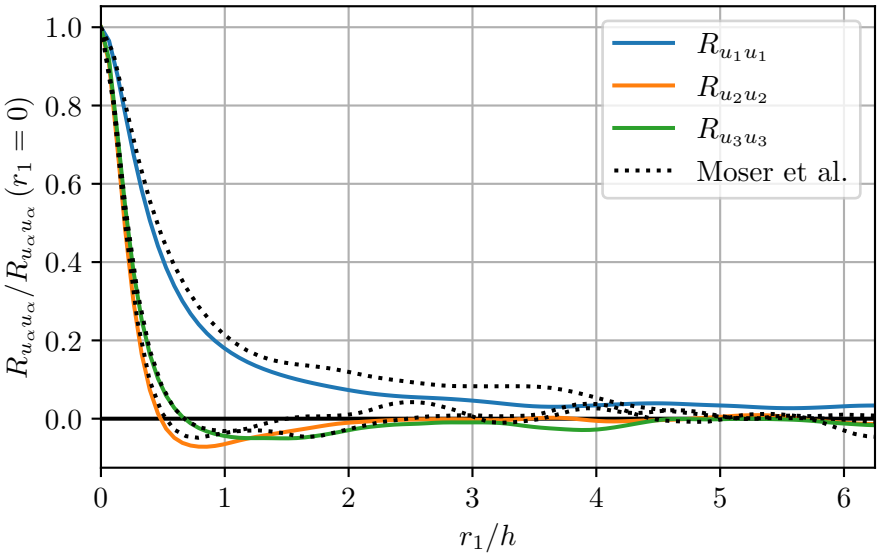

(a) Auto-covariance of velocity components

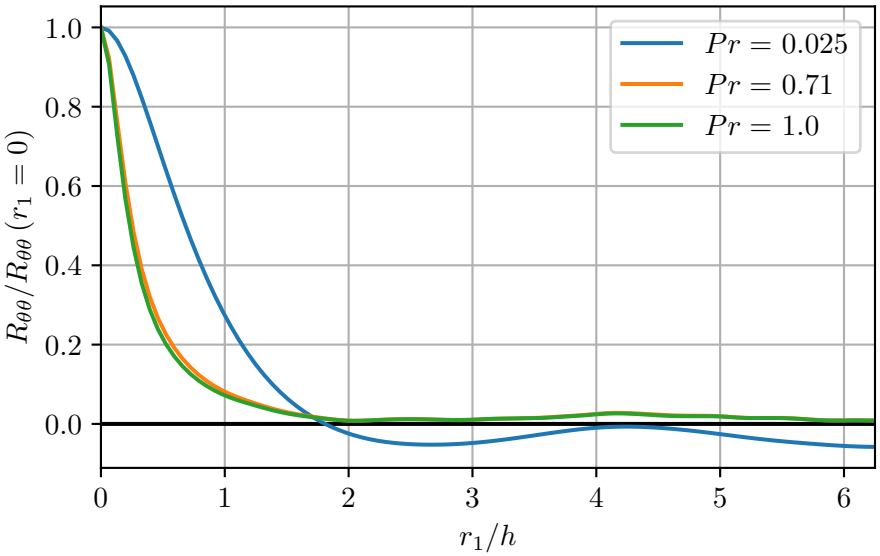

(b) Auto-covariance of passive scalars

Figure 4.6.: Streamwise auto-covariance profiles at $x_2^+ \approx 180$ (case p180)

can be observed again. However, the auto-covariance of the passive scalar with $Pr = 0.025$ is significantly larger than zero at a maximum streamwise separation, indicating that the periodic box is too small in the streamwise direction to capture all turbulent scales. This observation is in agreement with the expected behaviour that passive scalars of low Prandtl numbers form larger scales than their high Pr counterparts, as indicated by Kawamura et al. 1998 and Abe et al. 2004.
Since p180 shows that the streamwise length of the periodic box is too small to capture all turbulent structures of both the velocity and the scalar fields, L_1 is elongated for the main simulations, as listed in Table 3.1. The resulting channel lengths do not curtail the respective scale spectra as can be seen in figures B.13, B.14 and B.15.
Figure 4.7 shows the (space-time) auto-covariance of the velocity components as well as the passive scalars, this time with respect to the spanwise separation. As for Figure 4.6, the individual quantities are normalised by the channel half-width and the auto-covariance for vanishing separation ($r_3 = 0$), respectively. All mean quantities are calculated with respect to the two statistically homogeneous spatial directions and with respect to time, as before. To evaluate whether the periodic box is large enough to capture the spanwise expansions of the largest turbulent structures, the spanwise auto-covariance at the channel centre is considered up to a maximum dimensionless spanwise separation of $L_3/2h$. The results for the velocity components and the passive scalars in Figure 4.7a and Figure 4.7b, respectively, show vanishing auto-covariance values. This indicates that L_3 is large enough and does not need to be elongated with respect to further simulations. As before, data from Moser et al. 1999 are used for comparison. In their setup, they simulated a periodic channel of only $L_3/h = 4/3\ \pi$, which is evident from the reference curves depicted in Figure 4.7a. Therefore, and due to the less converged statistics, these results do not perfectly align with the data obtained from p180. However, they show a similar trend. Regarding the auto-covariances of the scalar fields, note that for $Pr = 0.025$ the largest correlations are present, and the two scalars of larger Prandtl numbers exhibit similar statistical behaviours, again.
Figure 4.8 shows the skewness distributions ($Skew(\ \cdot\ )$) of the velocity components (Figure 4.8a) and the passive scalars (Figure 4.8b), with respect to the wall distance, normalised by the channel half-width. To calculate the skewness, as well as the therefore needed standard deviations, averages in both statistically homogeneous directions and in time are used. The total channel width is presented, since by analysing whether the profiles are symmetric around $x_2/h = 1$, it can be assessed if enough time steps are used in the calculation of the mean values, as mentioned by Kim et al. 1987. All curves in figures 4.8a and 4.8b have a strong symmetry, showing that 100 (statistically fully developed) time steps are a reasonable amount for statistical averaging. Another indicator of this is the skewness distribution of the spanwise velocity component in Figure 4.8a. For a fully converged statistic, Kim et al. 1987 mention $Skew(u_3)$ to vanish, over the whole width of the channel. This is approximately true for the statistics obtained from p180. In contrast, the results taken from Moser et al. 1999 do not show this behaviour, thereby demonstrating that their statistics are not well-converged. However, there is still some overlap visible between the literature data and the results of p180. In Figure 4.8b, the statistical behaviours of the scalar with $Pr = 0.71$ and the scalar with $Pr = 1$ are once again nearly identical.
Figure 4.9 shows the flatness distributions ($Flat(\ \cdot\ )$) of the velocity components and the passive scalars in Figure 4.9a and Figure 4.9b, respectively. Their values are plotted with respect to the wall distance in outer units. As before, all averages are calculated with respect to x_1, x_3 and t. With the temporal means being taken over 100 statistically fully developed fields. The information of interest extracted from Figure 4.9 is once again whether enough time steps are used in averaging. This can be analysed by considering the symmetry of the flatness distributions with respect to the mid-plane of the channel, as in

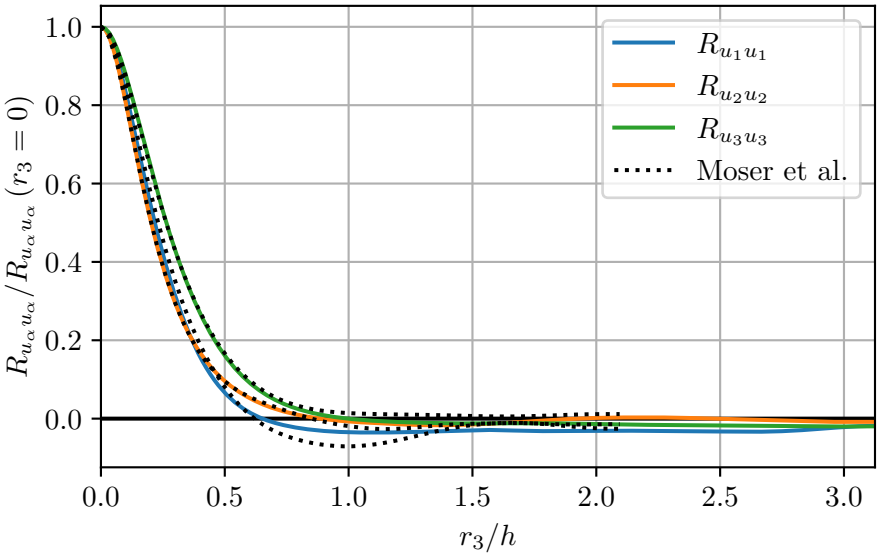

(a) Auto-covariance of velocity components

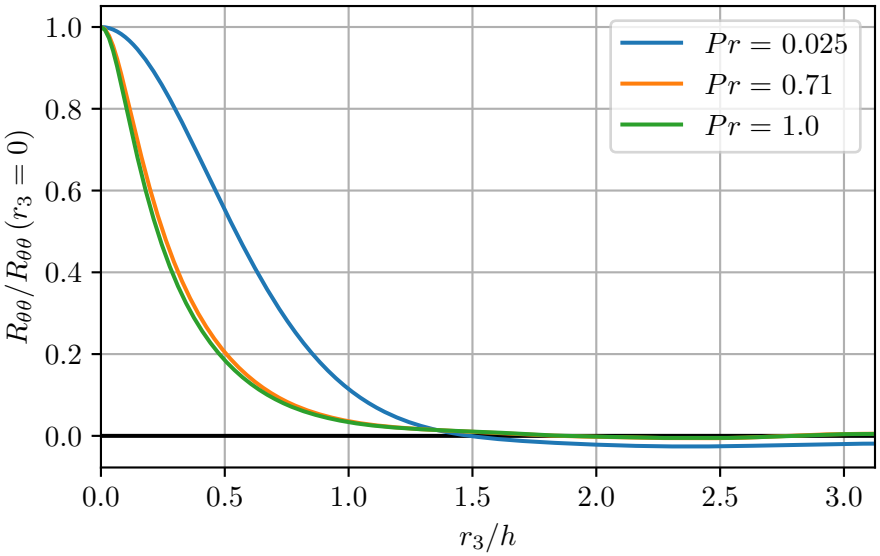

(b) Auto-covariance of passive scalars

Figure 4.7.: Spanwise auto-covariance profiles at $x_2^+ \approx 180$ (case p180)

the case of Kim et al. 1987. All curves of the velocity components, as well as the passive scalars, show strong symmetries, reassuring the results made by analysing Figure 4.8. Furthermore, Figure 4.9a shows the results from Moser et al. 1999. They are, in part, in good agreement with the data obtained by p180. However, the deviation between this case and the literature data could again be attributed to the marginal sample size, used in averaging by Moser et al. 1999. Considering Figure 4.9b, the statistical behaviour of the medium and large Prandtl number scalars is once again found to be similar.
In general, the strong statistical symmetries of Figure 4.8 and Figure 4.9, as well as the vanishing of $Skew(u_3)$, indicate the ability of the simulation and averaging setups used to reproduce high-order turbulence statistics.
The final typical statistics of turbulent plane channels, used for validation, are one-dimensional energy spectra. In the case considered, Equation 2.37 is evaluated for the velocity components and the passive scalars. This is done in the streamwise and spanwise directions, as well as at two different wall distances. Figure 4.10 shows the streamwise

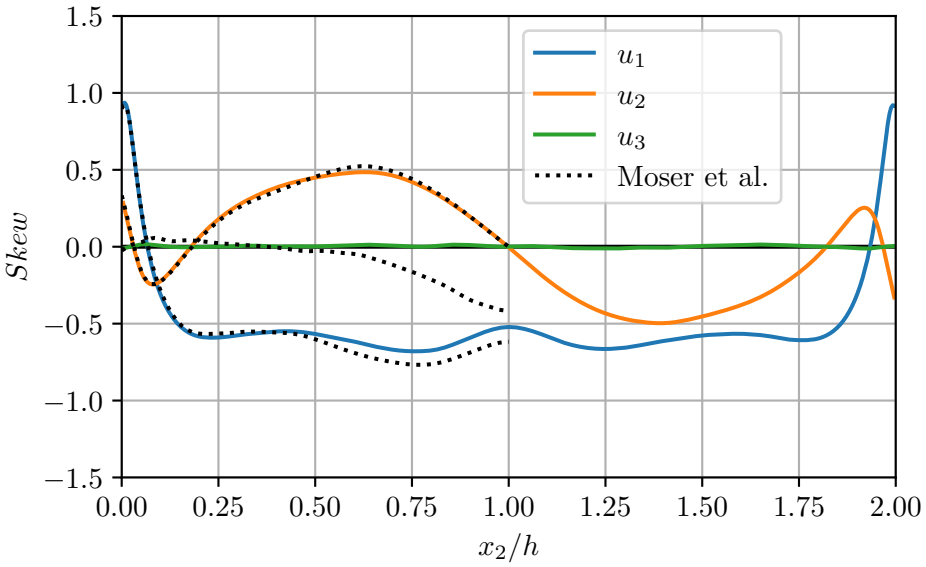

(a) Skewness of velocity components

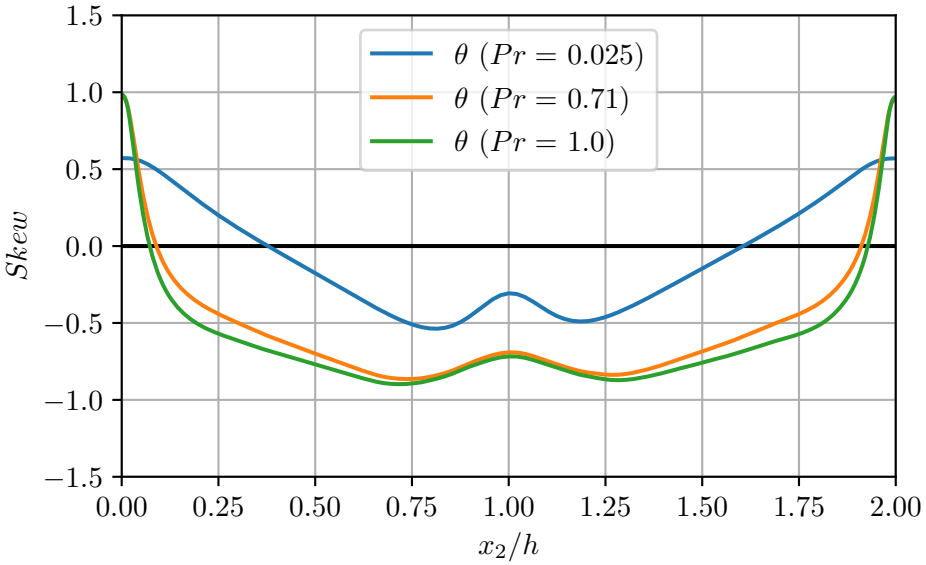

(b) Skewness of passive scalars

Figure 4.8.: Skewness distributions in turbulent plane channel flow (case p180)

energy spectra at $x_2^+ \approx 5$, Figure 4.11 shows the streamwise energy spectra at $x_2^+ \approx 180$, Figure 4.12 shows the spanwise energy spectra at $x_2^+ \approx 5$ and Figure 4.13 shows the spanwise energy spectra at $x_2^+ \approx 180$. All spectra are depicted in viscous units and plotted over their respective wavenumbers. The used averages are taken with respect to both statistically homogeneous spatial directions and with respect to 100 statistically fully developed fields in time. The goal of considering one-dimensional energy spectra, for validation, is to check whether energy pileups occur at large wavenumbers. Kim et al. 1987 mention that this would indicate that the solver resolution is not fine enough to resolve the dissipation range of the turbulent energy cascade. However, this is not the case for any of the curves in the figures 4.10 to 4.13. It can, therefore, be assumed that the Fourier modes, in the streamwise and the spanwise directions, are large enough to capture the turbulent behaviour of the smallest occurring structures. Again, results from Moser et al. 1999 are additionally depicted as a reference. They are in reasonably good agreement with the data obtained from p180. Slight deviations can be attributed to the marginal convergence of

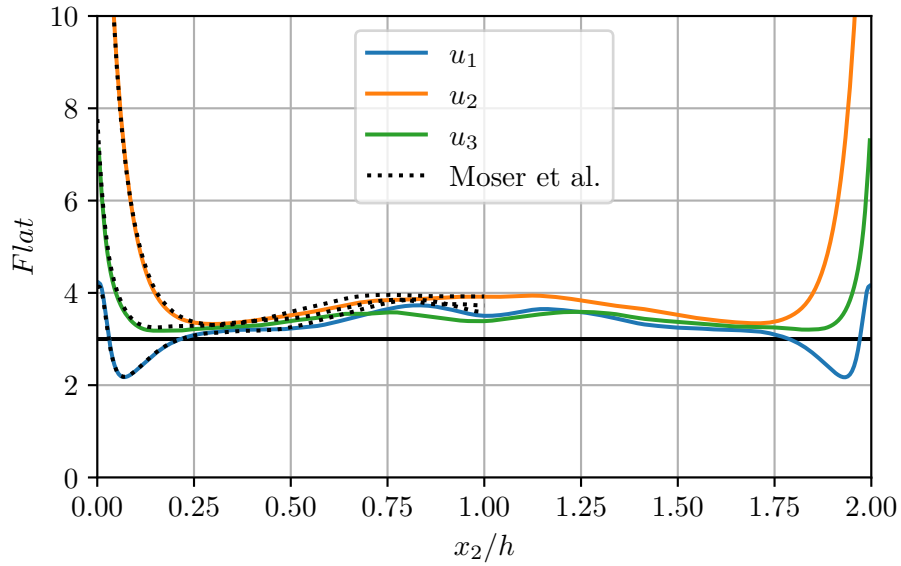

(a) Flatness of velocity components

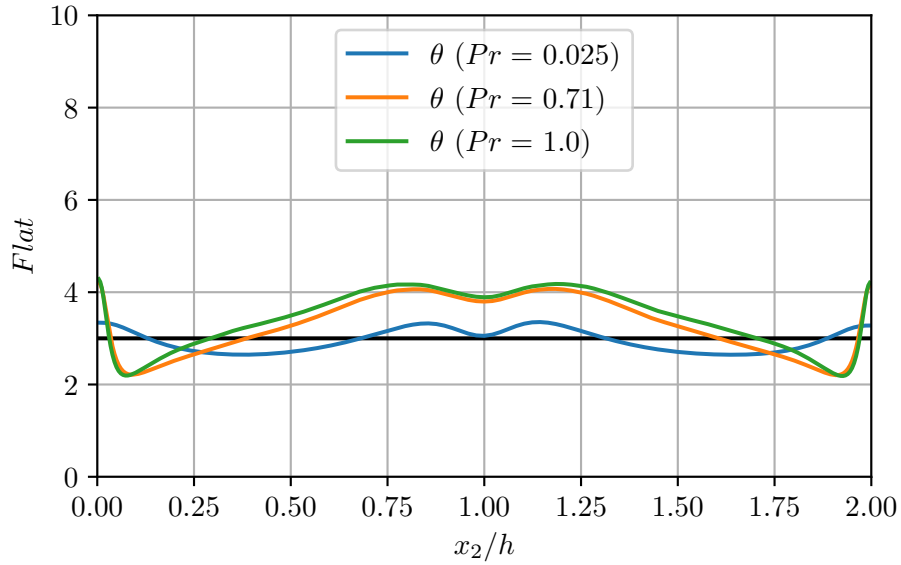

(b) Flatness of passive scalars

Figure 4.9.: Flatness distributions in turbulent plane channel flow (case p180)

the statistics given by Moser et al. and to the fact that the compared results are only approximately taken at the same wall distance. The latter might vary between this case and the literature, resulting in slightly different energy spectra. When considering the energy spectra of the passive scalars, shown in the figures 4.10b, 4.11b, 4.12b and 4.13b, it is evident that turbulent structures of the scalar with $Pr = 0.025$ carry significantly less energy than the structures of scalars associated with larger Prandtl numbers. This behaviour is well known (e.g. Abe et al. 2004) and further validates the simulation and averaging setups used. As was already shown in previous statistics, the behaviours of the scalars with $Pr = 0.71$ and $Pr = 1$ are similar, also for the one-dimensional energy spectra. As a result, a passive scalar with a medium Prandtl number of $Pr = 0.4$ (instead of $Pr = 0.71$) is chosen to be simulated in m180, m500 and m1000, which can be seen in Table 3.1. Therefore, the variable-space of the results is better distributed, leading to more reliable interpretations.

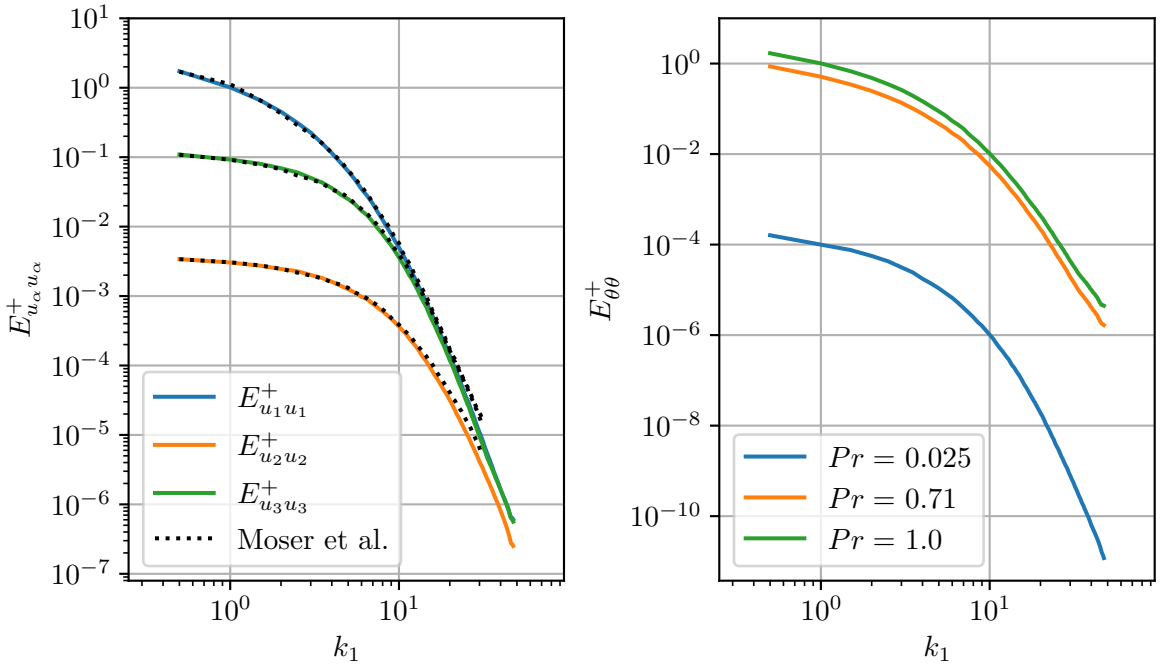

(a) Spectra of velocity components

(b) Spectra of passive scalars

Figure 4.10.: Streamwise one-dimensional energy spectra at $x_2^+ \approx 5$ (case p180)

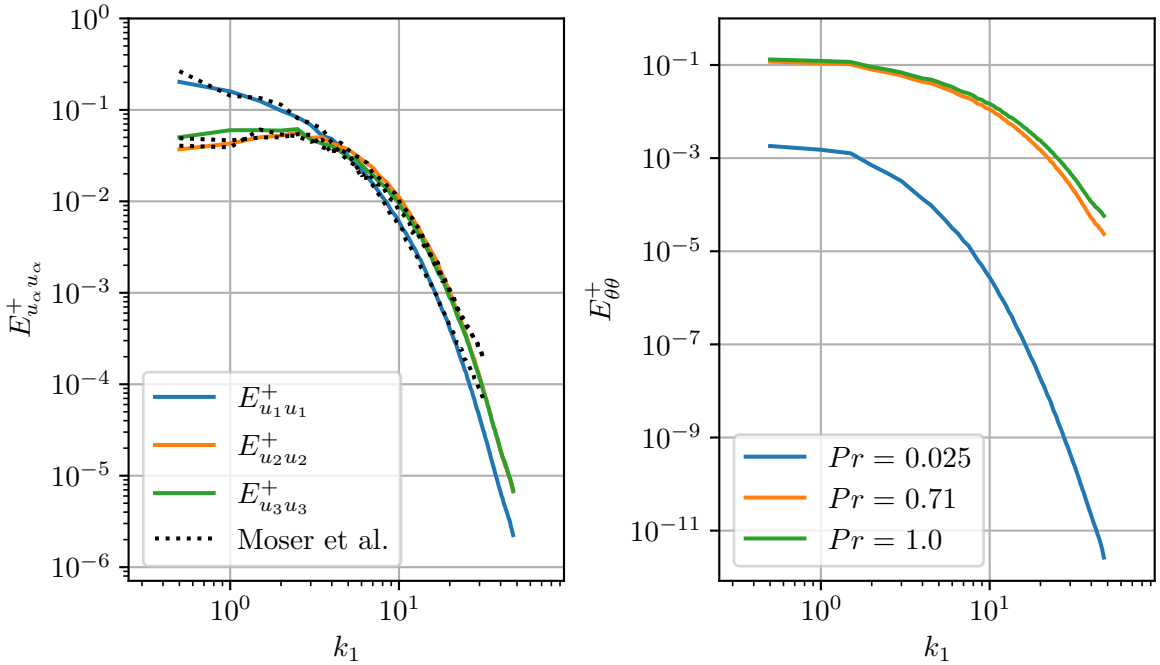

(a) Spectra of velocity components

(b) Spectra of passive scalars

Figure 4.11.: Streamwise one-dimensional energy spectra at $x_2^+ \approx 180$ (case p180)

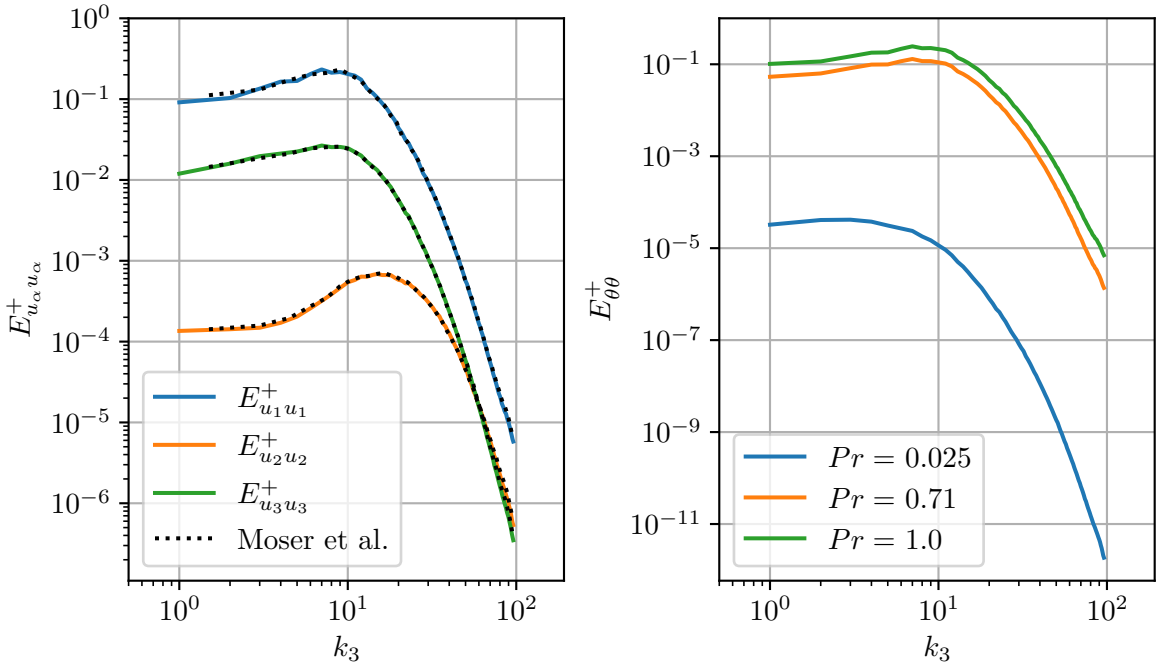

(a) Spectra of velocity components

(b) Spectra of passive scalars

Figure 4.12.: Spanwise one-dimensional energy spectra at $x_2^+ \approx 5$ (case p180)

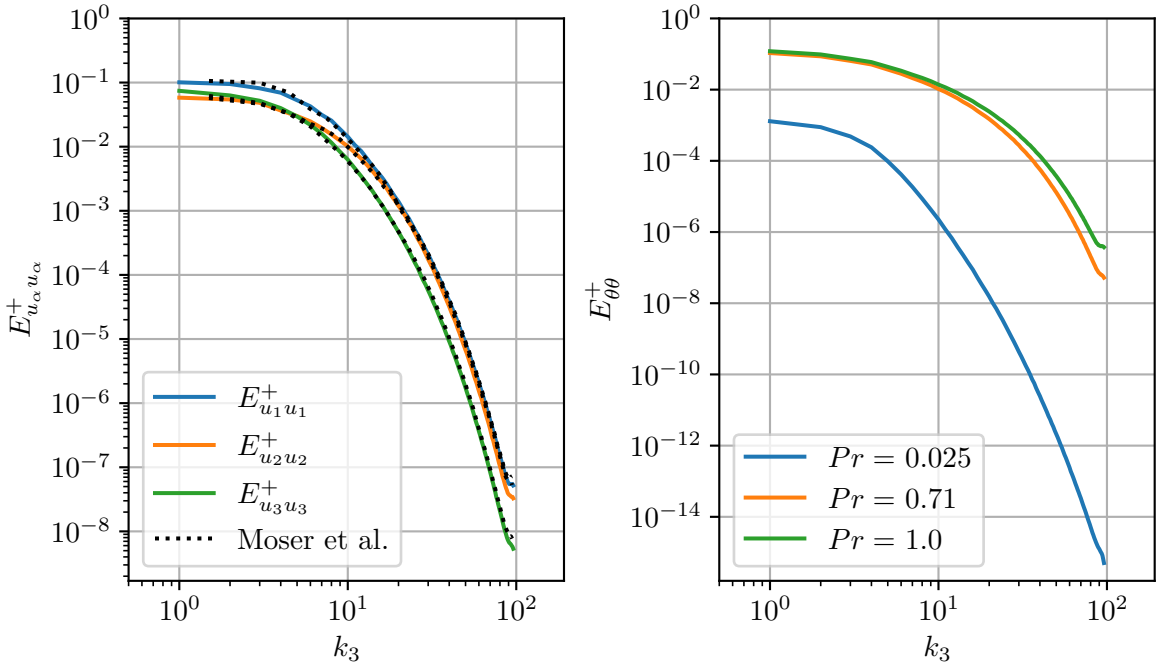

(a) Spectra of velocity components

(b) Spectra of passive scalars

Figure 4.13.: Spanwise one-dimensional energy spectra at $x_2^+ \approx 180$ (case p180)

In addition to the validation of the simulation and the averaging setups, the preliminary investigation is also used to identify symmetries of the convection velocity distributions. When considering $u_{c,\phi}$, defined in the (x_2-k_1-k_3)-space, it is reasonable to expect the convection velocity to be symmetrical with respect to the mid-plane of the channel, as it is a statistical quantity constructed from mean values, partially known to be symmetric around $x_2 = h$. To show that this symmetry holds for convection velocities in general, u_{c,u_1} is depicted with respect to the wall distance in outer units, at three different wavenumber pairs, in Figure 4.14. In this figure, the curves are shown to be symmetrical with respect to the channel centre, when disregarding statistical noise. Here, the focus should *not* yet be

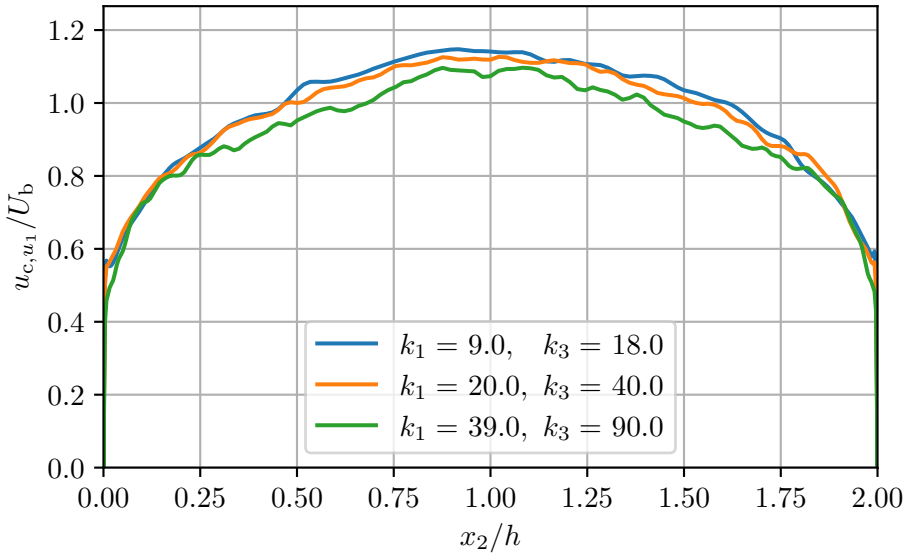

Figure 4.14.: u_{c,u_1} symmetry behaviour with respect to wall distance (case p180)

on the actual distribution of the convection velocity or its convergence behaviour, but only on its symmetry. The former will be discussed in detail in section 4.3. Averages are taken with respect to the statistically homogeneous spatial directions, as well as with respect to 100 statistically fully developed time steps. In Figure 4.14, one pair of "small", "medium", and "large" wavenumbers are depicted, each. This is to show that the symmetry behaviour holds over the whole range of turbulent scales, exemplary. Equivalent figures for the other velocity components and the passive scalars, for all simulations carried out within the scope of this thesis, can be found in subsection D.1.
Other possible symmetries to consider are those with respect to positive/negative wavenumbers. For a given wall distance, the (k_1-k_3)-space can be divided into four quadrants. One where k_1 and k_3 are both positive, one where k_1 and k_3 are both negative, and two where k_1 or k_3 is positive, while the other is negative. To analyse whether convection velocities behave differently depending on the quadrant, Figure 4.15 is plotted. The figure shows u_{c,u_1} with respect to the wall distance in viscous units, at three different *absolute* wavenumber-pairs. The values of the convection velocity in each quadrant are depicted separately. Averages are again taken with respect to the statistically homogeneous spatial directions, as well as with respect to 100 statistically fully developed time steps. The "small", "medium" and "large" wavenumbers are chosen to show that the symmetry behaviour is equivalent for different scales, as done for Figure 4.14. Figure 4.15 verifies the symmetry of u_{c,u_1} with respect to the four quadrants of the (k_1-k_3)-space, since the depicted curves seem to converge to the same values with increasing statistical accuracy. Again, equivalent figures for the other velocity components and the passive scalars, for all simulations carried out within the scope of this thesis, can be found in subsection D.2. Note that the lines in both ($k_3 < 0$)-cases as well as both ($k_3 > 0$)-cases (partially *not*

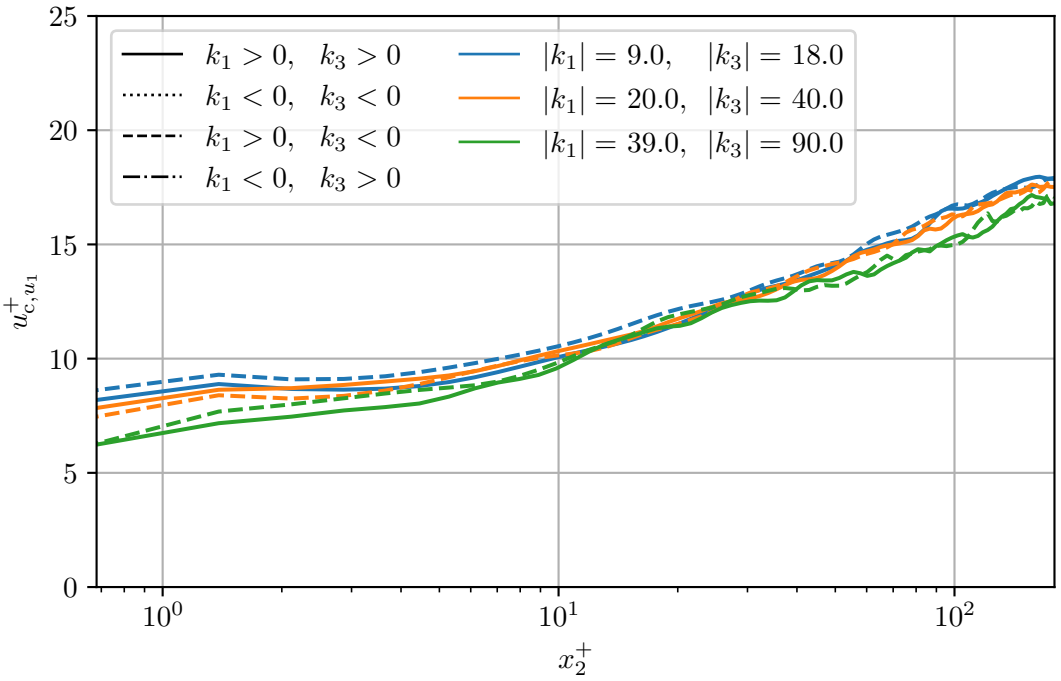

Figure 4.15.: u_{c,u_1} symmetry behaviour with respect to wavenumber-space (case p180)

visible in Figure 4.15) are already perfectly aligned, respectively. This is due to the fact that the Hermitian symmetry of k_1 is used in the DNS solver. The generated data are therefore inherently symmetric with respect to positive/negative values of k_1. However, by showing that this symmetry holds for the convection velocities as well, the implementation of their definitions is validated to some extent.
To provide better converged statistics, both symmetries (with respect to wall distance and wavenumber-space) of the convection velocities are used in all future averages. However, this is not specifically indicated by the notation, for the sake of simplicity.

4.2. Transport equation analysis

When working with the concept of convection velocities, it is important to keep in mind that Taylor's hypothesis is limited in its applicability, as mentioned in subsection 2.3.1. These limitations are the topic of publications by, for example, Lin 1953, Piomelli et al. 1989, Renard and Deck 2015 or Hilland and Christen 2024, and are shown to depend on the flow case analysed. In order to critically categorise the results of this thesis in the overall context, the applicability of Taylor's hypothesis with the implemented convection velocities in the case of turbulent plane channel flow is evaluated by means of a transport equation analysis. This procedure is introduced and explained in detail by Geng et al. 2015. They consider the same flow configuration as in this thesis, as well as the same definition for the convection velocity, based on the research of Del Álamo and Jiménez 2009.
The starting points for the transport equation analysis are the balance equations of the respective flow quantities. Here, the velocity components and passive scalars are analysed. Regarding $\boldsymbol{u}$, Geng et al. 2015 derive

$$\underbrace{\partial_{x_1}\boldsymbol{u}'}_{①} = \frac{1}{U_{c,\boldsymbol{u}}}\Big[\underbrace{-\partial_t\boldsymbol{u}'}_{②}\underbrace{+\nu\Delta\boldsymbol{u}'}_{③}\underbrace{-\nabla\cdot(\boldsymbol{u}\otimes\boldsymbol{u}')+\nabla\cdot\langle\boldsymbol{u}'\otimes\boldsymbol{u}'\rangle}_{④}\underbrace{+\triangle U_{c,\boldsymbol{u}}\,\partial_{x_1}\boldsymbol{u}'}_{⑤}\underbrace{-\frac{1}{\rho}\nabla p'}_{⑥}\Big] \tag{4.1}$$

by considering the balance equation for the momentum fluctuations (Equation 2.11) and applying $\langle u_2 \rangle = \langle u_3 \rangle = 0$, which holds for the case of turbulent plane channel flow as described in subsection 2.2.1. The function

$$\triangle U_{\mathrm{c},\phi} \equiv U_{\mathrm{c},\phi} - \langle u_1 \rangle \tag{4.2}$$

with the overall convection velocity (Equation 2.63) is introduced to isolate the terms ① and ②, which represent Taylor's hypothesis (Equation 2.50). Here, the quotient on the right-hand side of Equation 4.1 is considered to be a part of all terms ② to ⑥. Taylor's hypothesis (for $\boldsymbol{u}$-structures with the overall convection velocity $U_{\mathrm{c},\boldsymbol{u}}$) is thereby fulfilled instantaneously if ① ≈ ②, that is, when either the sum of all other terms is sufficiently small or when every other term vanishes independently. By considering the balance equation for the passive scalar fluctuations (Equation 2.14), the same procedure as before can be used to derive

$$\underbrace{\partial_{x_1}\theta'}_{①} = \frac{1}{U_{\mathrm{c},\theta}} \Big[\underbrace{-\partial_t\theta'}_{②} \underbrace{+ a\Delta\theta'}_{③} \underbrace{- \nabla\cdot(\theta\boldsymbol{u}') + \nabla\cdot\langle\theta'\boldsymbol{u}'\rangle}_{④} \underbrace{+ \triangle U_{\mathrm{c},\theta}\ \partial_{x_1}\theta'}_{⑤} \Big]. \tag{4.3}$$

The quotient on the right-hand side is considered to be a part of all terms ② to ⑤, as before. Again, Taylor's hypothesis (for θ-structures with the overall convection velocity $U_{\mathrm{c},\theta}$) is instantaneously fulfilled if ① ≈ ②, which is the case when either the sum of all other terms is sufficiently small or when every other term vanishes independently.
To analyse at which points of the channel Taylor's hypothesis holds and which physical reason might cause it to break for the transport of turbulent velocity or scalar structures, each term of the equations 4.1 and 4.3 is calculated during post-processing. All averages contained within these equations are taken with respect to the statistically homogeneous spatial directions of the channel, as well as with respect to 100 statistically fully developed time steps. Since the considered terms contain fluctuating quantities, simply averaging the entire equations would not allow for a useful statistical interpretation. Therefore, the root mean square (rms) is applied to analyse the behaviour of the transport equations, where the mean is again taken with respect to the same dependencies as for the averages contained within equations 4.1 and 4.3. Figure 4.16 and Figure 4.17 show the rms values with respect to the wall distance for the velocity components and the passive scalars, respectively. All quantities are depicted in viscous units. In addition to showing every term of the equations 4.1 and 4.3 separately, the plots also contain the rms values of the instantaneous sums of ③–⑥ and ③–⑤ for the velocity components and the passive scalars, respectively. The only case depicted is m500, while the corresponding figures for the other main simulations can be found in subsection C.1. Geng et al. 2015 note that the results of simulations at different Reynolds numbers do not show qualitatively different behaviours. This is also evident in the results of this thesis when comparing the figures 4.16 and 4.17 with the corresponding plots of other simulations shown in subsection C.1. The only outcome of an increase in Reynolds number is the effect of "pushing" the region closer to the wall in which Taylor's hypothesis breaks. The regions, with respect to wall distance, in which Taylor's hypothesis, based on the overall convection velocity, is a suitable approximation for the transport of velocity or scalar structures, are indicated by the curves of $rms(①)$ and $rms(②)$ being closely aligned in 4.16 and 4.17, respectively. However, since events of similar ① and ② magnitudes would yield similar $rms(①)$ and $rms(②)$ values regardless of the fact that the respective events might not show the same sign, this approach is somewhat flawed when analysing the applicability of Taylor's hypothesis. A better measure for this applicability is therefore given by the rms values of the sum of the remaining terms, since they have to vanish for Taylor's hypothesis to hold, which is independent of their instantaneous sign.

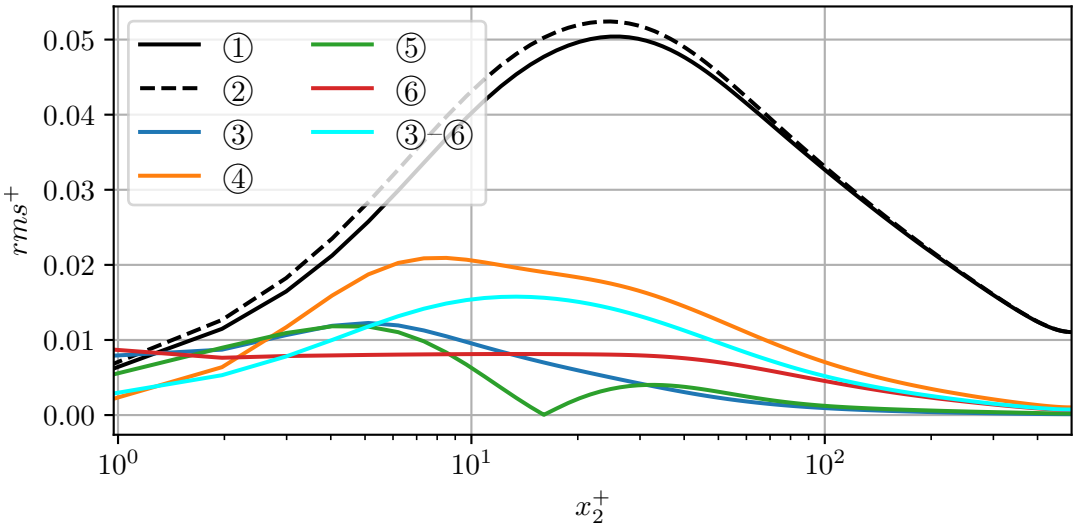

(a) Transport equation analysis of the streamwise velocity component

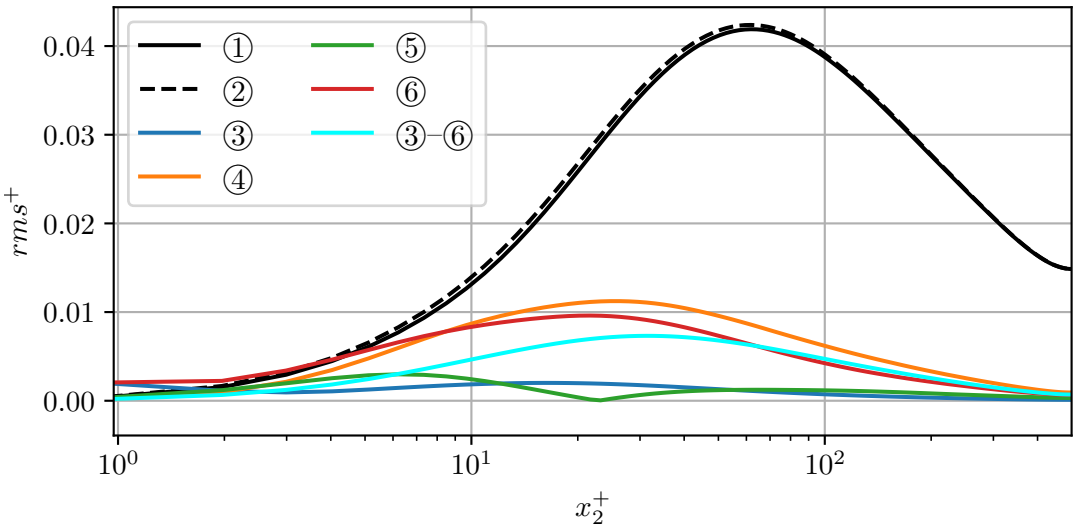

(b) Transport equation analysis of the wall-normal velocity component

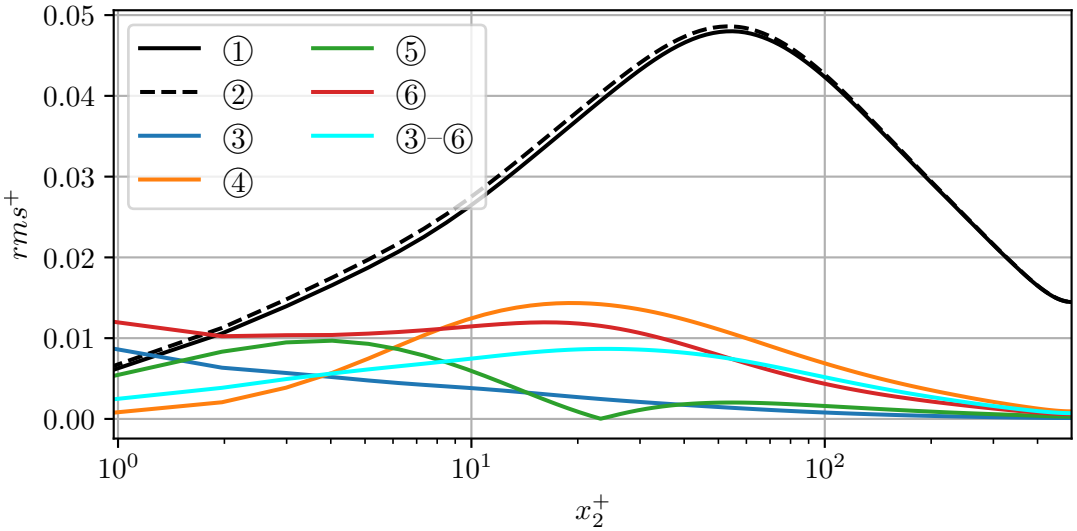

(c) Transport equation analysis of the spanwise velocity component

Figure 4.16.: Transport equation analysis *rms* of the velocity field (case m500)

The results obtained for the convection of velocity structures are in good agreement with those presented by Geng et al. 2015. The transport equation analysis *rms* values of the streamwise, wall-normal, and spanwise velocity components are all of the same order of magnitude, as can be seen in figures 4.16a, 4.16b, and 4.16c, respectively. Outside the viscous sublayer, $rms(①)$ and $rms(②)$, representing Taylor's hypothesis, are the dominant terms. They reach a maximum just around the border between the buffer layer and the log layer. This peak is ever so slightly closer to the channel wall in the case of the streamwise velocity component, and the subsequent drop towards the channel centre reaches a lower local minimum than for the other velocity components. Regarding $rms(③–⑥)$, which represents the instantaneous sum of all terms contributing to the breaking of Taylor's hypothesis for the transport of velocity structures, a similar behaviour is recognised. Its value reaches a maximum at the edge of the buffer layer (closer to the wall for the streamwise velocity component), while approaching zero towards the wall as well as towards the channel centre. The viscous term $rms(③)$ vanishes at the channel centre for all the velocity components. Its influence is negligible in the log layer, but increases towards the channel wall. In very close vicinity of the wall, $rms(③)$ is one of the dominant terms, overpowering $rms(①)$ and $rms(②)$. In contrast to this stands the behaviour of the non-linear term $rms(④)$. Its impact close to the wall is vanishingly small, while it is the dominant contributor to the breaking of Taylor's hypothesis in the buffer layer, as well as in the log layer, for all velocity components. Towards the channel centre, however, $rms(④)$ decreases again. The term $rms(⑤)$, representative of the difference between the mean velocity and the overall convection velocity of the respective velocity component, reaches a global maximum at the boundary between the viscous sublayer and the buffer layer. Additionally, the term exhibits another (local) maximum at the transition between the buffer layer and the log layer (depending on the component), while decreasing towards the channel wall and centre. Between these two maxima, $rms(⑤)$ drops to zero in the buffer layer, which is an effect of a change in sign of Equation 4.2. This behaviour is discussed in detail in subsection 4.3.1. The contribution of this term to the breaking of Taylor's hypothesis is small almost everywhere, except in the centre of the viscous sublayer for the transport of the streamwise velocity component, where $rms(⑤)$ is the largest of the terms $rms(③)$ to $rms(⑥)$. Finally, the pressure term $rms(⑥)$ plays a major role in the breaking of Taylor's hypothesis across the whole channel, except at the channel centre, where it approaches zero. In close proximity to the wall, it is dominant, like the viscous term $rms(③)$. Furthermore, $rms(⑥)$ is nearly as large as the non-linear term in the log layer for the wall-normal and spanwise velocity component. In case of the streamwise velocity component, the pressure term is smaller than for the other components in the log layer, but does not decrease when approaching the wall. It instead takes on a constant value across the buffer layer and viscous sublayer before increasing slightly in the very close vicinity to the wall.

For the scalar transport equation analyses, an increase in the *rms* values of nearly all terms can be observed along with an increase in Prandtl number. Especially $rms(①)$ and $rms(②)$, representing Taylor's hypothesis, show their lowest values for $Pr = 0.025$, medium values for $Pr = 0.4$, and their highest values for $Pr = 1$, in figures 4.17a, 4.17b, and 4.17c, respectively. Starting from zero at the wall, both terms increase monotonously until they reach their peaks in the log layer. The positions of these peaks move towards the channel wall with an increase in Prandtl number. After peaking, both terms decrease again, approaching the channel centre, but they do not vanish at $x_2 = h$. In contrast to the transport equation analyses of the velocity components, for the transport of passive scalar structures, $rms(①)$ and $rms(②)$ are not only the dominant terms *outside* the viscous sublayer, but also at all positions close to the wall. The term $rms(③–⑤)$, representative of the instantaneous sum of all terms contributing to the breaking of Taylor's hypothesis for the scalar transport equation analyses, shows again a similar behaviour as the dominant

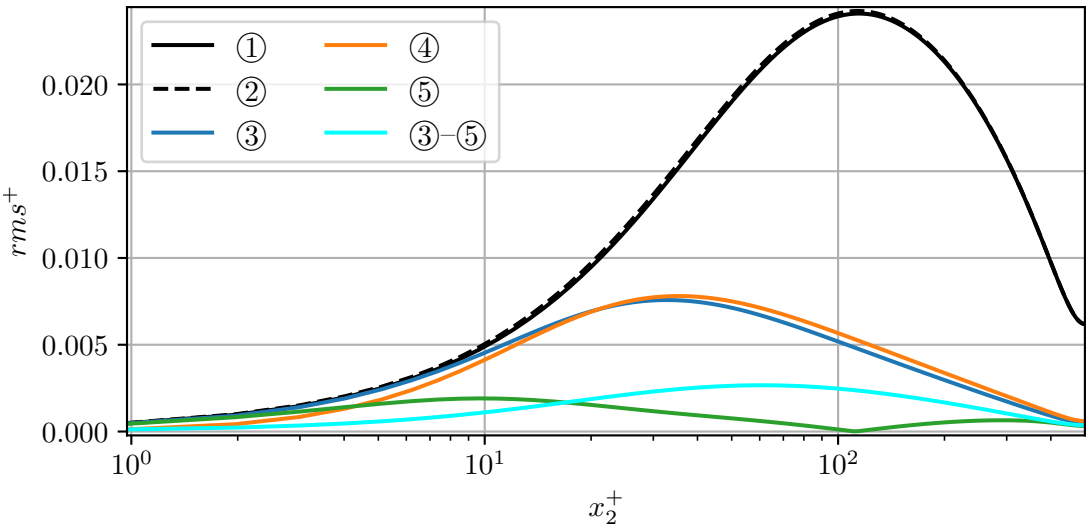

(a) Scalar transport equation analysis with $Pr = 0.025$

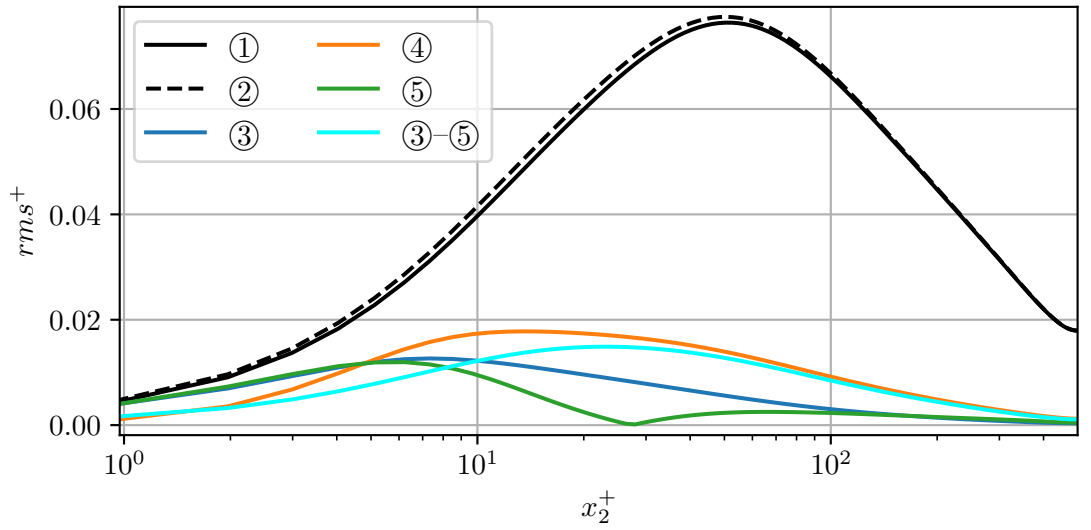

(b) Scalar transport equation analysis with $Pr = 0.4$

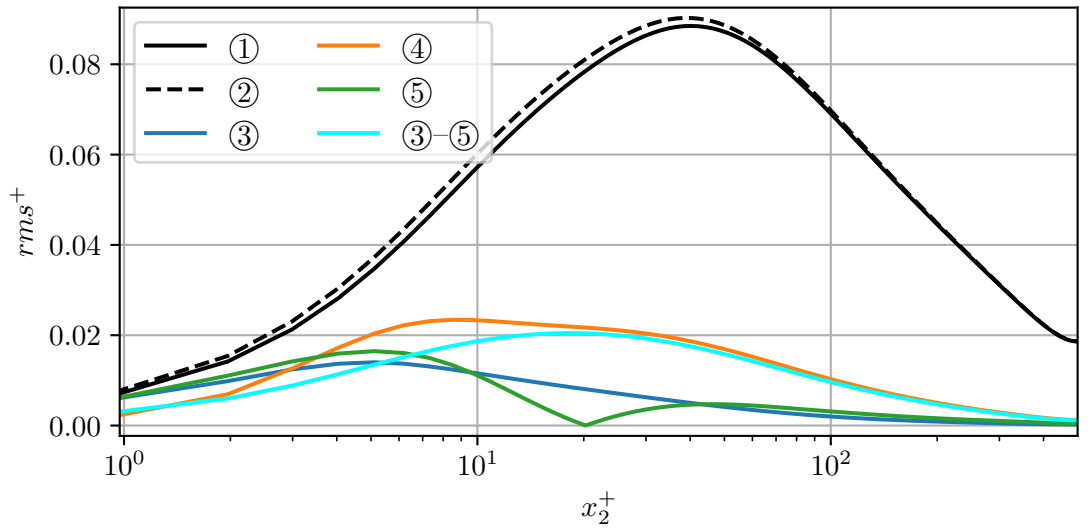

(c) Scalar transport equation analysis with $Pr = 1$

Figure 4.17.: Transport equation analysis *rms* of the passive scalars (case m500)

terms. The term vanishes at the wall, independently of the Prandtl number. From there on out it increases towards the channel centre, before reaching its peak at the transition between the buffer layer and the log layer. The position of this peak is again shifted towards the wall with an increase in Prandtl number. Following the global maximum, $rms(③–⑤)$ decreases again, approaching zero at the centre of the channel. In case of the conduction term $rms(③)$, a strong dependence on the Prandtl number can be observed. However, independent of Pr, the term vanishes at the wall and approaches zero at the channel centre with a single maximum in between. The position of this maximum lies within the buffer layer, close to the log layer, for the lowest Prandtl number and shifts towards the wall with larger values of Pr, reaching the viscous sublayer at $Pr = 1$. In case of the lowest Prandtl number, $rms(③)$ is one of the terms mostly contributing to the breaking of Taylor's hypothesis over the whole range of the channel. However, for $Pr = 0.4$ and $Pr = 1$, its influence drops significantly. The non-linear term $rms(④)$ behaves similarly, vanishing at the wall as well as at the channel centre and peaking in the buffer layer. Its peak also moves towards the channel wall with higher values of Pr. For the lowest Prandtl number, the profiles of $rms(③)$ and $rms(④)$ are nearly identical, while the non-linear term keeps its dominance regarding the breaking of Taylor's hypothesis in the buffer layer and log layer also for higher Prandtl numbers. In the viscous sublayer, however, $rms(④)$ falls more rapidly with decreasing distance to the wall, causing its influence to disappear in the close vicinity of the wall for all values of Pr. Lastly, $rms(⑤)$, representing the difference between the mean velocity and the overall convection velocity for a passive scalar structure with a certain Prandtl number, shows the same qualitative behaviour as its respective counterparts for the transport of any given velocity component. The term again features two peaks. The global maximum is located at the transition between the viscous sublayer and the buffer layer, while the other (smaller) local maximum lies closer to the channel centre. Outwards from both sides of these two peaks, $rms(⑤)$ is decreasing, approaching zero at $x_2 = 0$ and $x_2 = h$. Between the peaks, a minimum is reached where the term vanishes completely. This is again due to a change in the sign of Equation 4.2, which is explained further in subsection 4.3.1. However, this minimum is not always positioned in the same layer. Its location is affected by the Prandtl number. With increasing Pr, the minimum of $rms(⑤)$ shifts towards the channel wall, starting in the log layer for $Pr = 0.025$. While in close vicinity to the wall, $rms(⑤)$ is one of the dominant terms, whose relative influence decreases with increasing wall distance.

Note that small values of $rms(③–⑥)$ for the transport of velocity structures and small values of $rms(③–⑤)$ for the transport of scalar structures do *not* necessarily imply Taylor's hypothesis to hold, since the respective values of $rms(①)$ and $rms(②)$ could be small as well, as it is the case close to the channel walls. To quantify whether the terms representing Taylor's hypothesis are overpowered by the remaining terms in the case of all terms being of small magnitude, Geng et al. 2015 propose normalising all curves seen in figures 4.16 and 4.17 by the respective value of $rms(②)$. Such normalised representations can be seen in figures 4.18 and 4.19 for the transport of velocity and scalar structures, respectively. Again, m500 is the only case depicted for the same reasons as before. Figures of the normalised transport equation analysis rms values for the other main simulations are provided in subsection C.2. The distance from the channel wall is shown in viscous units. In these representations of the terms contained within Equation 4.1 and Equation 4.3, the applicability of Taylor's hypothesis is indicated by the ratio $rms(①)/rms(②)$ becoming unity. However, this approach again exhibits flaws, since $rms(①)/rms(②)$ can become unity for events where ① and ② have similar magnitudes even though their signs might differ. Therefore, better measures to consider are given by the ratios $rms(③–⑥)/rms(②)$ for the convection of velocity structures and $rms(③–⑤)/rms(②)$ for the convection of passive scalar structures, since these terms need to vanish altogether for Taylor's hypothesis to hold.

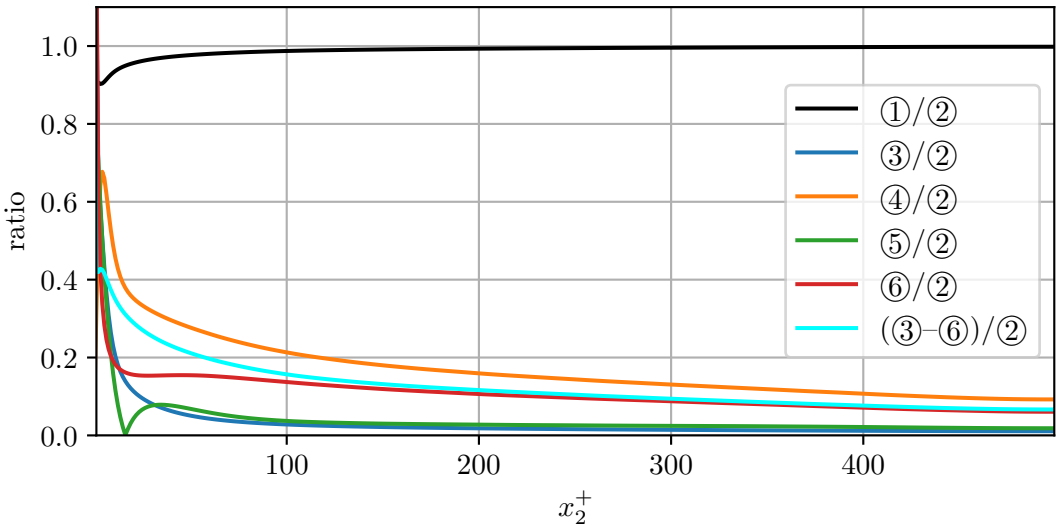

(a) Normalised transport equation analysis of the streamwise velocity component

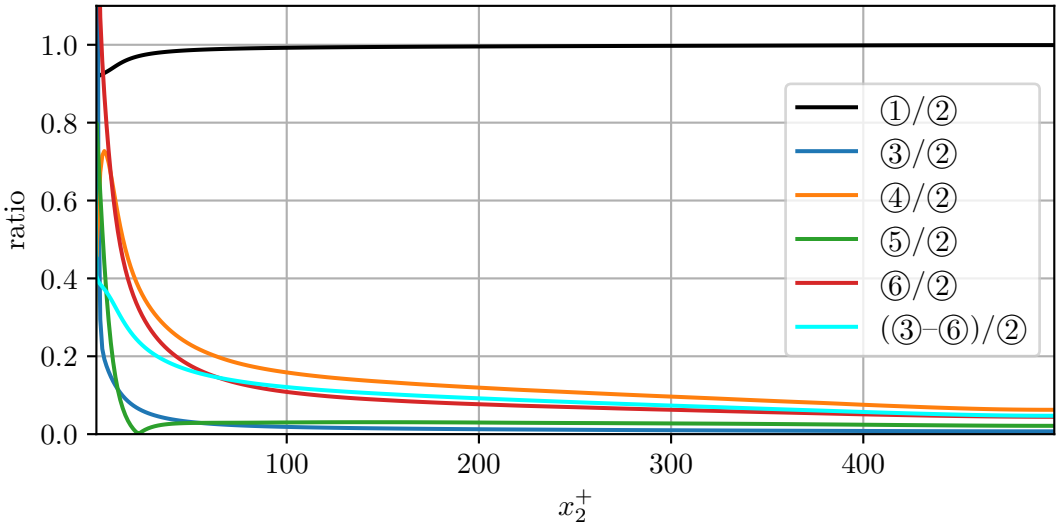

(b) Normalised transport equation analysis of the wall-normal velocity component

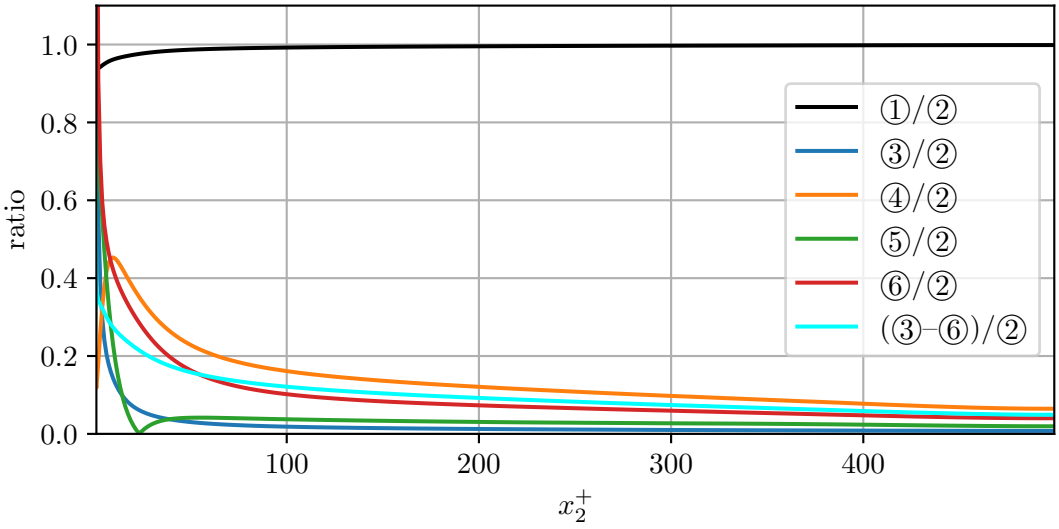

(c) Normalised transport equation analysis of the spanwise velocity component

Figure 4.18.: Normalised transport equation analysis *rms* of the velocity field (case m500)

Considering the normalised transport equation analysis, the respective rms values of the streamwise, wall-normal, and spanwise velocity components are all of the same order of magnitude. This can be seen in figures 4.18a, 4.18b, and 4.18c, respectively. Regarding $rms(③–⑥)/rms(②)$, which represents the relative sum of all terms contributing to the breaking of Taylor's hypothesis, it is shown that this term increases monotonously with a decrease in wall distance for the wall-normal and spanwise velocity component in Figure 4.18b and Figure 4.18c, respectively. However, for the streamwise velocity components in Figure 4.18a, a maximum is reached in the viscous sublayer, before the term decreases again in close proximity to the wall. Note that in general, $rms(③–⑥)/rms(②)$ does not vanish at any point of the channel, while $rms(①)/rms(②)$ reaches unity somewhere in the log layer for all velocity components. This proves the expected behaviour, resulting in the importance of using the latter measure with care when testing the applicability of Taylor's hypothesis. The viscous term $rms(③)/rms(②)$ is again seen to be one of the dominant terms in close vicinity of the wall. However, in this relative representation, it exhibits a monotonous decay towards the channel centre for all velocity components. The non-linear term $rms(④)/rms(②)$ does not exhibit such monotonous behaviour. As for the non-relative depiction, it is small at the wall and rises to a peak in the buffer layer. After that, it decays towards the channel centre, while still being the dominant contributor to the breaking of Taylor's hypothesis in the case of all velocity components. The term $rms(⑤)/rms(②)$, representing the difference between the overall convection velocity and the mean velocity, has its highest value closest to the wall in the normalised depiction. However, this maximum is never as large as the ratio representing the terms of Taylor's hypothesis. For all velocity components, $rms(⑤)/rms(②)$ decays rapidly towards its minimum in the buffer layer. Going on from there, the term increases again but stays small compared to most of the others. The pressure term $rms(⑥)/rms(②)$ for the wall-normal and spanwise velocity components behaves much like the viscous term. However, for the transport of streamwise velocity structures, the pressure term does dominate directly at the wall but decreases more rapidly than for the other velocity components in this relative representation. In the buffer layer and parts of the log layer, it has a nearly constant value. The relative sum of all terms contributing to the breaking of Taylor's hypothesis $rms(③–⑤)/rms(②)$ can be seen in figures 4.19a, 4.19b and 4.19c for the transport of scalar structures at low, medium, and high Prandtl numbers, respectively. The term takes its maximum directly at the wall and decreases monotonously towards the channel centre, independent of the Prandtl number. Like for the transport of velocity structures, the term never fully vanishes over the whole width of the channel. The normalised figures show that the conduction term $rms(③)/rms(②)$ is dominant at the wall for all values of Pr. It decreases monotonously towards the channel centre, reaching the lowest value of all terms contributing to the breaking of Taylor's hypothesis for the medium and high Prandtl numbers. However, for $Pr = 0.025$, the viscous term first increases in the buffer layer before decreasing again, while still being one of the larger terms across the entire channel. The non-linear term $rms(④)/rms(②)$ shows a similar behaviour, just with a steeper decay towards the wall of the channel. However, this relative term peaking in the buffer layer and decreasing towards the channel centre is also the case for the other Prandtl numbers. Lastly, the term $rms(⑤)/rms(②)$, representative of the difference between the mean velocity and the overall convection velocity, follows a similar course for all values of Pr. By reaching its maximum relative value directly at the wall, it is one of the dominant contributors to the breaking of Taylor's hypothesis. With an increase in wall distance, it drops to zero in a position that moves close to the channel wall with larger values of Pr. From there, it increases again but stays small in comparison to the other terms for all Prandtl numbers alike.

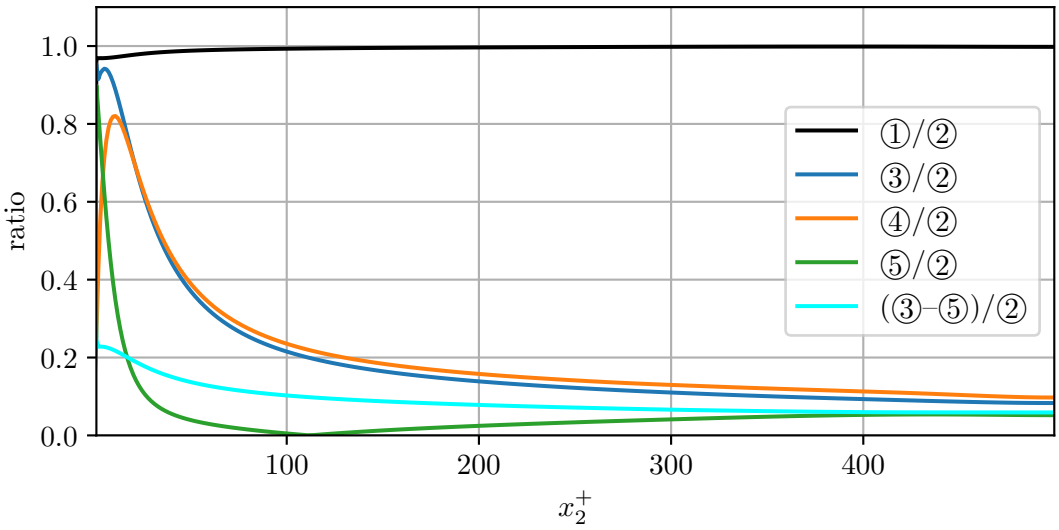

(a) Normalised scalar transport equation analysis with $Pr = 0.025$

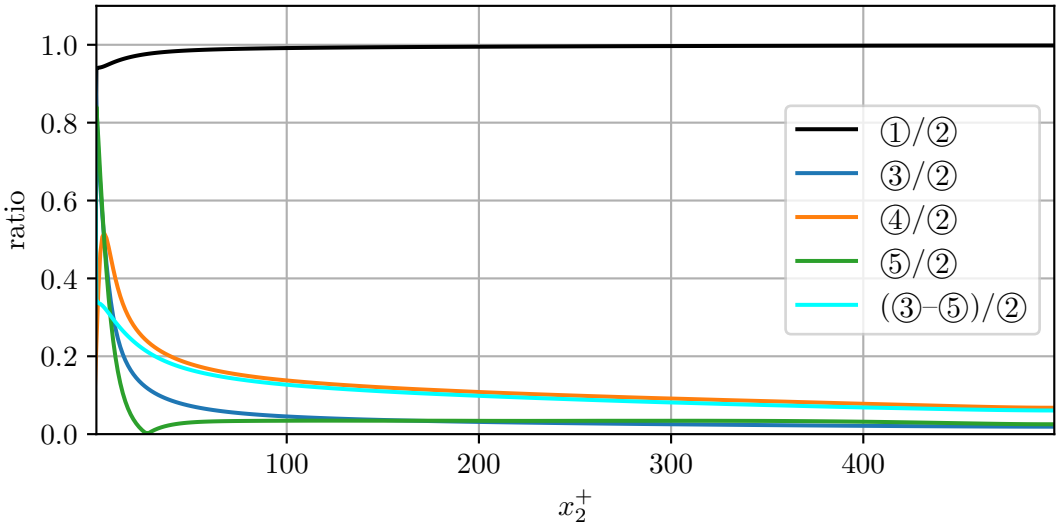

(b) Normalised scalar transport equation analysis with $Pr = 0.4$

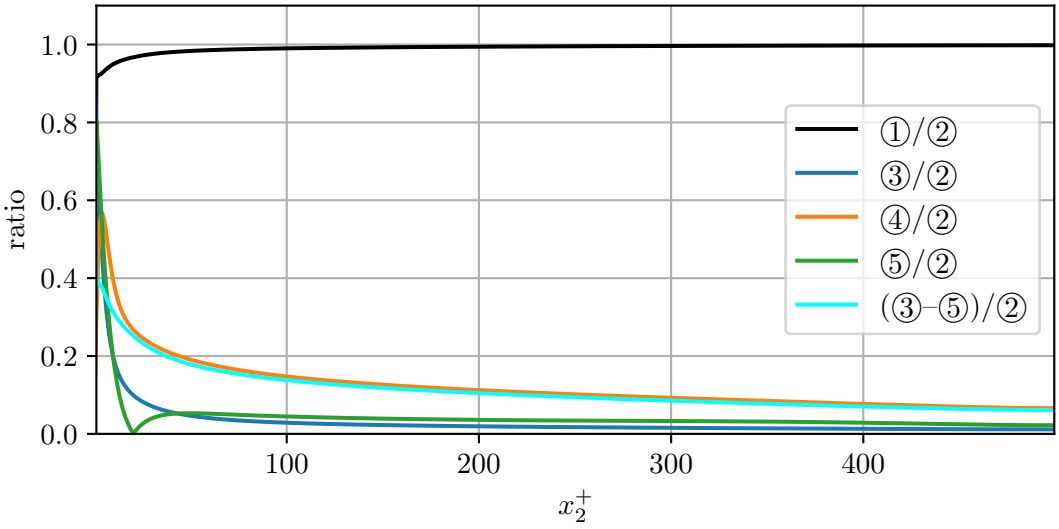

(c) Normalised scalar transport equation analysis with $Pr = 1$

Figure 4.19.: Normalised transport equation analysis *rms* of the passive scalars (case m500)

Since the dependence of the validity of Taylor's hypothesis on the Prandtl number is of special interest for the transport of turbulent passive scalar structures, $rms(③–⑤)/rms(②)$ is shown again for all investigated values of Pr in Figure 4.20. The figure contains the same curves as in Figure 4.19 and additionally the corresponding graphs for m180 and m1000. All means are again calculated with respect to the same quantities as before, except for the time-averages of m1000, which are taken with respect to only 2 statistically fully developed time steps.
With the log scale depicted, it can be observed that $rms(③–⑤)/rms(②)$ take on a nearly constant value close to the wall. The size of this region is independent of the Reynolds number, but decreases with an increase in the Prandtl number. It seems to be contained within the molecular sublayer, which is an effect that could be attributed to the constant wall-normal passive scalar gradient in this area. The reason for not observing such a dependency on Re_τ lies in the use of viscous units, which already scale the depicted quantities with their respective Reynolds number. Towards the channel centre, the "hypothesis breaking"-terms decrease until they reach a minimum, which is slightly larger for lower Re_τ-cases. This might be explained by the wall losing its influence on the outer flow with larger Reynolds numbers. With respect to different values of Pr at a constant value of Re_τ, the same minimum can be observed at the channel centre. However, in terms of the maximum value at the wall, a clear dependence can be seen on the Reynolds and Prandtl numbers. Here, an increase in either one of the dimensionless numbers yields an increase in $rms(③–⑤)/rms(②)$. Therefore, Taylor's hypothesis becomes less applicable in general with an increase in turbulent motion. This behaviour could be attributed to larger wall-normal gradients, which skew possible near-wall structures and interfere with their coherent convection. It is interesting to note, that figures 4.19a, 4.19b, and 4.19c show significant differences in $rms(③)/rms(②)$ and $rms(④)/rms(②)$, respectively. However, the curves in Figure 4.20 of the associated Prandtl numbers do not show an equivalent difference in $rms(③–⑤)/rms(②)$. It is therefore possible to assume some kind of counteracting effects between the viscous and non-linear terms with regard to the breaking of Taylor's hypothesis.

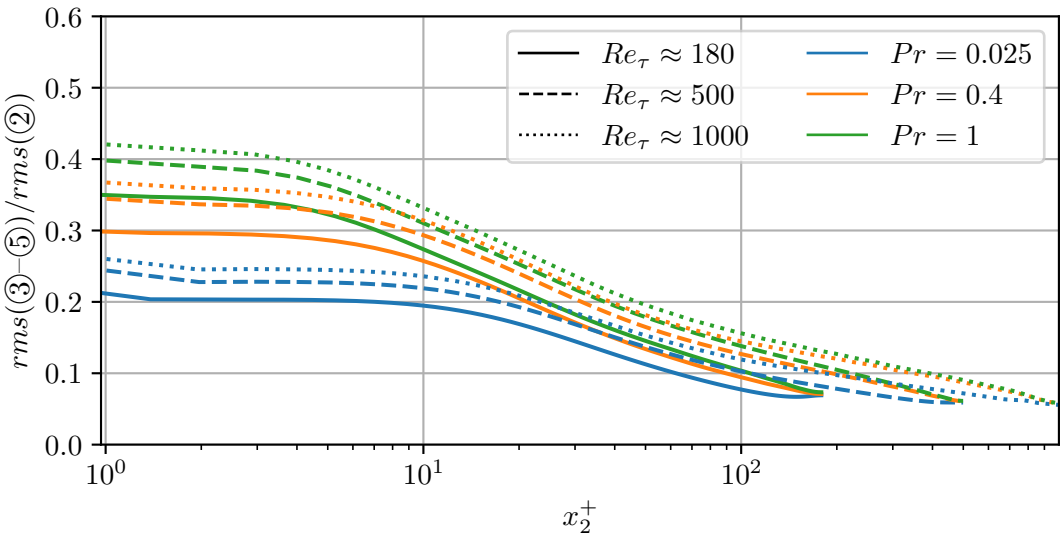

Figure 4.20.: Error terms of transport equation analysis of passive scalars

4.3. Convection velocity behaviour

4.3.1. Wall distance dependency

Studies investigating the behaviour of convection velocities in wall-bounded turbulence often analyse their dependence on the wall distance. Considering the velocity components as the transported properties of interest, this is done in publications of, for example, Kim and Hussain 1993, Romano 1995, Khoo et al. 2001, Renard and Deck 2015, or Atkinson et al. 2015. In the case of the convection of passive scalar structures, less information is present in the literature. However, if they are considered (e.g. Kowalewski et al. 2003, Hetsroni et al. 2004 or Liu et al. 2023), it is again their dependence on the wall distance that is analysed. Therefore, as a first step in investigating the convection velocity behaviour, these analyses are retraced. Figure 4.21 shows the overall convection velocities of velocity and scalar structures with respect to the wall distance. For these visualisations, the integrals of Equation 2.63 are taken with respect to the whole space of wavenumbers present in the simulation results. In addition to the overall convection velocities, the mean streamwise velocity profile as well as the bulk velocity are shown for comparison. All quantities are depicted in viscous units. The results shown are calculated from the data of the simulation case m500, while the respective results of m180 and m1000 can be seen in subsection D.3. This is sufficient for the initial analyses of the overall convection velocities, as their qualitative behaviour does not change significantly with varying Reynolds number, as can be seen when comparing Figure 4.21 with the results listed in subsection D.3. However, Del Álamo and Jiménez 2009 mention some low respectively high Reynolds number effects that might occur. These effects, as well as the general dependencies of the convection velocities on the Reynolds number, are examined in subsection 4.3.3. All averages included in the definitions of the depicted quantities are taken with respect to the two statistically homogeneous spatial directions, 100 statistically fully developed time steps, and the symmetries of the convection velocity distributions mentioned in section 4.1.

The quantitative behaviour of the overall convection velocities for turbulent velocity structures, depicted in Figure 4.21a, is in good agreement with the data provided by Del Álamo and Jiménez 2009. The figure shows similar slopes for U_{c,u_1}, U_{c,u_2}, and U_{c,u_3}, all three being exactly the same in close vicinity of the channel centre. All overall convection velocities demonstrate a slope similar to the mean streamwise velocity profile in the log layer close to $x_2 = h$. However, their values are slightly smaller than that of $\langle u_1 \rangle$. This trend changes closer to the buffer layer, where the decrease in the overall convection velocities is less prominent than that of the mean streamwise velocity component. The overall convection velocities are therefore larger than the mean velocity in the viscous sublayer, with a "cross-over" in the buffer layer. This cross-over is located closer to the channel wall for the convection of streamwise velocity structures, whereas it appears at the same wall distance for the other velocity components. Note that this is the reason for the minimum of ⑤ in the transport equation analyses, discussed in section 4.2. Inside the viscous sublayer, the decrease in the overall convection velocities stops, leaving them at a constant value. In close vicinity to the wall, the overall convection velocities seem to decrease again. However, this behaviour is not evident in the literature and might be an artefact of numerical inaccuracy. The use of ghost-nodes and the associated compact finite difference scheme could negatively affect all calculated quantities near the wall, since not all applied boundary conditions are physically motivated, as mentioned in section 3.1.

Similar shapes are taken by the plots of the overall convection velocities for passive scalar structures at different Prandtl numbers, as can be seen in Figure 4.21b. A dependency on the Prandtl number is evident in the fact that the overall convection velocity increases with a decrease in Pr, in the viscous sublayer, the buffer layer, and parts of the log layer. However, the opposite effect can be observed in close proximity to the channel centre.

Here, the overall convection velocity of a passive scalar structure decreases together with a decrease in Pr. As a result, the cross-over between the mean streamwise velocity profile and the overall convection velocity shifts towards smaller velocities and wall distances with larger values of the respective Prandtl number. This again explains the behaviour of ⑤, as mentioned in section 4.2. The change in $U_{c,\theta}$ with respect to Pr could be attributed to the tendency of the flow to form larger passive scalar structures with a decrease in the Prandtl number. Del Álamo and Jiménez 2009 mention longer wavelengths (their respective structures occupy larger regions of the channel) to propagate at a speed closer to the bulk velocity, while shorter wavelengths (they are related to structures which are contained within a limited local area) tend to move with the local value of the streamwise mean velocity. This explanation is further supported by the fact that the trend change mentioned regarding the dependence of the overall convection velocity on the Prandtl number occurs at a velocity very close to U_b, as shown by Figure 4.21b.

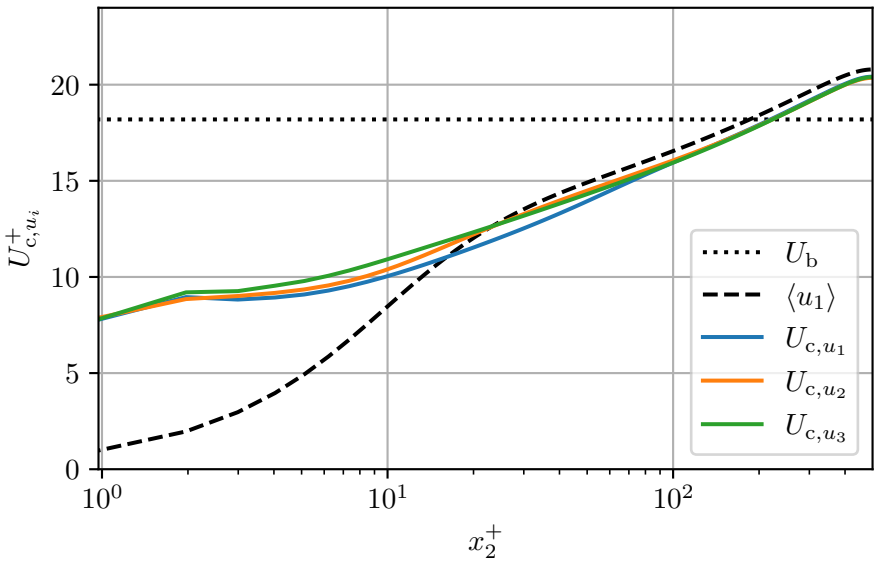

(a) Overall convection velocities of velocity structures

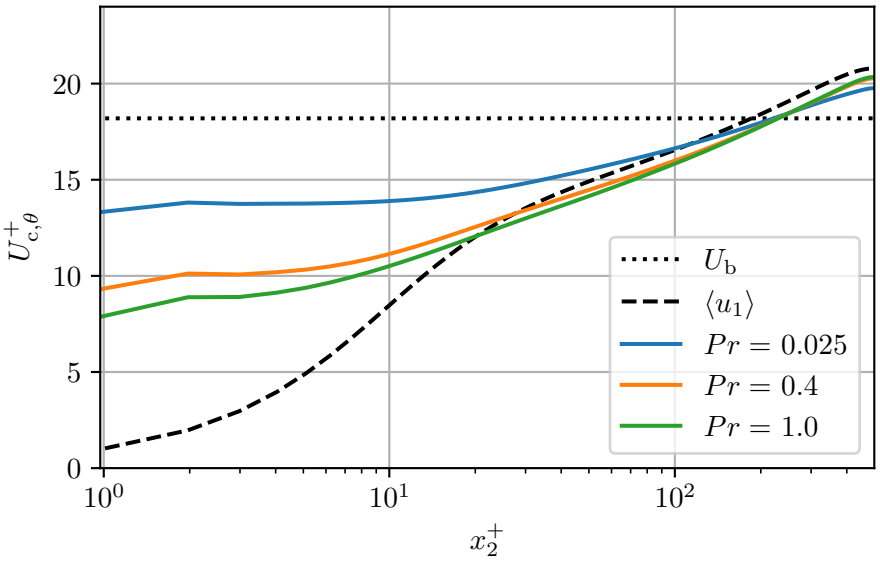

(b) Overall convection velocities of passive scalar structures

Figure 4.21.: Overall convection velocities (case m500)

To further analyse the influence of different-sized structures on the overall convection velocities, the same relationships as before are depicted for partitioned wavelength ranges of all transport quantities considered separately. Figure 4.22 and Figure 4.23 show these partitioned overall convection velocities for velocity and scalar structures, respectively. In addition to the overall convection velocities, which are calculated by integrating Equation 2.63 over "all" scales, the figures also show curves of overall convection velocities with respect to only "small" respectively "large" scales, independently. Here, a structure is considered "small" if its wavelengths $\lambda_i = 2\pi/k_i$ are bounded from above by $(\lambda_1, \lambda_3) < (h, h/4)$, while a structure is considered "large" if its wavelengths are bounded from below by $(\lambda_1, \lambda_3) \geq (h, h/4)$. Note that the unification of these small and large wavelength ranges does *not* yield the whole space of turbulent structures considered, since scales which have a large expansion in one of the periodic spatial directions and a small expansion in the other are not included. The mean streamwise velocity profile and the bulk velocity are again shown for comparison, and all quantities are depicted in viscous units. As for Figure 4.21, the only simulation case visualised is m500, while the corresponding figures of the other main simulations can be found in subsection D.4. The averages needed to calculate the quantities shown in Figure 4.22 and Figure 4.23 are taken with respect to the statistically homogeneous spatial directions, 100 statistically fully developed time steps, as well as the convection velocity symmetries regarding wall distance and wavenumber-space. A similar behaviour as for passive scalar structures at different Prandtl numbers (Figure 4.21b) can now also be observed in the depiction of the overall convection velocities of turbulent velocity structures at different wavelength ranges, shown in Figure 4.22. Close to the channel wall, in the viscous sublayer, a tendency of larger turbulent structures to move with a velocity closer to that of U_b is equally visible for all velocity components. However, the difference between large, small, and all scales is not strongly prominent. Close to the channel centre, where large structures are generally convected more slowly than small ones, this behaviour is only reasonably evident for turbulent structures of the wall-normal velocity component and not for the other velocity components. This might be due to the spectral distribution of u_{c,u_2} and the energy contained within wall-normal velocity structures, as will be explained in subsection 4.3.2. For the chosen values $(\lambda_1, \lambda_3) = (h, h/4)$, which divide the wavenumber-space into small and large structures, the smaller scales are dominant in their contribution to the overall convection velocities. This is evident by the partitioned overall convection velocities of the small scales being closely aligned with those of all scales for the convection of streamwise, wall-normal, and spanwise velocity structures in figures 4.22a, 4.22b, and 4.22c, respectively. This could be attributed to most of the respective energy being contained within the smaller scales, as will later be shown in figures 4.26 to 4.28, causing these scales to dominate the weighted integral in Equation 2.63. In addition, all structures not considered in the "small" or "large" scales might also be convected at velocities closer to those of the small scales. This could be relevant, since they *do* contribute to the overall convection velocity of "all" scales. However, in the case of streamwise velocity structures, a slight deviation from this alignment can be observed in the viscous sublayer. Here, the overall convection velocity for all scales has marginally larger values than that of the partitioned overall convection velocity for small scales, therefore approaching the convection behaviour of the large scales. The reason for this might again lie in the spectral distribution of the convection velocity for streamwise velocity structures in combination with the respective energy spectra. As will be shown in subsection 4.3.2, large u_1-structures penetrate the near-wall layers, transferring their (larger) energy and (faster) convection velocity to the largest local scales. Another interesting behaviour is shown by the convection of large u_2-structures. In contrast to the corresponding plots for the other velocity components, the curve of the partitioned overall convection velocity for large wall-normal velocity scales deviates only from the other quantities depicted in the viscous sublayer and buffer layer. In the log layer, it is more

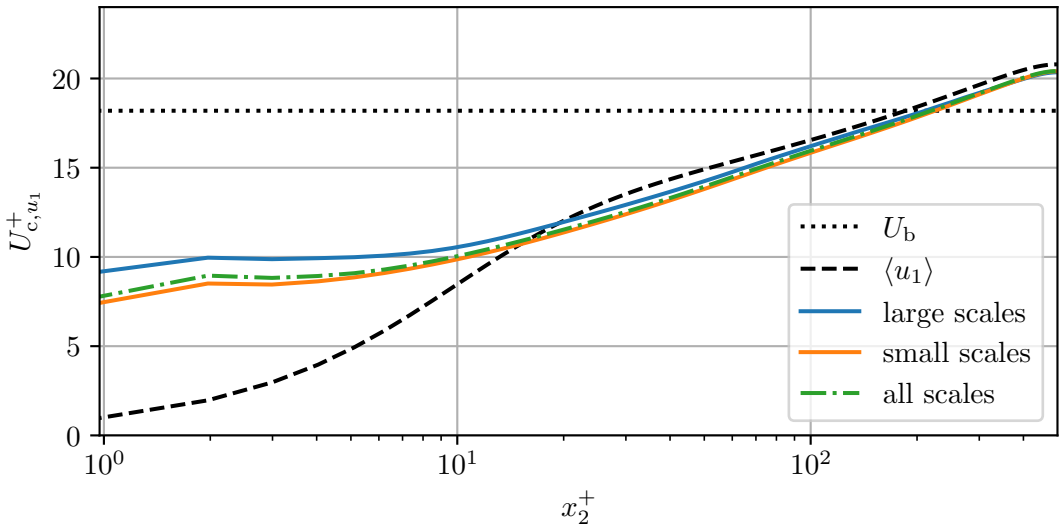

(a) Partitioned overall convection velocities of streamwise velocity structures

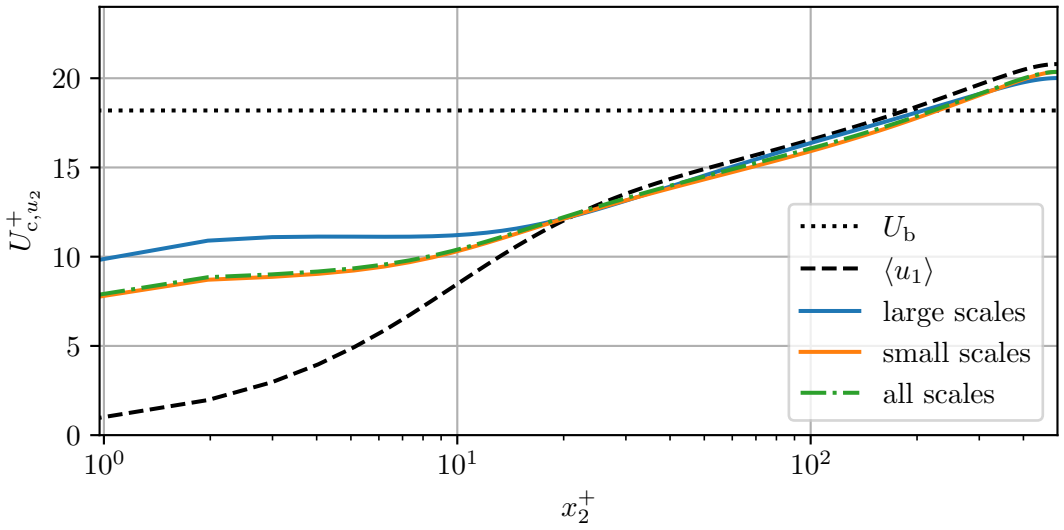

(b) Partitioned overall convection velocities of wall-normal velocity structures

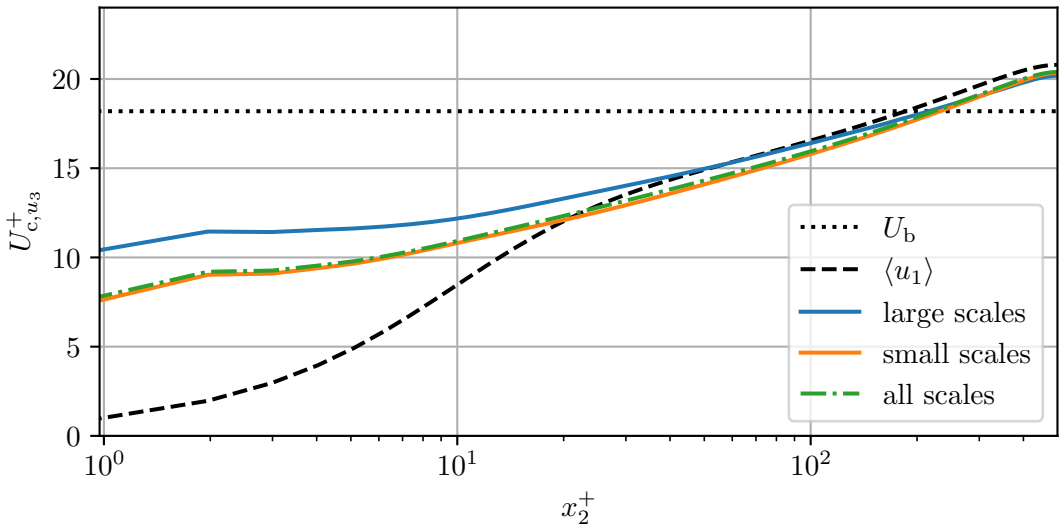

(c) Partitioned overall convection velocities of spanwise velocity structures

Figure 4.22.: Partitioned overall convection velocities of velocity structures (case m500)

closely aligned with the partitioned overall convection velocities of both small and all scales. Again, this could be attributed to the distribution of convection velocity and energy over the range of turbulent u_2 scales. As will be shown in subsection 4.3.2, the special shape of the wall-normal distributions yield a "fast" deceleration of the large scales as well as an equally "fast" acceleration of the small scales with an increase in wall distance. This results in all partitioned overall convection velocities approaching similar values at the start of the log layer, independent of the structure sizes considered.
The previously established behaviour of larger scales being convected at a velocity closer to U_b, while smaller scales are more influenced by $\langle u_1 \rangle$, is again visible for the partitioned overall convection velocities of scalar structures in Figure 4.23. The influence of the bulk velocity on the large scales decreases with an increase in Pr. For the values $(\lambda_1, \lambda_3) = (h, h/4)$, which are chosen to characterise "small" and "large" scales in the shown representation, this is strongly visible when comparing the data for $Pr = 0.025$ in Figure 4.23a with their counterparts for $Pr = 1$ in Figure 4.23c. The reason for this might be the property of lower Prandtl number flows to carry more respective (passive scalar) energy at larger wavelengths. This would result in a greater influence of these structures, and in extension the bulk velocity, on the overall convection velocity calculations, since in Equation 2.63 each scale is weighted by the respective energy it carries. Another interesting effect of a change in the Prandtl number is that the overall convection velocity of all scales approaches the partitioned overall convection velocity of the small scales with an increase in Pr. This could be attributed to the same energy-related property of lower respectively high Prandtl number flows mentioned before. In general, the difference in the partitioned overall convection velocity of small and large scales decreases with larger Prandtl number values. Regarding the (potentially numerically-induced) deviation of the overall convection velocities from their constant values in close vicinity to the wall, this behaviour can again be observed for all Prandtl numbers and partitioned wavelength ranges alike. However, the region where the respective partitioned overall convection velocity is constant extends deeper into the buffer layer for smaller values of Pr and larger turbulent scales. This might be attributed to the extended molecular sublayer of low Prandtl number flows. Since most turbulent passive scalar structures form in the scalar buffer layer, their influence is carried towards the wall by means of conduction. The area, in which the local overall convection velocity is only a footprint of effects closer to the channel centre, extends therefore further into the channel for smaller values of Pr. As a result, an equilibrium state between this footprint and potential local effects is also reached at higher wall distances, leading to a larger area of constant overall convection velocity.
Besides the analyses of different wavelength ranges, the consideration of individual physical contributions to the overall convection velocities is of additional interest. As explained in section 3.3, the chosen implementations offer the possibility of calculating each term of the definitions of the convection velocities independently. Taking only these contributions into account instead of the "whole" convection velocities when evaluating Equation 2.63, the respective contributions to the overall convection velocities can be calculated. Visualisations of the overall convection velocity contributions can be seen in Figure 4.24 and Figure 4.25 for the transport of velocity and scalar structures, respectively. In addition, the overall convection velocities are shown again as dashed lines. Hence, it is clear that the sums of all contributions again yield the corresponding overall convection velocities. Note that the profiles in Figure 4.24 and Figure 4.25 do *not* necessarily show the quantities listed in their legends, but rather those parts of equations 3.22 to 3.25 corresponding to each entry of the respective legend. All quantities are depicted in viscous units. Since the qualitative behaviours of the overall convection velocity contributions do not differ for a change in Reynolds number, only the simulation case m500 is listed here. The results of m180 and m1000 can be seen in subsection D.5. All the averages needed in the calculations of the quantities shown in Figure 4.24 and Figure 4.25 are taken again with respect to the two

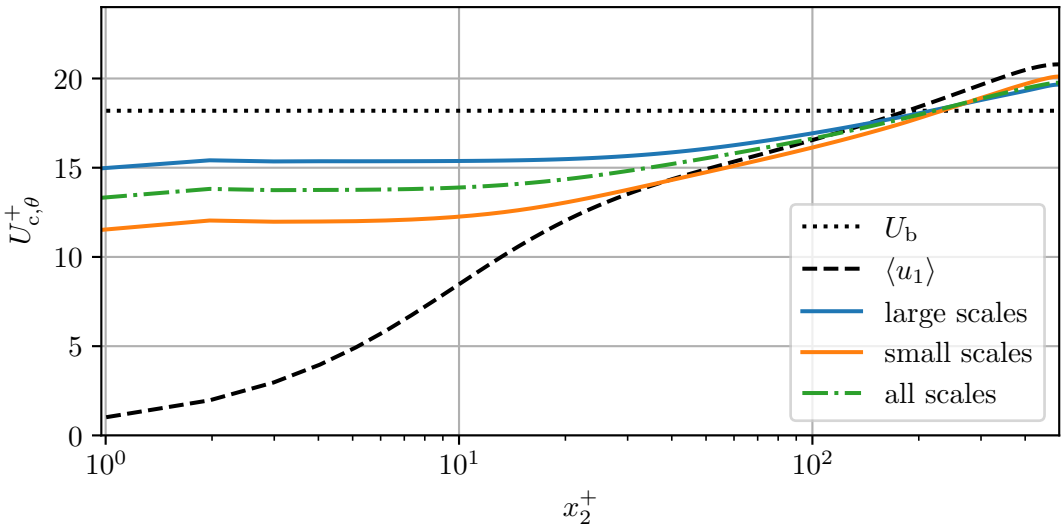

(a) Partitioned overall convection velocities with $Pr = 0.025$

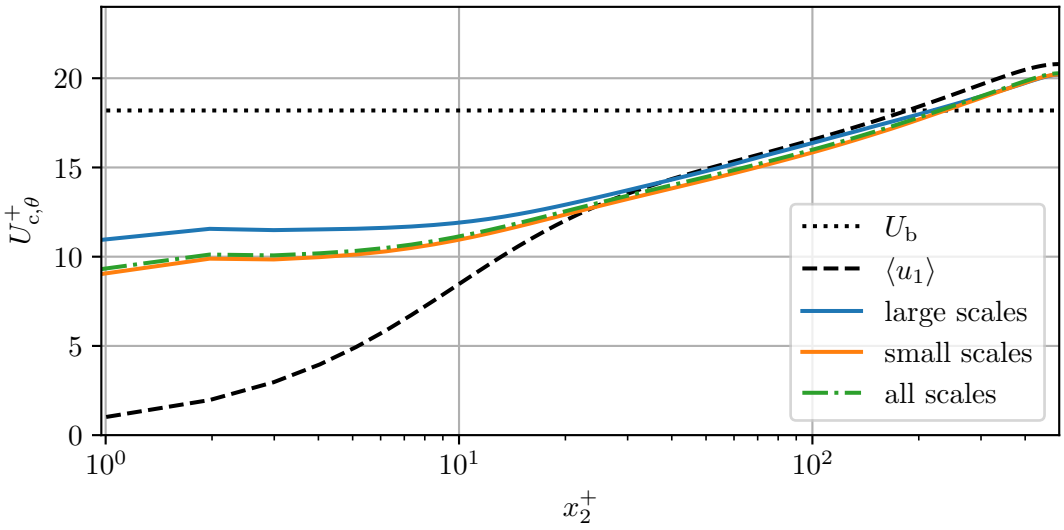

(b) Partitioned overall convection velocities with $Pr = 0.4$

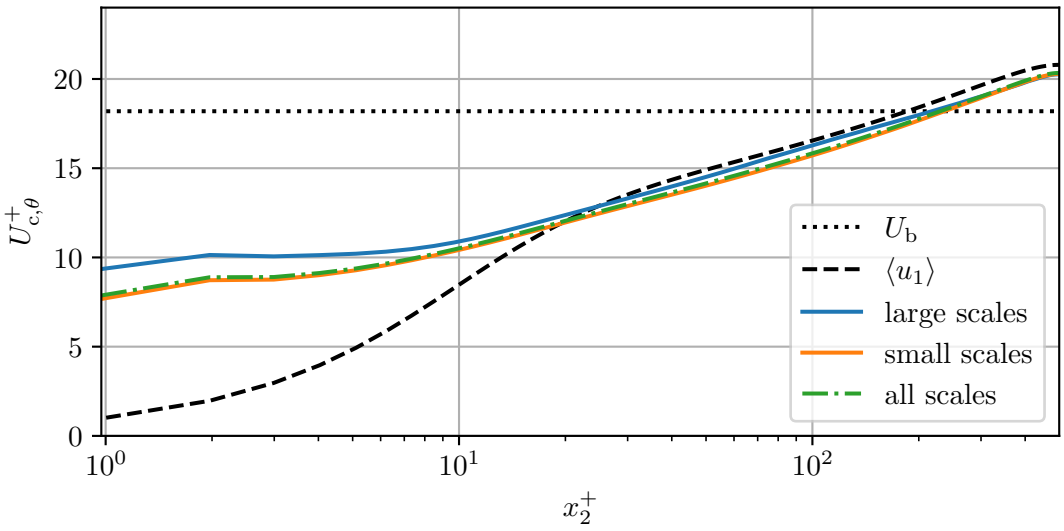

(c) Partitioned overall convection velocities with $Pr = 1$

Figure 4.23.: Partitioned overall convection velocities of scalar structures (case m500)

statistically homogeneous spatial directions, 100 statistically fully developed time steps, and the symmetries of the convection velocity distributions.
For the overall convection velocity contributions of velocity structures seen in Figure 4.24 a clear dominance of the streamwise mean velocity can be observed in the log layer. In this region, all other contributing terms are comparatively small. This is especially the case for the convection of spanwise velocity structures, while it is the least prominent in case of streamwise velocity structures. Closer to the channel wall, the dominance of $\langle u_1 \rangle$ decreases for the overall convection velocities of all velocity structures alike. In the viscous sublayer and the buffer layer, other contributions than the streamwise mean velocity have a non-negligible influence on $U_{\mathrm{c},\boldsymbol{u}}$. It is interesting to note that there is a trend change for the other contributors in the buffer layer (at $x_2^+ \approx 12$ for m500) for some velocity structures. Here, terms that have a negative influence on the overall convection velocity close to the channel centre become positive with a further decrease in wall distance and vice versa. This behaviour is clearly visible for the convection of u_1-structures and can also marginally be seen in the case of u_2-structures. A reason for this could not be found in the scope of the presented thesis. However, this trend change appears at a channel height where significant amounts of turbulent structures are created. From there, these structures are transported towards the channel wall and the channel centre. Since the relationship between the mean streamwise velocity and the overall convection velocity also differs in sign in the area closer to the channel wall in comparison to the area closer to the channel centre, it can be reasoned that the created structures also introduce opposing effects in either direction. In the viscous sublayer, where the mean streamwise velocity drops significantly but the overall convection velocities take on a nearly constant value, other contributions must play a dominant role. In case of the overall convection velocity contribution of streamwise velocity structures, this role is taken by the viscous term. Its influence increases in the viscous sublayer with decreasing wall distance before becoming constant in close proximity to the wall. The viscous term *not* vanishing at the wall, in contrast to most other terms, is an expected behaviour, since the value of this term is not damped by the boundary conditions, which force all quantities that are directly influenced by any velocity component to vanish. However, a physical explanation for the positive sign of the viscous term can only be assumed to originate from the faster convected scales at larger wall distances. Streamwise velocity structures which arise further from the wall could carry their influence via the viscous term into the near-wall layers. For the streamwise velocity component, the only other contribution which does not approach zero at $x_2 = 0$ is the pressure term. It also increases towards the wall in the viscous sublayer, but with less intensity than the viscous term. Again, the fact that the pressure term does not vanish is connected to it not being influenced by the no-slip or impermeability conditions at the wall. An explanation for the positive sign as well as its small magnitude compared to the viscous term remains an open question in the scope of this thesis. In accordance with the previously made argument, it could be suspected that pressure fluctuations are not as dominant in the transport of streamwise velocity structures towards the channel wall. Thereby, no significant increase in the overall convection velocity is visible due to their effects. A different behaviour can be observed for the convection of wall-normal and spanwise velocity structures. Here, the viscous term sharply decreases with a decrease in wall distance in the viscous sublayer. This decrease is substantial enough that the viscous term takes on negative values, even slowing down the overall convection velocities. However, its influence is balanced by the pressure term, which increases (even more) steeply towards the channel wall in the viscous sublayer. Therefore, the driving physical mechanisms vary for the overall convection velocities of different velocity structures in the vicinity of the wall. This could be due to the redistributive character of pressure fluctuations often seen in turbulent shear flows. However, how this redistributive character is to be interpreted in the context of convection velocities is hardly intuitive and therefore still

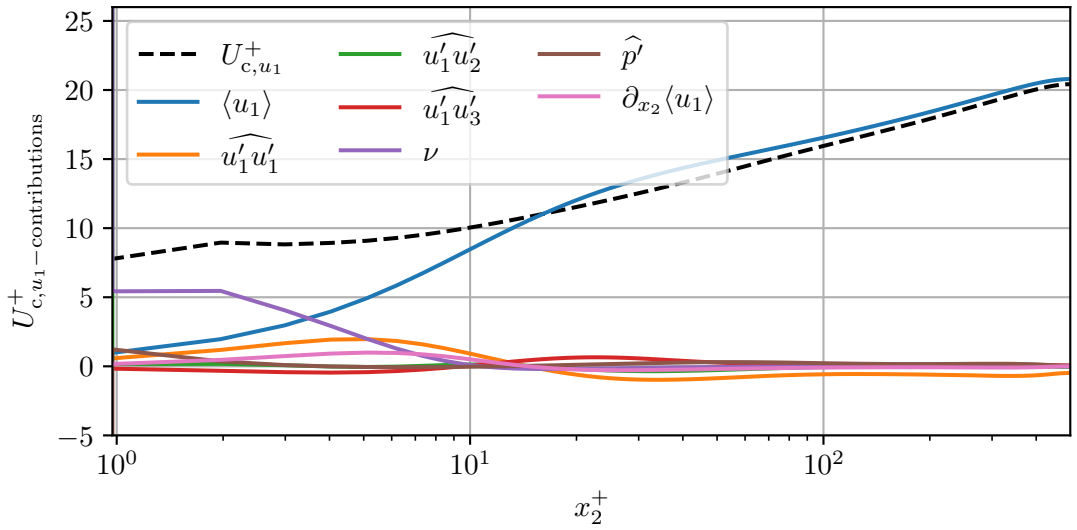

(a) Overall convection velocity contributions of streamwise velocity structures

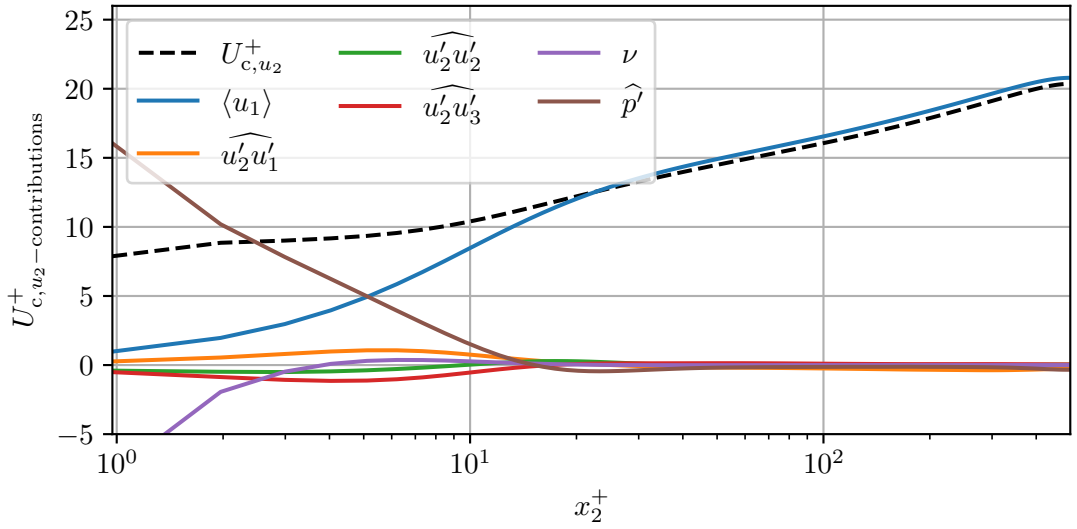

(b) Overall convection velocity contributions of wall-normal velocity structures

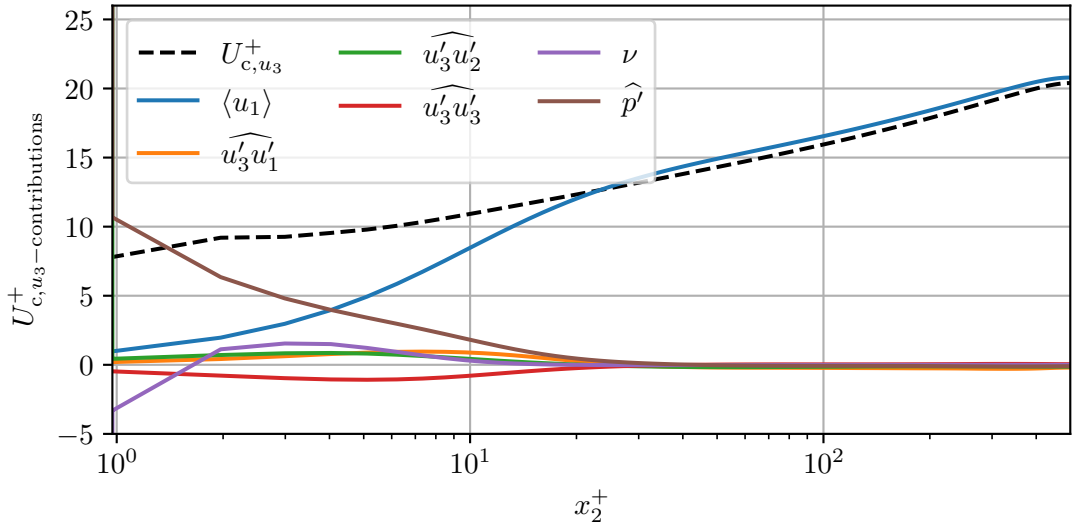

(c) Overall convection velocity contributions of spanwise velocity structures

Figure 4.24.: Overall convection velocity contributions of velocity structures (case m500)

unclear. Like in the case of streamwise velocity structures, the interpretation of the viscous term is difficult, especially since in the case of the other velocity components, it shows an opposite behaviour as before. Note that the quantities in close vicinity to the wall might be error-prone due to numerical inaccuracies, as mentioned before. Considering the behaviour of the viscous term for the convection of spanwise velocity structures in particular, the depicted near-wall behaviour could be non-physical. When the data point closest to the wall is ignored, no sharp decrease in the viscous term is seen. It could therefore be possible that the viscous term actually further decreases in magnitude towards the channel wall for the convection of turbulent u_3-structures. As a result, the pressure term would be the only dominant contributor near the channel wall. Note that the behaviour of the viscous term would be more intuitive to explain in this case. As mentioned before, the influence of fast u_1-structures is transferred into regions close to the wall by this term. For spanwise velocity structures, no such behaviour might be taking effect. However, for wall-normal velocity structures, the viscous transfer of outer-flow influences could lead to the deceleration or destruction of near-wall structures, causing the viscous term to slow down the overall convection velocity of u_2-structures.
The influence of the different terms that contribute to the overall convection velocity of passive scalar structures depicted in Figure 4.25 is closely related to that of the streamwise velocity component. In the case of $U_{c,\theta}$, the mean streamwise velocity has a dominant influence in the log layer, whereas the conduction term takes on this role close to the channel wall. However, the position at which the conduction term takes on non-negligible values moves closer to the wall with an increase in the Prandtl number. The same shift towards the wall can be observed for the wall distance at which the mean streamwise velocity is overpowered by the conduction term. For the given simulation case (m500), this point lies in the buffer layer for $Pr = 0.025$ and in the viscous sublayer for $Pr = 1$, while it is located at the border of both layers in the case of $Pr = 0.4$. Additionally, a decrease in the maximum value, which the conduction term reaches in close vicinity of the wall, can be observed with an increase in the Prandtl number. This is consistent with the previous results of the overall convection velocity taking the largest wall-values for the smallest Prandtl number, since the conduction term is the only term that does *not* approach zero at the wall. The reason for this is again due to the fact that the conduction term is not damped by the boundary conditions. The increasing influence with decreasing Prandtl number could trivially be explained by the increase in conductivity with lower values of Pr, which is visible in its definition (Equation 2.19). The influence of all other physical mechanisms on the overall convection velocity of passive scalar structures is small in comparison. Still, there is an area which overlaps with the viscous sublayer and the buffer layer, where the other terms increase slightly. This increase is more significant (but still small) for larger values of Pr while less visible for smaller Prandtl numbers. This behaviour could be attributed to the tendency of lower Prandtl number flows to behave somewhat "laminar" with regard to the passive scalars. As was shown in Figure 4.5, the turbulent scalar flux is small for $Pr = 0.025$. Since the other non-linear components do not carry much energy either, their respective terms in Figure 4.25 are small as well for smaller Prandtl numbers. Note that this area also moves closer to the channel wall with increasing Prandtl numbers. Lastly, in Figure 4.25, the same trend change in the values of most of the contribution terms is visible as in Figure 4.24a. Those terms that have an accelerating effect on the overall convection velocity close to the channel centre become negative in closer vicinity to the wall, while the previously decelerating terms take positive values. The reason for this is again unclear but could be attributed to the same effects mentioned before, since the trend change appears to be located at a wall distance where a significant amount of passive scalar structures arises.

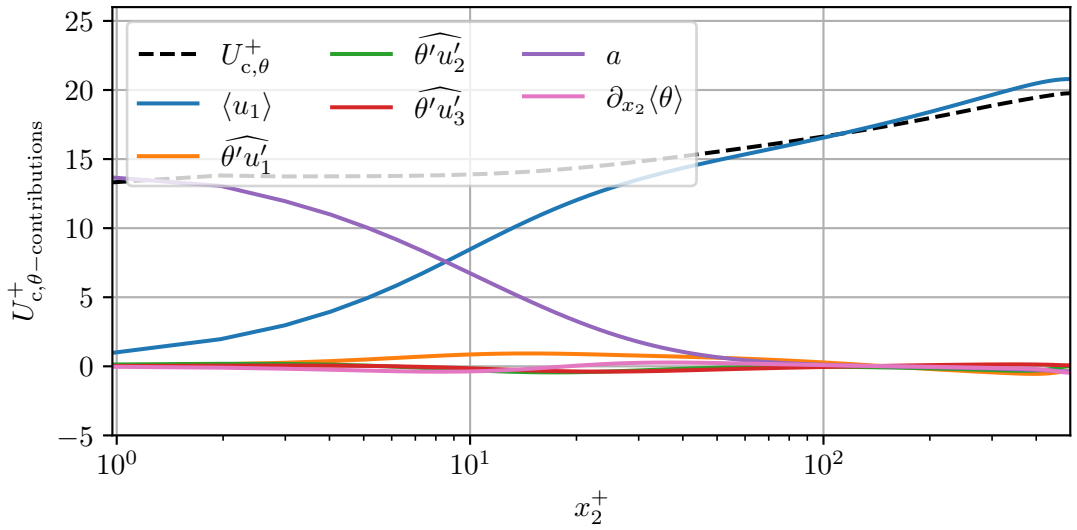

(a) Overall convection velocity contributions with $Pr = 0.025$

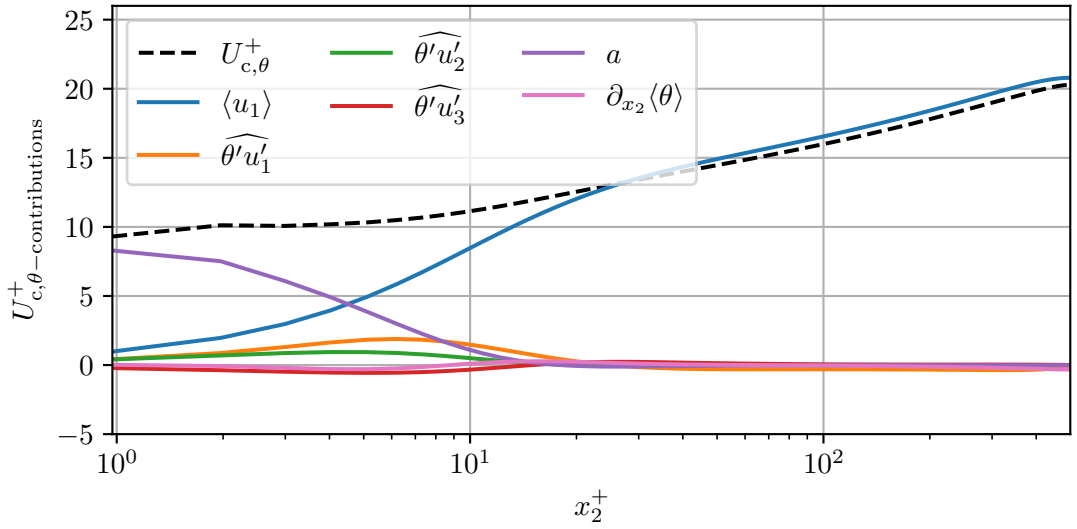

(b) Overall convection velocity contributions with $Pr = 0.4$

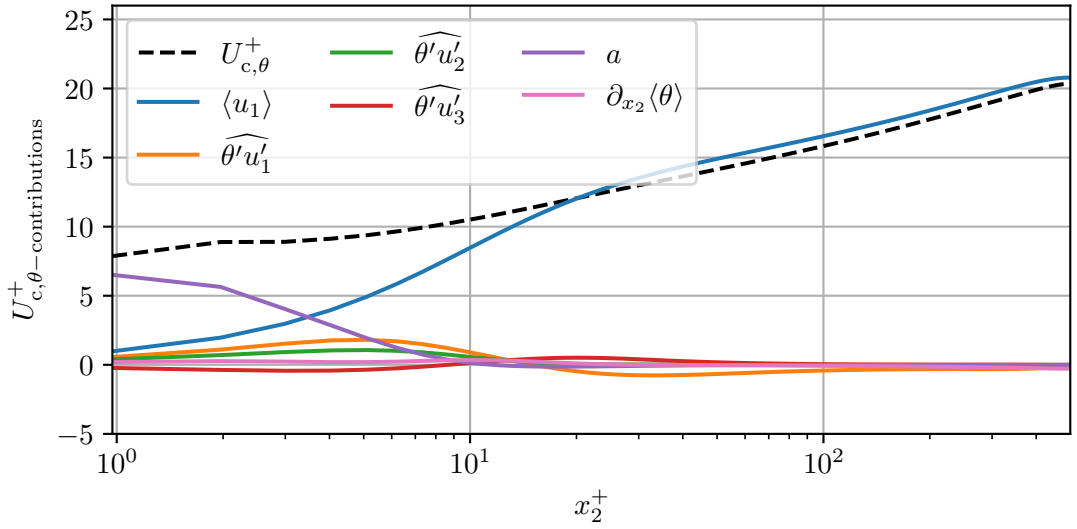

(c) Overall convection velocity contributions with $Pr = 1$

Figure 4.25.: Overall convection velocity contributions of scalar structures (case m500)

4.3.2. Wavenumber dependency

As mentioned in subsection 2.3.2, the convection velocities depend not only on the wall distance but also on other parameters such as the scales of turbulence and their respective wavenumbers. To analyse this dependency, the spectral distributions of the convection velocities, defined by equations 3.22 to 3.25, are considered. Figures 4.26, 4.27, and 4.28 (adapted from Del Álamo and Jiménez 2009) depict the behaviour of turbulent velocity structures, while figures 4.29, 4.30, and 4.31 consider passive scalars at different Prandtl numbers as the transported quantities of interest. All figures show the same two different wall distances, one at the edge of the viscous sublayer ($x_2^+ \approx 5$) and another in the log layer ($x_2^+ \approx 265$). Two quantities are visualised in each subplot, on the one hand a heat map of the respective wavenumber spectrum (Equation 2.36) pre-multiplied with the two wavenumbers k_1 and k_3, and on the other hand isolines of the corresponding convection velocities. Note that only a finite range of isoline values is depicted in all figures. All shown behaviours might therefore be interpolated respectively extrapolated to the otherwise "empty" parts of each plot. Both quantities are shown in viscous units over the wavelengths in the streamwise and spanwise directions. The latter are normalised by the channel half-width. Note the difference from a depiction in the (k_1-k_3)-space. Here, the largest scales are located at the top right corner of each figure, while the smallest scales correspond to the bottom left corner. The only simulation results depicted in this chapter are those of case m500. Spectral distributions evaluated from the other main simulations are shown in subsection D.6, while specific differences between these cases at different Reynolds numbers are addressed separately in subsection 4.3.3. All averages applied in the calculations of the depicted quantities are taken with respect to both statistically homogeneous spatial directions and 100 statistically fully developed time steps. In case of the convection velocities, averages are also taken with respect to their symmetries. Since their isolines still show a considerable amount of statistical noise, the data are additionally smoothed by means of a simple moving average. For this purpose a rolling (3,3)-window is applied to the discrete (k_1,k_3)-space. Note that in all figures 4.26 to 4.31, the scales of the premultiplied energy spectra and convection velocities differ for the individual wall distances. Direct comparisons between the two should therefore be made with care.
Regarding the spectral convection velocity distribution of streamwise velocity structures close to the channel wall (Figure 4.26a), the highest speeds can be observed at the largest wavelengths. This is consistent with the previously found behaviour that larger scales tend to move with speeds closer to the bulk velocity. In the viscous sublayer and the buffer layer, U_b is larger than the local mean velocity. With a decrease in λ_1 or λ_3, the convection velocity decreases as well, in general. However, for large spanwise structures, there is again an increase in u_{c,u_1} for very small values of λ_1. This (secondary) area of high convection velocities could be attributed to some kind of fast coherent structures with small streamwise and large spanwise expansion, forming in close vicinity of the wall. However, which physical mechanisms would form such structures remains unclear at this point and should be investigated further in upcoming projects. For the represented simulation case and wall distance, the convection velocities span over a range of 2.5 u_τ. This is again due to the influence of $\langle u_1 \rangle$ on the small scales and U_b on the large scales. At the considered wall distance, there is a significant difference between the values of the local mean velocity and the bulk velocity. As can be seen in the premultiplied energy spectrum, most energy is contained within the medium wavelengths. For the given case, they are convected at velocities around $u_{c,u_1}^+ \approx 9.5$. Considering the overall convection velocity (Equation 2.63) to be a weighted average of the shown distribution, the behaviour seen in Figure 4.21a is explained in the sense that the overall convection velocity of streamwise velocity structures moves at around $U_{c,u_1}^+ \approx 9.5$ for $x_2^+ \approx 5$. The same argument can be made when considering the spectral convection velocity distribution closer to the channel centre in Figure 4.26b.

Here, most of the energy resides within medium to large structures, which are convected at velocities of around $u^+_{c,u_1} \approx 19$. This is again consistent with the overall convection velocity of streamwise velocity structures at $x_2^+ \approx 265$, seen in Figure 4.21a. It is interesting to note that at this wall distance, the fastest structures are not necessarily the largest ones but rather those of medium size. The convection velocity decreases from the centre of the spectral plane outwards. This could be attributed to the behaviour, that the (respectively slower) bulk velocity decelerates the large scales, while the (respectively faster) mean velocity accelerates the small scales at $x_2^+ \approx 265$. Additionally, $\langle u_1 \rangle$ and U_b take almost similar values at the given wall distance, which could lead to the shrinking of the span of values taken by the convection velocity. Here, u_{c,u_1} ranges over 1.5 u_τ. In general, both wall distance figures 4.26a and 4.26b still show some strong effects of statistical noise. This is especially the case for structures of large streamwise and small spanwise dimensions (at the bottom right of the respective depiction). Based on statements of Del Álamo and Jiménez 2009, this could be explained by the *noisy-scales* losing their coherence in less time than it would take them to travel along the streamwise length of the channel. Since structures with $\lambda_3 < \lambda_1$ have lifetimes proportional to their spanwise extension, they do not consistently exist long enough to be detected by the mathematical framework defining a streamwise convection velocity. According to Del Álamo and Jiménez, this effect further worsens with an increase in wall distance. Regarding the general behaviour of the convection velocity being noisier for smaller structures, this could be attributed to the difficulty of detecting such scales. In a turbulent flow, random fluctuations can be misinterpreted as the coherent convection of very small scales. An additional (probably dominant) reason lies in the use of a logarithmic plot in combination with the wavelength-distribution of the considered data. The chosen representation "squeezes" more points into the bottom left corner of each figure, resulting in a noisier appearance.

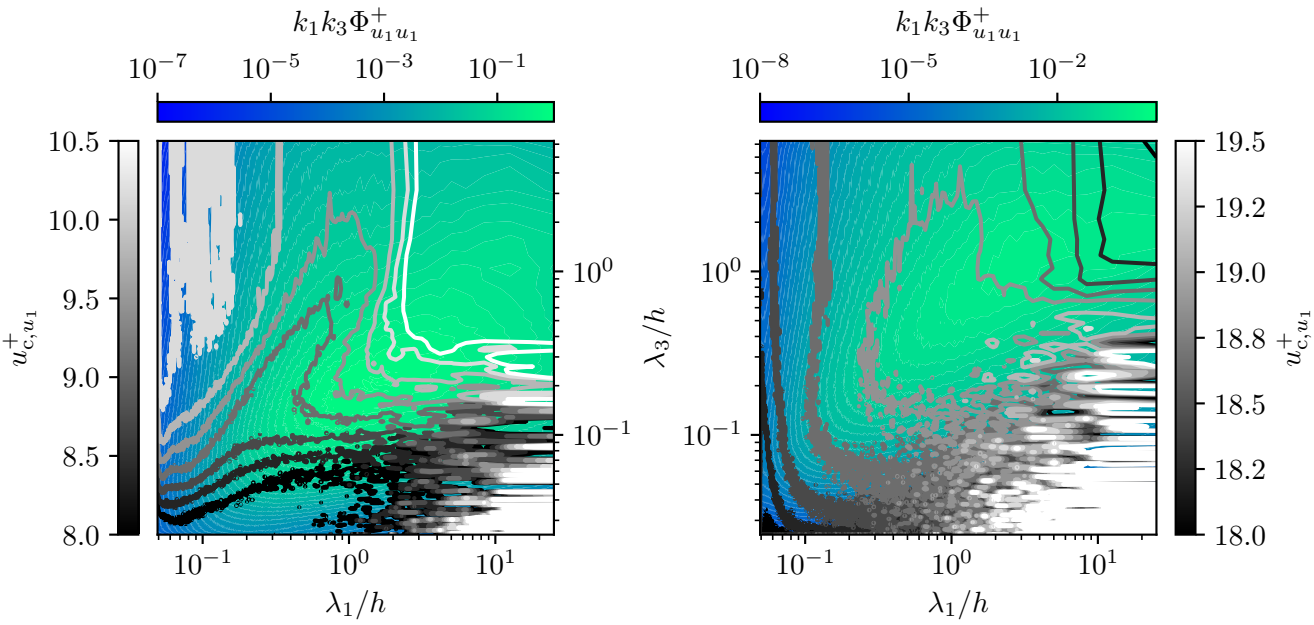

(a) Distribution at $x_2^+ \approx 5$

(b) Distribution at $x_2^+ \approx 265$

Figure 4.26.: Spectral distributions of u_{c,u_1} (case m500)

The spectral convection velocity distribution of wall-normal velocity structures close to the channel wall (Figure 4.27a) shows a slightly different behaviour than in the case of u_{c,u_1}. Here, the highest convection velocities are *not* those of the largest scales but rather those of medium spanwise wavelengths. However, regarding the streamwise dimension of

turbulent u_2-structures, the convection velocity still increases with an increase in λ_1, in general. An explanation for this L-shaped distribution could lie in the influence of the wall on wall-normal velocity structures. Large u_2-structures close to the wall could be more likely to be slowed down or die out due to the impermeability condition and an increased probability of "collision" with the solid surface. The range of values taken by the convection velocity spans over 3 u_τ for the shown simulation case and wall distance. As before, this can be attributed to the difference in values of $\langle u_1 \rangle$ and U_b, which each dominantly influence convected structures of different scales. In the depicted case, the most energy resides within structures of small to medium size. Like in the case of u_{c,u_1}, these high-energy scales are convected at a speed around $u^+_{\mathrm{c},u_2} \approx 9.5$. This leads to the overall convection velocity of wall-normal velocity structures also having a value close to $U^+_{\mathrm{c},u_2} \approx 9.5$ at a wall distance of $x_2^+ \approx 5$, as can be seen in Figure 4.21a. For a spatial position closer to the channel centre, as depicted in Figure 4.27b, larger values of u_{c,u_2} can be observed. The largest values are again connected to medium-sized structures, disregarding statistical noise. Note that some resemblance to the L-shaped distribution, observed closer to the channel wall, can be seen again in the convection velocity isolines extending towards large spanwise wavelengths. The reason for the shift in peak convection velocity with respect to the wall distance is again given by the connection of the small and large scales to the mean and bulk velocity, respectively. At a wall distance of $x_2^+ \approx 265$, $\langle u_1 \rangle$ accelerates the small scales, while U_b decelerates the large scales, leading to the depicted distribution. The span of values taken by the convection velocity close to the channel centre ranges only around 1 u_τ, since the local mean velocity and the bulk velocity are similar in magnitude at this position. Regarding the premultiplied energy spectrum, a shift of the energy peak towards larger structures can be observed with an increase in wall distance. For $x_2^+ \approx 265$, the most energetic structures are convected with a velocity of $u^+_{\mathrm{c},u_2} \approx 19$, which again explains the overall convection velocity seen in Figure 4.21a. However, the largest structures are convected at a particularly slow velocity due to the special shape of the shown distribution. This results in the visible drop in the large-scale partitioned overall convection velocity of wall-normal velocity structures, mentioned in subsection 4.3.1. Similarly to the case of streamwise velocity structures, a non-negligible amount of statistical noise can be observed

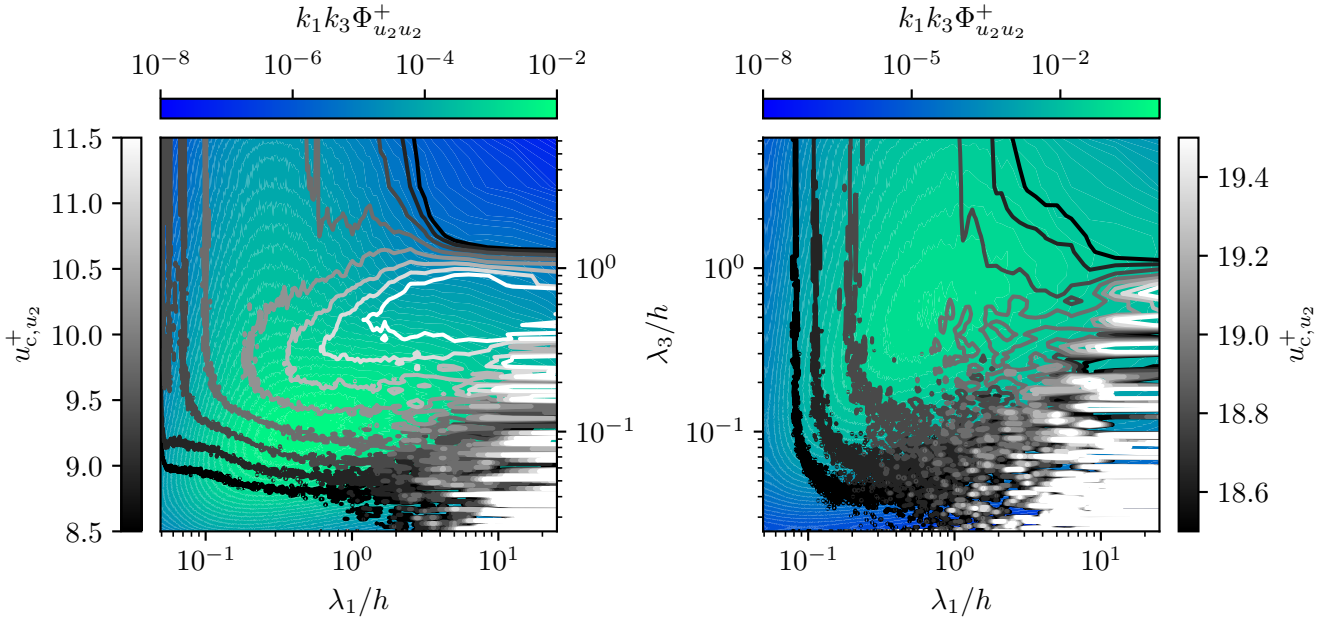

(a) Distribution at $x_2^+ \approx 5$

(b) Distribution at $x_2^+ \approx 265$

Figure 4.27.: Spectral distributions of u_{c,u_2} (case m500)

in some parts of figures 4.27a and 4.27b. This can again be attributed to structures with $\lambda_3 < \lambda_1$ losing their coherence, to random fluctuations being misinterpreted as small-scale convection and to the chosen type of representation.
The spectral distribution of the convection velocity of spanwise velocity structures at $x_2^+ \approx 5$ can be seen in Figure 4.28a. Similarly to the case of streamwise velocity structures, close to the wall, the highest values of u_{c,u_3} can be found at the largest values of both streamwise and spanwise wavelengths. This is due to the accelerating influence of the bulk velocity on the larger scales. Towards smaller scales (regarding both depicted wavelengths), the convection velocity u_{c,u_3} decreases. The span of values taken by the convection velocity of spanwise velocity structures close to the channel wall ranges over 2.5 u_τ, due to the large difference between $\langle u_1 \rangle$ and U_b. Regarding the premultiplied energy spectrum, the most energy is contained within scales that are convected at around $u_{c,u_3}^+ \approx 10$. This is a slightly larger velocity than in the cases of the other two velocity components. Therefore, an equally larger overall convection velocity of $U_{c,u_3}^+ \approx 10$ can also be observed for the spanwise velocity structures in Figure 4.21a as well. For a wall distance closer to the channel centre, at $x_2^+ \approx 265$, there is again a shift in the spectral position of the highest convection velocity. As can be seen in Figure 4.28b, the structures of medium spanwise expansion and medium-high streamwise expansion are convected with the highest velocity. Here, areas of the wavenumber-space which are overpowered by statistical noise are disregarded. This behaviour differs from the results of the other velocity components in the sense that the fastest turbulent u_3-structures tend towards a larger spanwise expansion, rather than keeping a more balanced shape. A reason for this could be the formation of fast u_3-structures with large spanwise dimensions. These structures seem to carry a non-negligible amount of energy, which can be seen in the distribution of the premultiplied energy spectrum. However, what exactly these structures are and why they form in the case of plane channel flow is not clearly evident at this point. The range of values which the convection velocity takes over the spectral distribution is again smaller for a spatial position further from the channel wall. For the depicted case, the span is as broad as 1.5 u_τ, since U_b and $\langle u_1 \rangle$ are of similar magnitude. The most energetic scales again travel at a speed of $u_{c,u_3}^+ \approx 19$. Since they are the dominant factor in the definition of the overall

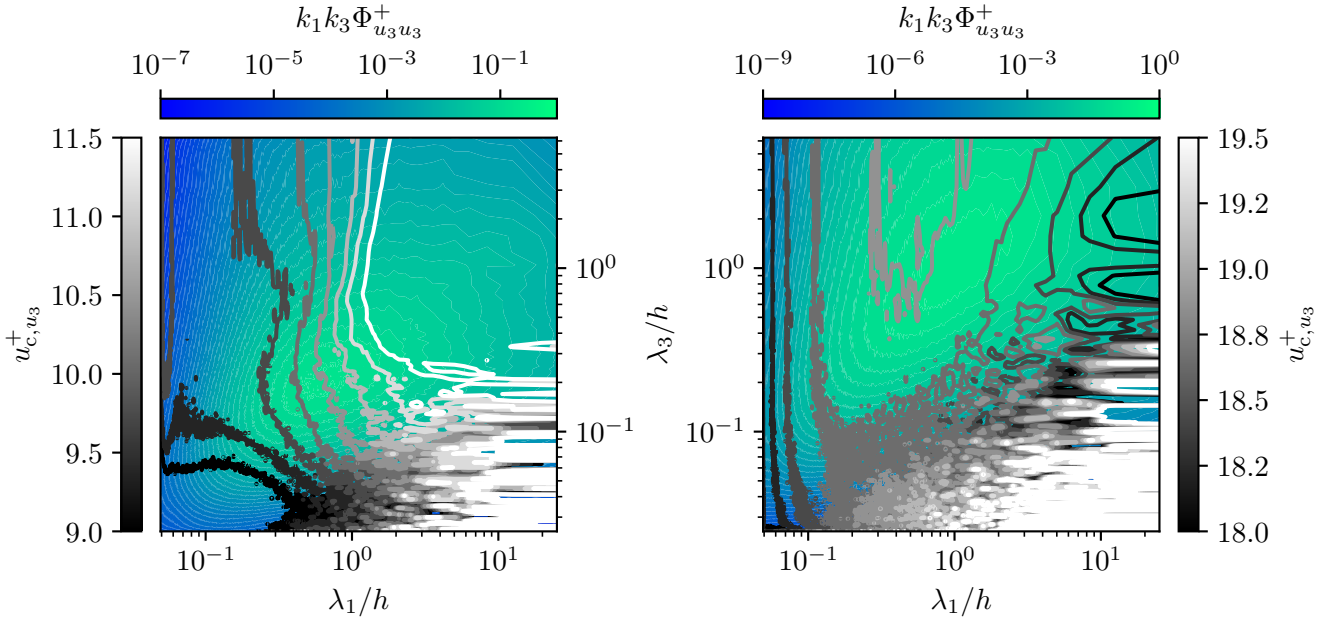

(a) Distribution at $x_2^+ \approx 5$ (b) Distribution at $x_2^+ \approx 265$

Figure 4.28.: Spectral distributions of u_{c,u_3} (case m500)

convection velocity, it is not surprising that the latter takes a similar velocity of $U^+_{c,u_3} \approx 19$. Regarding structures with $\lambda_3 < \lambda_1$, a great deal of statistical noise can be observed for Figure 4.28a and Figure 4.28b. In addition, some noise can also be observed for the isolines of the small-scale convection velocities. This behaviour might be due to the same reasons as in the case of the other two velocity components.
Finally, considering the spectral distributed convection velocities of passive scalars close to the channel wall, a clear dependence on the Prandtl number can be observed in figures 4.29a, 4.30a, and 4.31a. The highest convection velocities reside within the largest scales with regard to both wavelengths, as these scales are mostly influenced by the fast-moving bulk velocity. For the lowest value of $Pr = 0.025$, the area of highest convection velocity spreads over proportionally more streamwise wavelengths, while the respective area for $Pr = 1$ takes a wider range of spanwise than streamwise wavelengths into account. For the medium value of $Pr = 0.4$, the area of maximum convection velocity at $x_2^+ \approx 5$ is almost of quadratic shape (in the depicted representation). Leading to this behaviour might be the formation of additional structures with large spanwise expansion at higher Prandtl numbers. This could also be the reason for the shift of the energy peak with an increase in Pr at close wall distances towards smaller values of λ_3. However, what exactly these structures are is unclear. Nevertheless, the change in Prandtl number could also be interpreted as a change in wall layer when considering passive scalar structures. As it was introduced in subsection 2.2.3, the molecular sublayer grows with $Pr \cdot x_2^+$, which in this case results in Figure 4.31a depicting the scalar buffer layer rather than the molecular sublayer. Therefore, different spectral distributions at changing values of Pr could be attributed to similar mechanisms as due to varying wall distances. In addition, the isolines of $u_{c,\theta}$ are more sophisticated in the case of the lower Prandtl numbers, where a clear decrease in their value towards smaller scales is visible. With an increase in Pr, the convection velocity distributions become noisier. Moreover, with larger Prandtl numbers, a secondary area of high convection velocity emerges at the smallest streamwise wavelengths. This is especially the case for $Pr = 1$ and can be compared to the behaviour of u_{c,u_1} in Figure 4.26a. An explanation for this second high-speed area could again be the formation of fast coherent structures with small streamwise and large spanwise expansions. However, their origin cannot be explained in the scope of this thesis and should be investigated by further research. A special focus should thereby lie on the effects of the Prandtl number on this behaviour. Due to the difference in bulk and mean velocities near the channel wall, there is a large range of values over which the convection velocities of scalar structures span. This range decreases from 5.5 u_τ, over 2.5 u_τ, to 2 u_τ with an increase in Prandtl number. The reason for these larger ranges at lower values of Pr could lie in the property of such flows to form larger passive scalar structures than their counterparts at higher Prandtl numbers. Del Álamo and Jiménez 2009 explain that the bulk velocity influences the near wall convection velocity distributions by large-scale structures of the outer flow, which penetrate into the layers closer to $x_2 = 0$. This influence might therefore be stronger if larger structures exist in the outer flow, as it is the case for lower values of Pr. The tendency of low Prandtl number flows to contain larger passive scalar structures can also be seen in the premultiplied energy spectra. A clear shift of the energy peak towards larger scales can be observed with a decrease in Pr. However, it is also shown that the total energy contained within these scales decreases with a decrease in Prandtl number. Still, more respective energy combined with, in general, faster convected large-scale structures strongly influence the behaviour of the overall convection velocity (Equation 2.63) at low values of Pr. This effect is visible in Figure 4.21b, where close to the wall $U_{c,\theta}$ increases significantly with a decrease in Prandtl number. Regarding $x_2^+ \approx 265$ closer to the channel centre, the effects of a change in Prandtl number are less substantial. The respective data for $Pr = 0.025$, $Pr = 0.4$, and $Pr = 1$ are shown in figures 4.29b, 4.30b, and 4.31b. The structures which are convected with the highest velocity are located at the centre of the spectral plane,

independent of Pr. However, the depicted distributions show some resemblance to the L-shaped spectra also seen for wall-normal velocity structures in Figure 4.27, at least in the case of the convection velocity $u_{c,\theta}$. Since passive scalars are known to behave similarly to the streamwise velocity components and *not* to the wall-normal one, this behaviour is somewhat unexpected and not explainable at this point. For the depicted case and wall distance, there seems to be no difference between the different Prandtl numbers in the accelerating effects $\langle u_1 \rangle$ has on the small scales and the decelerating effect U_b has on the large scales. This is also evident when considering the range of values taken by the respective convection velocities. For all given Prandtl numbers, $u_{c,\theta}$ ranges over the same span of 1 u_τ at the depicted wall distance. This can also be observed in Figure 4.23, where the small and large scale partitioned overall convection velocities align in the case of $x_2^+ \approx 265$ for all Prandtl numbers alike. A different behaviour might be observed even closer to the centre-line of the channel or at larger Reynolds numbers. However, the premultiplied energy spectrum is more substantially affected by a change in Pr. Due to the previously mentioned nature of smaller Prandtl numbers to form larger scales, the energy peaks are located closer to the largest wavelengths for the smaller values of Pr. Since structures of these wavelengths are convected more slowly, independently of the Prandtl number, an equally slower overall convection velocity is obtained. This is again due to the definition of $U_{c,\theta}$ as a weighted (with the respective energies) integral over the wavenumber-space. Figure 4.21b shows this behaviour slightly. The statistical noise, in general seen in the isolines of slow convection velocities, could once more be attributed to the misinterpretation of random fluctuations as the convection of tiny turbulent structures and the nature of the chosen visualisation. In addition, the previously mentioned explanation for the noisy area at $\lambda_3 < \lambda_1$ should also be applicable for the convection of passive scalar structures. However, this area of high statistical noise increases in size together with an increase in Pr, possibly due to all structures being convected slower at higher Prandtl numbers. This is at least the case close to the wall, where a slower convection worsens the problem of the *noisy-scales* dying, before being recognised as coherently convected structures. However, close to the channel centre no increase in $u_{c,\theta}$ is seen for an increase in Pr. Therefore, another possible explanation could be that passive scalar structures at lower Prandtl numbers are generally long-living compared to their high-Pr counterparts.

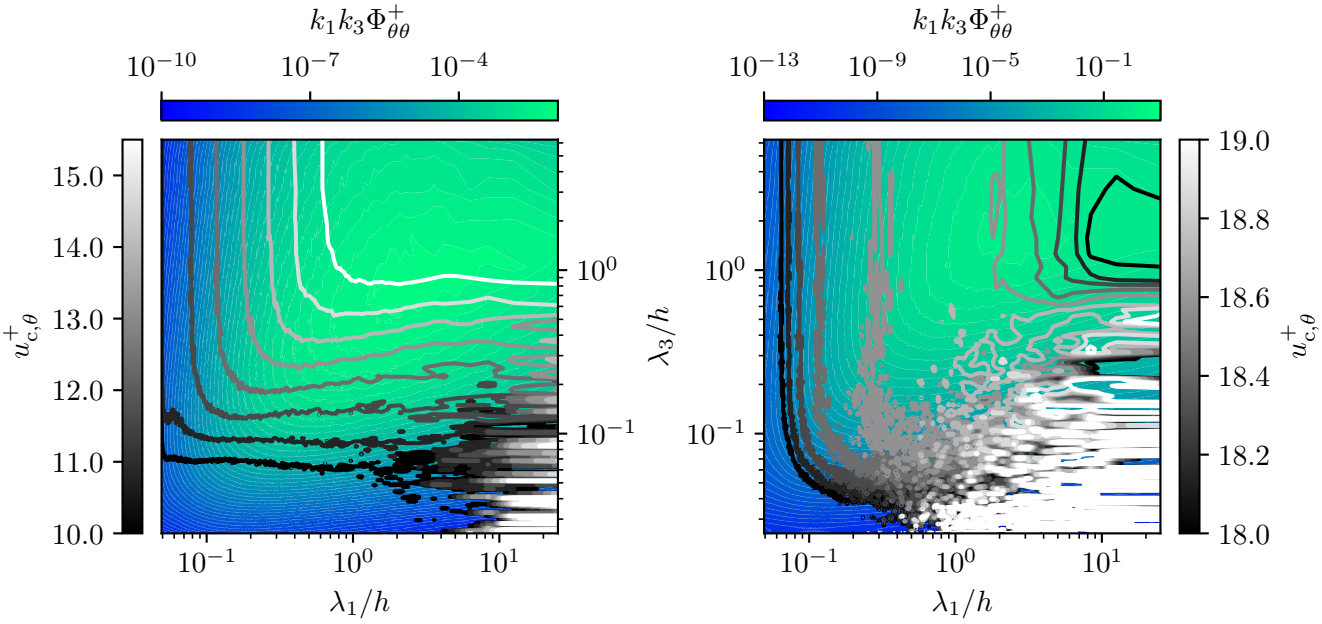

(a) Distribution at $x_2^+ \approx 5$

(b) Distribution at $x_2^+ \approx 265$

Figure 4.29.: Spectral distributions of $u_{c,\theta}$ with $Pr = 0.025$ (case m500)

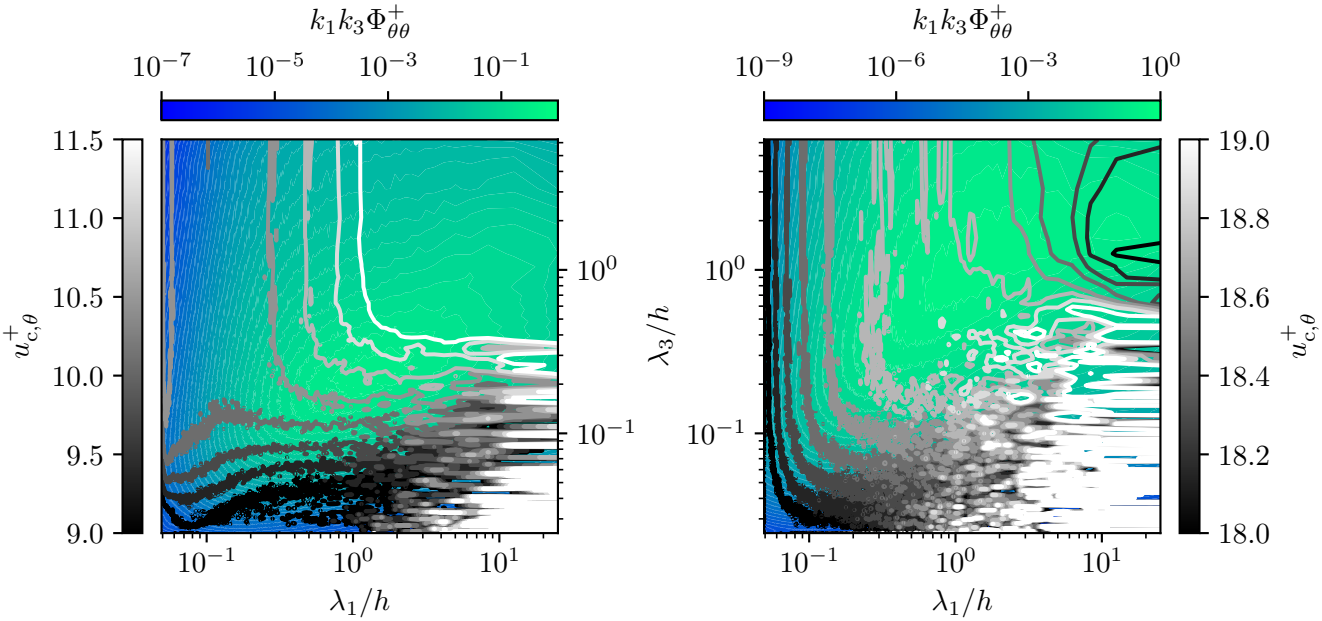

(a) Distribution at $x_2^+ \approx 5$ (b) Distribution at $x_2^+ \approx 265$

Figure 4.30.: Spectral distributions of $u_{c,\theta}$ with $Pr = 0.4$ (case m500)

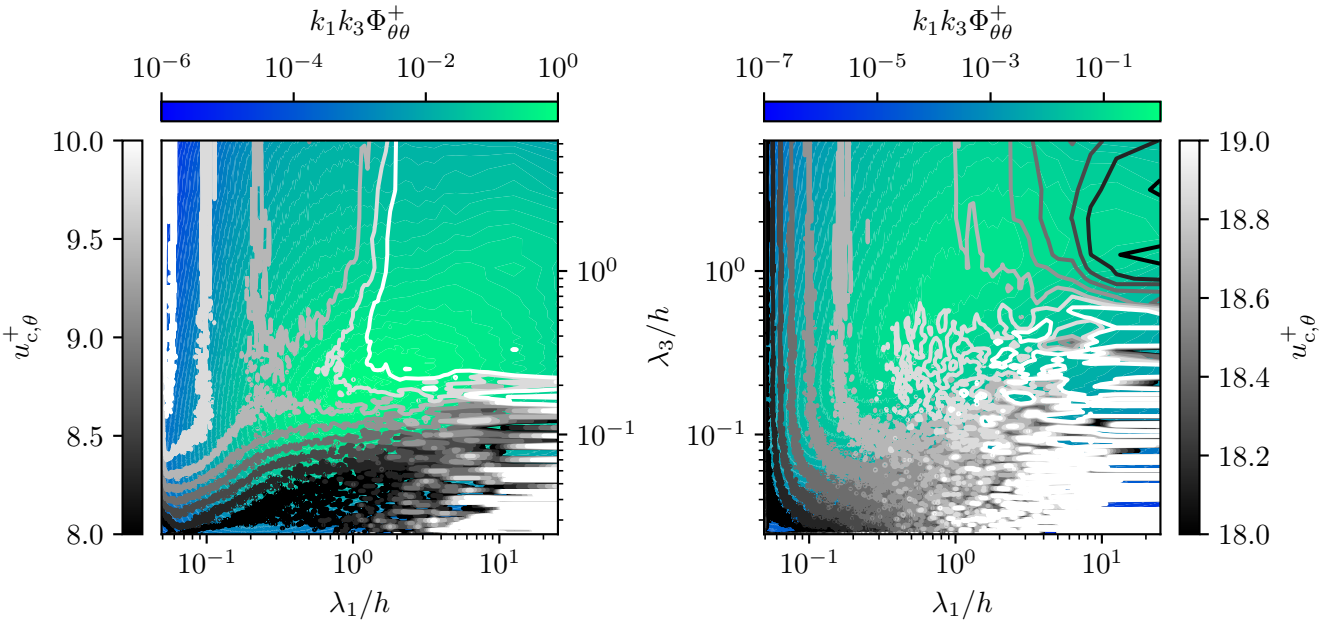

(a) Distribution at $x_2^+ \approx 5$ (b) Distribution at $x_2^+ \approx 265$

Figure 4.31.: Spectral distributions of $u_{c,\theta}$ with $Pr = 1$ (case m500)

4.3.3. Reynolds number dependency

In a final consideration of the behaviour of the convection velocities, their dependence on a change in Reynolds number is analysed. Therefore, previously discussed results (of simulation case m500) are shown again, this time in comparison with their respective counterparts of simulations m180 and m1000. Note that in general, all the averages calculated from the data of m180 and m1000 are taken with respect to both statistically homogeneous spatial directions and the symmetries of the convection velocity distributions. In case of m180, means are also taken with respect to 100 statistically fully developed time steps, while only 16 such fields are used in the case of m1000. Since viscous units are used in the following comparisons, it is important to note that some effects of a change in the Reynolds number might not be obvious. Such effects are already considered in this scaling, but will additionally be mentioned if necessary.
Figure 4.32 shows the (partitioned) overall convection velocities of passive scalar structures, on the basis of Figure 4.23. The cut-off, which characterises "small" and "large" scales is again $(\lambda_1, \lambda_3) = (h, h/4)$, for all simulated cases alike. Figure 4.32a depicts the overall convection velocities of each Prandtl and Reynolds number. In contrast to previously shown plots, the partitioned overall convection velocities of the corresponding small-scale and large-scale structures are shown in individual representations. They can be seen in figures 4.32b and 4.32c, respectively. Since the dependence of the quantities depicted on Re_τ is the focus at this point, no other velocities ($\langle u_1 \rangle$ or U_b) are shown for comparison. Similar results for the partitioned overall convection velocities of velocity structures can be found in subsection E.1. It is not necessary to show them here as well, because of their resemblance in behaviour to the presented data of passive scalar structures with respect to the Reynolds number. This similarity is especially strong when considering the convection of streamwise velocity structures in comparison to passive scalars at $Pr = 1$. Del Álamo and Jiménez 2009 considered the Re_τ-dependence of partitioned overall convection velocities of velocity structures as well. Their quantitative results are in good agreement with the data obtained within this work. Regarding the cases of different Reynolds numbers in Figure 4.32, it can be observed that not all simulations cover the same range of x_2^+ values. Note that this is a result of the scaling with viscous units.
When considering the overall convection velocities of all passive scalar scales in Figure 4.32a, an acceleration can be observed for the smallest Prandtl number with an increase in Re_τ, while the overall convection velocities of both other passive scalars decrease for larger Reynolds numbers. This effect is slightly stronger closer to the wall than at the channel centre. A reason for this behaviour might lie in the spectral distributions of both energy and convection velocity. As will later be shown in comparisons of these distributions, the spectral areas of high convection velocities as well as high premultiplied energies shift towards smaller structures with an increase in Reynolds number. However, these shifts are not equally "fast". This results in different effects on the overall convection velocities of passive scalars at different values of Pr, since they already form different-sized structures to begin with. What strengthens this conjecture, is the consideration of only small respectively large scales in the form of the partitioned overall convection velocities seen in figures 4.32b and 4.32c. For most of the channel width, there is a clear tendency of large-scale structures to be convected faster at higher Reynolds numbers, while a decrease in partitioned overall convection velocity is visible for small-scale structures at larger values of Re_τ. The only exceptions from this are passive scalars with $Pr = 0.025$, whose (partitioned) overall convection velocities are accelerated with increasing Reynolds number, regardless of the wavelength subspace considered. This might again be attributed to these flows' tendency to form respectively larger passive scalar structures, regardless of the intensity of turbulent motion. The observed behaviour for the small and large scales also results from the chosen wavelength cut-off, classifying these two wavelength spaces,

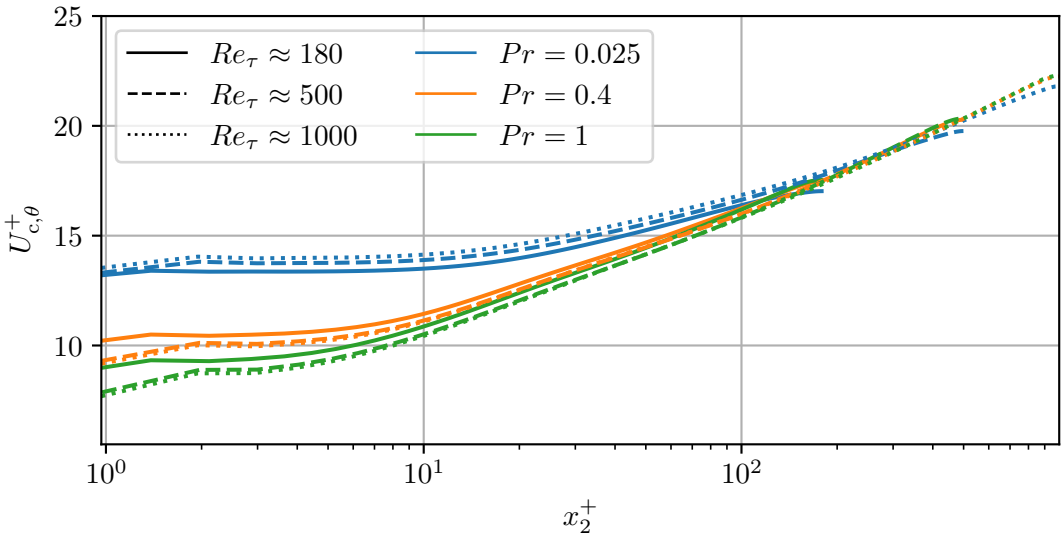

(a) Comparison of all-scale structures

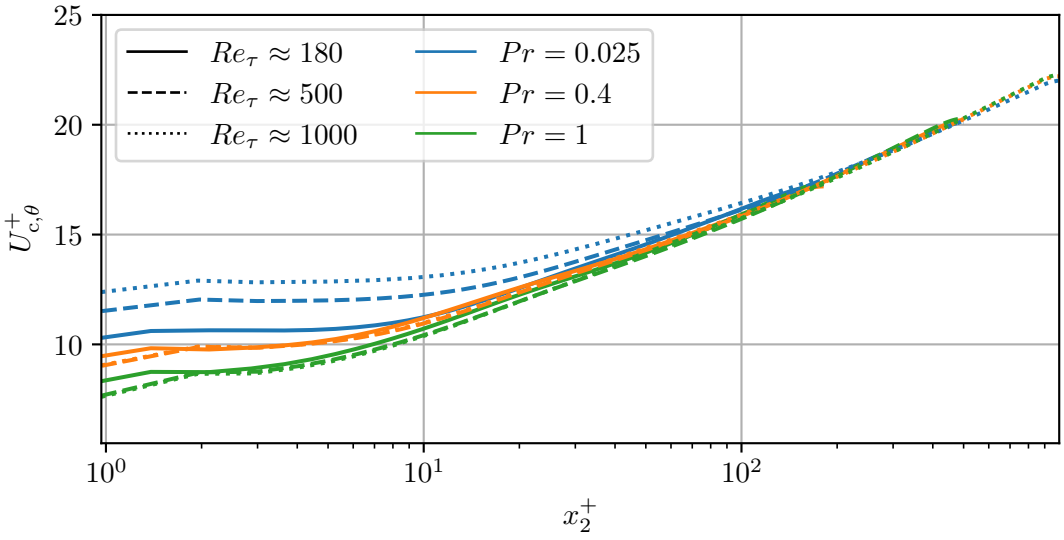

(b) Comparison of small-scale structures

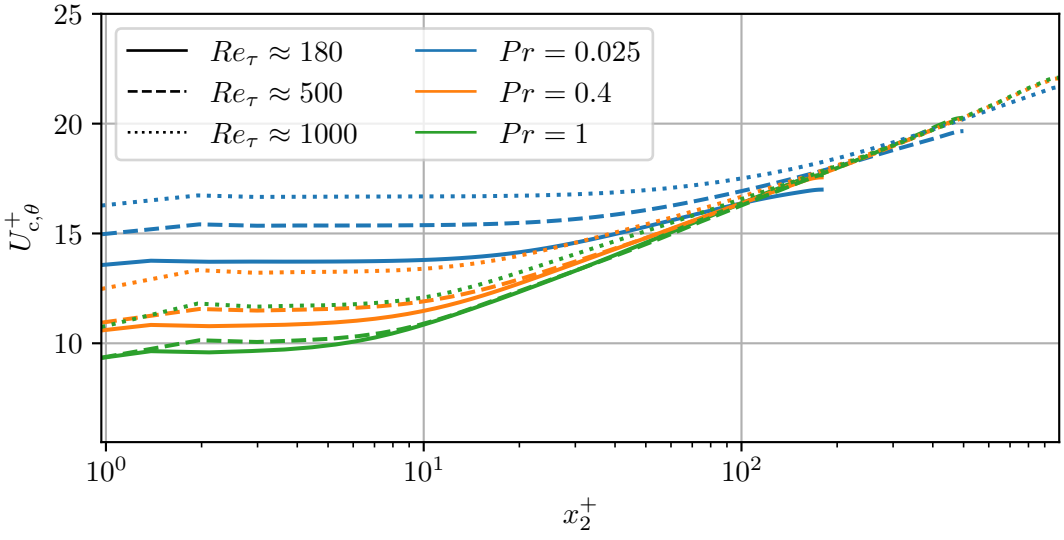

(c) Comparison of large-scale structures

Figure 4.32.: Comparison of overall convection velocities of scalar structures

staying unchanged. Regarding structures with $(\lambda_1, \lambda_3) \geq (h, h/4)$, the same spectral shifts of convection velocities and energies occur, as mentioned before. This results in larger partitioned overall convection velocities for an increase in Reynolds number. However, for structures with $(\lambda_1, \lambda_3) < (h, h/4)$, an additional effect becomes relevant. Higher-Re_τ flows form smaller structures and, in general, more of them. Because these structures are convected at relatively slow speeds due to their strong relation to the local streamwise mean velocity, they decelerate the partitioned overall convection velocities.
In Figure 4.33, contributions to the overall convection velocities of velocity structures are depicted, in accordance to Figure 4.24. Each subfigure 4.33a to 4.33c shows the data of an individual velocity component for all simulation cases m180, m500, and m1000, respectively. No overall convection velocities are shown for comparison, since the focus of these representations should lie on the Reynolds number dependencies of the contribution terms. In subsection E.2, the corresponding figures of contributions to the overall convection velocities of passive scalar structures are provided. Here, it is, however, sufficient to show only the figures of the velocity components, as their qualitative behaviour with respect to a change in Re_τ does not differ from the results shown in Figure E.80. Note that due to the used scaling in viscous units, there are again some values of x_2^+ only reached by the simulation results of higher Reynolds numbers.
For every contribution shown in figures 4.33a, 4.33b, and 4.33c, small differences in their respective influences can be observed with an increase in Re_τ. Note that these differences are partially small because all quantities are depicted in viscous units, which are already dependent on the Reynolds number. However, these minor changes in magnitude due to an increase in Reynolds number *do* influence the overall convection velocities. This is evident from the previously shown Figure 4.32 resp. the corresponding Figure E.79 for the convection of velocity structures. Especially the viscous term in Figure 4.33a as well as the pressure term in Figure 4.33b and Figure 4.33c decrease with an increase in Re_τ. This explains the drop in the overall convection velocities, since these terms are the dominant contributors for the respective velocity components in the close vicinity to the wall. Regarding the other contributing terms, already minor in general, the influence of a change in Reynolds number is vanishingly small. In the layers close to the channel wall, most of these terms become slightly larger in magnitude with an increase of Re_τ, while past the previously introduced trend change, the opposite effect can be observed. The only exception to this behaviour is the mean wall-normal gradient term in the overall convection velocity for streamwise velocity structures, seen in Figure 4.33a. All terms containing one-point correlations like the Reynolds stresses might be enhanced close to the wall because of the increase in turbulent kinetic energy resulting from an increase in Reynolds number. Regarding the opposing effect, seen in the mean wall-normal gradient term, this could result from a combination of Re_τ-effects influencing the respective term of Equation 3.22. Note that the wall distance at which the trend change in values, as well as in the influence of the Reynolds number, occurs, does not differ for all simulation cases considered. This leads to the assumption that the trend change is connected to other effects present in the viscous sublayer and buffer layer of the channel, since it remains located at the same wall distance in the case of viscous scaling.
In order to analyse the effects of a change in Reynolds number on the spectral convection velocity distributions, the figures 4.34 to 4.39 are considered. These representations show the spectral distributions of the convection velocities of each transport quantity considered, as well as their respective premultiplied energy spectra, like in subsection 4.3.2. Here, only the wall distance at the boundary between the viscous sublayer and the buffer layer ($x_2^+ \approx 5$) is depicted in each figure. Analyses of a position in the log layer are more difficult to compare since the flow behaviour is less universal further away from the wall in the case of different Reynolds numbers. In addition, most interesting phenomena previously shown are located close to the wall, further motivating the focus on these values of x_2^+. However,

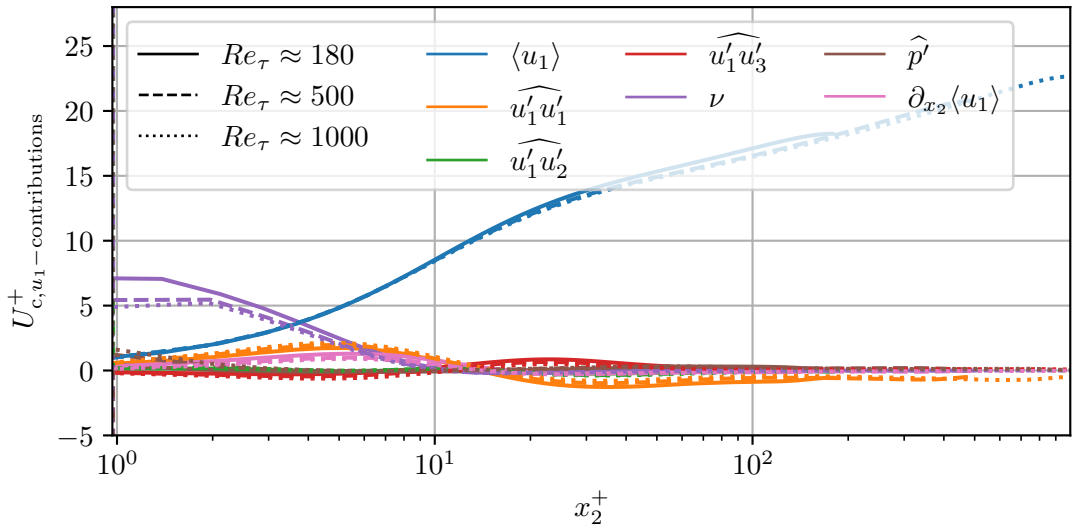

(a) Comparison of streamwise velocity structures

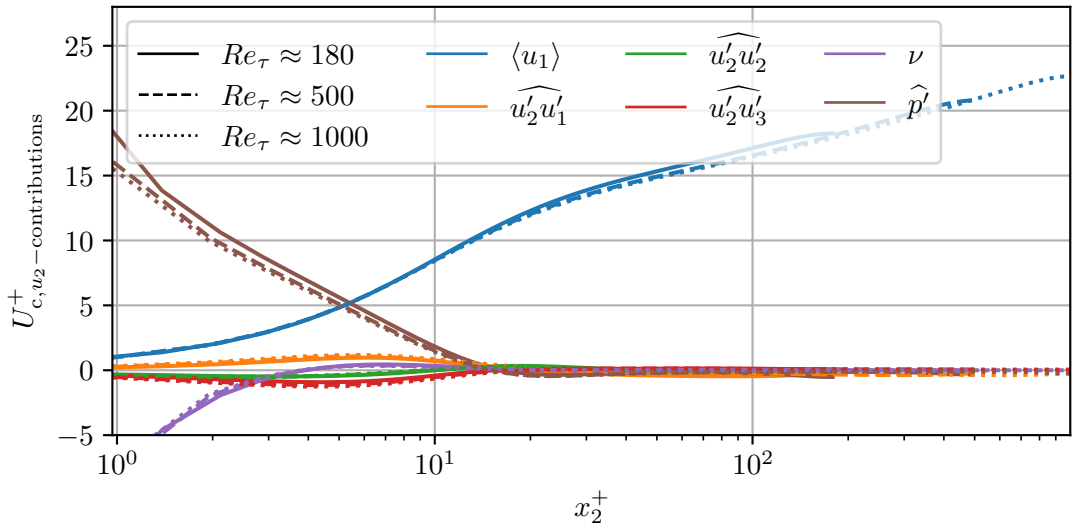

(b) Comparison of wall-normal velocity structures

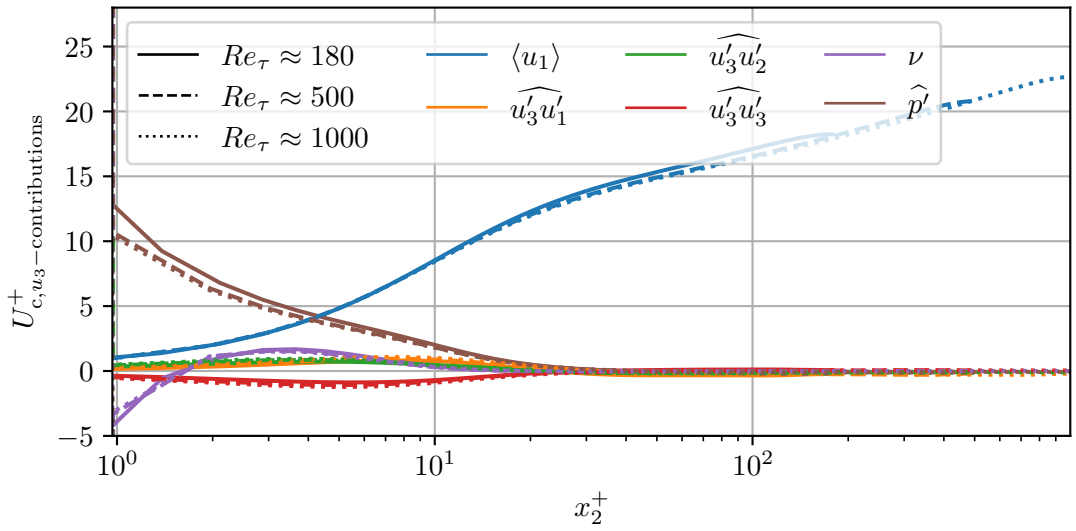

(c) Comparison of spanwise velocity structures

Figure 4.33.: Comparison of U_{c,u_i} contributions

corresponding figures for comparisons of the spectral convection velocity distributions at positions closer to the centre of the channel can be found in subsection E.3. The most notable effect they show is a general acceleration in all convection velocities with an increase in Re_τ. However, this is because each simulation's result are *not* plotted at the same viscous wall distance, but instead at $x_2^+ \approx (Re_\tau/2 + 15)$. In this case, higher Reynolds number flows having higher convection velocities can already be expected from Figure 4.32. In figures 4.34 to 4.39, data from the simulation cases m180 and m1000 are shown for comparison, in addition to the previously presented results of m500. Note that the wavenumber-spaces are enlarged for simulations at higher Re_τ, since these flows form smaller turbulent scales. However, each distribution shown is cropped to the spectral dimensions of m180 for better comparability. In case of any relevant small-scale behaviour being concealed by this representation, a respective comment will be made.
Figure 4.34 shows the spectral convection velocity distributions of streamwise velocity structures at $x_2^+ \approx 5$. With an increase in Reynolds number, slightly larger convection velocities arise within the largest structures. This is visible by the "fastest" isoline enclosing a larger area of turbulent scales for higher values of Re_τ. This could be due to larger-scale structures penetrating the near-wall layers, carrying their high energies and large convection velocities with them. The range of convection velocity values taken by any turbulent structure is enlarged in general. Not only are the largest structures convected faster for larger Reynolds numbers, but the smallest scales are additionally convected more slowly. This second effect is only partially depicted in the cropped representations of the convection velocity distributions. With respect to the second high-speed convection velocity area, which was found to emerge at small streamwise and large spanwise wavelengths, a shift towards even smaller streamwise structures can be observed with rising values of Re_τ. Therefore, the area seems to remain contained within structures of low respective energies. This could hint at the responsible structures being destroyed by large energy-containing eddies, which more prominently influence the near-wall layers for higher values of Re_τ. In general, more energy is contained within the spectral plane for higher Reynolds numbers, with the peak of the distribution shifting towards smaller wavelengths. This happens because the flow forms smaller and more energetic structures at larger values of Re_τ. Together with the change in convection velocities, this explains the Reynolds number dependency of the overall convection velocity of streamwise velocity structures, since Equation 2.63 takes both spectral distributions into account. It is interesting to note

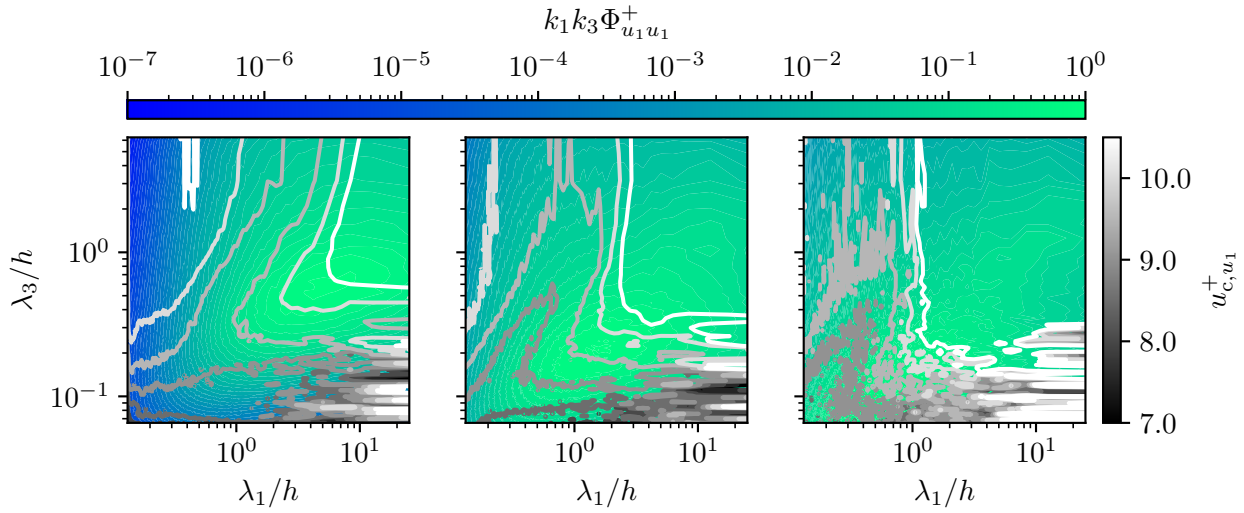

(a) $Re_\tau \approx 180$ (b) $Re_\tau \approx 500$ (c) $Re_\tau \approx 1000$

Figure 4.34.: Comparison of spectral distributions of u_{c,u_1} at $x_2^+ \approx 5$

that the convection velocity isolines become less skewed towards larger values of λ_1 at high values of λ_3,- when increasing the Reynolds number. This could be attributed to more structures of high convection velocity and large spanwise expansion penetrating the near-wall layer from positions closer to the channel centre. What supports this hypothesis is the increase in energy of such structures for higher values of Re_τ, which must result from outside influences, since at $x_2^+ \approx 5$ most behaviour is only a footprint of effects occurring at larger wall distances. Note that no significant change in the spectral area of high statistical noise can be observed. This could be attributed to the convection velocities of the respective structures not changing either for an increase in Reynolds number.
In Figure 4.35, the spectral convection velocity distributions of wall-normal velocity structures are shown at a wall distance of $x_2^+ \approx 5$. Like in the case of u_{c,u_1}, slightly larger convection velocities can be observed with an increase in Reynolds number. This is visible by the fastest-velocity isoline reaching deeper into the wavelength-space, thereby enclosing more (even faster convected) turbulent structures. This might again be explained by structures of higher convection velocity penetrating into the near-wall region from layers closer to the channel centre. Such phenomena intensify with an increase in Re_τ. The span of values taken by the convection velocities of wall-normal velocity structures increases in general. In addition to the higher maximum values of u_{c,u_2}, the distributions at larger Reynolds numbers show lower minima. This is visible in the emerging slow-speed area at the largest scales of the wavelength plane. This behaviour of extremely slow large-scale structures can be attributed to the increasing influence of the wall on higher-Re_τ flows at a wall distance of $x_2^+ \approx 5$. Another effect of the growth of this spectral area is that the largest convection velocities are shifted towards structures with smaller spanwise expansions. Likewise, the peak of the premultiplied energy distribution shifts towards smaller structures in general. This is due to the fact that flows at larger values of Re_τ form smaller scales, which contain more respective energy. Both shifts, in peak convection velocity and peak premultiplied energy, contribute to the behaviour of the overall convection velocities of wall-normal velocity structures. Regarding the spectral area of high statistical noise, no dependence on the Reynolds number can be observed. As for the case of streamwise velocity structures, this can be attributed to those scales being convected at similar velocities in all cases considered. The effect of eddies with $\lambda_3 < \lambda_1$ vanishing before they can be recognised as coherently convected is therefore equally present in every simulation.

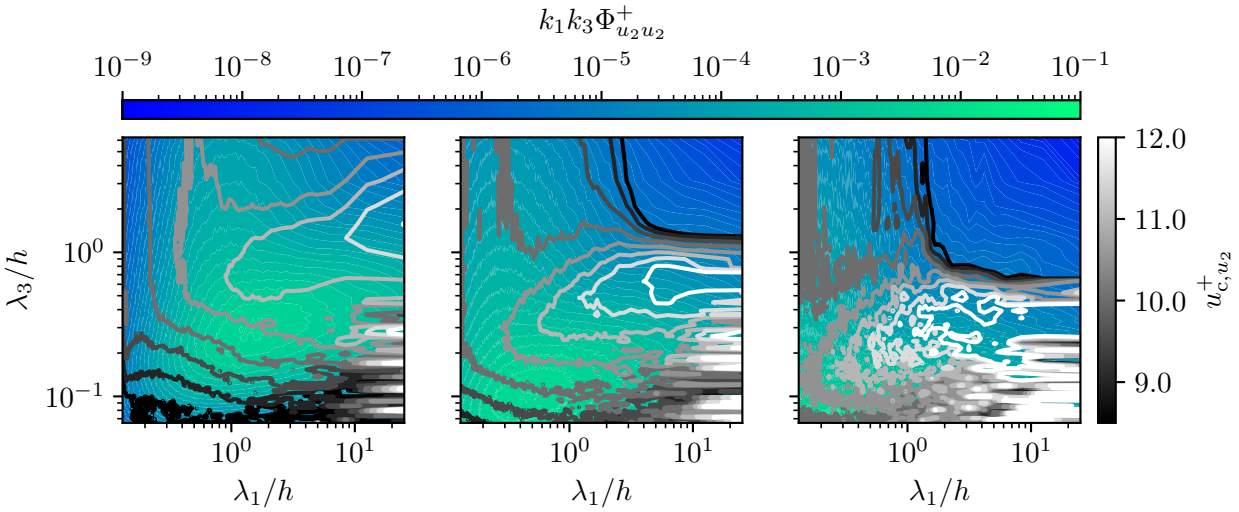

(a) $Re_\tau \approx 180$ (b) $Re_\tau \approx 500$ (c) $Re_\tau \approx 1000$

Figure 4.35.: Comparison of spectral distributions of u_{c,u_2} at $x_2^+ \approx 5$

The spectral convection velocity distributions of spanwise velocity structures at $x_2^+ \approx 5$ are depicted in Figure 4.36. Together with an increase in Reynolds number, an increase in the peak convection velocities can be observed. The fastest convected structures remain located at the largest streamwise and spanwise wavelengths. However, their convection velocities are larger for the higher-Re_τ cases, which is visible by the "fastest" isolines being located closer to the medium-sized structures. As in the cases of the other velocity components, this is due to the influence of large scales present in the flow close to the channel centre. The influence of these scales, regarding high energies and large convection velocities, increasingly reaches into the near-wall layers with larger Reynolds numbers. In addition to this, the smallest structures, which decrease in size for an increase in Re_τ, are convected at slower speeds. As a result, the overall range of convection velocities broadens with increasing values of the Reynolds number. Note that the smallest scales are only visible in the depiction of m180 (Figure 4.36a). In addition to the general formation of smaller structures, higher-Re_τ flows also carry more energy at shorter wavelengths. This leads to a shift in the depicted premultiplied energy spectrum towards minor structures. Considering the spectral area at $\lambda_3 < \lambda_1$, a lot of statistical noise can be observed independent of the simulation case. This again shows the previously made observations that short-lived structures stay undetected by the convection velocity framework, independent of their Reynolds number.

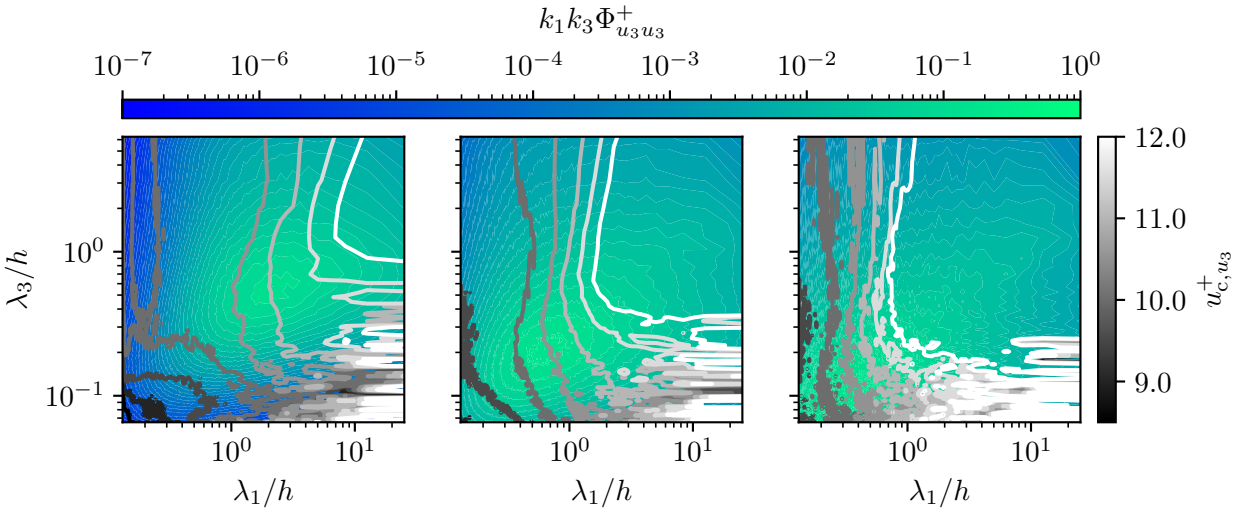

(a) $Re_\tau \approx 180$ (b) $Re_\tau \approx 500$ (c) $Re_\tau \approx 1000$

Figure 4.36.: Comparison of spectral distributions of u_{c,u_3} at $x_2^+ \approx 5$

Figure 4.37, Figure 4.38, and Figure 4.39 show the spectral convection velocity distributions of passive scalar structures at a wall distance of $x_2^+ \approx 5$ for the low, medium and high Prandtl numbers, respectively. For all Prandtl numbers, an increase in the maximum convection velocity can be observed, resulting from an increase in the Reynolds number. This is evident by the fact that the "fastest" isolines of each representation enclose a larger spectral area at higher values of Re_τ. In case of $Pr = 0.025$, the figures of the larger Reynolds numbers even contain convection velocity isolines so fast, that they are *not* present in the other cases. Like in the case of any velocity structure, this change in maximum convection velocity can be attributed to the rising influence of structures, which exist closer to the channel centre. The footprints of these structures extend further into the near-wall layers, with increasing values of Re_τ. Their energies and high convection velocities are therefore visible in the largest scales, even close to the wall. In addition, higher Reynolds number flows form smaller passive scalar scales for all Prandtl numbers.

These smallest structures are even more influenced by the local mean velocity, leading to slower minimal convection velocities at higher values of Re_τ. Note that this is *not* visible in the figures shown, since only the spectral distributions of the simulation case m180 are fully depicted. However, this behaviour leads to larger convection velocity ranges at $x_2^+ \approx 5$ for an increase in Reynolds number. An interesting observation made previously is the growth of a second spectral area of high convection velocities with an increase in the Prandtl number. This area is located in the wavelength-space at small streamwise and large spanwise expansions. Regarding the effect of an increase in Reynolds number on this area, a shift towards smaller streamwise structures can be seen, similar to the corresponding area of convection velocities in the case of streamwise velocity structures (Figure 4.34). For the passive scalar with $Pr = 0.025$, only the simulation case m180 marginally shows this behaviour. Therefore, the additional high convection velocities stay contained within the wavelengths of lowest energy. An explanation for this dependency on Re_τ can again be suspected in the influence of outer-flow structures. These outer structures, increasingly penetrating into the near-wall layers with larger Reynolds numbers, seem to interfere with the formation of those additional scales convected at high velocities in close vicinity to the wall. Another effect of the shift in this second high-speed area with an increase in Reynolds number is a change in the spectral position of the main area of highest convection velocities. This occurs in addition to the previously mentioned increase in size of the area. For the chosen isolines, this behaviour is most prominently visible in the case of $Pr = 0.025$, where the fastest convected scales are located at medium streamwise wavelengths in the case of the lowest Reynolds number. For larger values of Re_τ, the spectral position shifts towards larger wavelengths in general. The spectral position of the premultiplied energy peak shifts towards smaller structures with an increase in Reynolds number, independent of the Prandtl number. However, the influence of this shift on quantities like the overall convection velocities is more substantial for larger Pr values, as is shown by the different behaviours seen in Figure 4.32a. Note that when comparing this behaviour for the different passive scalars, it should be considered that figures 4.37 to 4.39 are scaled logarithmically. As mentioned before, the changes in the premultiplied energy spectra arise because flows of larger Reynolds numbers form smaller and more energetic structures (with respect to the scaling in viscous units). Regarding the high statistical noise at structures with $\lambda_3 < \lambda_1$, no significant change can be observed with an increase in Reynolds number for each passive scalar individually. Even if a decrease in this noise could be suspected for the lowest Prandtl number, this can be attributed to the chosen convection velocity isolines not capturing the behaviour of the relevant structures.

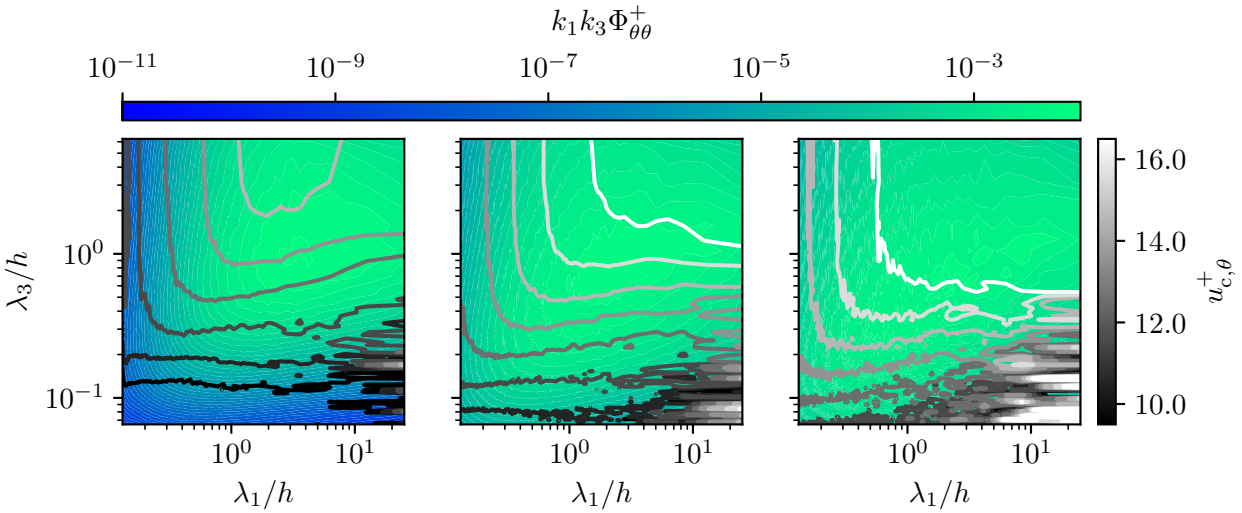

(a) $Re_\tau \approx 180$ (b) $Re_\tau \approx 500$ (c) $Re_\tau \approx 1000$

Figure 4.37.: Comparison of spectral distributions of $u_{c,\theta}$ with $Pr = 0.025$ at $x_2^+ \approx 5$

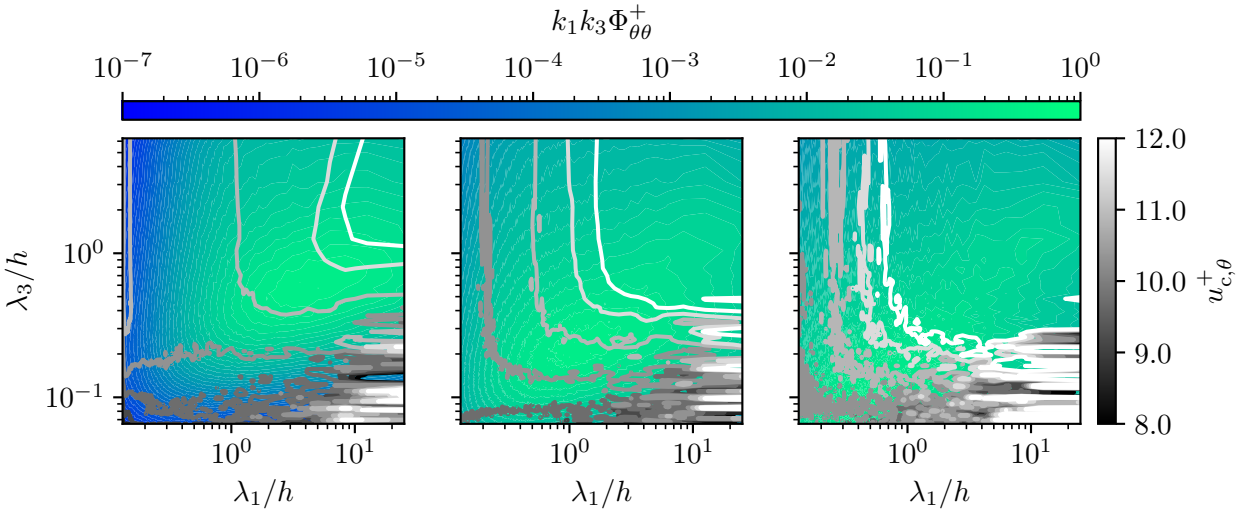

(a) $Re_\tau \approx 180$ (b) $Re_\tau \approx 500$ (c) $Re_\tau \approx 1000$

Figure 4.38.: Comparison of spectral distributions of $u_{c,\theta}$ with $Pr = 0.4$ at $x_2^+ \approx 5$

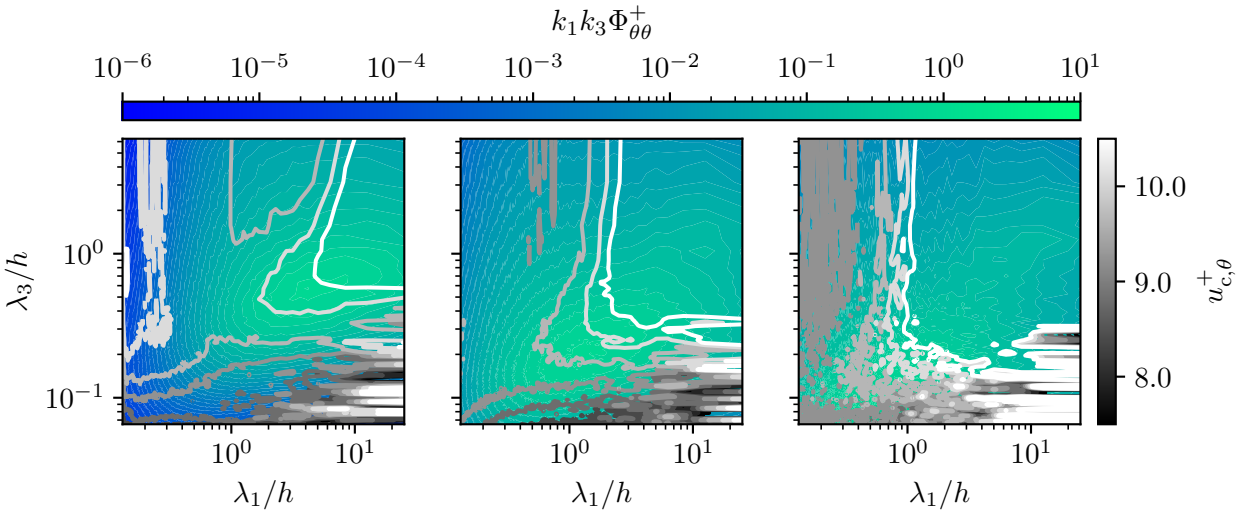

(a) $Re_\tau \approx 180$ (b) $Re_\tau \approx 500$ (c) $Re_\tau \approx 1000$

Figure 4.39.: Comparison of spectral distributions of $u_{c,\theta}$ with $Pr = 1$ at $x_2^+ \approx 5$

5. Conclusion and outlook

This thesis aimed to gain a deeper insight into the physics of convection velocities of different turbulent structures in wall-bounded flows. A special focus was directed at the behaviour of passive scalars. The results of Del Álamo and Jiménez 2009 were chosen as a starting point for the presented research and their convection velocity definition was adopted. Direct numerical simulations of plane channel flow were conducted, starting with a preliminary simulation at a friction Reynolds number of $Re_\tau \approx 180$. In addition to the velocity and pressure fields, passive scalars at $Pr \in \{0.025,\ 0.71,\ 1\}$ were analysed. To validate the simulation setup, typical turbulence statistics were considered and compared to data from the literature, which showed good agreement. The mean fields of all transport quantities agreed well with the expected results. The same outcome was achieved with the analyses of one-point auto-correlations. In general, all the averages considered were calculated with respect to both statistically homogeneous spatial directions and 100 statistically fully developed time steps. To evaluate whether a time step was statistically fully developed, shear stress and passive scalar flux profiles (only averaged in space) were considered. They showed a linear dependence on the wall-normal coordinate at a particular time, proving that the current time step was statistically fully developed. Profiles of the streamwise and spanwise auto-covariances were evaluated to check whether the channel's chosen periodic dimensions were large enough to capture all scales of turbulence. Thus, the streamwise expansion L_1 was found to be insufficient in size. As a consequence, a longer channel was used in the following simulations. Higher-order statistics were considered to validate the applied averaging setups. They showed the expected behaviour, ensuring that enough time steps were used in each mean to capture such statistical effects. One-dimensional energy spectra were considered to ensure that the spectral resolution is fine enough to resolve the dissipation range of the turbulent energy cascade. They showed no pile-up of energy at higher values of k, thus validating the chosen wavenumber-range. In general, the passive scalars at the medium and large Prandtl numbers behaved similarly in most of the considered statistics. As a result, the medium Pr value was adjusted ($0.71 \rightarrow 0.4$) to obtain more meaningful results from the following studies. An additional first look at the convection velocities was made to find possible symmetries in their distributions. They were observed to be symmetrical with respect to the channel centre-plane as well as with respect to all four quadrants of the wavenumber-space. These symmetries were later used to refine all means based on values of the convection velocities. After the preliminary investigation, three main simulations were performed at $Re_\tau \in \{180,\ 500,\ 1000\}$. All validation steps mentioned so far have been retraced for these simulations to ensure reliable data generation. The resulting fields were then used to analyse the convection velocity behaviour of both velocity and passive scalar structures. Further research could benefit from additional simulations at higher values of Re and Pr to make more sophisticated statements about the dependency of the convection velocities on these dimensionless numbers.

The first analysis of the generated data focused on each respective quantity's transport equations. The physical reason why Taylor's hypothesis might break could be investigated by formulating the transport equations into representations that contain the terms of the hypothesis. Since the quantities considered were fluctuating values, their rms values were considered to gain statistically relevant results. Each term of the transport equations was analysed separately. However, since the respective terms contributing to the breaking

of Taylor's hypothesis can have interfering effects, the best measure to investigate them showed to be an analysis of their instantaneous sums. In addition, it proved to be good practice to normalise each considered term by one of the terms that represents Taylor's hypothesis. In doing so, the relative influence of the "hypothesis breaking"-terms could be investigated, even at wall distances where all quantities were small in magnitude. For the transport of velocity as well as passive scalar structures, an increase in the effects leading to the breaking of Taylor's hypothesis was observed with a decrease in wall distance. This was in good agreement with the data from the literature that considered velocity and vorticity structures in turbulent plane channel flow. With regard to the physical reasons behind these effects, all velocity components showed to behave similarly. The influence of the non-linear terms on the breaking of Taylor's hypothesis was found to be dominant in the log layer, while the pressure and viscous terms were strongest in a closer vicinity of the wall. Near the channel centre, the same behaviour was observed for the transport of passive scalar structures. However, at the channel wall, the term representative of the difference between the overall convection velocity and the streamwise mean velocity was shown to dominate, along with the conductive term. For the lowest Prandtl number, a strong influence of the non-linear terms was observed in the close vicinity of the wall as well. This effect was found to decrease with increasing values of Pr. Based on this, future projects could conduct respective analyses for the individual contributions to the convection velocities, leading to a deeper physical understanding of the underlying mechanisms. Regarding the behaviour of the "hypothesis breaking"-terms with respect to an increase in Reynolds and Prandtl numbers, an increase in their magnitude at the channel wall was observed. This was attributed to the steeper wall-normal gradients corresponding to the larger dimensionless numbers. In addition, an area in which these terms take their maximum value was found to be constant inside the molecular sublayer. Future research might profit from considering a wider range of Re and Pr, since being limited to only three values of each dimensionless number resulted in difficulties extrapolating the findings made throughout this thesis. In addition, further investigations of the dependency on the Reynolds and Prandtl numbers might lead to a scaling parameter that collapses the curves of the "hypothesis breaking"-terms.

The first analysis directly related to the convection velocities was performed by investigating their dependence on the wall distance. Therefore, the *overall* convection velocities of each considered quantity were calculated. These velocities are defined as integrals of the wavenumber-dependent convection velocities with respect to the spectral plane. The respective values of every turbulent scale are additionally weighted by the energy they carry. The overall convection velocities are thereby best-approximations of Taylor's hypothesis and closely related to other definitions typically found in the literature. The qualitative behaviour of the overall convection velocities with respect to wall distance was found to be similar for all velocity structures, as well as passive scalar structures. Close to the channel centre, $U_{\mathrm{c},\phi}$ showed a slope similar to the mean streamwise velocity, however, with slightly lesser magnitude. With a decrease in wall distance, the overall convection velocities could be observed to flatten in the buffer layer, before finally becoming constant in the viscous sublayer. In closest proximity to the wall, an additional decrease in their values was depicted. However, this was in disagreement with data from the literature and might therefore be an artefact of limited numerical accuracy. All main simulation results showed the same quantitative behaviour. Some Prandtl number effects were observed regarding a change in Pr in the case of passive scalar structures. With an increase in Pr, faster overall convection velocities were seen at the channel centre, while slower speeds were found closer to the wall. This effect was attributed to the physical tendency of larger Prandtl numbers to form smaller passive scalar structures. This could be connected to the overall convection velocities in the sense that large structures exist in regions as large as the channel cross-section, thereby being convected at speeds close to the bulk velocity.

However, smaller scales occupy only a local region of the channel and are thus mostly influenced by the mean streamwise velocity. To further analyse this behaviour, additional simulations with a broader range of Prandtl numbers would again benefit future studies, since this was a limiting factor in the presented research.
To investigate the behaviour of different-sized structures in general, partitioned overall convection velocities were evaluated. Therefore, a wavelength cut-off of $(\lambda_1, \lambda_3) = (h, h/4)$ was chosen. Every structure above this value-pair was considered "large", while every structure below was considered "small". The previously regarded investigations concerning wall distance were then retraced for these small and large scales individually. As expected, the partitioned overall convection velocities of large structures proved to be strongly influenced by the bulk velocity, while in the case of small structures, the local streamwise mean velocity had a dominant influence on the partitioned overall convection velocity. This effect was visible for all velocity and passive scalar structures, with an increasing impact for passive scalars of low Prandtl number. This dependency on Pr was argued to arise from the larger structures in low Prandtl number flows. The overall convection velocities of all scales were shown to be convected at velocities close to those of the partitioned overall convection velocities of the small scales. This was argued to be either an effect of the chosen wavelength cut-off or the spectral distribution of energy and convection velocity. The latter was therefore analysed in the following parts of this thesis. Regarding the former, future research might consider different cut-offs to ensure that such limiting factors are not included in the analysis of partitioned overall convection velocities.
In a final consideration of the convection velocities' wall distance dependence, the individual terms of their definitions were investigated. For every transported quantity, each contributing term was calculated in accordance with the way in which its overall convection velocity was calculated. The results of this showed that the streamwise mean velocity is the dominant contributor to all overall convection velocities considered in the log layer. Another effect, observed to hold for velocity and passive scalar structures alike, is the influence of the boundary conditions close to the wall, damping all terms directly including one of the transport quantities. In the viscous sublayer, different terms were found to be dominant for different velocity components. Although u_1-structures are mostly convected due to a positive influence of the viscous term, this term decreases the convection velocities of both u_2-structures and u_3-structures. In contrast, the pressure term showed to be significantly larger for the wall-normal and streamwise velocity components, overpowering the negative effect of the viscous term. However, this behaviour could not be explained during the presented work and might arise from numerical problems of the finite difference scheme used. Due to limitations in the wall-normal resolution, a proper investigation of these terms' limit behaviour as they approach the wall could not be performed. For passive scalar structures, the conductive term dominated the overall convection velocity near the wall. With an increase in the Prandtl number, a decrease in this dominance was observed. This was attributed to the decrease in conductivity at higher values of Pr. The influence of all other terms was shown to be small in comparison. However, an increase in these terms towards the channel wall was detected for all transported quantities alike. In the case of the passive scalars, the magnitude of these other terms was observed to increase with an increase in the Prandtl number. This was explained by the rising influence of turbulent scalar fluxes for larger values of Pr. Future research could investigate the fundamental physics behind the overall convection velocity contributions by considering the effects of simple elemental structures in an otherwise homogeneous flow.
To extend the convection velocity analyses, their spectral distributions were considered. Therefore, plots of premultiplied energy spectra were analysed together with the wavenumber-dependent convection velocities. This was done at two distances from the wall, to gain deeper insights into the behaviour near the wall and the channel centre. However, limiting the investigation to only two values of x_2 resulted in equally limited

interpretation possibilities and should be extended in further projects. The reason for considering both the convection velocities and the energy spectra was that both quantities contribute to the overall convection velocities analysed before. In general, it was found that large scales are convected fastest close to the wall, while this peak in convection velocity shifts towards more minor scales with an increase in wall distance. Nevertheless, slightly different behaviours could be seen for every component of the velocity tensor as well as for the convection of passive scalars. The convection velocity distribution of u_1-structures showed a second region of high-speed convection at small streamwise wavelengths. This could also be observed in the case of passive scalar structures, where the effect intensified with an increase in the Prandtl number. However, the insights into the relevant flow physics gathered within this work were insufficient to explain the origin of this behaviour. With respect to the distribution of the convection velocities related to wall-normal velocity structures, a special shape was observed in the wavenumber-space. Especially close to the wall, the largest scales showed to be relatively slow, while scales of medium streamwise and large spanwise dimensions were convected at high velocities. This unexpected effect was later also seen in the near-centre distribution of $u_{\mathrm{c},\theta}$. With regard to the u_2-structures, this was attributed to the effects of the wall, while no explanation was found regarding the convection of passive scalar structures. In the case of the spanwise velocity structures, peak convection velocities far from the channel wall were found to reside within larger spanwise structures than expected. This could have been the contribution of special u_3-structures forming close to the channel centre. An analogues change in which kind of scales are fastest was also observed close to the channel wall in the case of passive scalar structures. With an increase in Pr, the percentage of spanwise wavelengths contained within the same area of convection velocity magnitude also increased. An explanation for this could not be found. However, arguments were made that a change in the Prandtl number is equivalent to a change in wall layer when regarding the scaling of passive scalars in wall-bounded flows. All convection velocity distributions showed a considerable amount of statistical noise. Some of it was attributed to the chosen type of representation and the misinterpretation of random fluctuations as the convection of tiny structures. However, another significant area of noise was explained to occur due to scales with $\lambda_3 < \lambda_1$ not living long enough to be reliably noticed as coherently convected structures. This effect worsened with an increase in Pr for the convection of passive scalar structures. Reasons for this were suspected in either slower convection velocities or shorter lifespans of these scalar structures at higher Prandtl numbers. More sufficient statistical results could not be gained due to limitations in the used averaging setups as well as smoothing-algorithms. In future research, more elaborate investigations could be conducted considering normalised convection velocity distributions. Special overall convection velocities, obtained by integrating semicircles of constant absolute magnitude in the (k_1-k_3)-plane, could be used as normalisation factors. To combine some of the individual analyses made throughout this thesis, further work might also consider spectral distributions of the individual contributions, which influence the convection velocities.

To conclusively investigate the dependency of previously found results on the Reynolds number, data from all simulation cases were compared for some selected analyses. In the case of partitioned overall convection velocities, large structures were found to be accelerated, while small structures decelerated with an increase in Re_τ. This was argued to be an effect of the in general faster convection velocities in combination with shifting premultiplied energy peaks, for larger Reynolds numbers. Regarding the overall convection velocity contributions, no significant Reynolds number effects which were not already captured by the viscous scaling used were observed. Comparisons between the spectral distributions of convection velocities and energy spectra were made for ranging values of Re_τ. Some Reynolds number effects could be seen at positions close to the channel wall. Most of these were assumed to arise from outer-flow structures increasingly penetrating

layers closer to the wall. Future investigations could evaluate this behaviour by considering simple turbulent structures in an otherwise homogeneous flow.
Furthermore, future research could apply all averages concerning even more statistically fully developed time steps, leading to higher statistical convergence. Additionally, special statistical schemes could be used to distinguish between errors resulting from the averaging setups and those originating from incorrectly implemented code. Simulations with temperature-dependent material properties could be conducted to compare numerical results with possible experimental data of turbulent heat transfer. In view of this, considering different thermal boundary conditions than the one used in this thesis might yield additional information.

List of Figures

List of Tables

Bibliography

Abe, H., H. Kawamura, and Y. Matsuo (May 2004). Surface heat-flux fluctuations in a turbulent channel flow up to Re=1020 with Pr=0.025 and 0.71. In: *International Journal of Heat and Fluid Flow* 25, pp. 404–419. DOI: 10.1016/j.ijheatfluidflow.2004.02.010.

Alcántara-Ávila, F. and S. Hoyas (Sept. 2021). Direct numerical simulation of thermal channel flow for medium–high Prandtl numbers up to Re=2000. In: *International Journal of Heat and Mass Transfer* 176, p. 121412. DOI: 10.1016/j.ijheatmasstransfer.2021.121412.

Aliabadi, A. A. (Oct. 2022). *Turbulence*. Cham, Switzerland: Springer. DOI: 10.1007/978-3-030-95411-6.

Atkinson, C., N. Buchmann, and J. Soria (Dec. 2015). An Experimental Investigation of Turbulent Convection Velocities in a Turbulent Boundary Layer. In: *Flow, Turbulence and Combustion* 94, pp. 79–95. DOI: 10.1007/s10494-014-9582-0.

Choi, H. and P. Moin (Sept. 1990). On the Space-Time Characteristics of Wall-Pressure Fluctuations. In: *Physics of Fluids A* 2, pp. 1450–1460. DOI: 10.1063/1.857593.

Del Álamo, J. C. and J. Jiménez (Dec. 2009). Estimation of turbulent convection velocities and corrections to Taylor's approximation. In: *Journal of Fluid Mechanics* 640, pp. 5–26. DOI: 10.1017/S0022112009991029.

Durbin, P. A. and B. A. P. Reif (Aug. 2010). *Statistical Theory and Modeling for Turbulent Flows*. Hoboken, United States of America: John Wiley & Sons, Ltd. DOI: 10.1002/9780470972076.

Ferziger, J. H., M. Perić, and R. L. Street (Aug. 2019). *Computational Methods for Fluid Dynamics*. Cham, Switzerland: Springer. DOI: 10.1007/978-3-319-99693-6.

Geng, C. et al. (Feb. 2015). Taylor's hypothesis in turbulent channel flow considered using a transport equation analysis. In: *Physics of Fluids* 27, p. 025111. DOI: 10.1063/1.4908070.

Goldschmidt, V., M. Young, and E. Ott (Apr. 1981). Turbulent convective velocities (broadband and wavenumber dependent) in a plane jet. In: *Journal of Fluid Mechanics* 105, pp. 327–345. DOI: 10.1017/S0022112081003236.

Hetsroni, G. et al. (Oct. 2004). Convection Velocity of Temperature Fluctuations in a Turbulent Flume. In: *Journal of Heat Transfer* 126, pp. 843–848. DOI: 10.1115/1.1797032.

Hilland, R. and A. Christen (Apr. 2024). A Systematic Investigation of the Applicability of Taylor's Hypothesis in an Idealized Surface Layer. In: *Boundary-Layer Meteorology* 190. DOI: 10.1007/s10546-024-00861-1.

Hirsch, C. (June 2007). *Numerical computation of internal and external flows*. Amsterdam, Netherlands: Elsevier. DOI: 10.1016/B978-0-7506-6594-0.X5037-1.

Horiuti, K. (Apr. 1992). Assessment of two-equation models of turbulent passive-scalar diffusion in channel flow. In: *Journal of Fluid Mechanics* 238, pp. 405–433. DOI: 10.1017/S0022112092001769.

Hussain, F. and R. Clark (Dec. 1980). Measurements of wavenumber-celerity spectrum in plane and axisymmetric jets. In: *AIAA Journal* 19, pp. 51–55. DOI: 10.2514/3.7747.

Jeon, S. et al. (Oct. 1999). Space-time characteristics of the wall shear-stress fluctuations in a low-Reynolds-number channel flow. In: *Physics of Fluids* 11, pp. 3084–3094. DOI: 10.1063/1.870166.

Jiménez, J. and M. Simens (May 2001). The Largest Scales in Turbulent Flow: The Structures of the Wall Layer. In: Berlin, Germany: Springer, pp. 39–57. DOI: 10.1007/3-540-44698-2_3.

Kader, B. (Sept. 1981). Temperature and concentration profiles in fully turbulent boundary layers. In: *International Journal of Heat and Mass Transfer* 24, pp. 1541–1544. DOI: 10.1016/0017-9310(81)90220-9.

Kawamura, H. et al. (Oct. 1998). DNS of Turbulent Heat Transfer in Channel Flow with Low to Medium-High Prandtl Number Fluid. In: *International Journal of Heat and Fluid Flow* 19, pp. 482–491. DOI: 10.1016/S0142-727X(98)10026-7.

Khoo, B., Y. Chew, and C. Teo (Nov. 2001). Near-wall hot-wire measurements . Part II: Turbulence time scale, convective velocity and spectra in the viscous sublayer. In: *Experiments in Fluids* 31, pp. 494–505. DOI: 10.1007/s003480100304.

Kim, J. and F. Hussain (Mar. 1993). Propagation velocity of perturbations in turbulent channel flow. In: *Physics of Fluids* 5, pp. 695–706. DOI: 10.1063/1.858653.

Kim, J. and P. Moin (May 1990). Transport Of Passive Scalars In A Turbulent Channel Flow. In: *Turbulent Shear Flows* 6, pp. 85–96. DOI: 10.1007/978-3-642-73948-4_9.

Kim, J., P. Moin, and R. Moser (May 1987). The Turbulence Statistics in Fully Developed Channel Flow at Low Reynolds Number. In: *Journal of Fluid Mechanics* 177, pp. 133–166. DOI: 10.1017/S0022112087000892.

Kong, H., H. Choi, and J. Lee (Oct. 2000). Direct numerical simulation of turbulent thermal boundary layers. In: *Physics of Fluids* 12, p. 2555. DOI: 10.1063/1.1287912.

Kowalewski, T., A. Mosyak, and G. Hetsroni (May 2003). Tracking of Coherent Thermal Structures on a Heated Wall. In: *Experiments in Fluids* 34, pp. 390–396. DOI: 10.1007/s00348-002-0574-9.

Lee, S., S. Lele, and P. Moin (Aug. 1992). Simulation of spatially evolving compressible turbulence and the application of Taylors hypothesis. In: *Physics of Fluids A Fluid Dynamics* 4, pp. 1521–1530. DOI: 10.1063/1.858425.

Lele, S. K. (Nov. 1992). Compact finite difference schemes with spectral-like resolution. In: *Journal of Computational Physics* 103, pp. 16–42. DOI: 10.1016/0021-9991(92)90324-R.

Lin, C. (Jan. 1953). On Taylor's hypothesis and the acceleration terms in the Navier-Stokes equations. In: *Quarterly of Applied Mathematics* 10, pp. 154–165. DOI: 10.1142/9789814415651_0011.

Liu, I.-S. (May 2002). *Continuum Mechanics*. Berlin, Germany: Springer. DOI: 10.1007/978-3-662-05056-9.

Liu, T., T. Chen, and M. Miozzi (Dec. 2023). Correlation between skin friction and enstrophy convection velocity in near-wall turbulence. In: *European Journal of Mechanics - B/Fluids* 104, pp. 224–230. DOI: 10.1016/j.euromechflu.2023.12.009.

Luchini, P. and M. Quadrio (June 2005). A low-cost parallel implementation of direct numerical simulation of wall turbulence. In: *Journal of Computational Physics* 211, pp. 551–571. DOI: 10.1016/j.jcp.2005.06.003.

Moin, P. (Dec. 2009). Revisiting Taylor's hypothesis. In: *Journal of Fluid Mechanics* 640, pp. 1–4. DOI: 10.1017/S0022112009992126.

Moser, R. D., J. Kim, and N. N. Mansour (Apr. 1999). Direct numerical simulation of turbulent channel flow up to Re=590. In: *Physics of Fluids* 11, pp. 943–945. DOI: 10.1063/1.869966.

Nitsche, W. and A. Brunn (Jan. 2006). *Strömungsmesstechnik*. Berlin, Germany: Springer. DOI: 10.1007/3-540-32487-9.

Ould-Rouiss, M., M. Bousbai, and A. Mazouz (May 2013). Large-Eddy simulation of turbulent heat transfer in pipe flows with respect to Reynolds and Prandtl number effects. In: *Acta Mechanica* 224, pp. 1133–1155. DOI: 10.1007/s00707-012-0796-8.

Piller, M. (Oct. 2005). Direct numerical simulation of turbulent forced convection in a pipe. In: *International Journal for Numerical Methods in Fluids* 49, pp. 583–602. DOI: 10.1002/fld.994.

Piomelli, U., J.-L. Balint, and J. Wallace (Mar. 1989). On the validity of Taylor's hypothesis for wall-bounded flows. In: *Physics of Fluids* 1, pp. 609–611. DOI: 10.1063/1.857432.

Pirozzoli, S., M. Bernardini, and P. Orlandi (Feb. 2016). Passive scalars in turbulent channel flow at high Reynolds number. In: *Journal of Fluid Mechanics* 788, pp. 614–639. DOI: 10.1017/jfm.2015.711.

Pope, S. B. (Aug. 2000). *Turbulent Flows*. Cambridge, United Kingdom: Cambridge University Press. DOI: 10.1017/CBO9781316179475.

Quadrio, M. and P. Luchini (Aug. 2003). Integral space–time scales in turbulent wall flows. In: *Physics of Fluids* 15, pp. 2219–2227. DOI: 10.1063/1.1586273.

Renard, N. and S. Deck (June 2015). On the scale-dependent turbulent convection velocity in a spatially developing flat plate turbulent boundary layer at Reynolds number ReTheta = 13 000. In: *Journal of Fluid Mechanics* 775, pp. 105–148. DOI: 10.1017/jfm.2015.290.

Romano, G. (Jan. 1995). Analysis of two-point velocity measurements in near-wall flows. In: *Experiments in Fluids* 20, pp. 68–83. DOI: 10.1007/BF01061584.

Saha, S. et al. (Mar. 2014). Scaling properties of the equation for passive scalar transport in wall-bounded turbulent flows. In: *International Journal of Heat and Mass Transfer* 70, pp. 779–792. DOI: 10.1016/j.ijheatmasstransfer.2013.11.057.

Schlichting, H. and K. Gersten (May 2006). *Grenzschicht-Theorie*. Berlin, Germany: Springer. DOI: 10.1007/3-540-32985-4.

Spurk, J. and N. Aksel (Feb. 2019). *Strömungslehre*. Berlin, Germany: Springer. DOI: 10.1007/978-3-662-58764-5.

Straub, S. et al. (Dec. 2019). The influence of thermal boundary conditions on turbulent forced convection pipe flow at two Prandtl numbers. In: *International Journal of Heat and Mass Transfer* 144, p. 118601. DOI: 10.1016/j.ijheatmasstransfer.2019.118601.

Taylor, G. (Feb. 1938). The Spectrum of Turbulence. In: *Proceedings of The Royal Society A: Mathematical, Physical and Engineering Sciences* 164, pp. 476–490. DOI: 10.1098/rspa.1938.0032.

Wills, J. (Nov. 1964). On convection velocities in turbulent shear flows. In: *Journal of Fluid Mechanics* 20, pp. 417–432. DOI: 10.1017/S002211206400132X.

Zierep, J. and K. Bühler (Oct. 2023). *Grundzüge der Strömungslehre*. Berlin, Germany: Springer. DOI: 10.1007/978-3-658-42223-3.

Appendix

A. Additional examples and explanations

A.1. Historical convection velocity definitions

The historical convection velocity definitions $u^{(2)}_{c,\phi}$ and $u^{(3)}_{c,\phi}$ carry some physical meaning. For interpretation purposes, a simplified example is considered, depicted in Figure A.1. The figure shows the space of the spatial (r_1) and temporal ($\triangle t$) separations, such as Figure 2.5, divided into discrete intervals. The convection behaviour of a turbulent structure, starting at $r_1 = 0$ and $\triangle t = 0$ is analysed. The considered structure is idealised as a superposition of two modes. The blue mode moves fast through space and dissipates quickly in time, while the orange mode has a slower velocity but is also long-lived. The dissipative characteristics of each mode are visualised by their opacity. To keep the example as simple as possible, the actual size of each mode is considered to remain unchanged.
The definitions $u^{(2)}_{c,\phi}$ and $u^{(3)}_{c,\phi}$ construct convection velocities at points of maximum space-time auto-covariance at either a constant spatial or a constant temporal separation, respectively. By considering, for example, a constant temporal separation of $\triangle t = 4$, the orange mode with a spatial separation of $r_1 = 1$ has the largest similarity to the original structure and, therefore, the maximum space-time auto-covariance. However, when a constant spatial separation of $r_1 = 1$ is fixed, the blue mode with a temporal separation of $\triangle t = 1$ shows to be the most similar to the original structure. The convection velocity defined by $u^{(2)}_{c,\phi}$ would therefore more accurately depict the actual velocity of the blue mode, while the definition $u^{(3)}_{c,\phi}$ rather belongs to the orange mode.

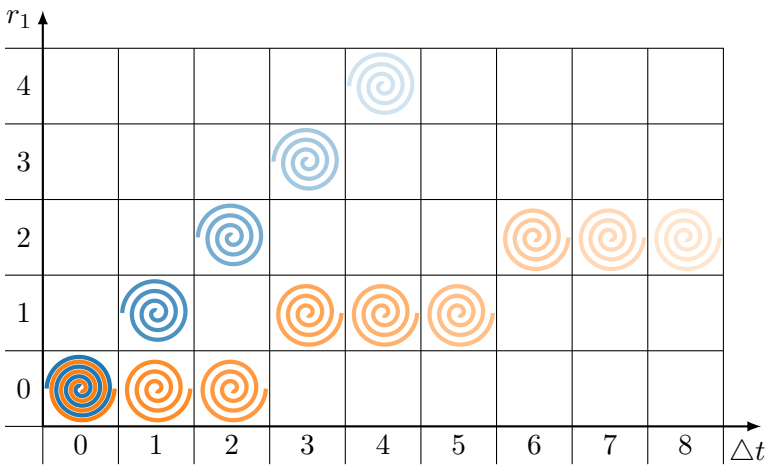

Figure A.1.: Simplified convection behaviour of turbulent structures

Since the complexity of a real turbulent structure exceeds this example by far, it is obvious that the historical convection velocity definitions cannot capture the whole behaviour of turbulent phenomena. Choosing one definition over the other is always a trade-off between

which characteristics should be reflected best by the convection velocity. Hussain and Clark 1980 mention, for example, $u_{c,\phi}^{(2)}$ being the preferred definition for the study of aerodynamic noise and other wave phenomena, since in these cases optimising the time scale has a higher priority over optimising the length scale.

A.2. Wall-normal pressure gradient calculation

In the scope of this thesis, the pressure field p and the wall-normal pressure gradient field $\partial_{x_2} p$ are calculated via individual Poisson solvers, rather than calculating the latter by taking the wall-normal derivative of the former. The reason for this is numerical accuracy. When considering Equation 3.23, where (the fluctuation of) the wall-normal pressure gradient is needed, the individual terms of the quotients reach very small numerical values near the channel walls. This behaviour is depicted in Figure A.2, where all terms (the denominator of Equation 3.23 is shown separately) of the convection velocity implementations of the smallest turbulent u_2 structures are plotted over the wall distance. Note that the curves in this figure do *not* show the quantities listed in its legends, but rather the corresponding terms of Equation 3.23. The very small orders of magnitude depicted in Figure A.2 show the need for high numerical accuracy because the error-prone terms would otherwise lead to incorrectly calculated convection velocities. Since the compact finite difference scheme used for numerical derivation in the wall-normal direction is not exact, its use should be avoided when possible. However, its use is necessary when solving the Poisson equation, but applying it again to calculate $\partial_{x_2} p$ from p can be omitted by solving a Poisson equation for the wall-normal pressure gradient itself. Note that the need for numerical accuracy goes so far that the compact finite difference scheme used for solving the Poisson equation needs to be implemented with great care. A satisfying solution is only reached by using the continuity equation $\partial_{x_2} u_2 = -\partial_{x_1} u_1 - \partial_{x_3} u_3$ to eliminate all wall-normal derivatives within products on the right-hand side (of the Poisson equation), and grouping the remaining terms with respect to the order of their wall-normal derivatives, to avoid applying the derivation matrices of the compact finite difference scheme more often than necessary. As a result, the implemented Poisson equation for the wall-normal pressure gradient takes the form:

$$\begin{aligned}\Delta\left(\partial_{x_2} p\right) = &-2\partial_{x_2}\Big[\partial_{x_1} u_1 \partial_{x_1} u_1 + \partial_{x_3} u_3 \partial_{x_3} u_3 + \partial_{x_1} u_1 \partial_{x_3} u_3 + \partial_{x_1} u_3 \partial_{x_3} u_1 \\ &\qquad + u_1 \partial^2_{x_1 x_1} u_1 + u_1 \partial^2_{x_1 x_3} u_3 + u_3 \partial^2_{x_1 x_3} u_1 + u_3 \partial^2_{x_3 x_3} u_3\Big] \\ &-2\partial^2_{x_2 x_2}\Big[u_1 \partial_{x_1} u_2 + u_3 \partial_{x_3} u_2\Big].\end{aligned} \tag{5.1}$$

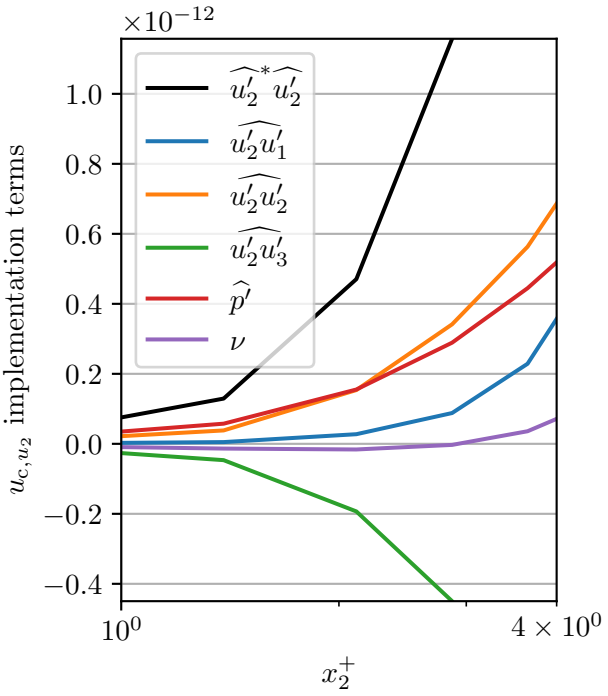

(a) Near-wall behaviour for case p180

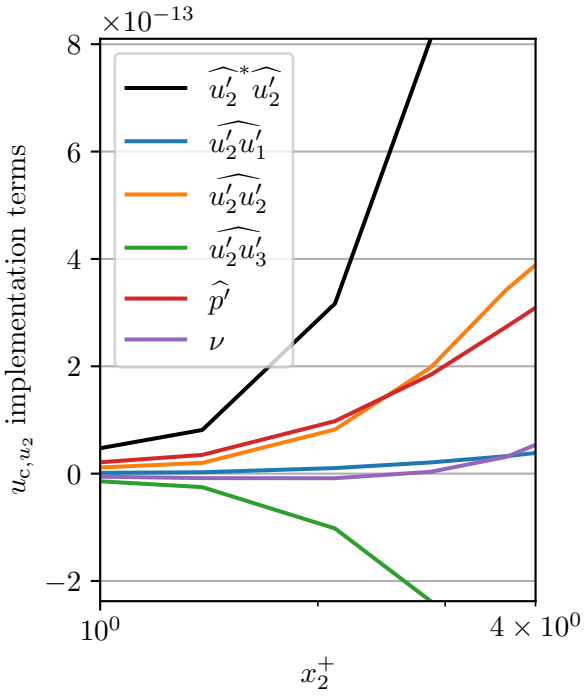

(b) Near-wall behaviour for case m180

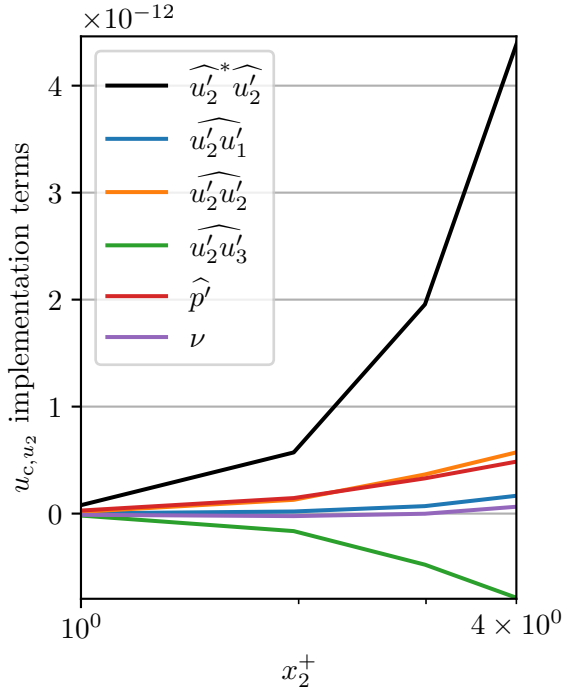

(c) Near-wall behaviour for case m500

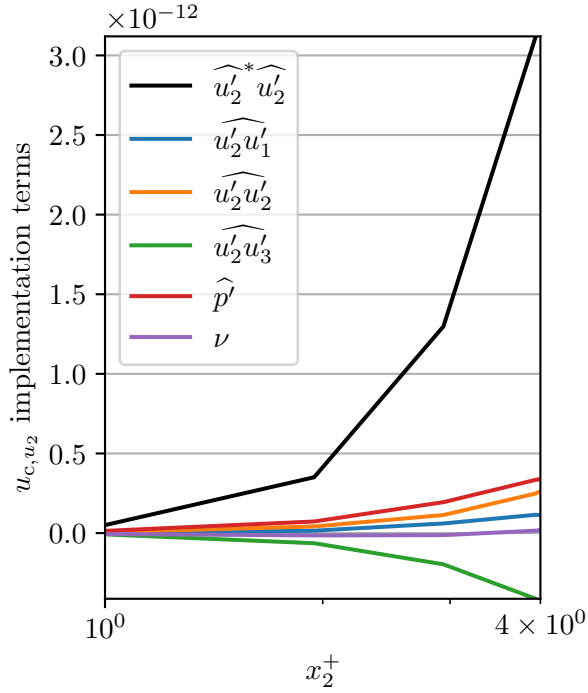

(d) Near-wall behaviour for case m1000

Figure A.2.: Near-wall behaviour of individual Equation 3.23 terms (smallest structures)

A.3. Overall convection velocity scaling for passive scalar structures

Hetsroni et al. 2004 investigated the overall convection velocities of passive scalar structures in a turbulent boundary layer at $Re_\tau = 171$. In agreement with this thesis, they found that $U_{c,\theta}$ becomes constant near the wall, while this constant value decreases with an increase in the Prandtl number. They analysed passive scalars with $Pr \in \{1,\ 5.4,\ 54\}$ and found a possible dependence of the corresponding overall convection velocities on the Prandtl number. In close vicinity to the wall, where the overall convection velocities are constant, their data could be expressed (approximately) by the relationship

$$U_{c,\theta} = \frac{U_{c,u_1}}{Pr^{\frac{1}{3}}}, \tag{5.2}$$

with the overall convection velocity of streamwise velocity structures U_{c,u_1}. To investigate whether Equation 5.2 holds for lower values of Pr, which are considered in this work, Figure A.3 is depicted. The figure shows the relationship between a quotient of the respective overall convection velocities at $x_2^+ < 2$ and the Prandtl number. In addition to the results of Hetsroni et al. 2004, data from m180, m500, and m1000 are shown.
As is evident from Figure A.3, the values of the lower Prandtl number scalars do *not* follow the proposed trend. For all the cases considered, $U_{c,\theta}/U_{c,u_1}$ deviates from $1/Pr^{\frac{1}{3}}$ towards smaller values. This behaviour seems to be amplified for smaller Reynolds numbers. For the overall convection velocities of passive scalar structures at Prandtl numbers smaller than unity, the relationship

$$U_{c,\theta} = \frac{U_{c,u_1}}{Pr^{\frac{1}{29}} Re_\tau^{0.19}} \tag{5.3}$$

might be a better fit. The corresponding lines of Equation 5.2 and Equation 5.3 are also shown in Figure A.3. The general reason for the trend change at $Pr = 1$ could lie in the ratio between the sizes of the viscous and molecular sublayers. Although the molecular sublayer is fully contained within the viscous sublayer for $Pr > 1$, the opposite is the case for smaller Prandtl numbers. Therefore, the influence of passive scalar structures from the outer flow suddenly becomes more dominant for $Pr < 1$.

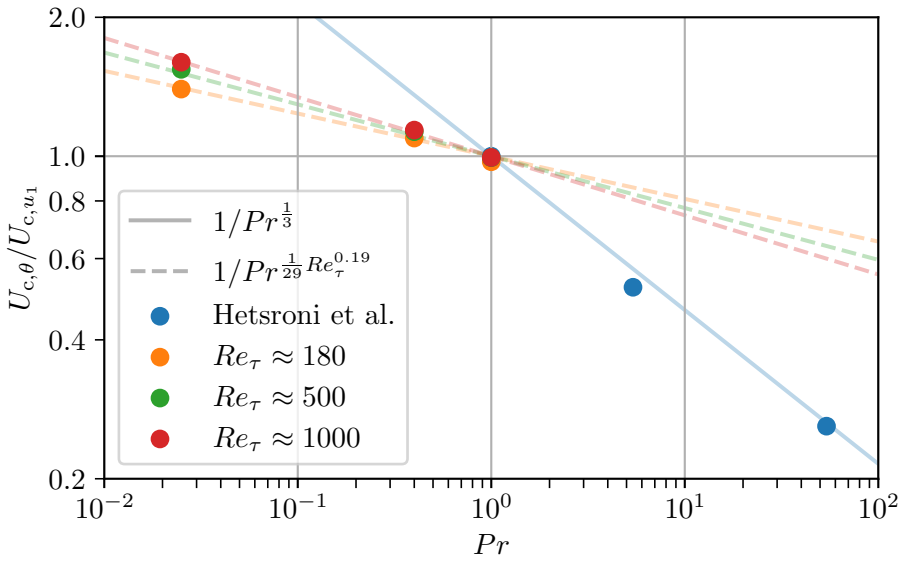

Figure A.3.: Dependence of $U_{c,\theta}$ on Pr (Partially adapted from Hetsroni et al. 2004)

B. Additional standard turbulence statistics

B.1. Mean fields

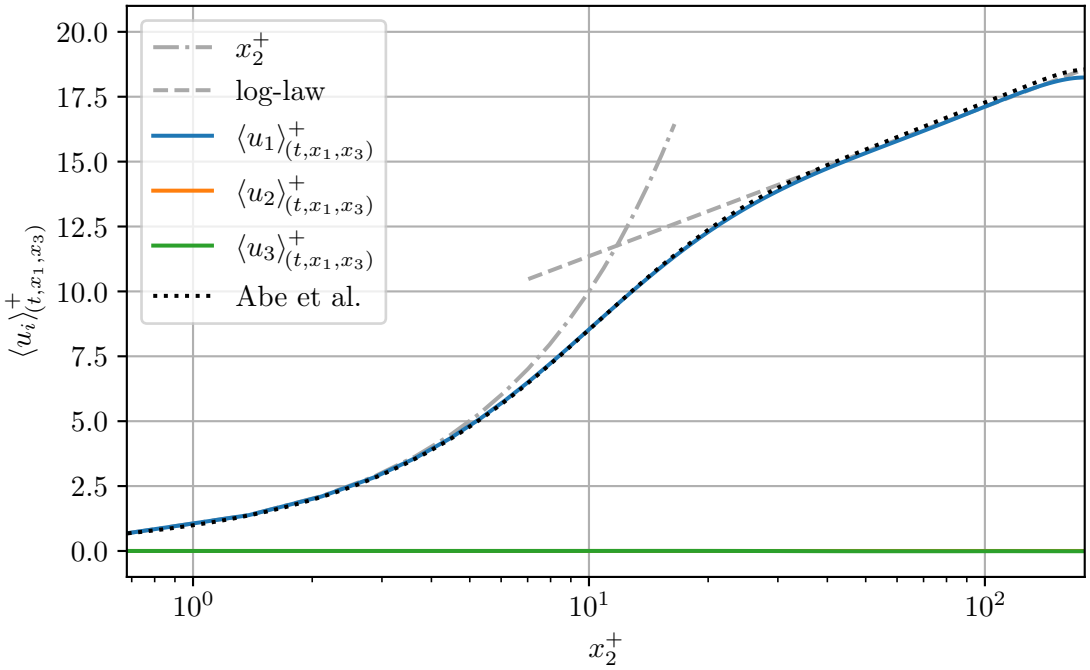

(a) Mean velocity profiles (reference: Abe et al. 2004)

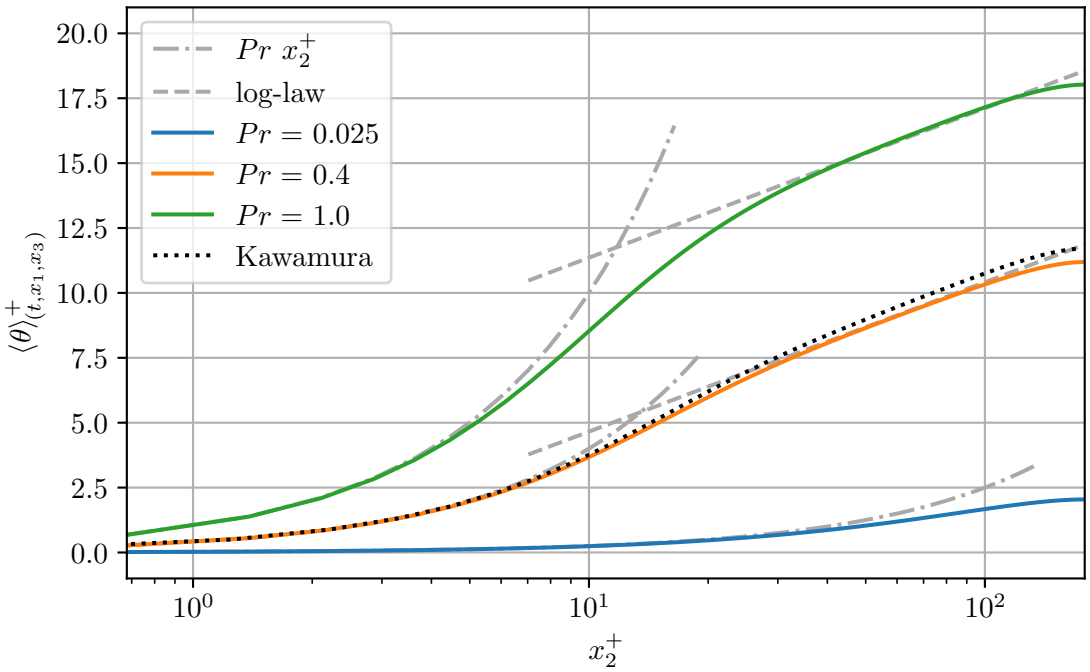

(b) Mean scalar profiles (reference: Kawamura et al. 1998)

Figure B.4.: Mean quantities in turbulent plane channel flow (case m180)

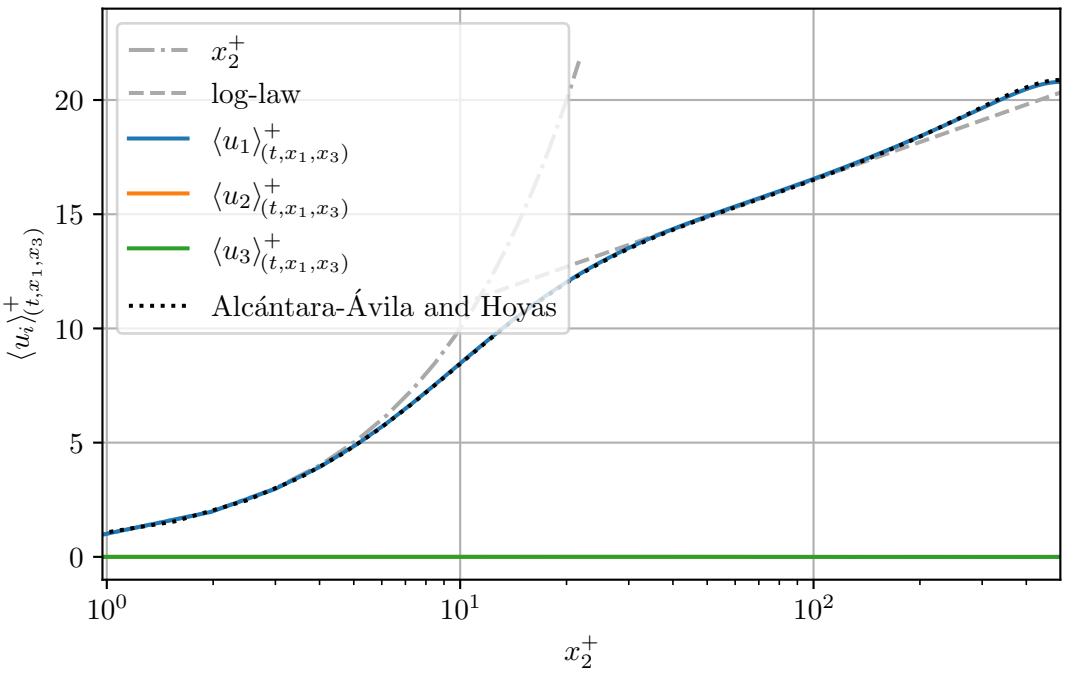

(a) Mean velocity profiles (reference: Alcántara-Ávila and Hoyas 2021)

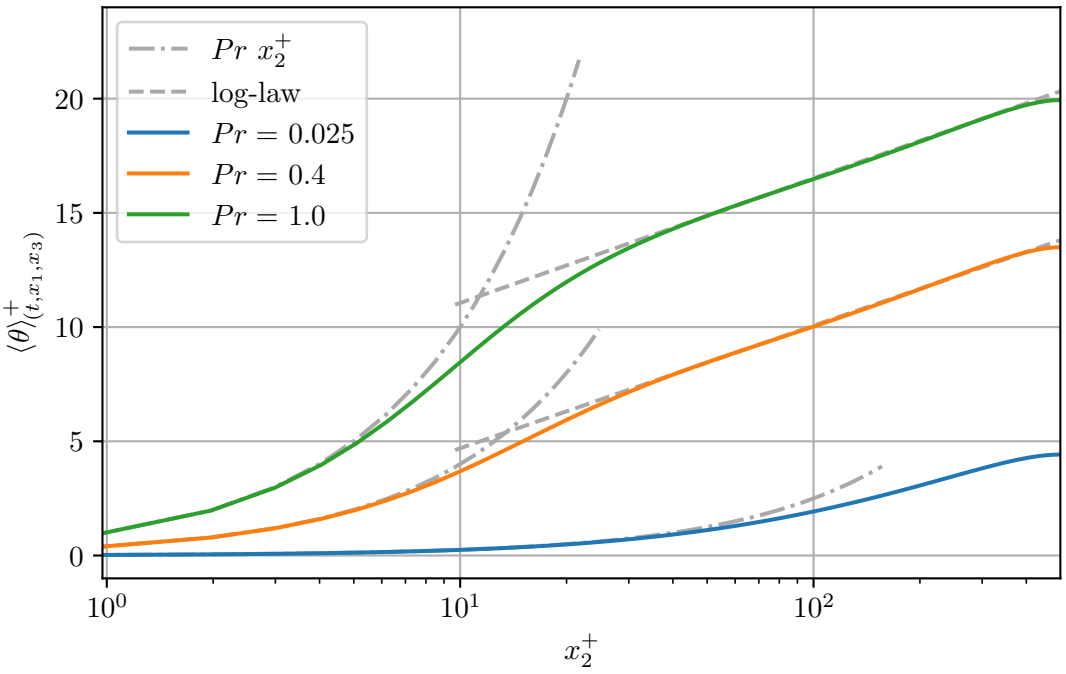

(b) Mean scalar profiles

Figure B.5.: Mean quantities in turbulent plane channel flow (case m500)

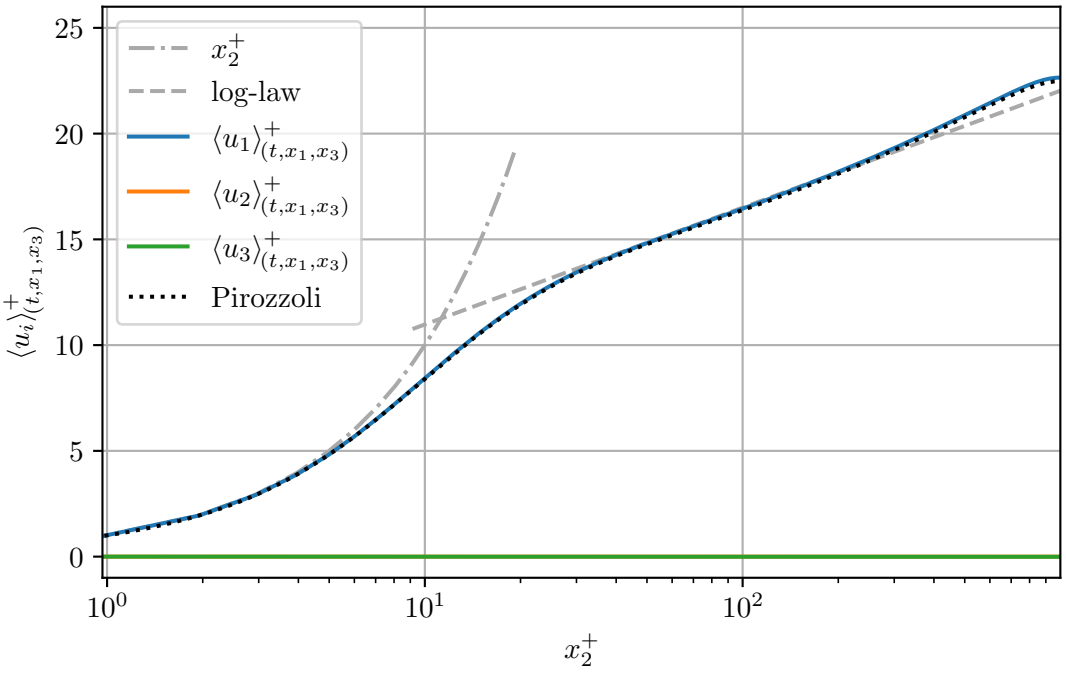

(a) Mean velocity profiles (reference: Pirozzoli et al. 2016)

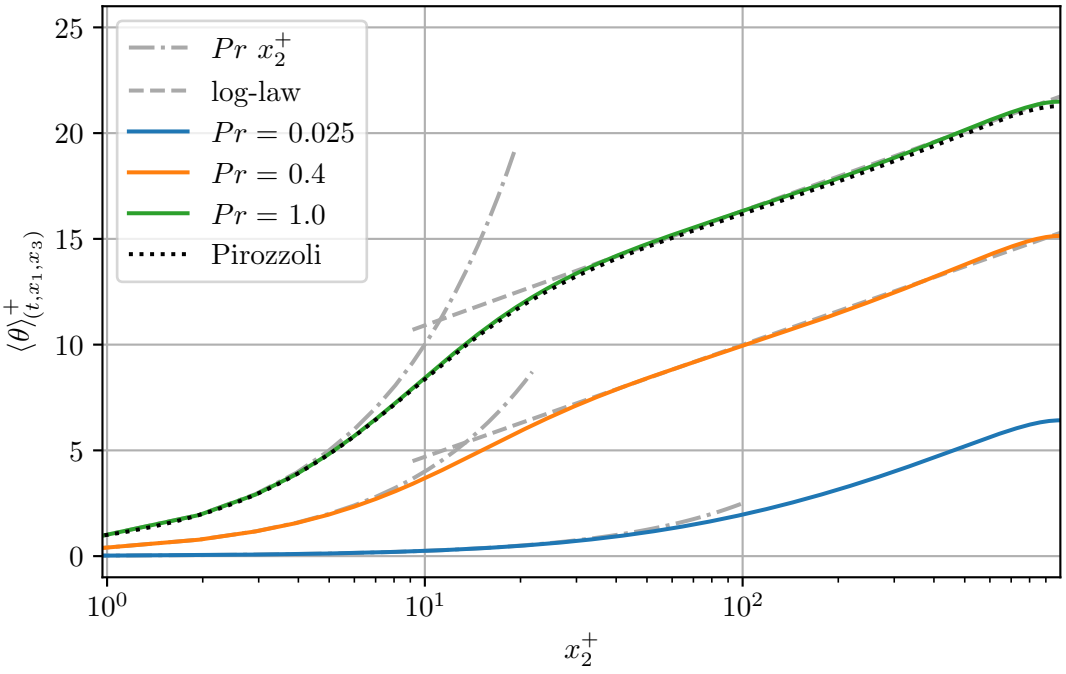

(b) Mean scalar profiles (reference: Pirozzoli et al. 2016)

Figure B.6.: Mean quantities in turbulent plane channel flow (case m1000)

B.2. Reynolds stress and scalar correlation

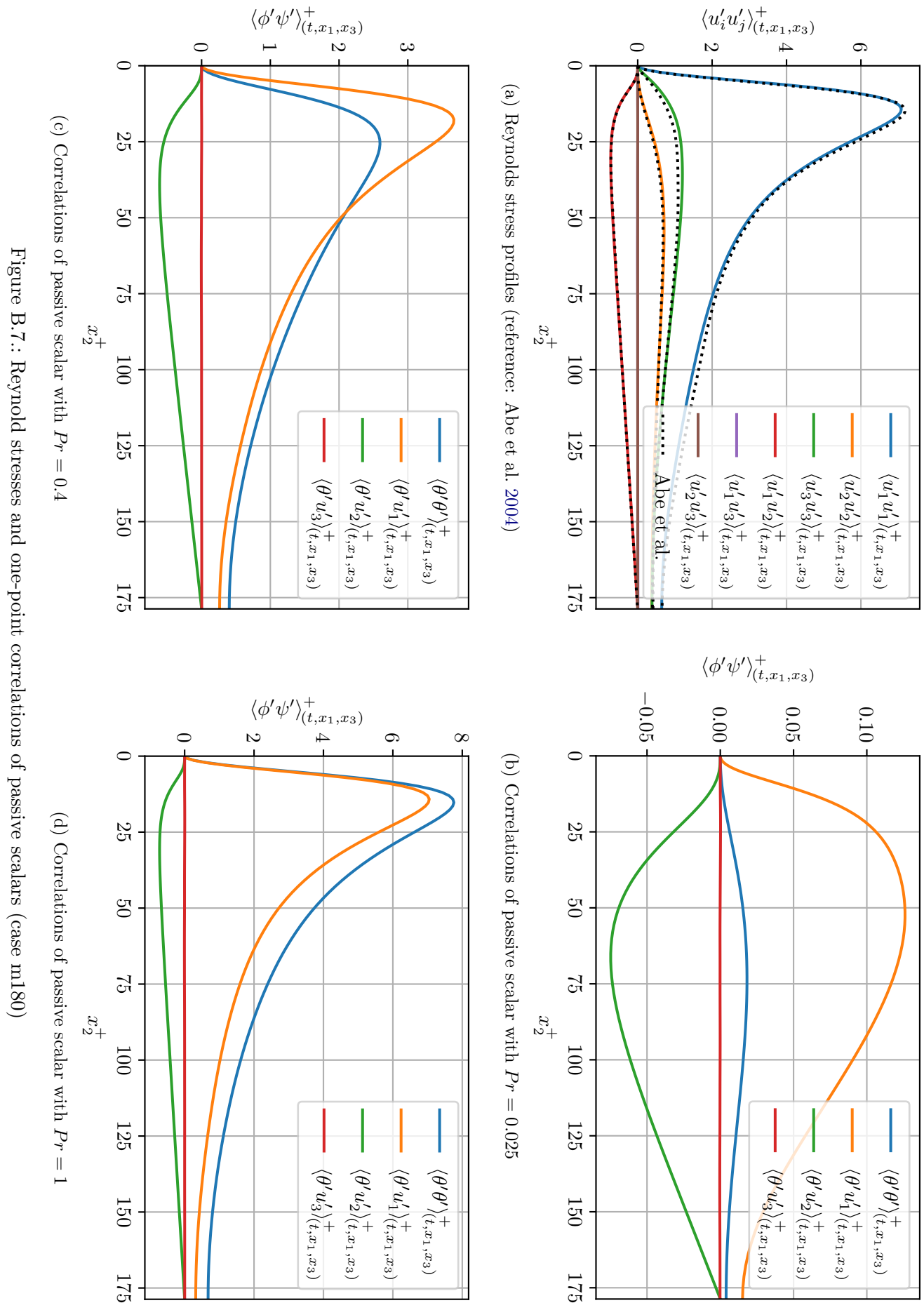

(a) Reynolds stress profiles (reference: Abe et al. 2004)

(b) Correlations of passive scalar with $Pr = 0.025$

(c) Correlations of passive scalar with $Pr = 0.4$

(d) Correlations of passive scalar with $Pr = 1$

Figure B.7.: Reynold stresses and one-point correlations of passive scalars (case m180)

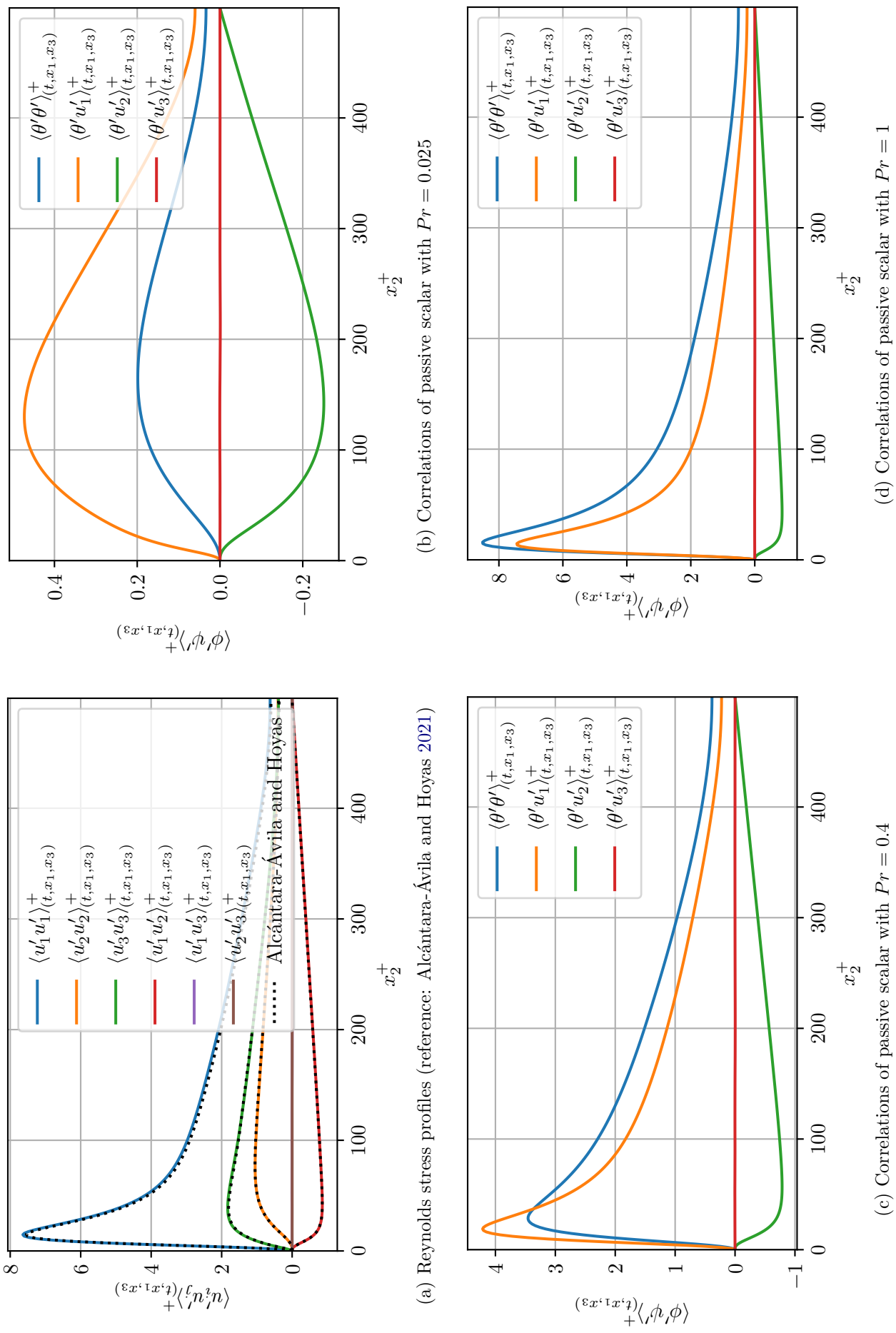

(a) Reynolds stress profiles (reference: Alcántara-Ávila and Hoyas 2021)

(b) Correlations of passive scalar with $Pr = 0.025$

(c) Correlations of passive scalar with $Pr = 0.4$

(d) Correlations of passive scalar with $Pr = 1$

Figure B.8.: Reynold stresses and one-point correlations of passive scalars (case m500)

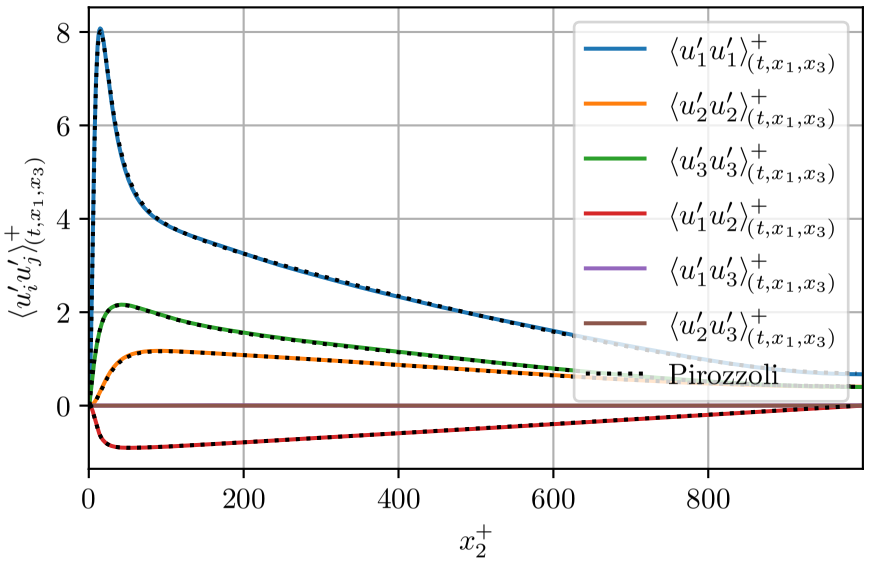

(a) Reynolds stress profiles (reference: Pirozzoli et al. 2016)

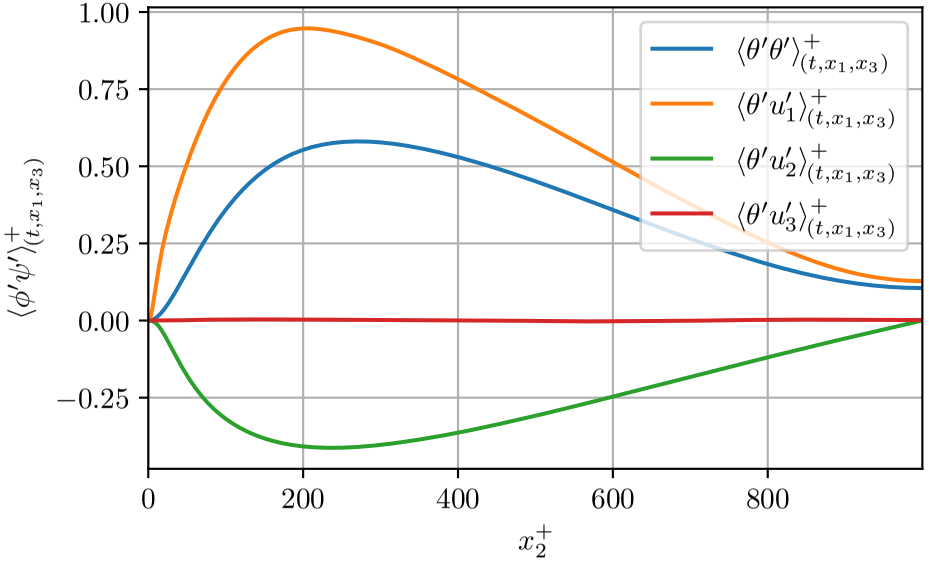

(b) Correlations of passive scalar with $Pr = 0.025$

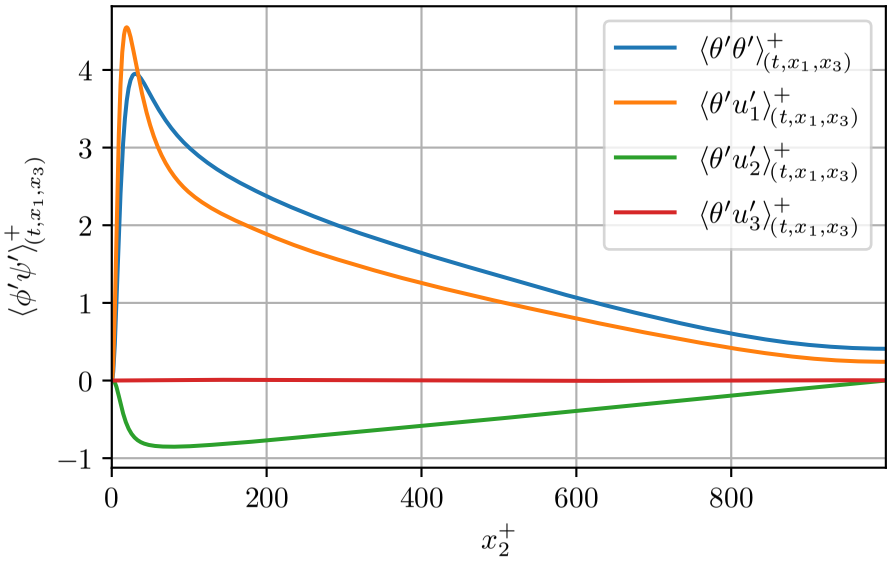

(c) Correlations of passive scalar with $Pr = 0.4$

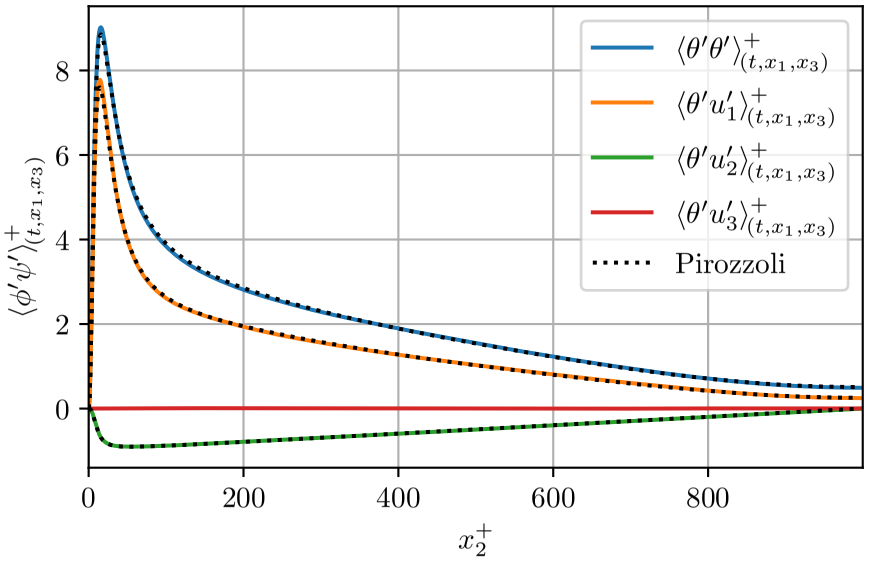

(d) Correlations of passive scalar with $Pr = 1$ (ref.: Pirozzoli et al. 2016)

Figure B.9.: Reynold stresses and one-point correlations of passive scalars (case m1000)

B.3. Shear stress and scalar flux

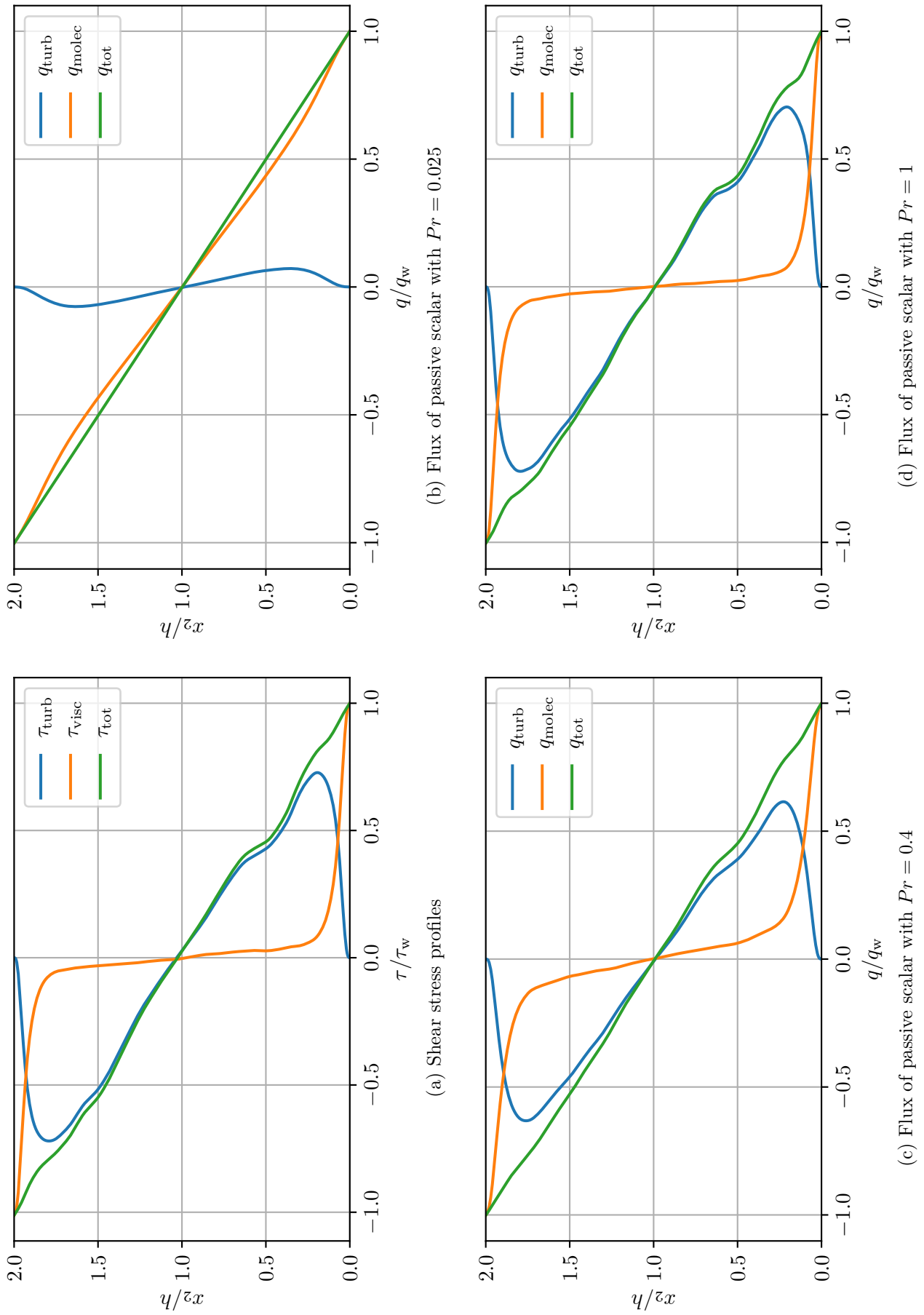

(a) Shear stress profiles

(b) Flux of passive scalar with $Pr = 0.025$

(c) Flux of passive scalar with $Pr = 0.4$

(d) Flux of passive scalar with $Pr = 1$

Figure B.10.: Shear stress and passive scalar flux contributions (case m180)

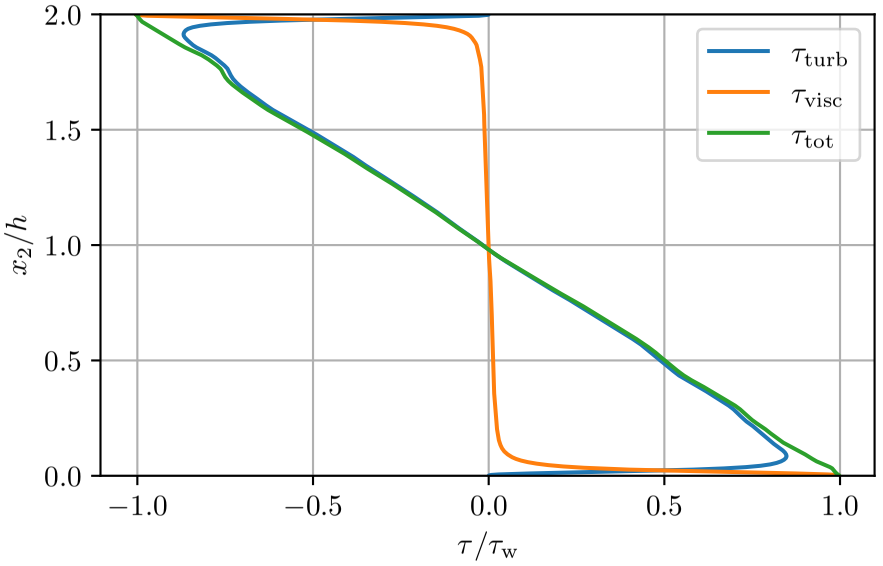

(a) Shear stress profiles

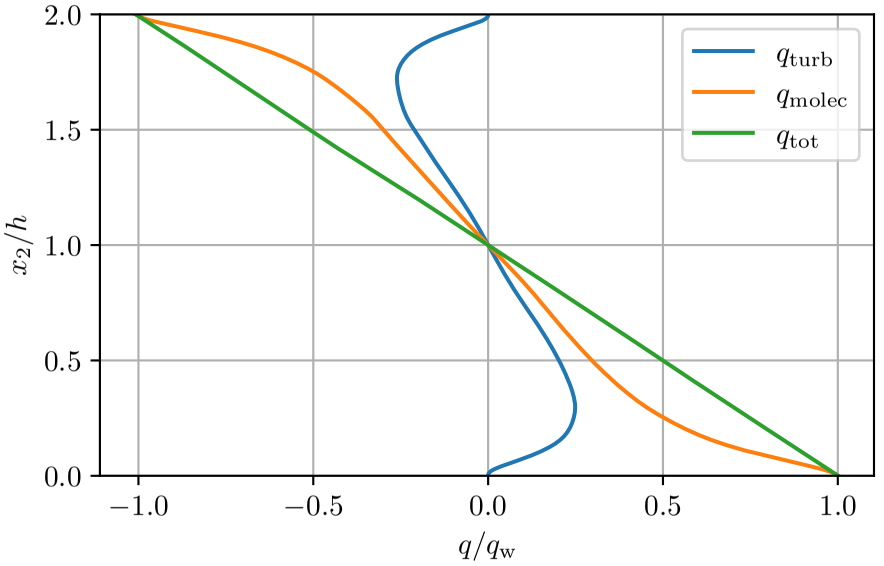

(b) Flux of passive scalar with $Pr = 0.025$

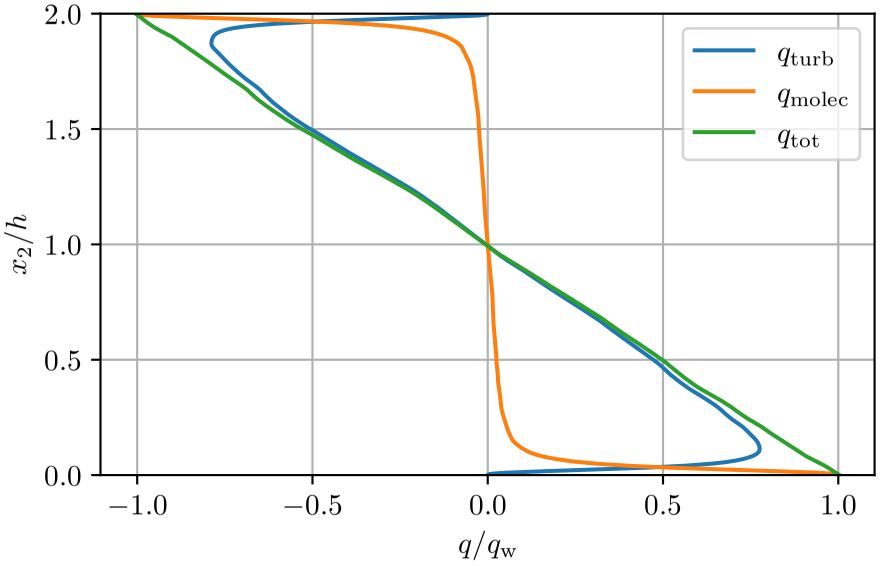

(c) Flux of passive scalar with $Pr = 0.4$

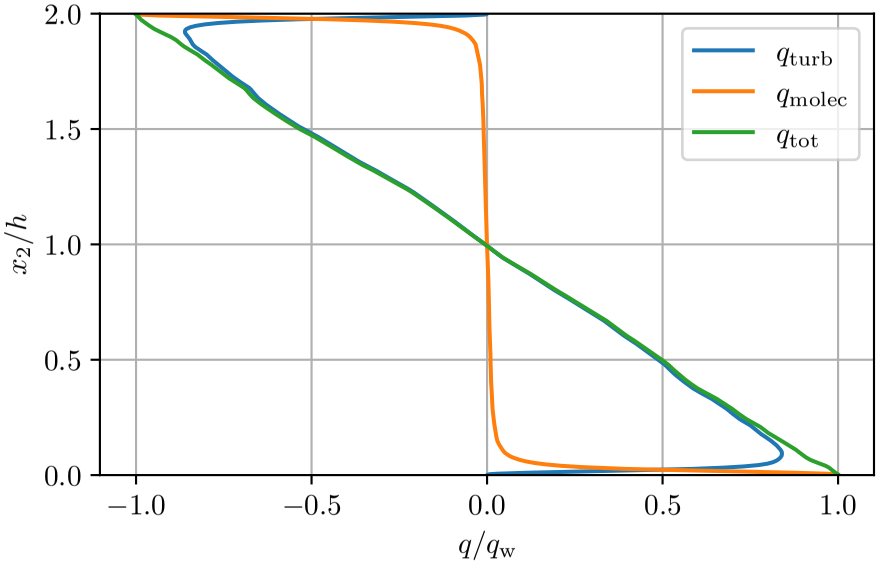

(d) Flux of passive scalar with $Pr = 1$

Figure B.11.: Shear stress and passive scalar flux contributions (case m500)

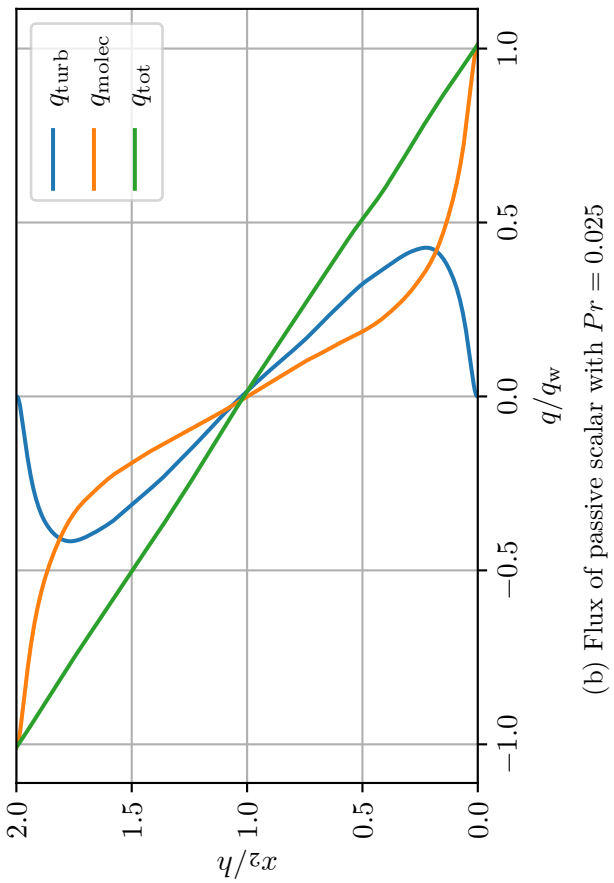

(a) Shear stress profiles

(b) Flux of passive scalar with $Pr = 0.025$

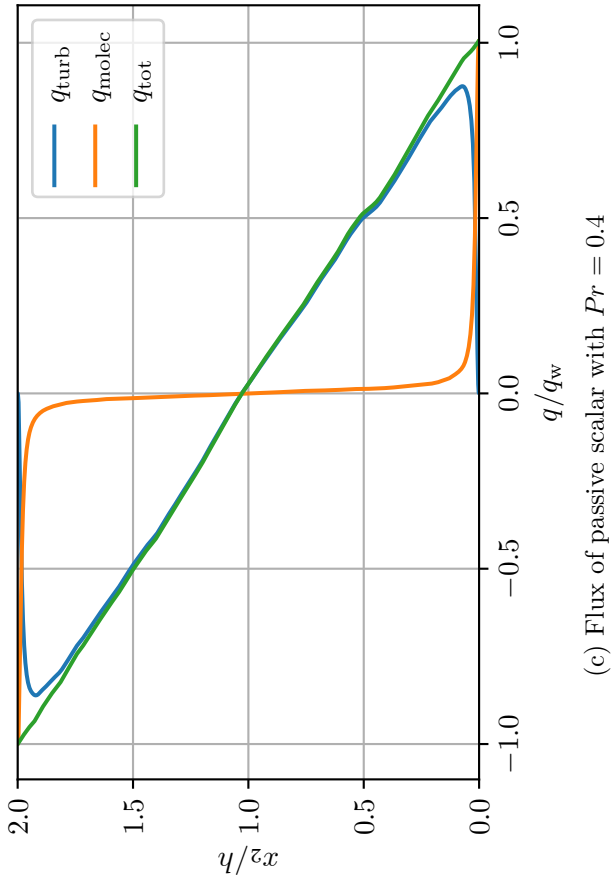

(c) Flux of passive scalar with $Pr = 0.4$

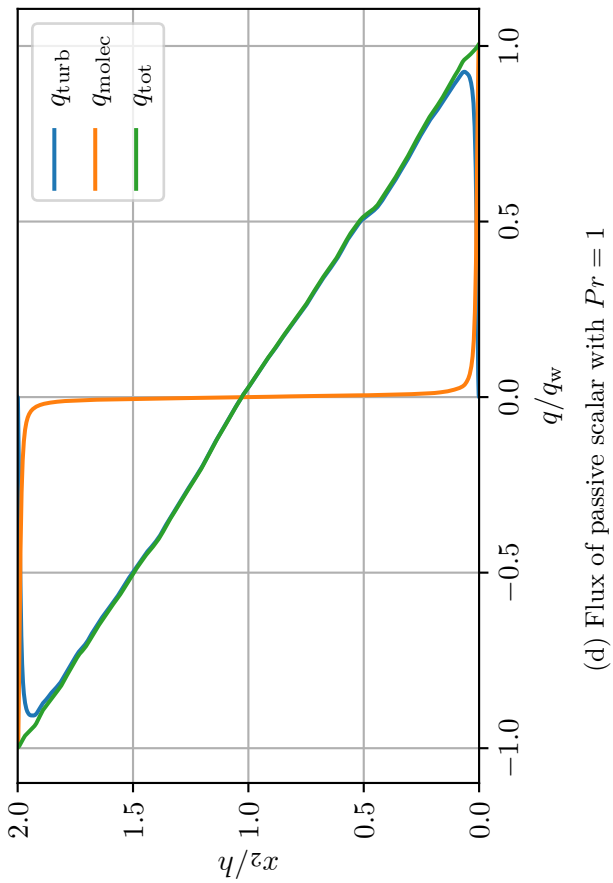

(d) Flux of passive scalar with $Pr = 1$

Figure B.12.: Shear stress and passive scalar flux contributions (case m1000)

B.4. Streamwise auto-covariance

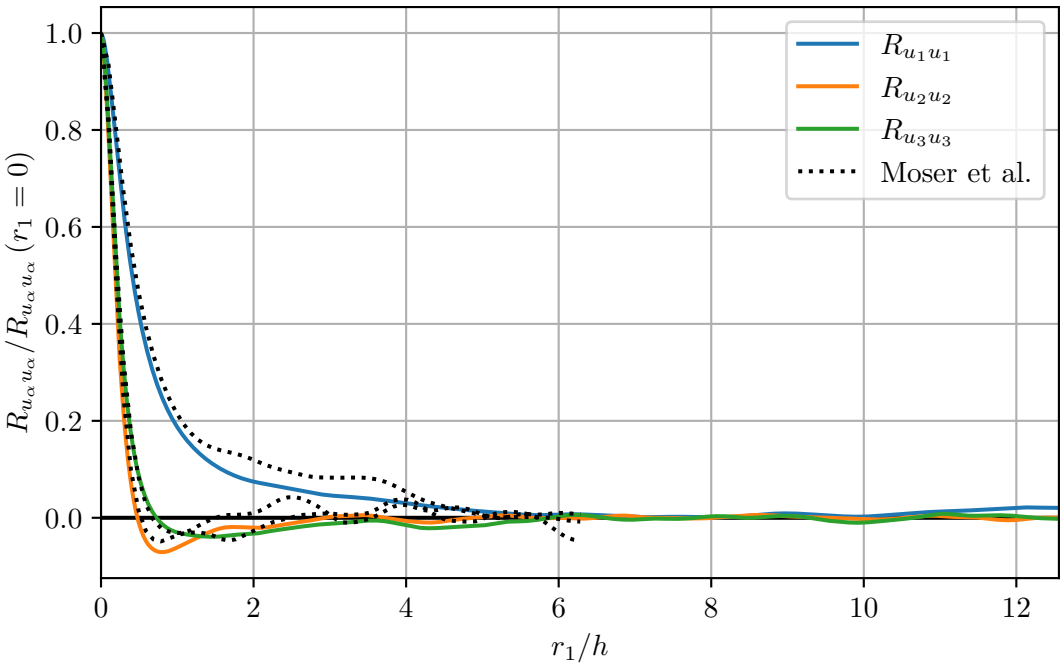

(a) Auto-covariance of velocity components (reference: Moser et al. 1999)

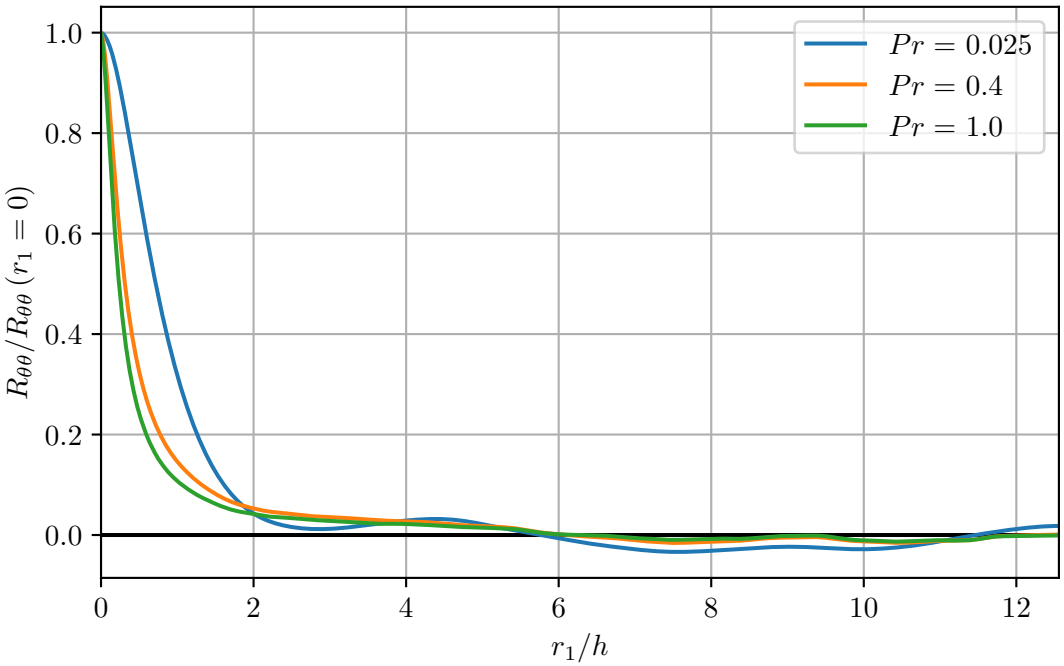

(b) Auto-covariance of passive scalars

Figure B.13.: Streamwise auto-covariance profiles at $x_2^+ \approx 180$ (case m180)

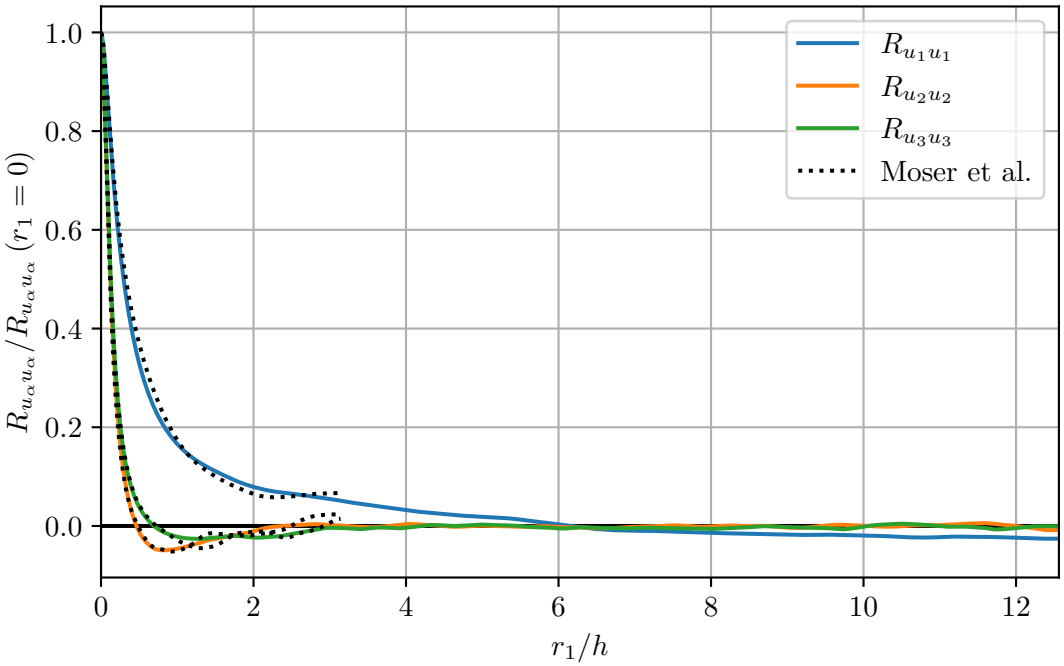

(a) Auto-covariance of velocity components (reference: Moser et al. 1999)

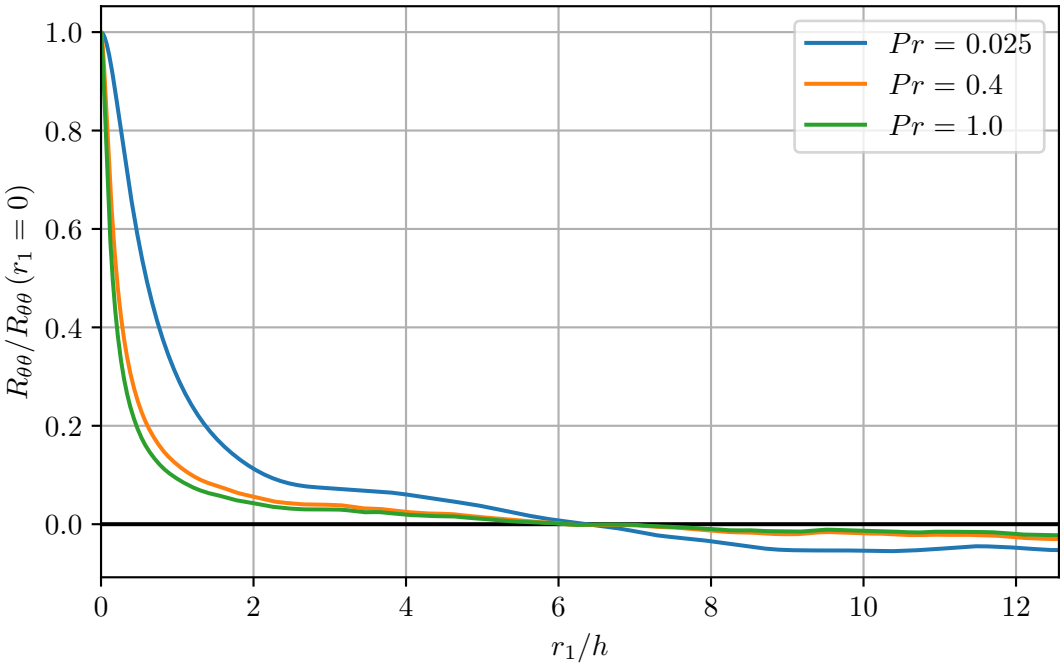

(b) Auto-covariance of passive scalars

Figure B.14.: Streamwise auto-covariance profiles at $x_2^+ \approx 500$ (case m500)

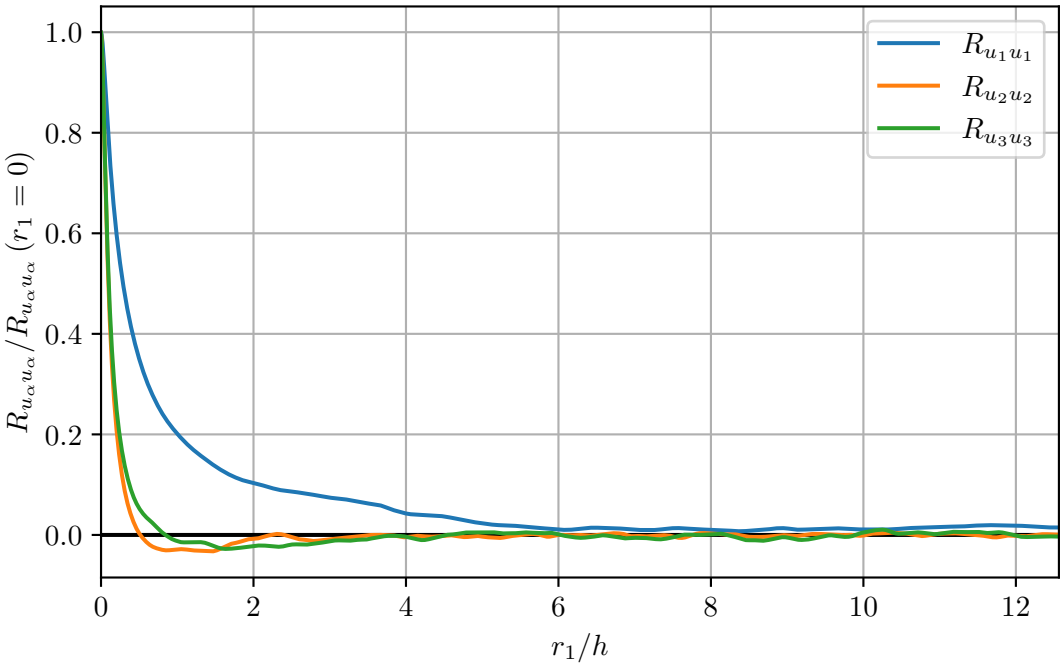

(a) Auto-covariance of velocity components

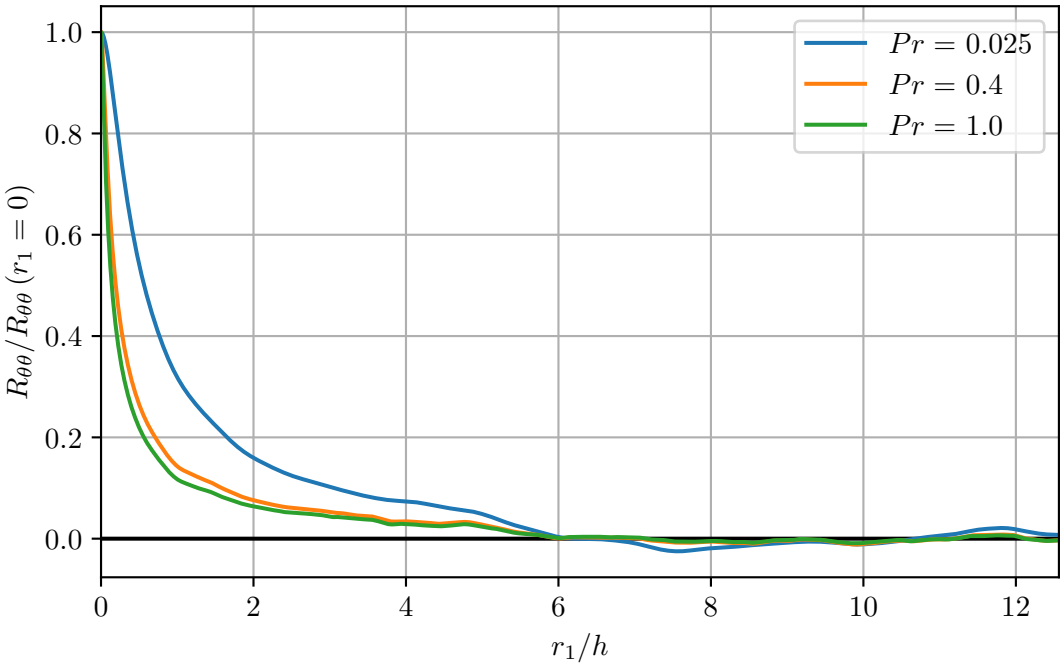

(b) Auto-covariance of passive scalars

Figure B.15.: Streamwise auto-covariance profiles at $x_2^+ \approx 1000$ (case m1000)

B.5. Spanwise auto-covariance

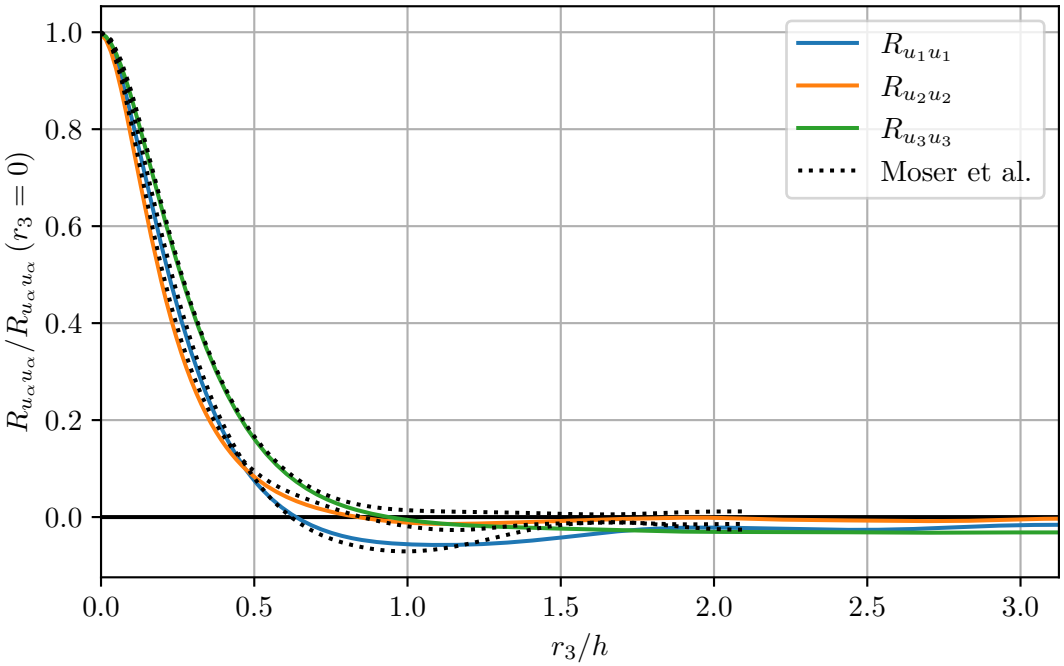

(a) Auto-covariance of velocity components (reference: Moser et al. 1999)

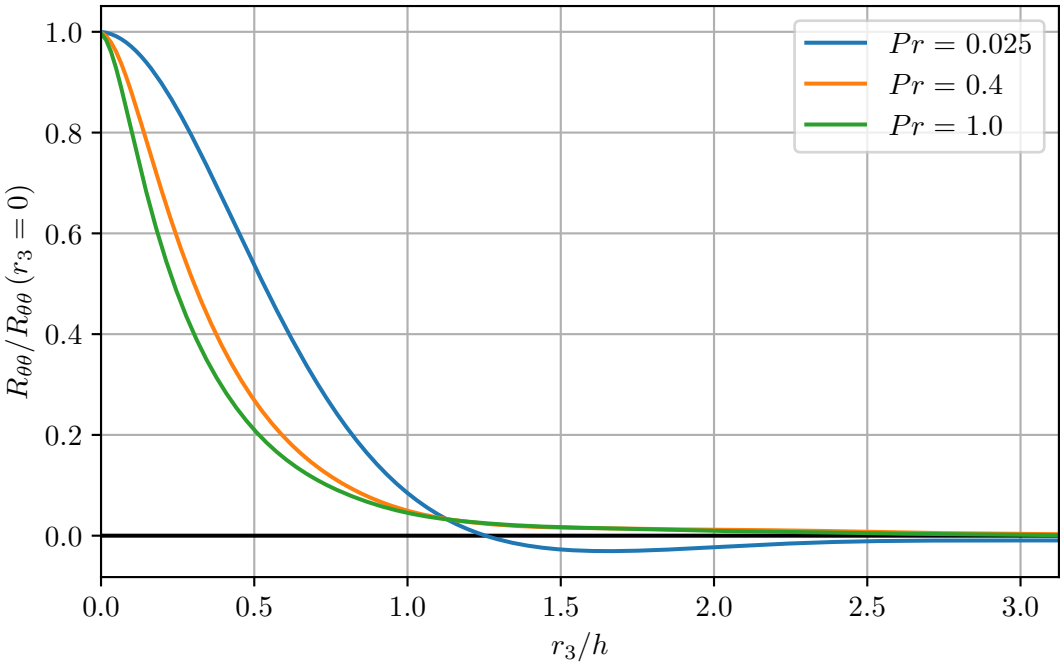

(b) Auto-covariance of passive scalars

Figure B.16.: Spanwise auto-covariance profiles at $x_2^+ \approx 180$ (case m180)

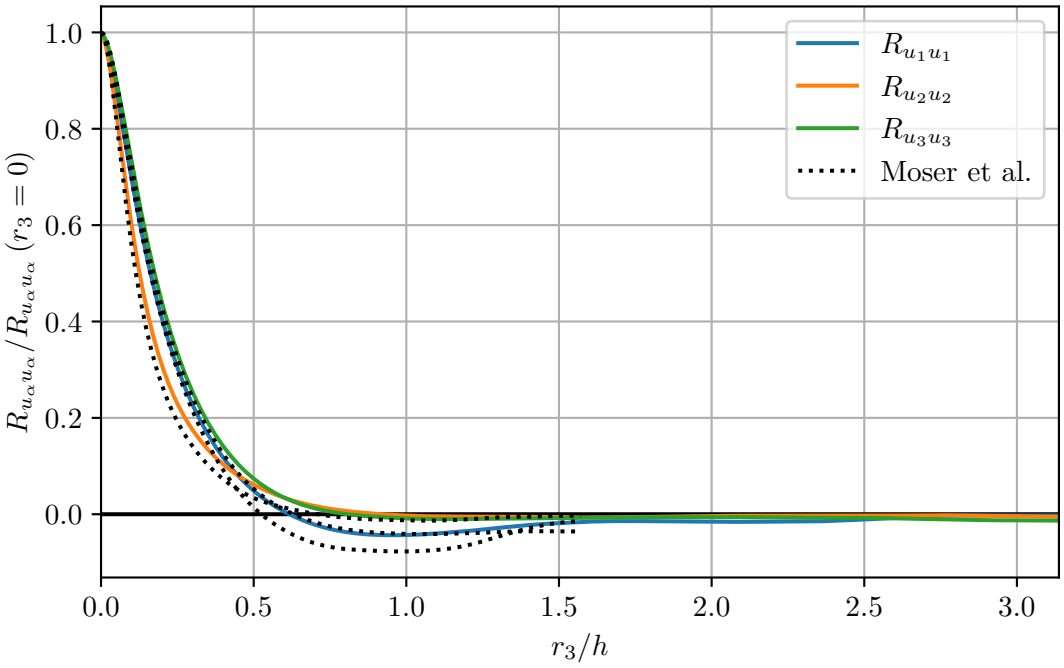

(a) Auto-covariance of velocity components (reference: Moser et al. 1999)

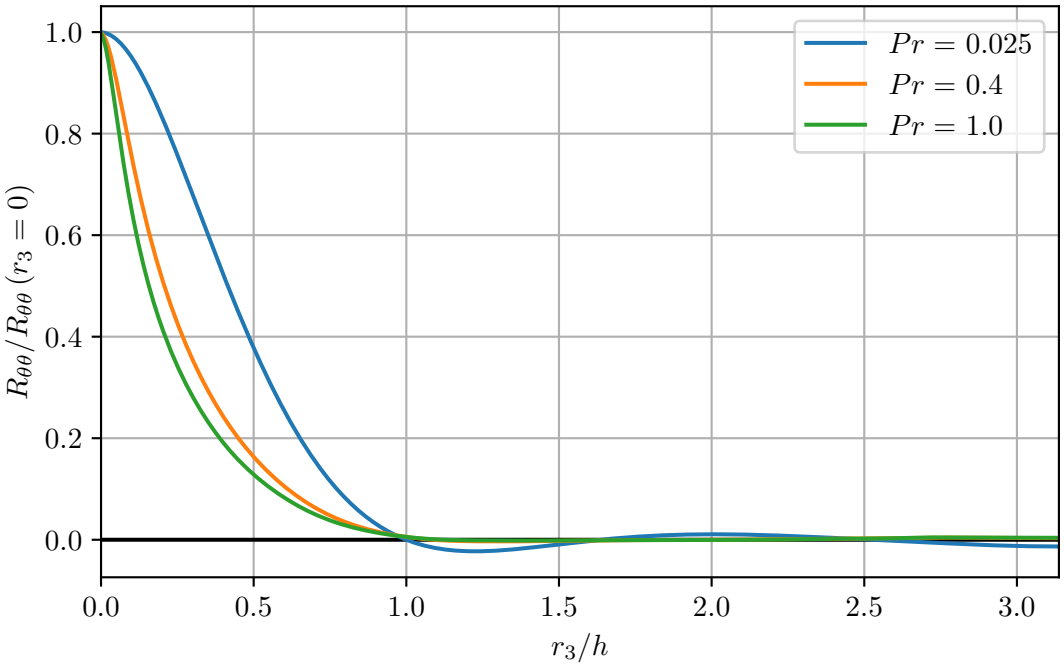

(b) Auto-covariance of passive scalars

Figure B.17.: Spanwise auto-covariance profiles at $x_2^+ \approx 500$ (case m500)

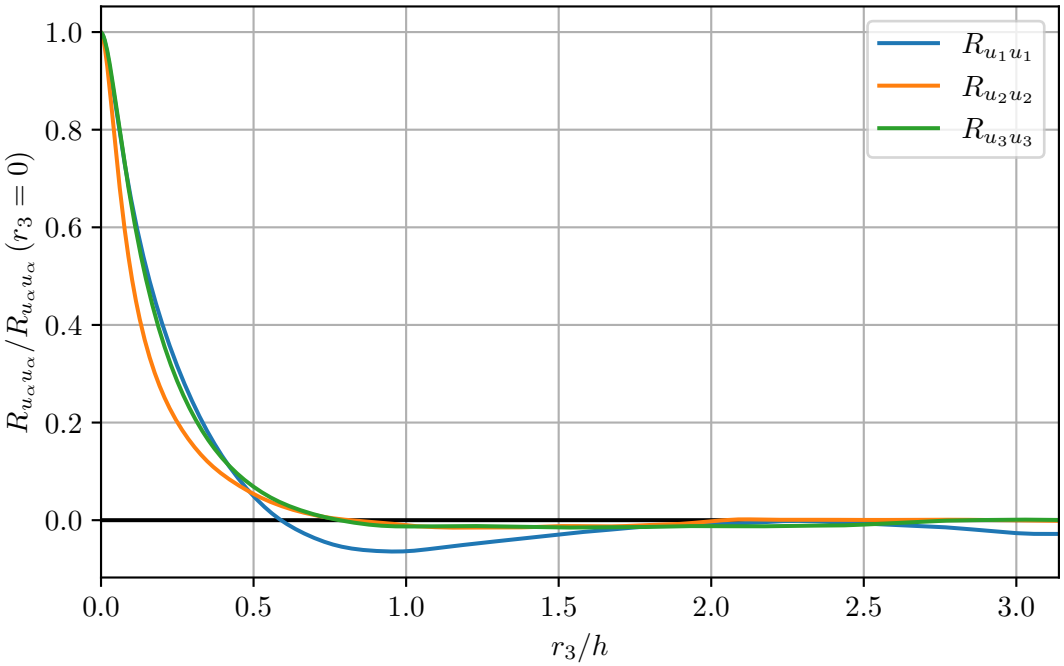

(a) Auto-covariance of velocity components

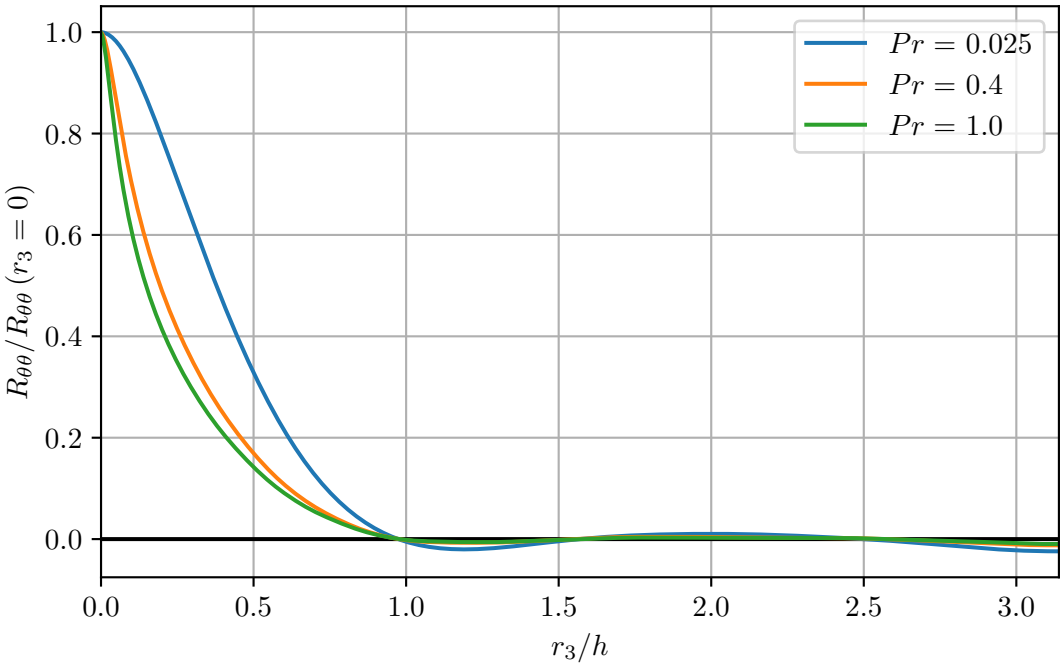

(b) Auto-covariance of passive scalars

Figure B.18.: Spanwise auto-covariance profiles at $x_2^+ \approx 1000$ (case m1000)

B.6. Skewness

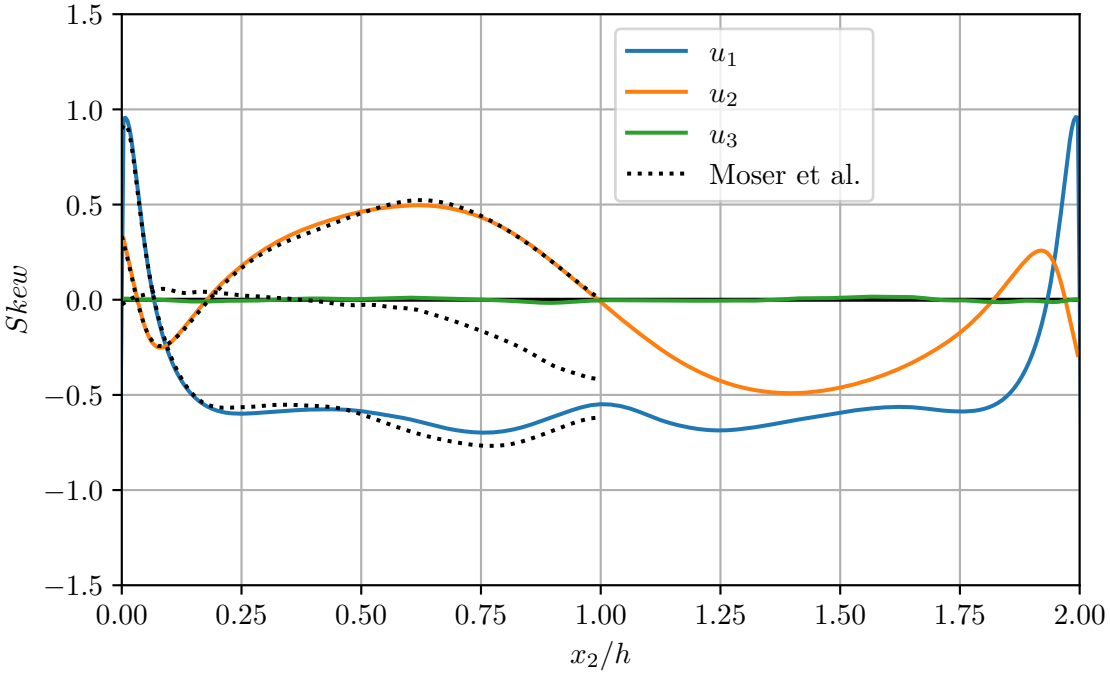

(a) Skewness of velocity components (reference: Moser et al. 1999)

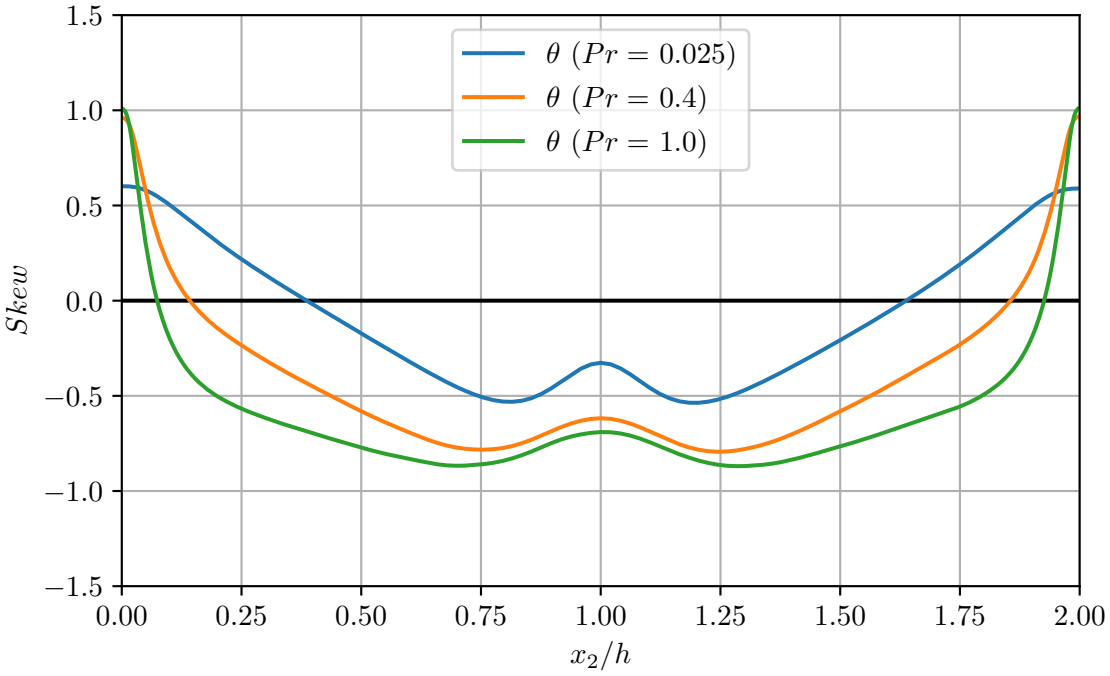

(b) Skewness of passive scalars

Figure B.19.: Skewness distributions in turbulent plane channel flow (case m180)

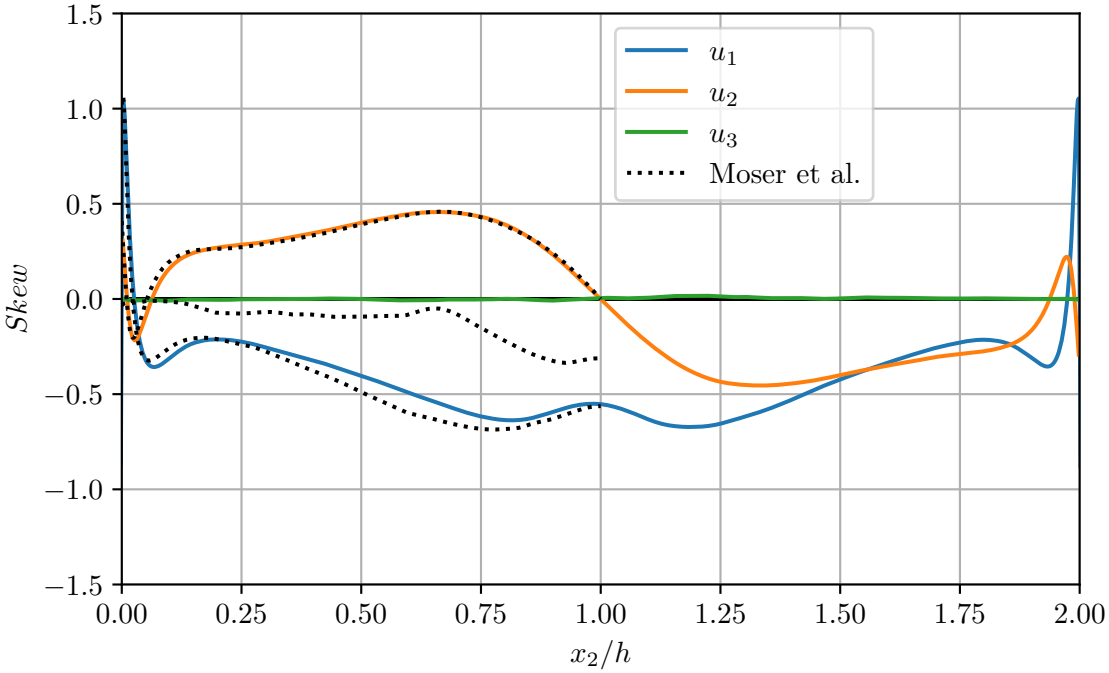

(a) Skewness of velocity components (reference: Moser et al. 1999)

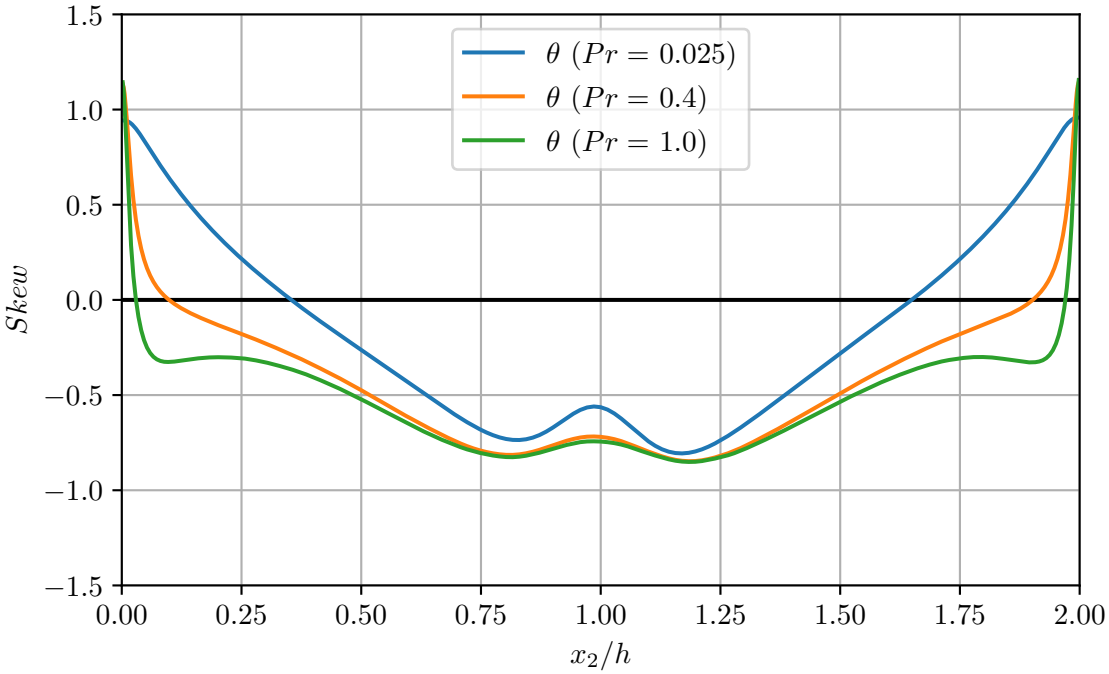

(b) Skewness of passive scalars

Figure B.20.: Skewness distributions in turbulent plane channel flow (case m500)

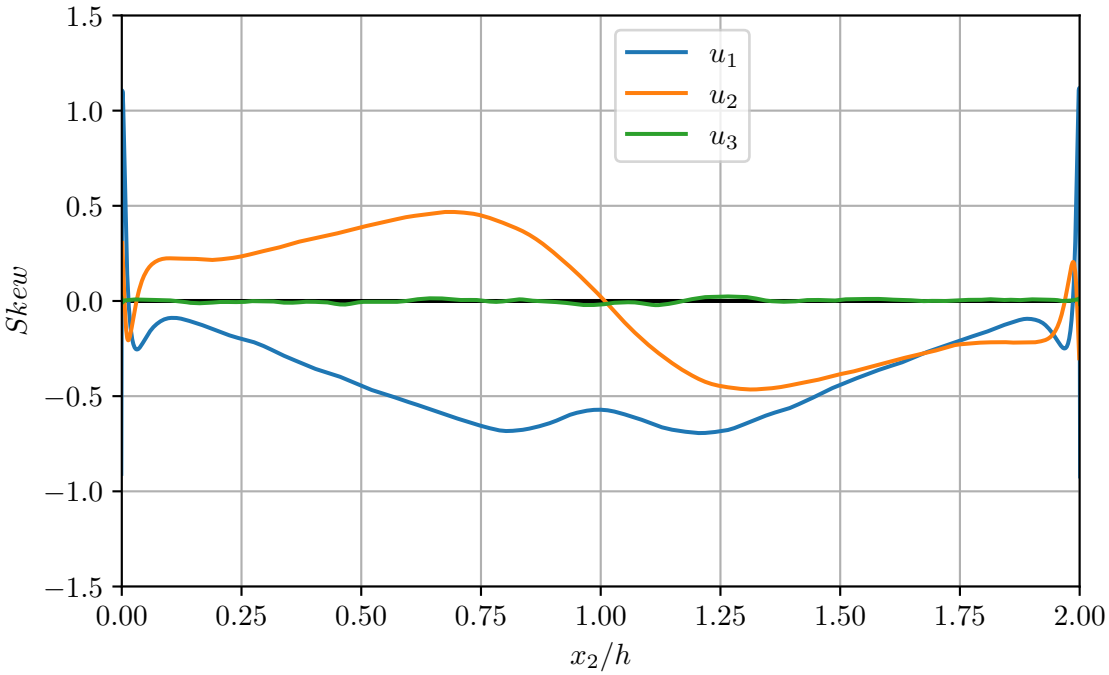

(a) Skewness of velocity components

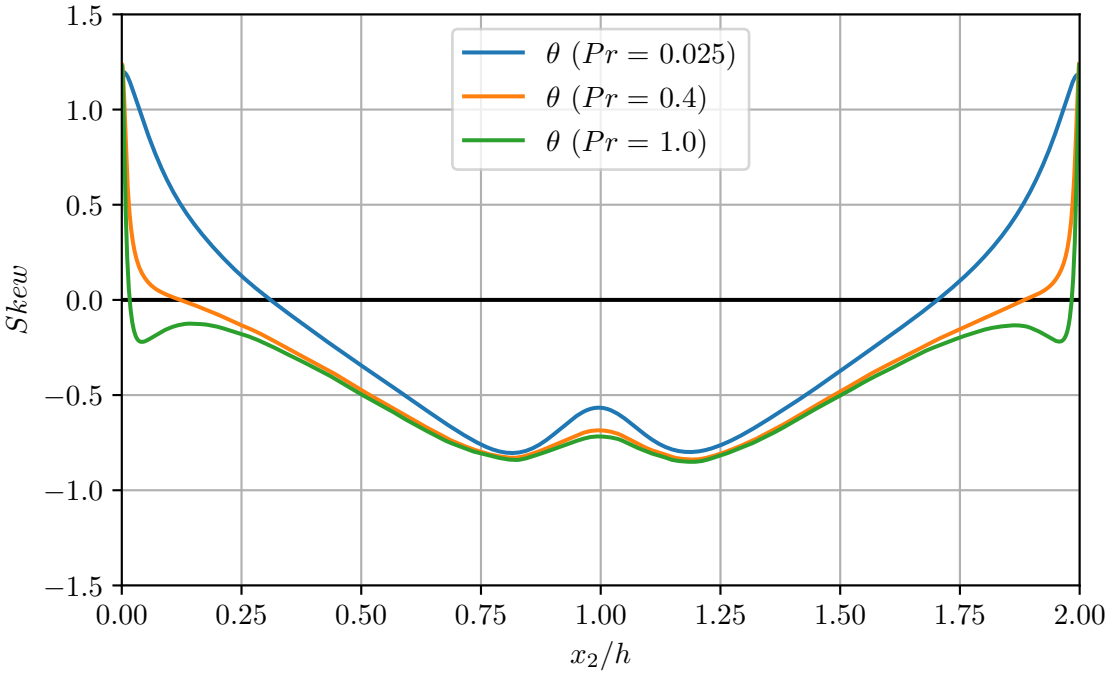

(b) Skewness of passive scalars

Figure B.21.: Skewness distributions in turbulent plane channel flow (case m1000)

B.7. Flatness

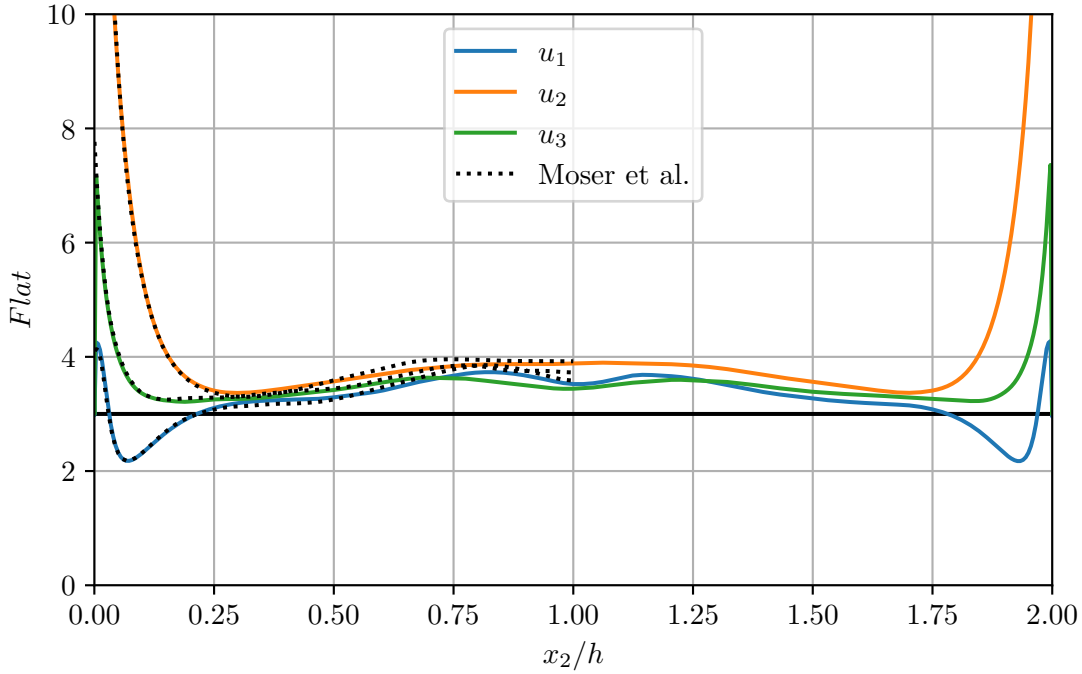

(a) Flatness of velocity components (reference: Moser et al. 1999)

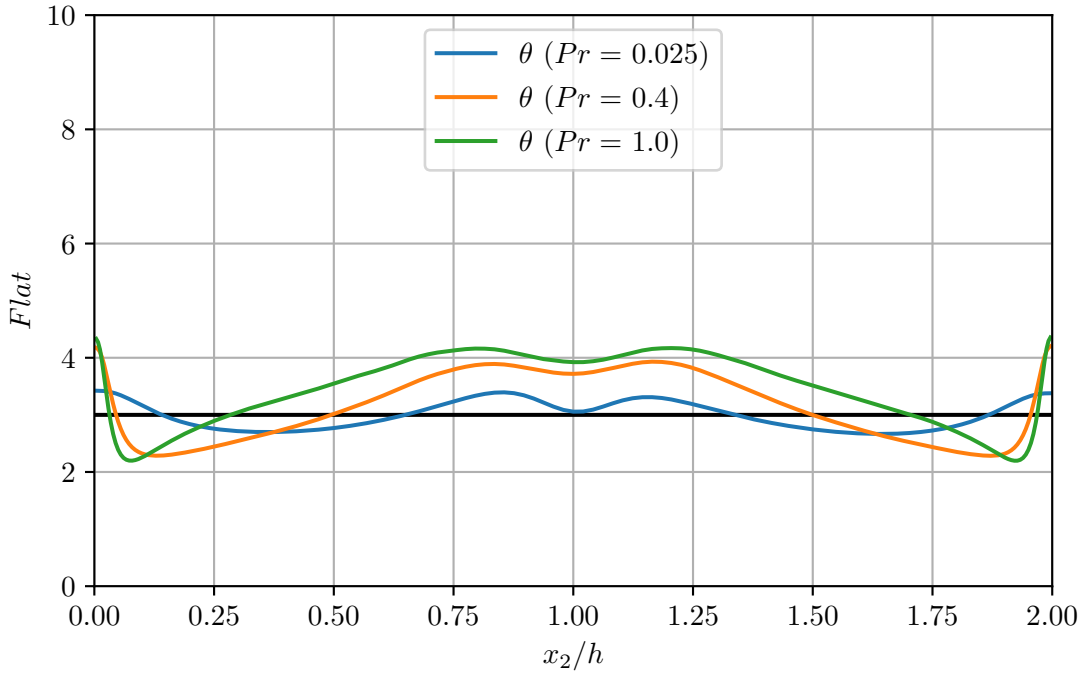

(b) Flatness of passive scalars

Figure B.22.: Flatness distributions in turbulent plane channel flow (case m180)

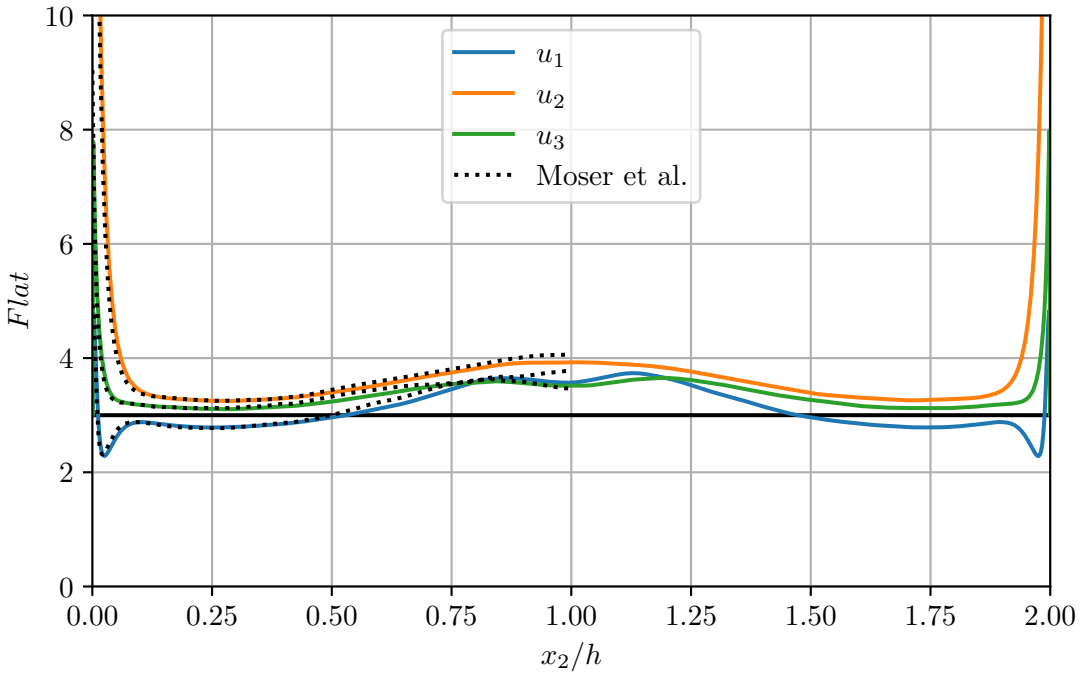

(a) Flatness of velocity components (reference: Moser et al. 1999)

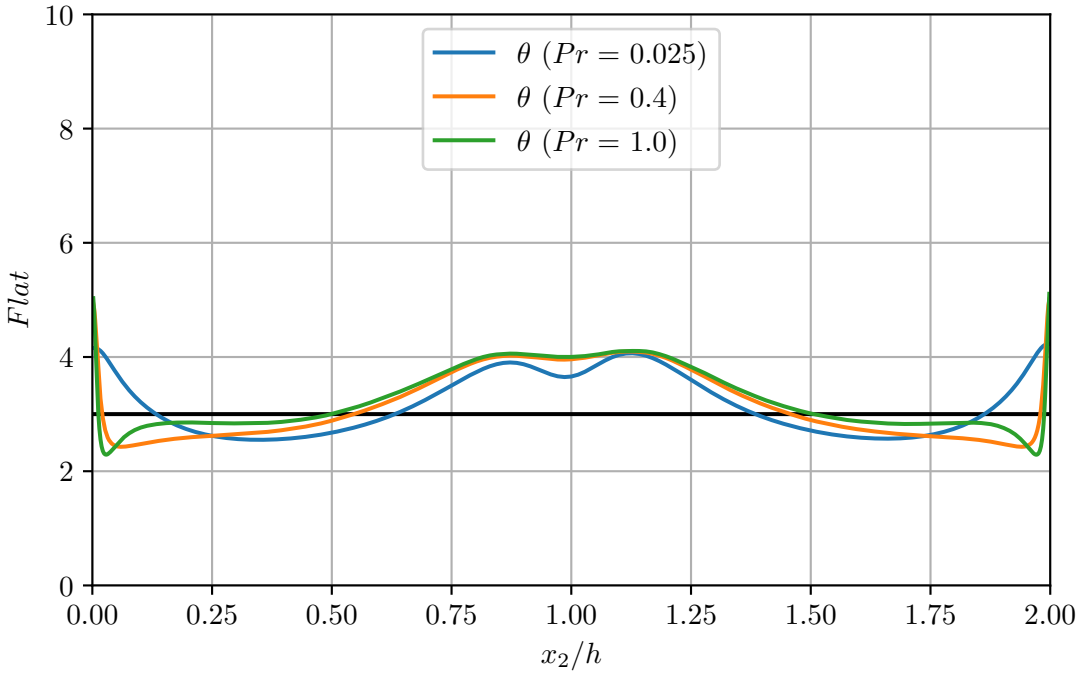

(b) Flatness of passive scalars

Figure B.23.: Flatness distributions in turbulent plane channel flow (case m500)

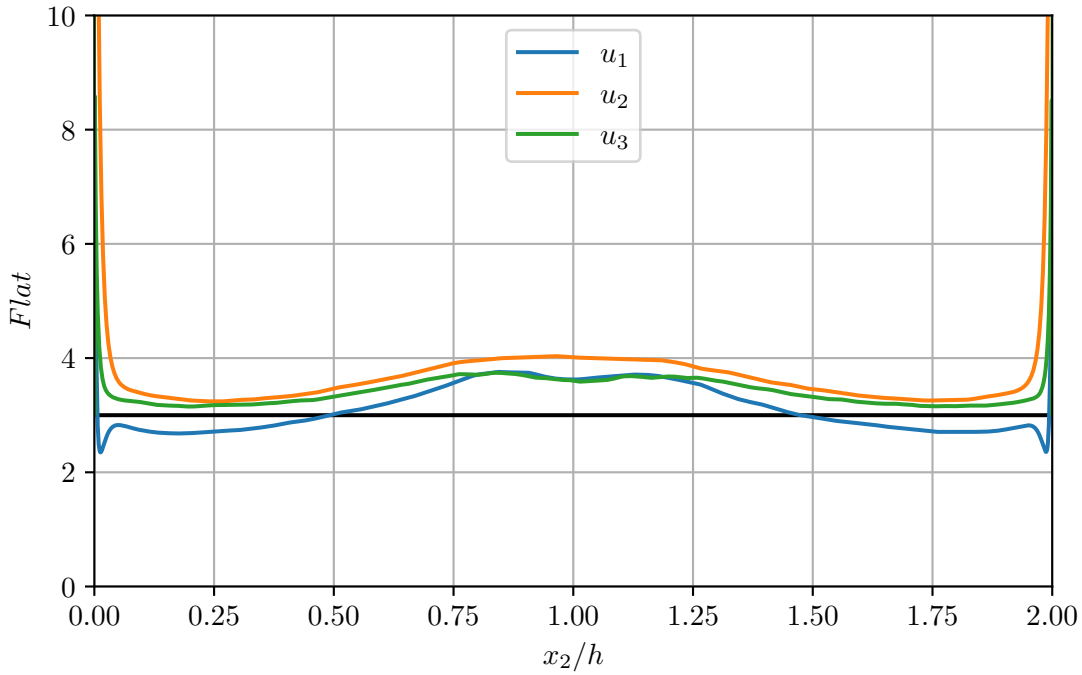

(a) Flatness of velocity components

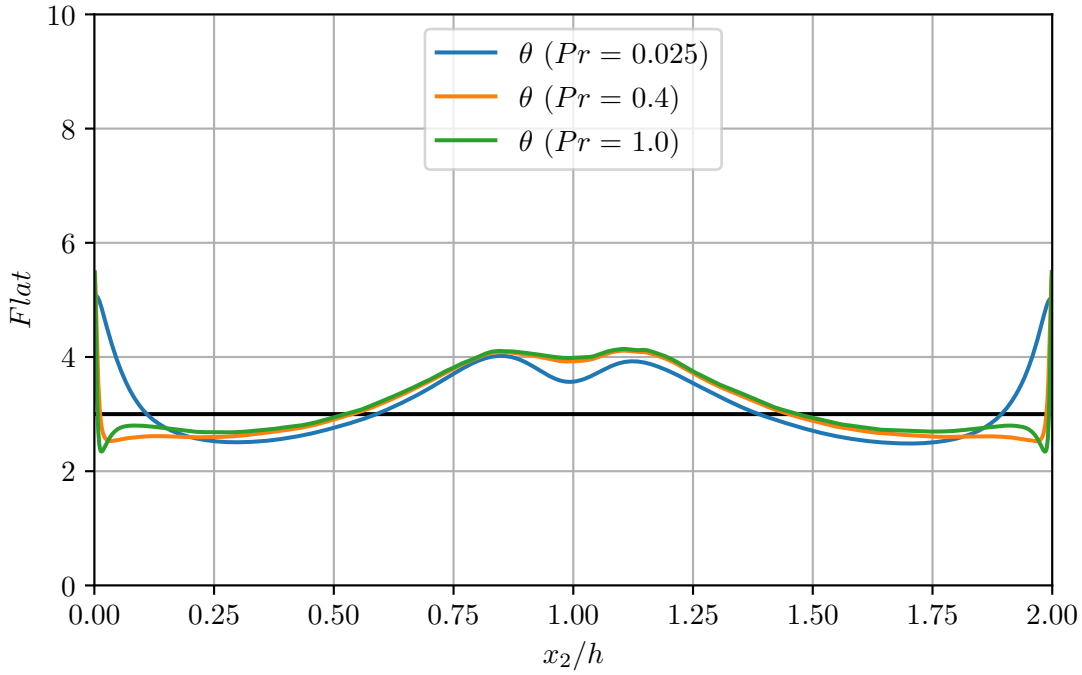

(b) Flatness of passive scalars

Figure B.24.: Flatness distributions in turbulent plane channel flow (case m1000)

B.8. One-dimensional energy spectra

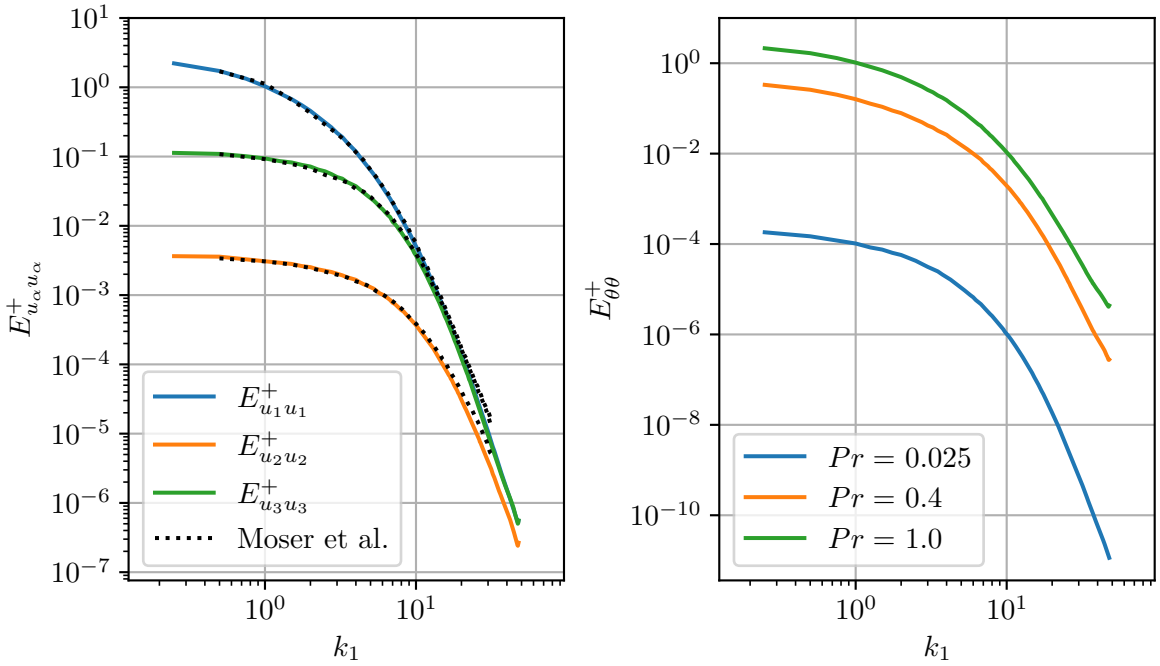

(a) Spectra of velocity components

(b) Spectra of passive scalars

Figure B.25.: Streamwise one-dimensional energy spectra at $x_2^+ \approx 5$ (case m180, velocity reference: Moser et al. 1999)

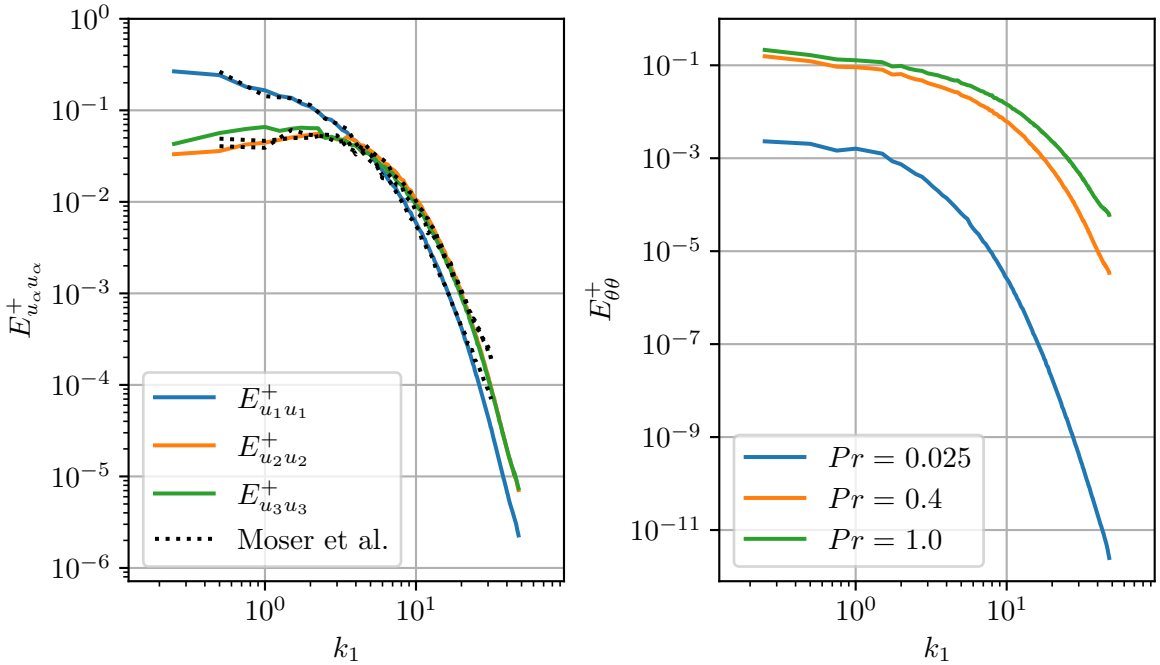

(a) Spectra of velocity components

(b) Spectra of passive scalars

Figure B.26.: Streamwise one-dimensional energy spectra at $x_2^+ \approx 180$ (case m180, velocity reference: Moser et al. 1999)

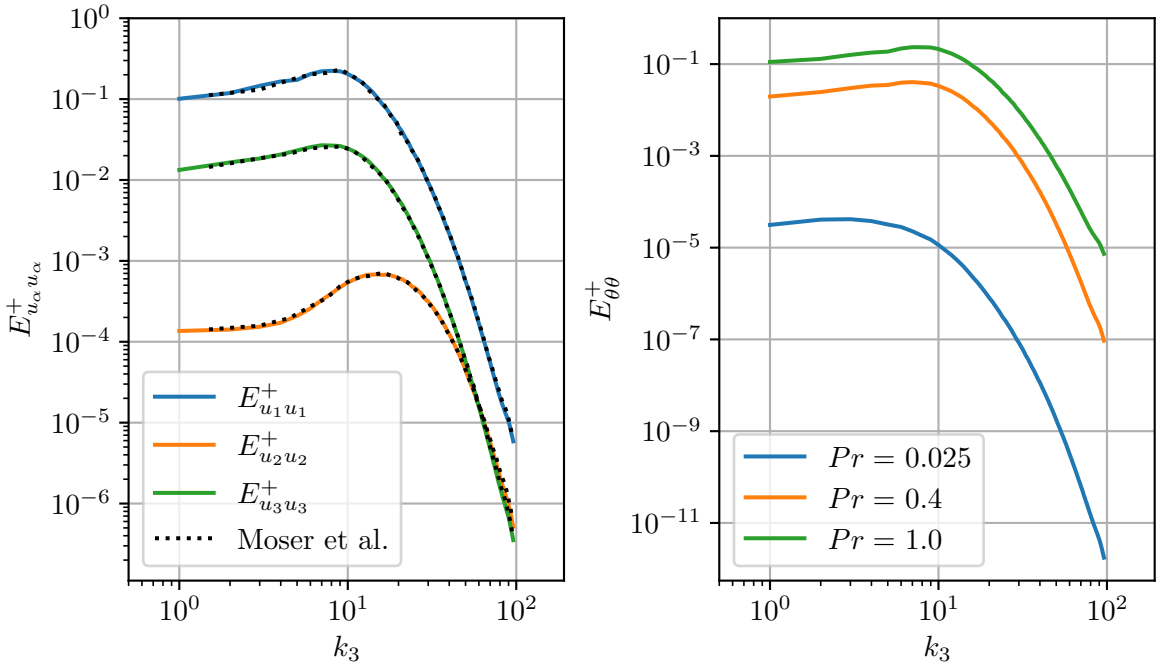

(a) Spectra of velocity components

(b) Spectra of passive scalars

Figure B.27.: Spanwise one-dimensional energy spectra at $x_2^+ \approx 5$ (case m180, velocity reference: Moser et al. 1999)

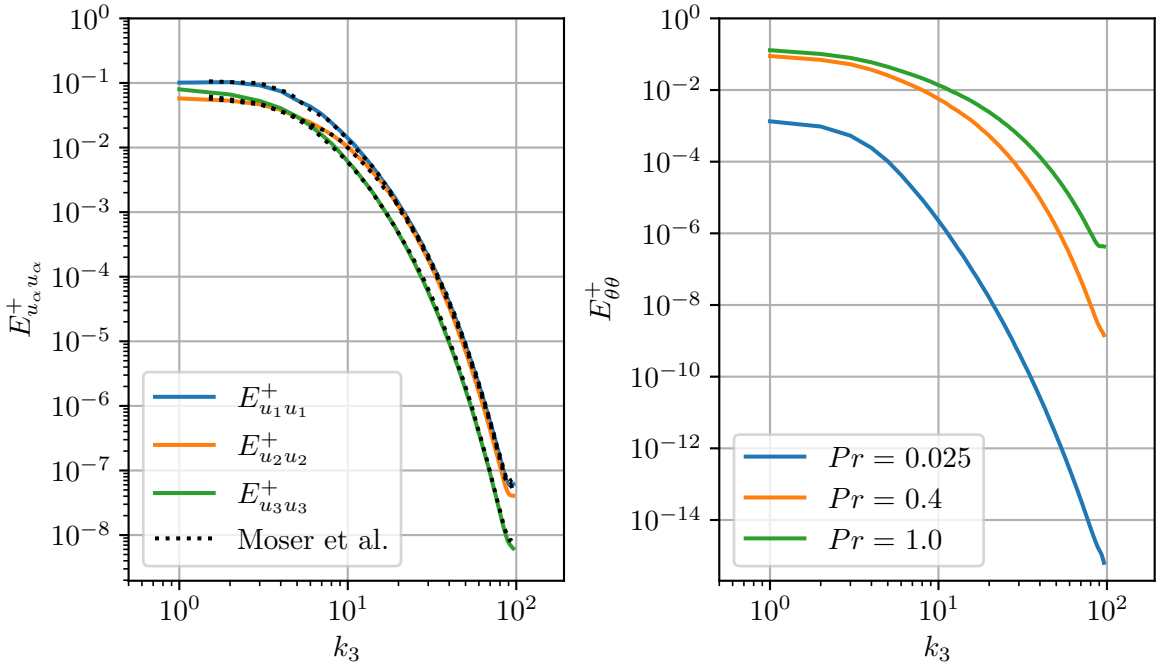

(a) Spectra of velocity components

(b) Spectra of passive scalars

Figure B.28.: Spanwise one-dimensional energy spectra at $x_2^+ \approx 180$ (case m180, velocity reference: Moser et al. 1999)

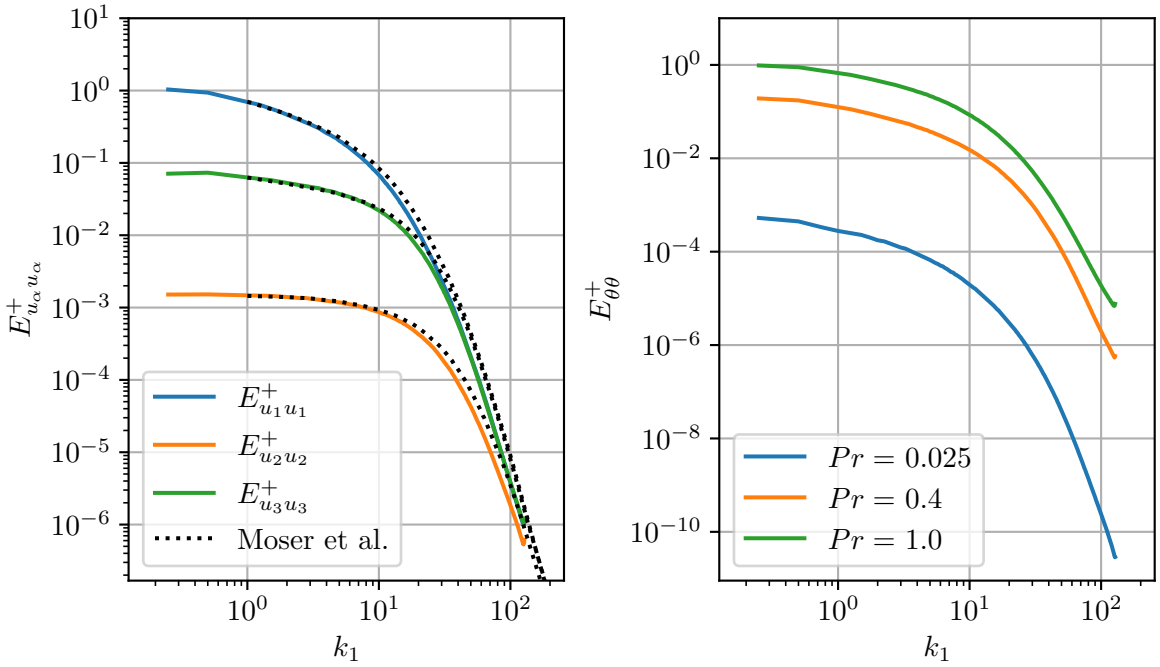

(a) Spectra of velocity components (b) Spectra of passive scalars

Figure B.29.: Streamwise one-dimensional energy spectra at $x_2^+ \approx 5$ (case m500, velocity reference: Moser et al. 1999)

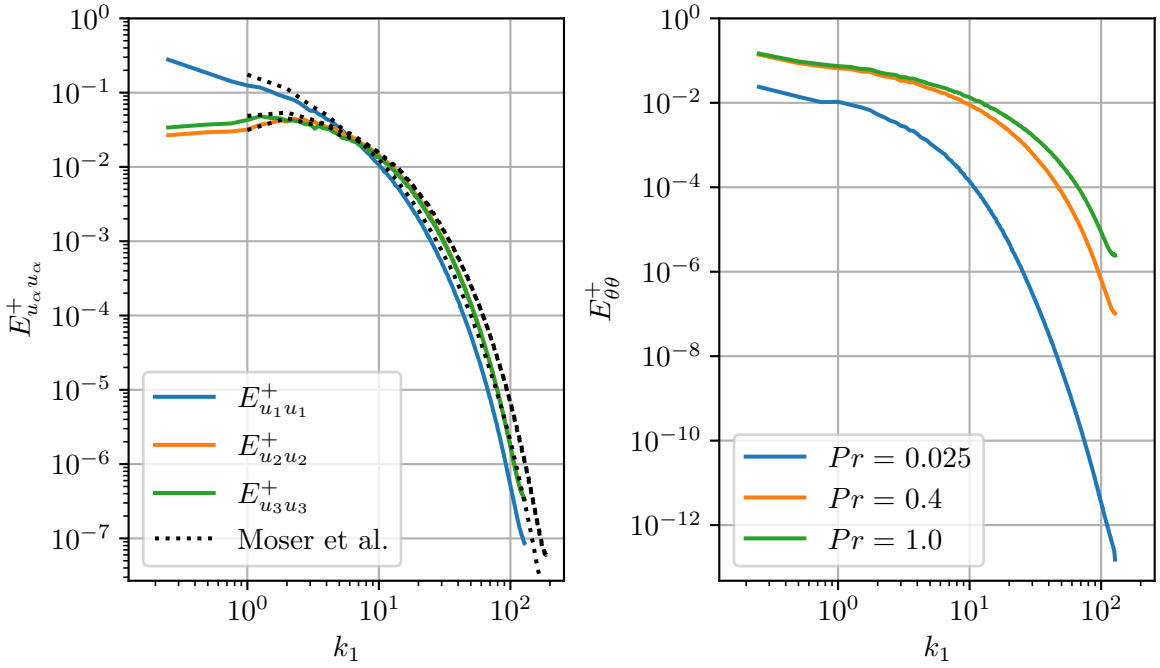

(a) Spectra of velocity components (b) Spectra of passive scalars

Figure B.30.: Streamwise one-dimensional energy spectra at $x_2^+ \approx 500$ (case m500, velocity reference: Moser et al. 1999)

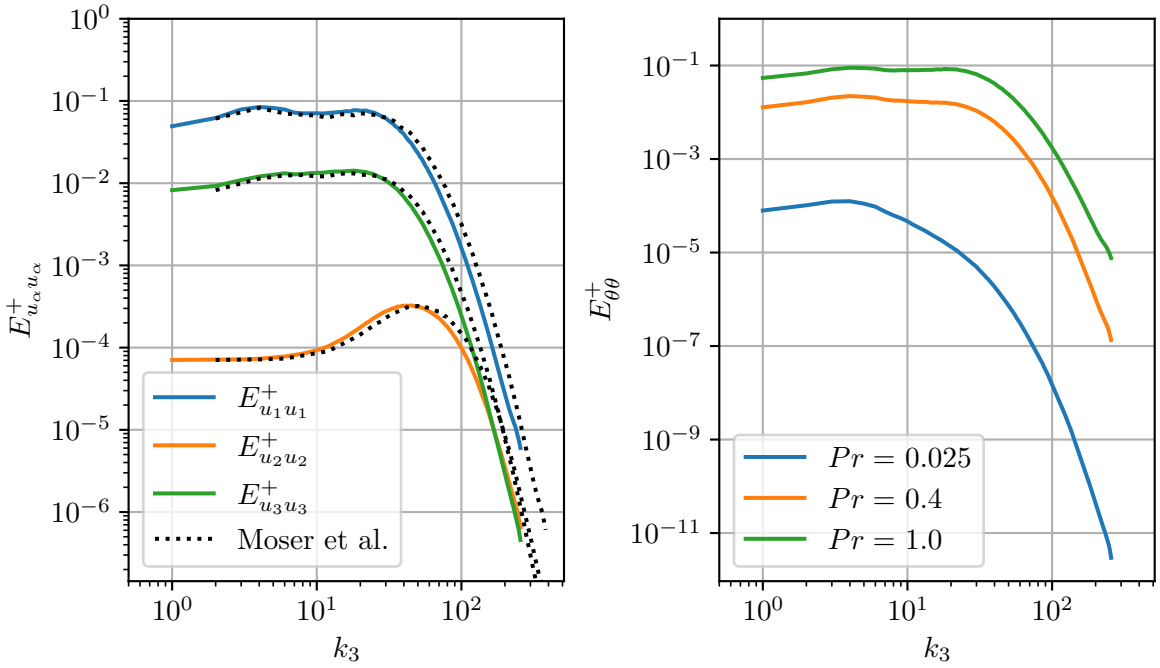

(a) Spectra of velocity components (b) Spectra of passive scalars

Figure B.31.: Spanwise one-dimensional energy spectra at $x_2^+ \approx 5$ (case m500, velocity reference: Moser et al. 1999)

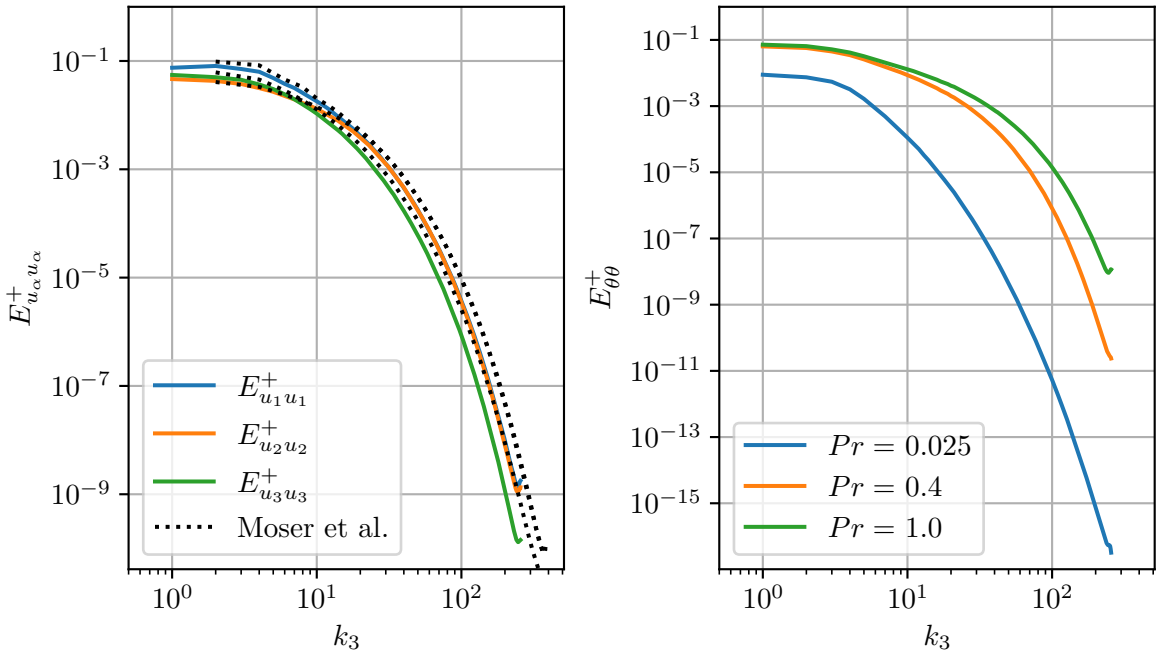

(a) Spectra of velocity components (b) Spectra of passive scalars

Figure B.32.: Spanwise one-dimensional energy spectra at $x_2^+ \approx 500$ (case m500, velocity reference: Moser et al. 1999)

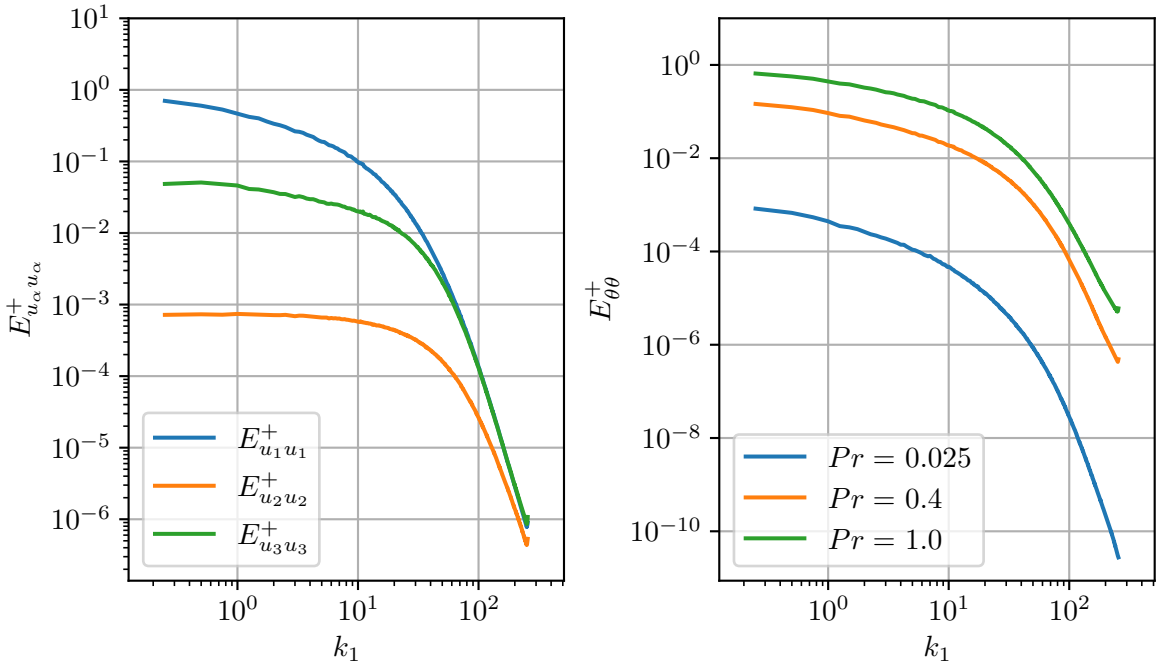

(a) Spectra of velocity components

(b) Spectra of passive scalars

Figure B.33.: Streamwise one-dimensional energy spectra at $x_2^+ \approx 5$ (case m1000)

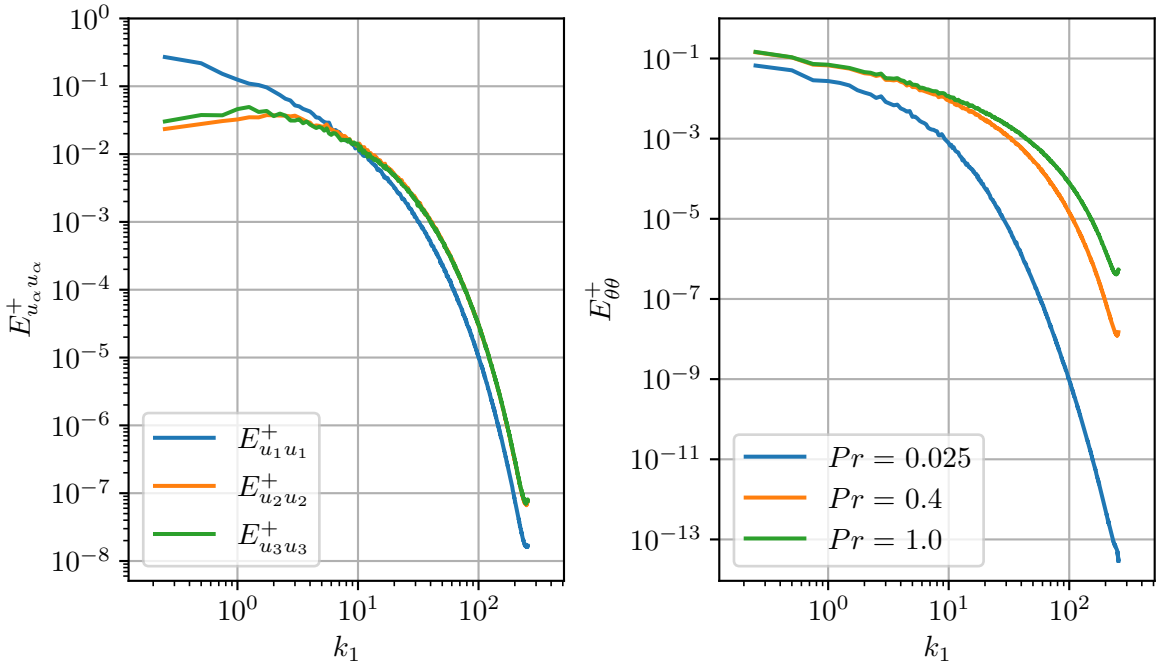

(a) Spectra of velocity components

(b) Spectra of passive scalars

Figure B.34.: Streamwise one-dimensional energy spectra at $x_2^+ \approx 1000$ (case m1000)

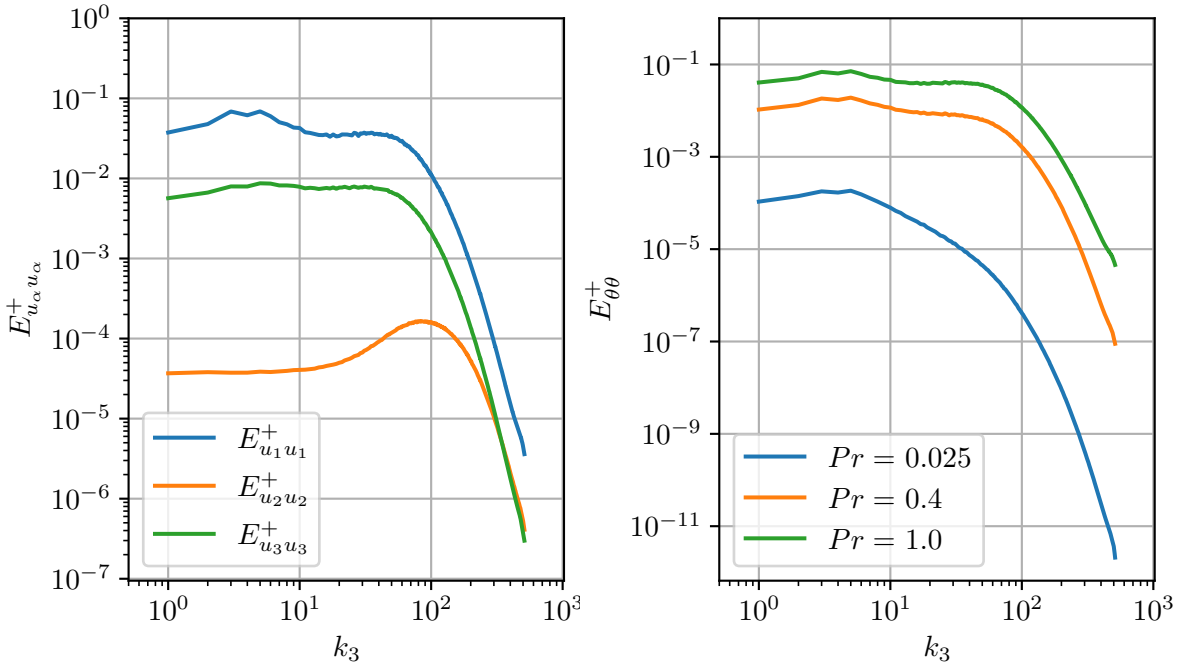

(a) Spectra of velocity components (b) Spectra of passive scalars

Figure B.35.: Spanwise one-dimensional energy spectra at $x_2^+ \approx 5$ (case m1000)

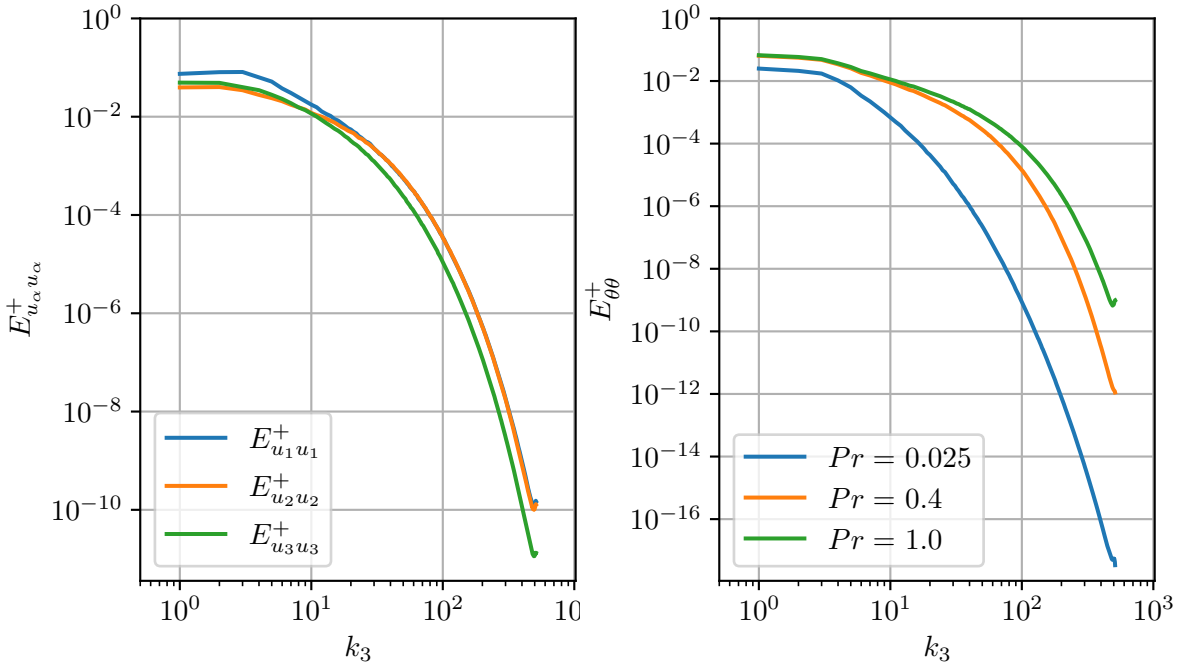

(a) Spectra of velocity components (b) Spectra of passive scalars

Figure B.36.: Spanwise one-dimensional energy spectra at $x_2^+ \approx 1000$ (case m1000)

C. Additional transport equation analyses

C.1. Root-mean-square distributions

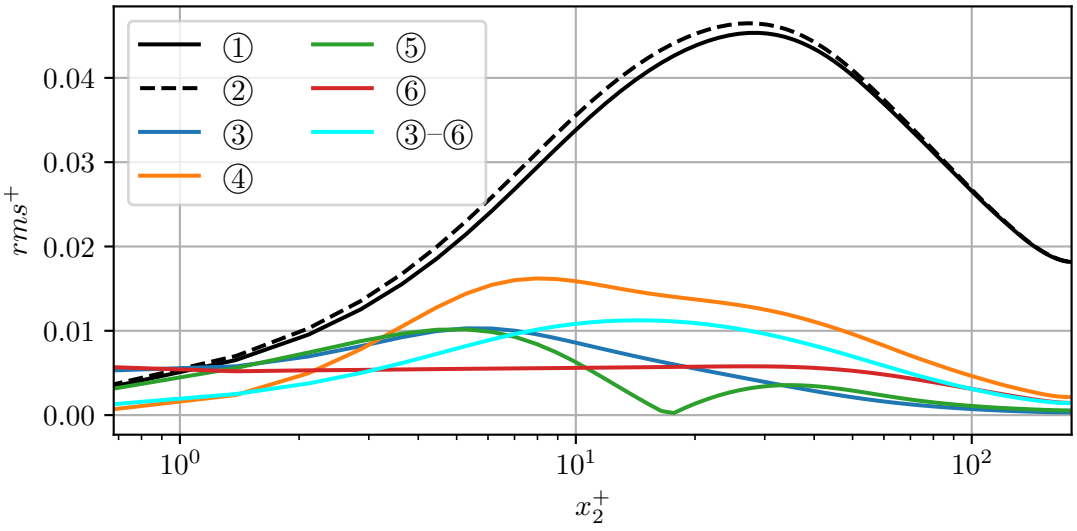

(a) Transport equation analysis of the streamwise velocity component

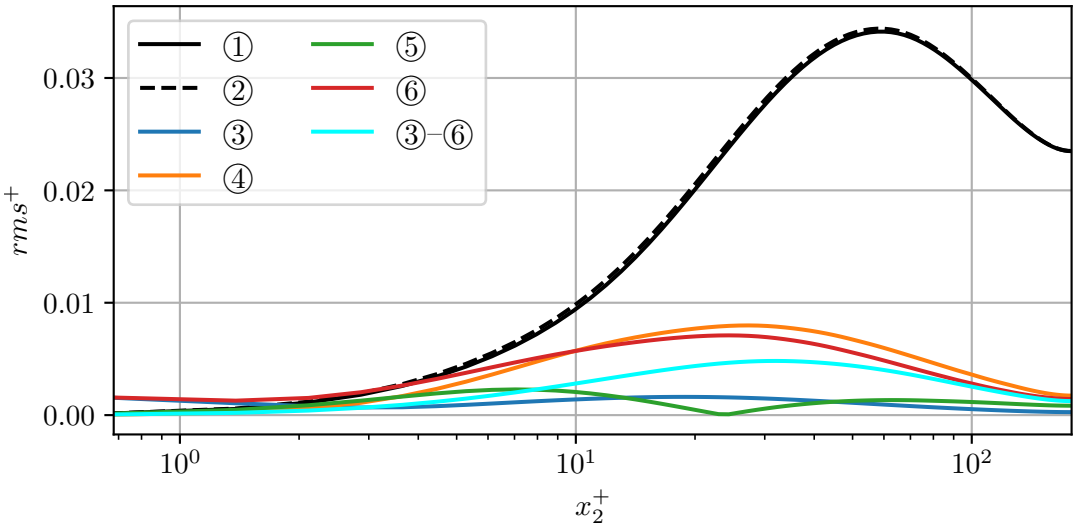

(b) Transport equation analysis of the wall-normal velocity component

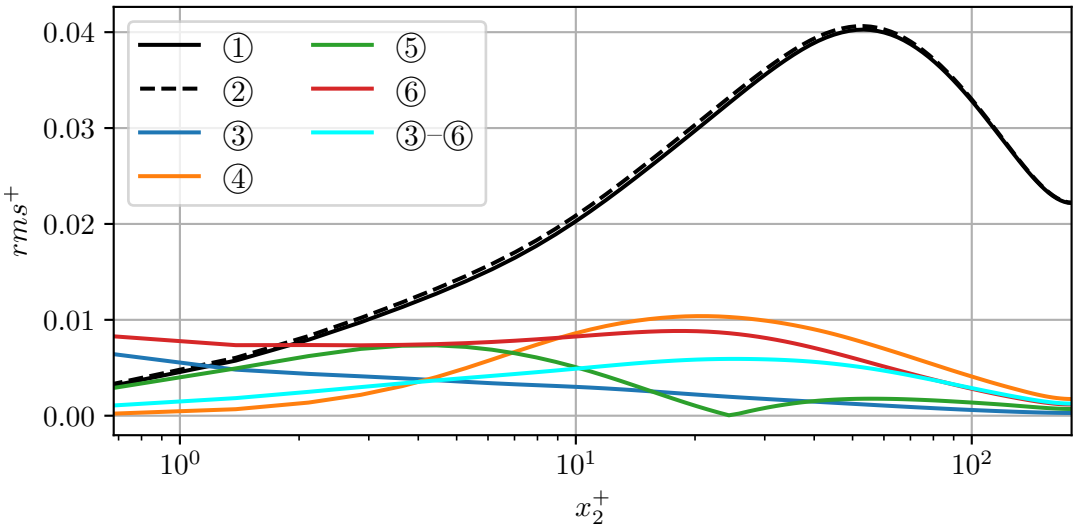

(c) Transport equation analysis of the spanwise velocity component

Figure C.37.: Transport equation analysis *rms* of the velocity field (case m180)

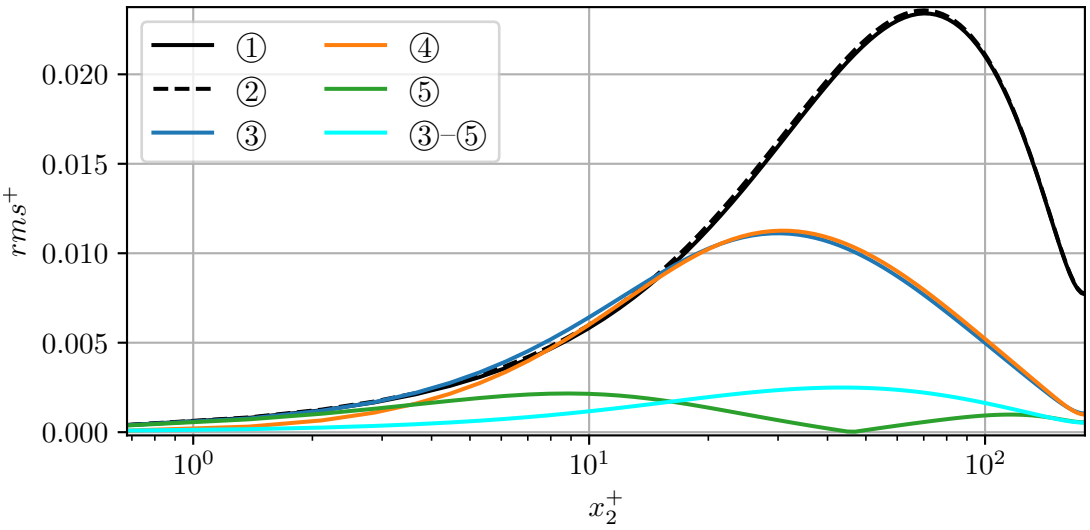

(a) Scalar transport equation analysis with $Pr = 0.025$

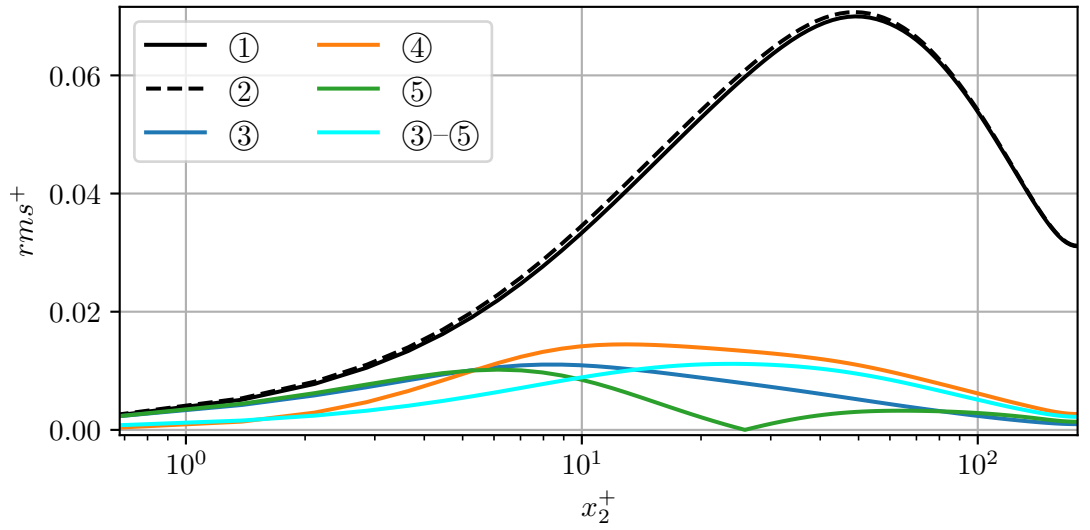

(b) Scalar transport equation analysis with $Pr = 0.4$

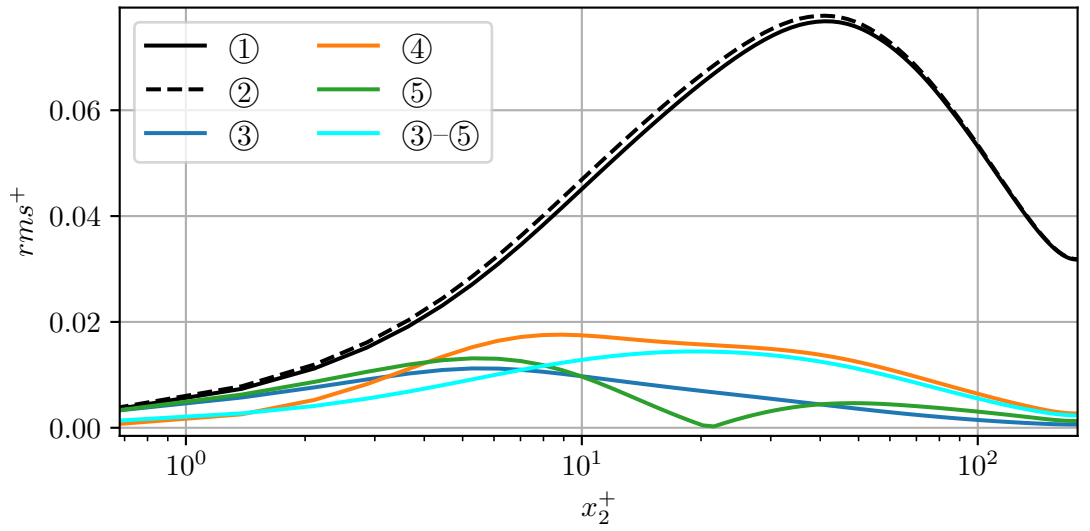

(c) Scalar transport equation analysis with $Pr = 1$

Figure C.38.: Transport equation analysis *rms* of passive scalars (case m180)

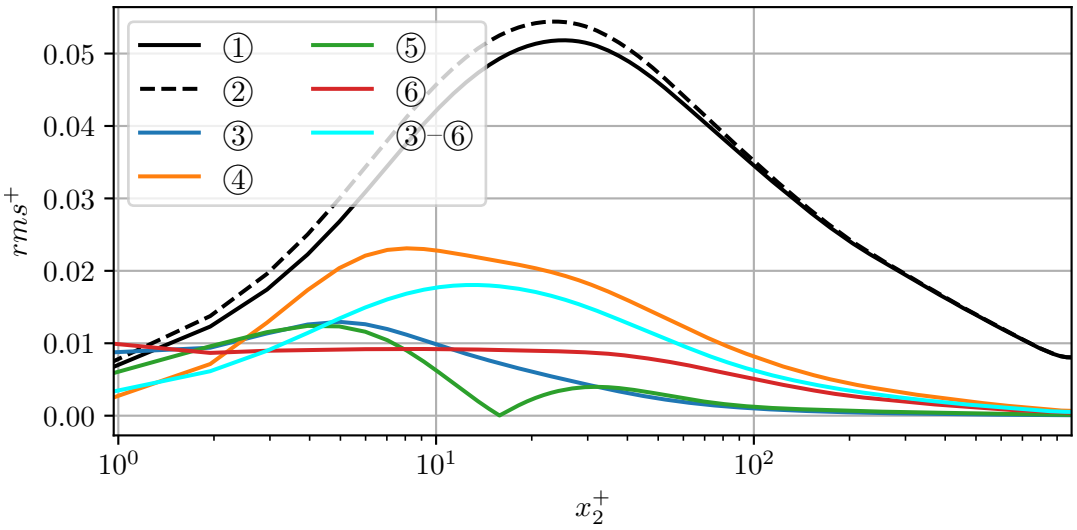

(a) Transport equation analysis of the streamwise velocity component

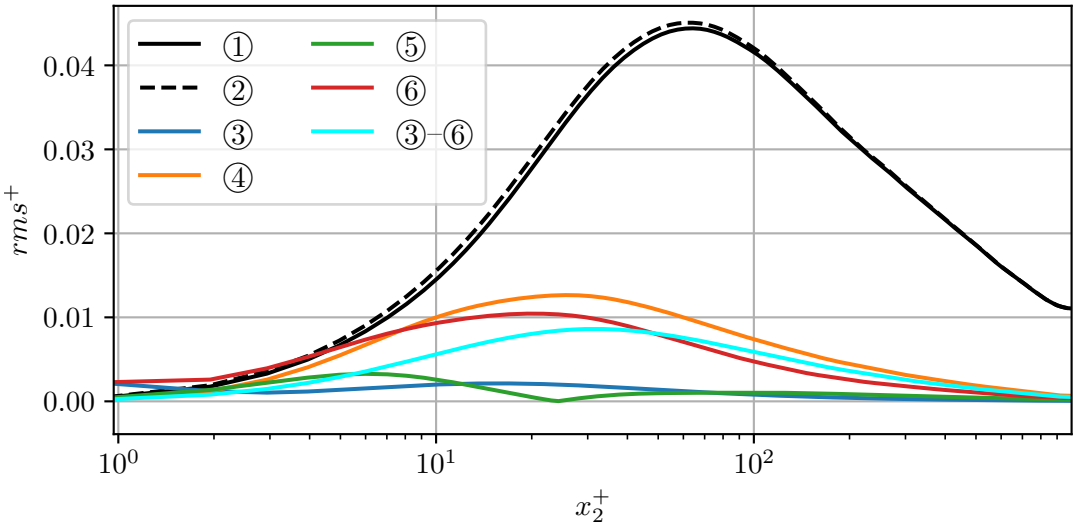

(b) Transport equation analysis of the wall-normal velocity component

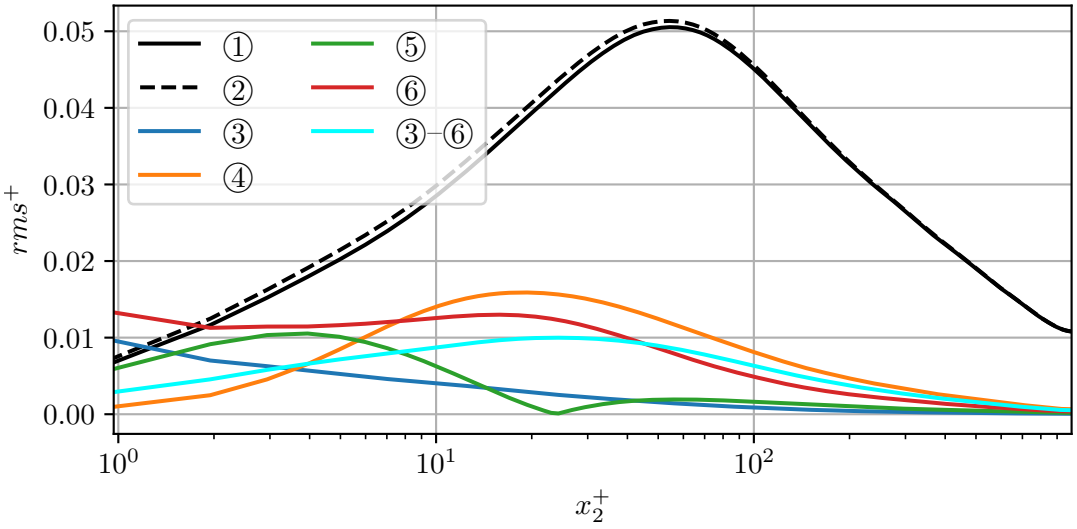

(c) Transport equation analysis of the spanwise velocity component

Figure C.39.: Transport equation analysis rms of the velocity field (case m1000)

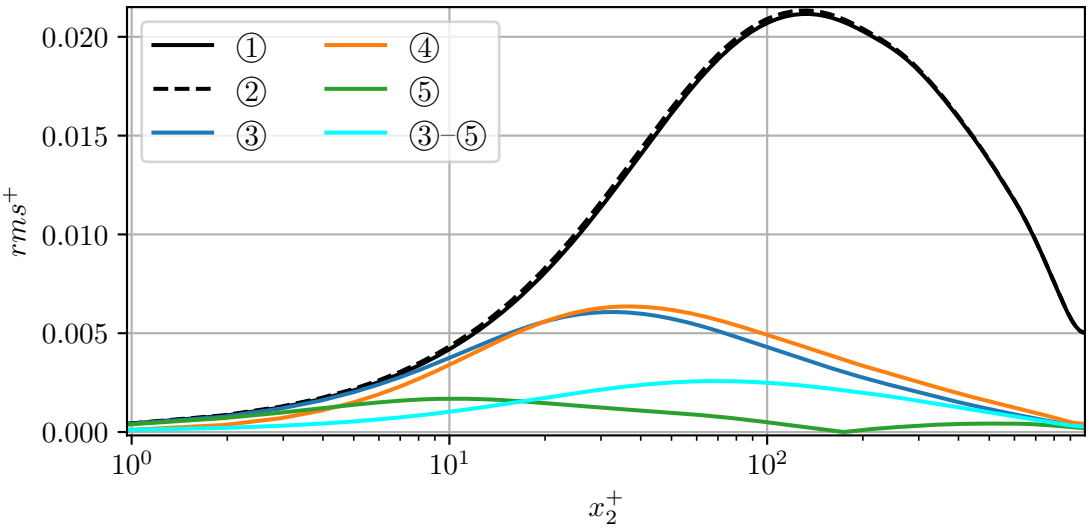

(a) Scalar transport equation analysis with $Pr = 0.025$

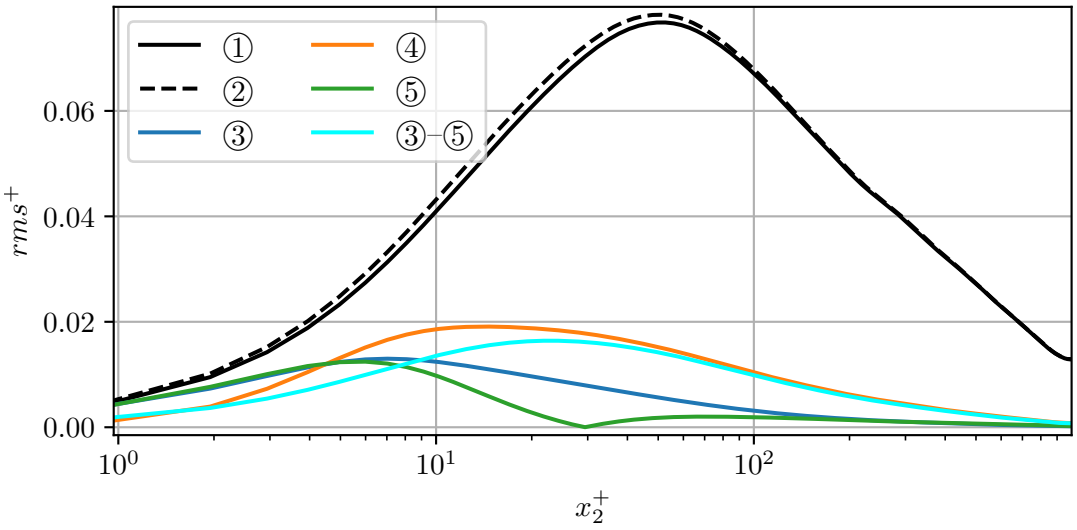

(b) Scalar transport equation analysis with $Pr = 0.4$

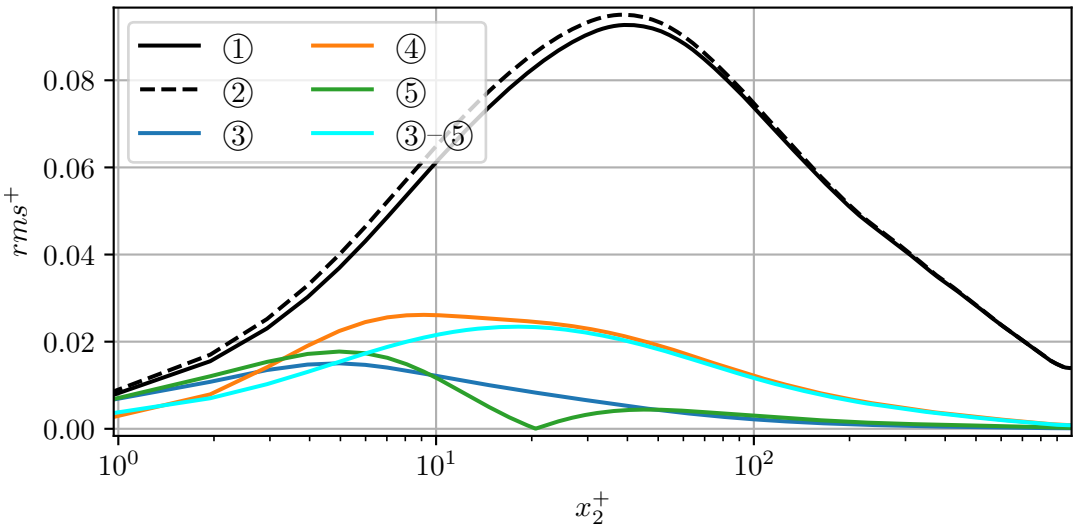

(c) Scalar transport equation analysis with $Pr = 1$

Figure C.40.: Transport equation analysis *rms* of passive scalars (case m1000)

C.2. Normalised root-mean-square distributions

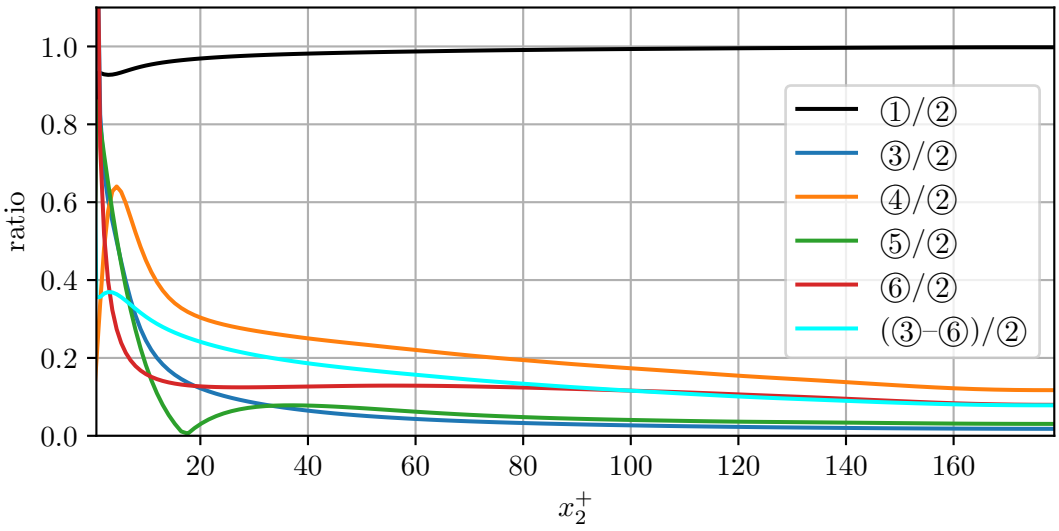

(a) Normalised transport equation analysis of the streamwise velocity component

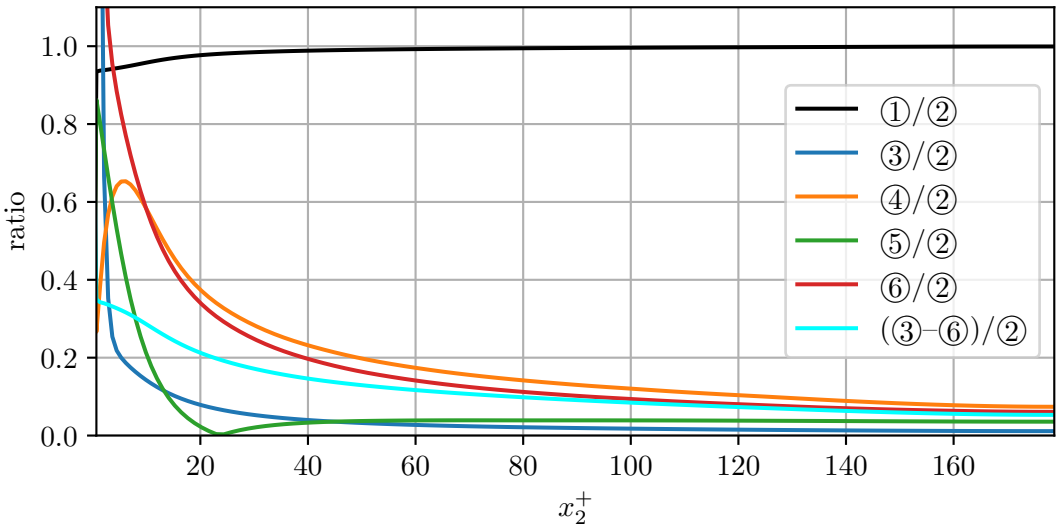

(b) Normalised transport equation analysis of the wall-normal velocity component

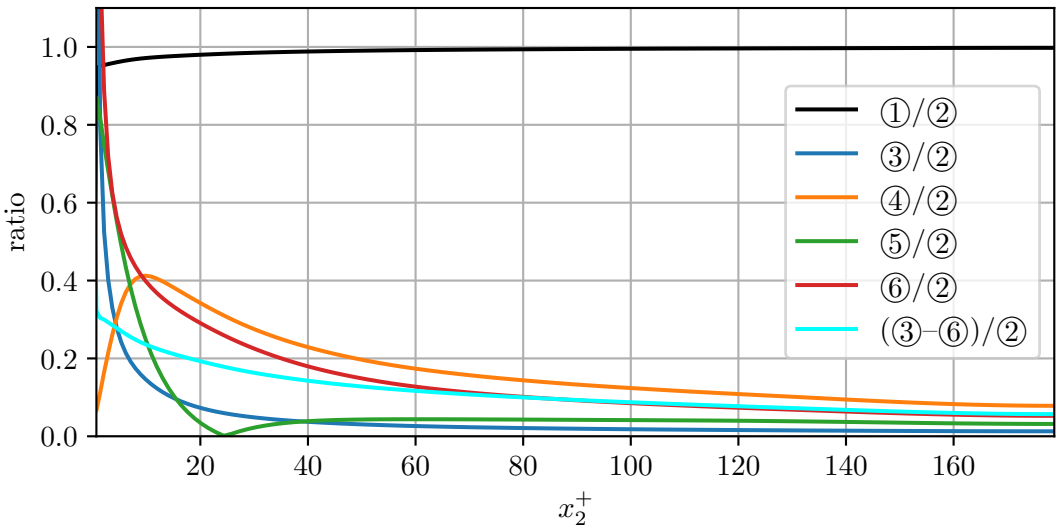

(c) Normalised transport equation analysis of the spanwise velocity component

Figure C.41.: Normalised transport equation analysis *rms* of the velocity field (case m180)

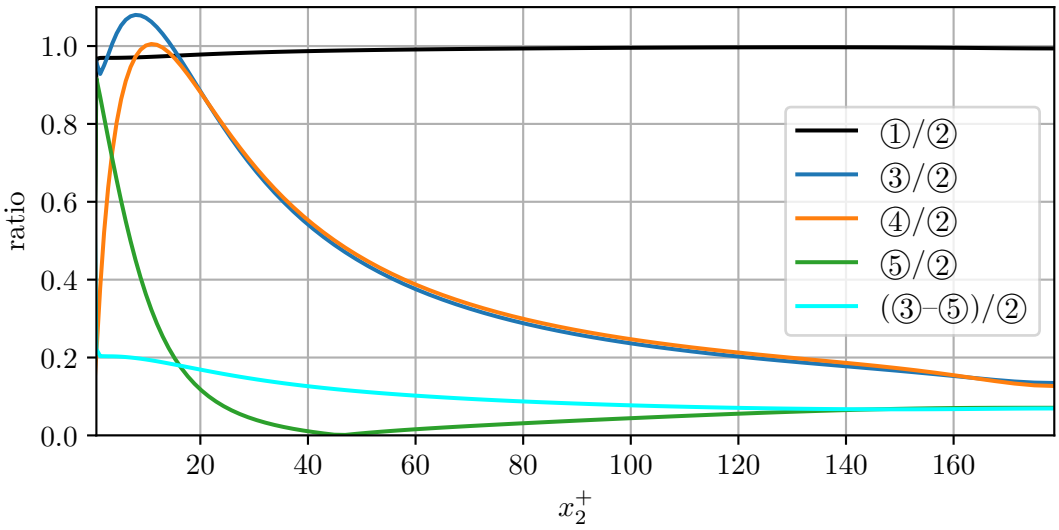

(a) Normalised scalar transport equation analysis with $Pr = 0.025$

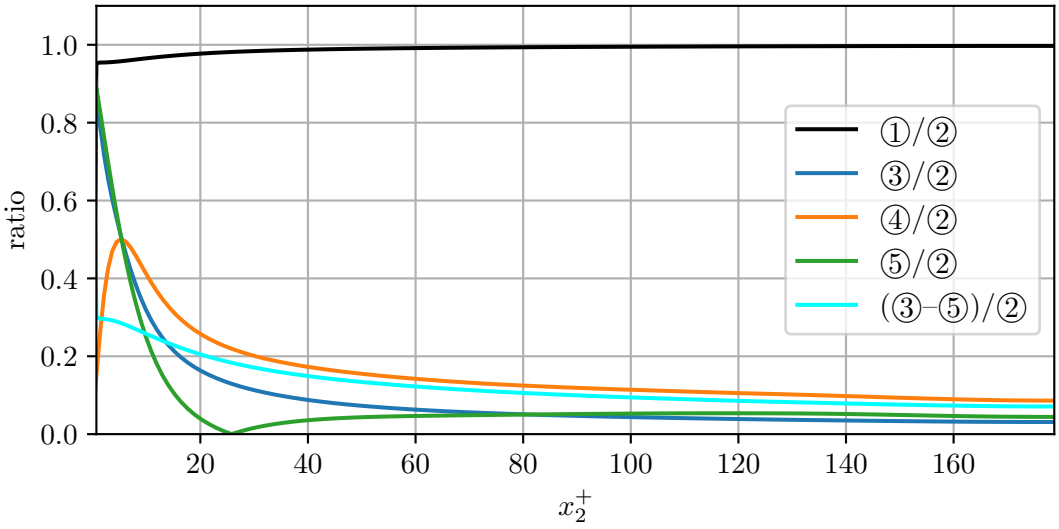

(b) Normalised scalar transport equation analysis with $Pr = 0.4$

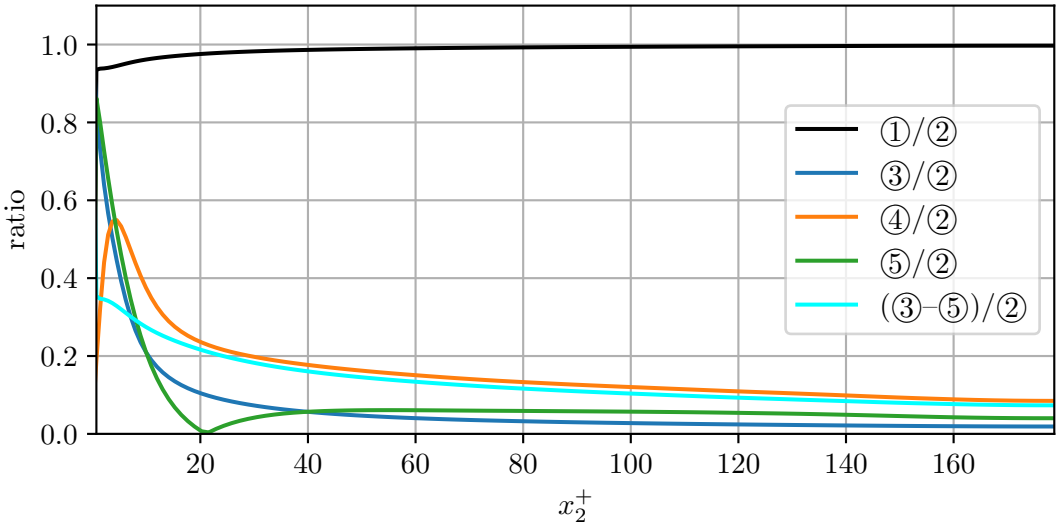

(c) Normalised scalar transport equation analysis with $Pr = 1$

Figure C.42.: Normalised transport equation analysis *rms* of passive scalars (case m180)

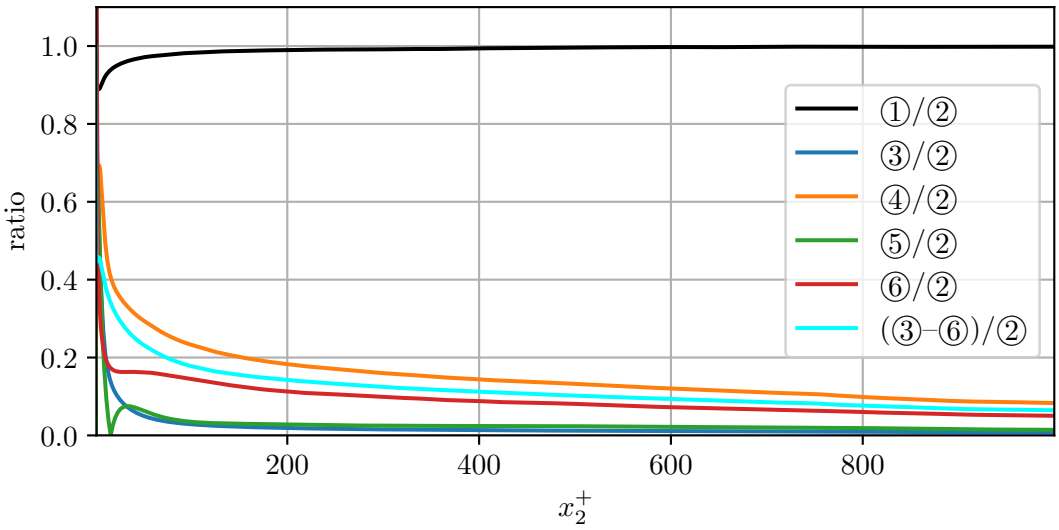

(a) Normalised transport equation analysis of the streamwise velocity component

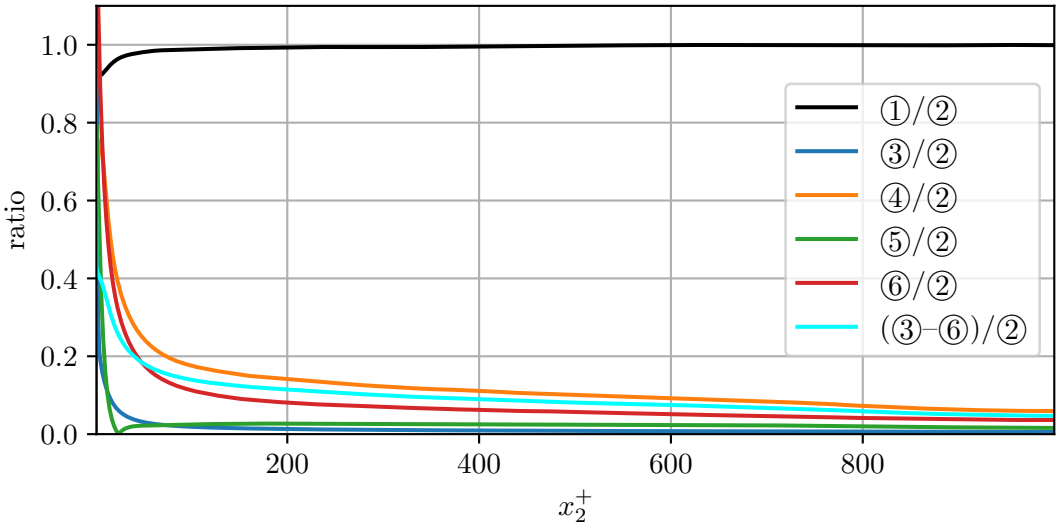

(b) Normalised transport equation analysis of the wall-normal velocity component

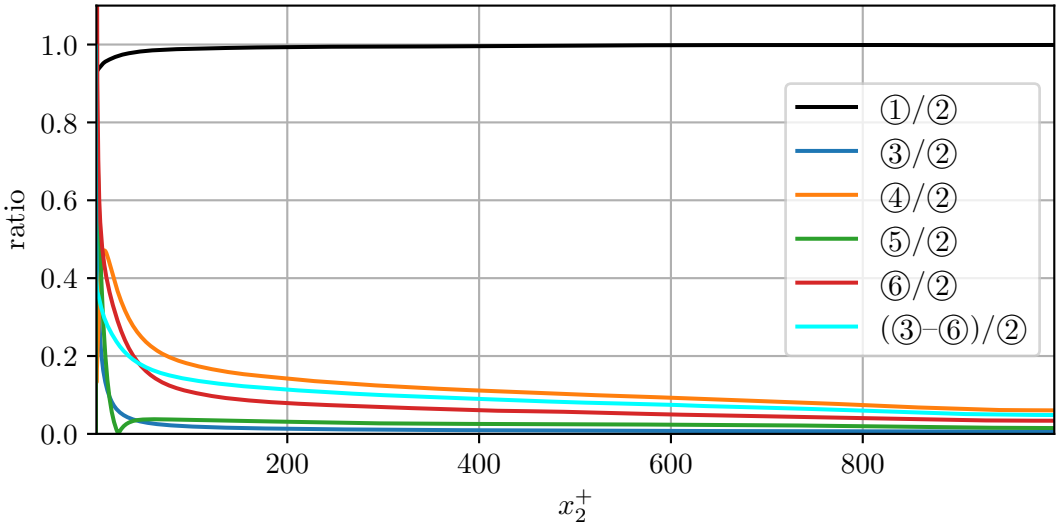

(c) Normalised transport equation analysis of the spanwise velocity component

Figure C.43.: Normalised transport equation analysis *rms* of the velocity field (case m1000)

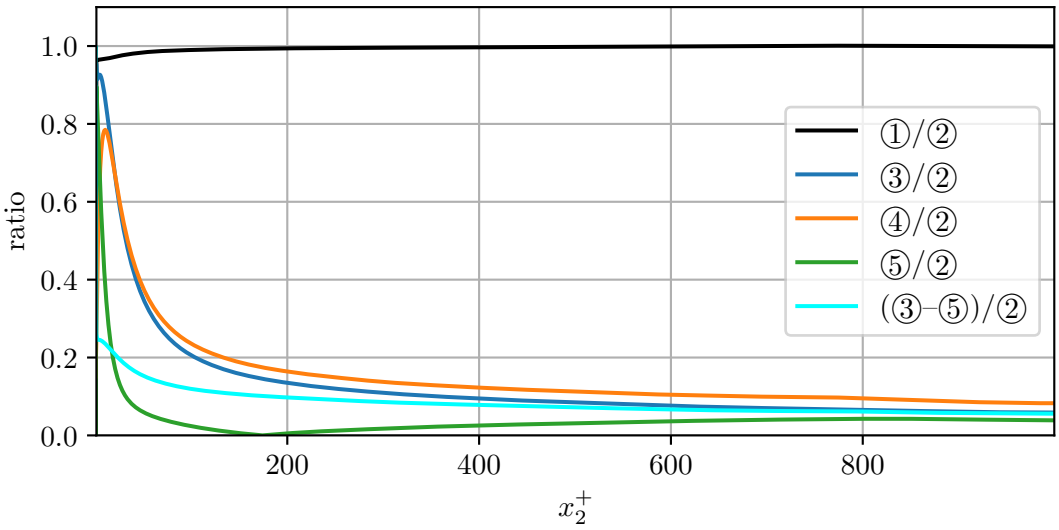

(a) Normalised scalar transport equation analysis with $Pr = 0.025$

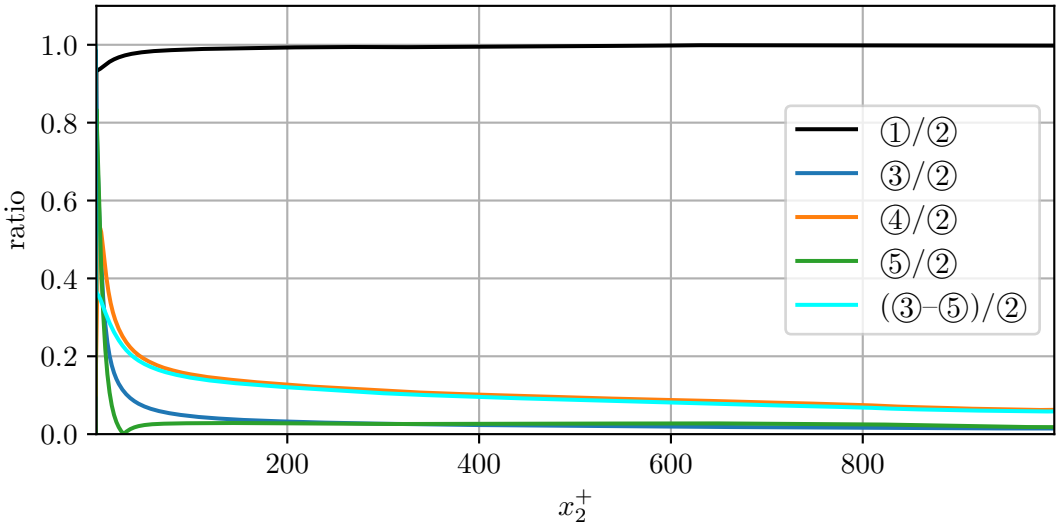

(b) Normalised scalar transport equation analysis with $Pr = 0.4$

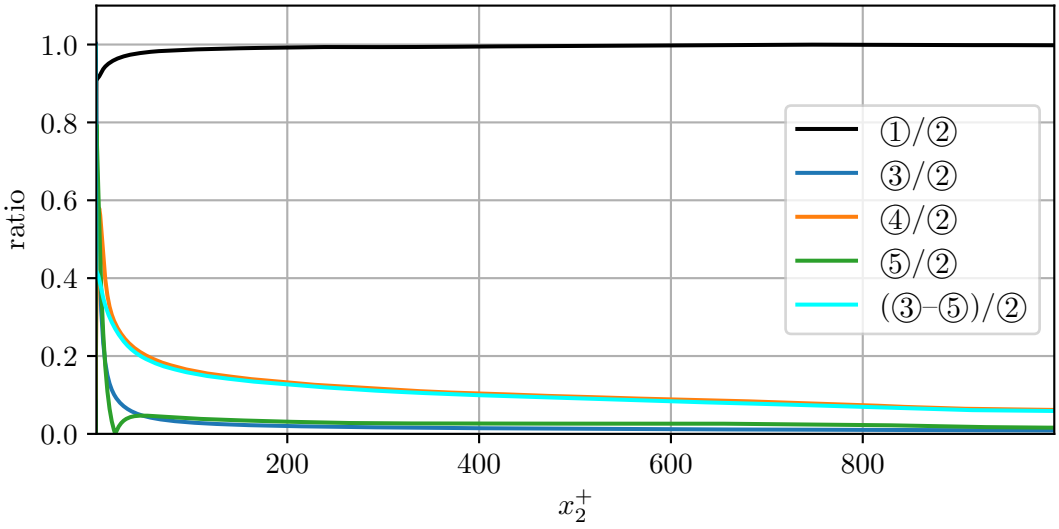

(c) Normalised scalar transport equation analysis with $Pr = 1$

Figure C.44.: Normalised transport equation analysis rms of passive scalars (case m1000)

D. Additional convection velocity statistics

D.1. Wall distance symmetry

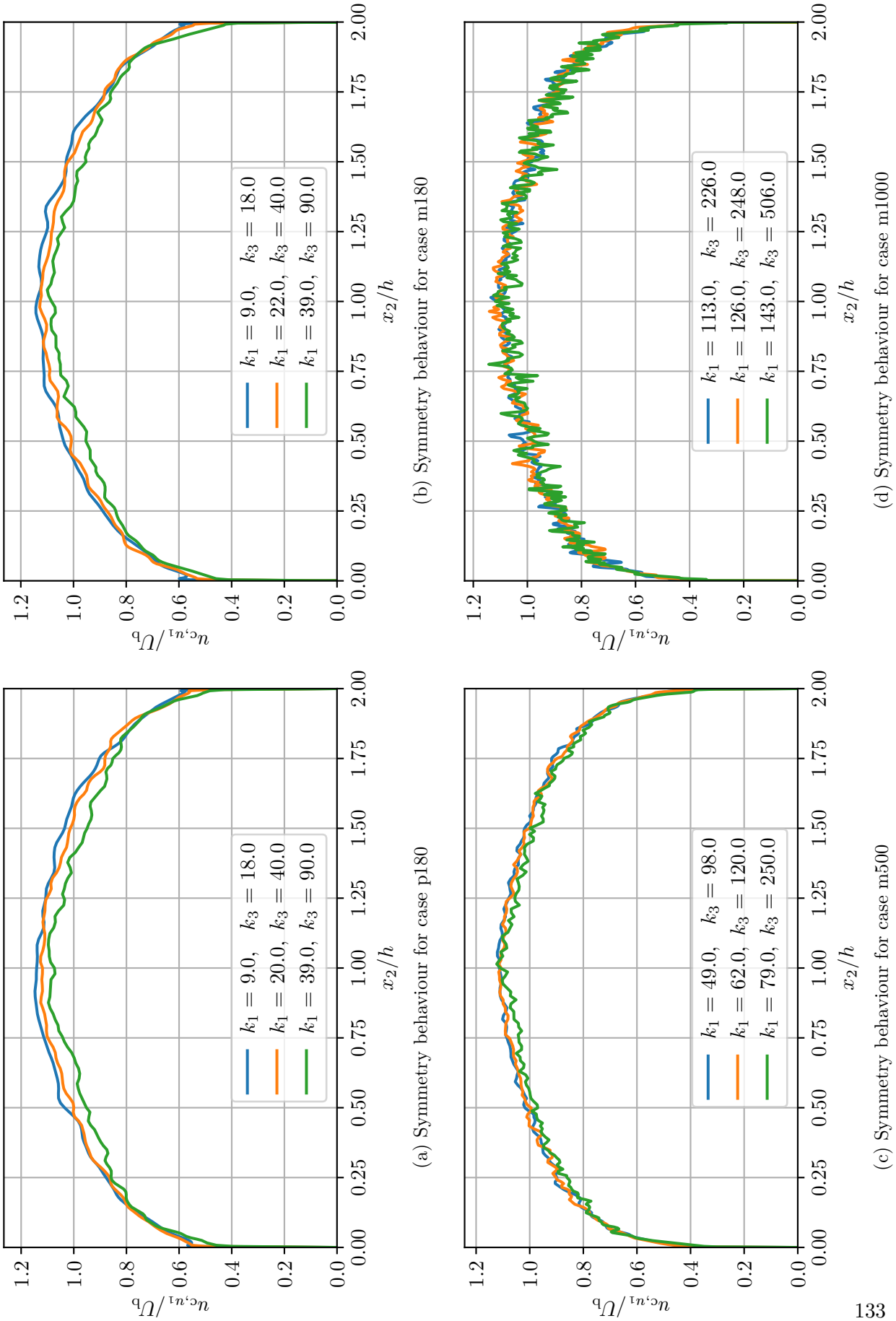

(a) Symmetry behaviour for case p180

(b) Symmetry behaviour for case m180

(c) Symmetry behaviour for case m500

(d) Symmetry behaviour for case m1000

Figure D.45.: u_{c,u_1} symmetry behaviour with respect to wall distance

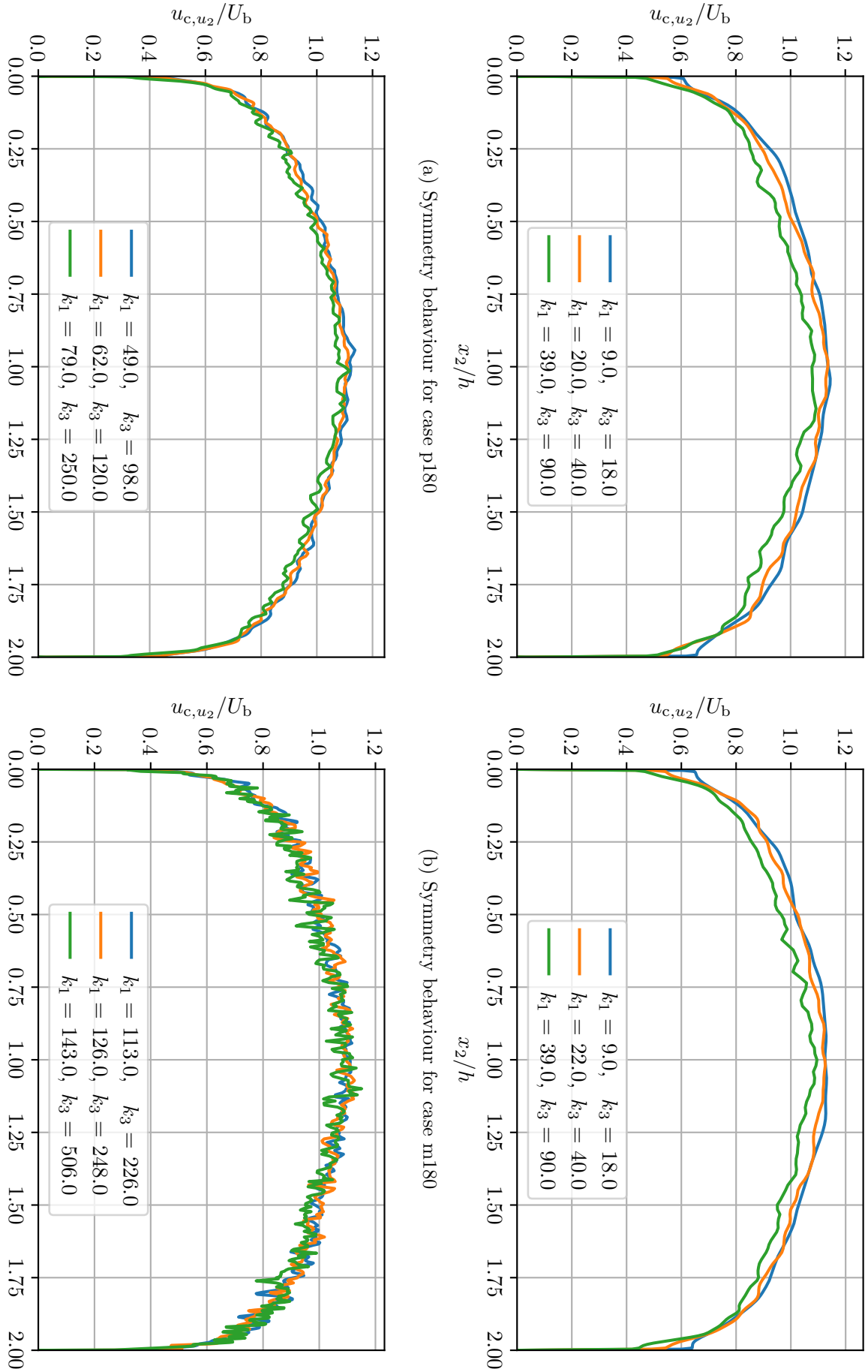

(a) Symmetry behaviour for case p180

(b) Symmetry behaviour for case m180

(c) Symmetry behaviour for case m500

(d) Symmetry behaviour for case m1000

Figure D.46.: u_{c,u_2} symmetry behaviour with respect to wall distance

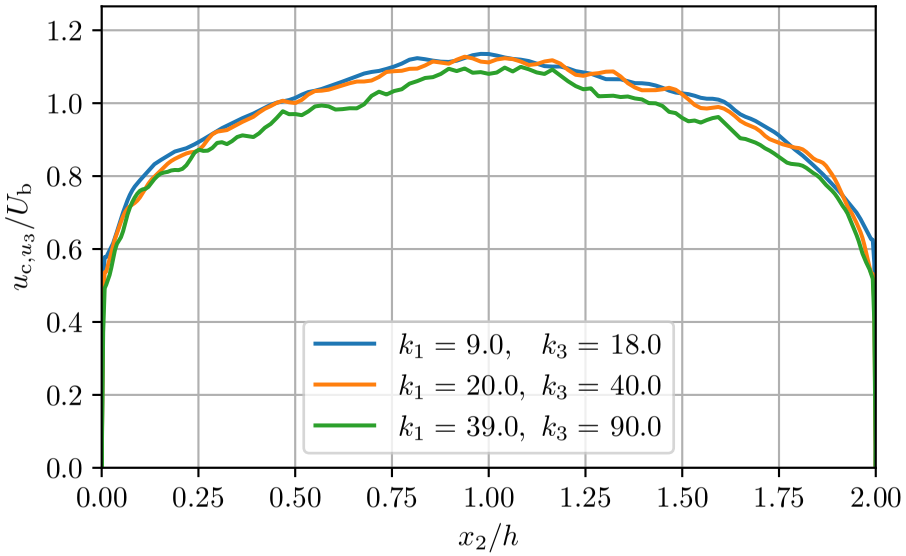

(a) Symmetry behaviour for case p180

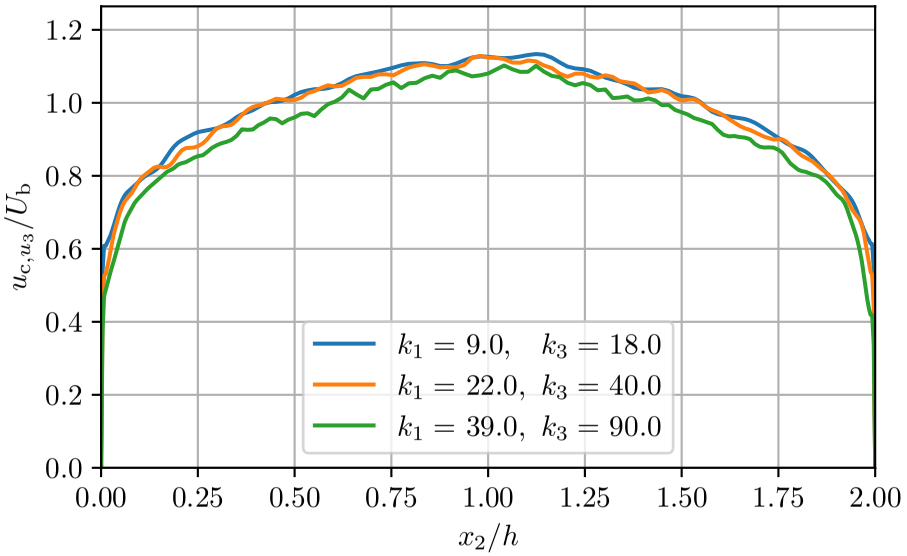

(b) Symmetry behaviour for case m180

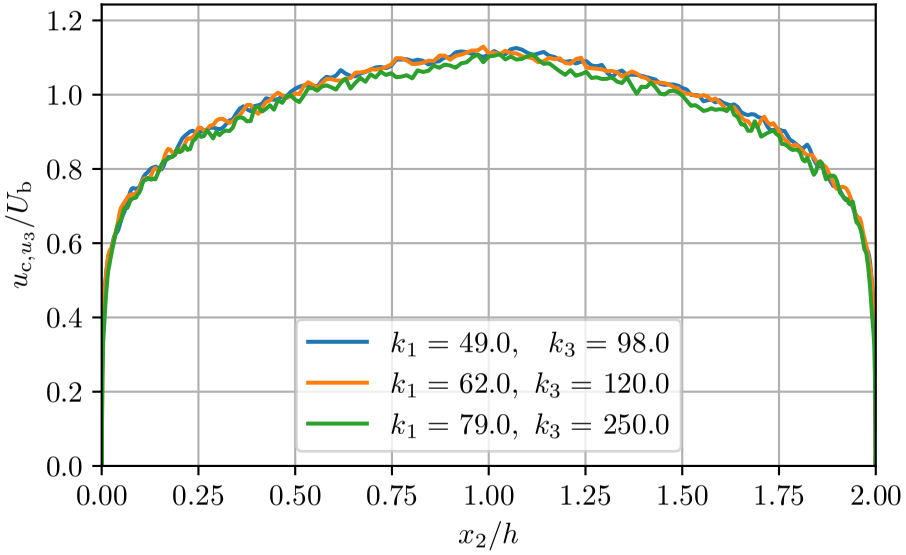

(c) Symmetry behaviour for case m500

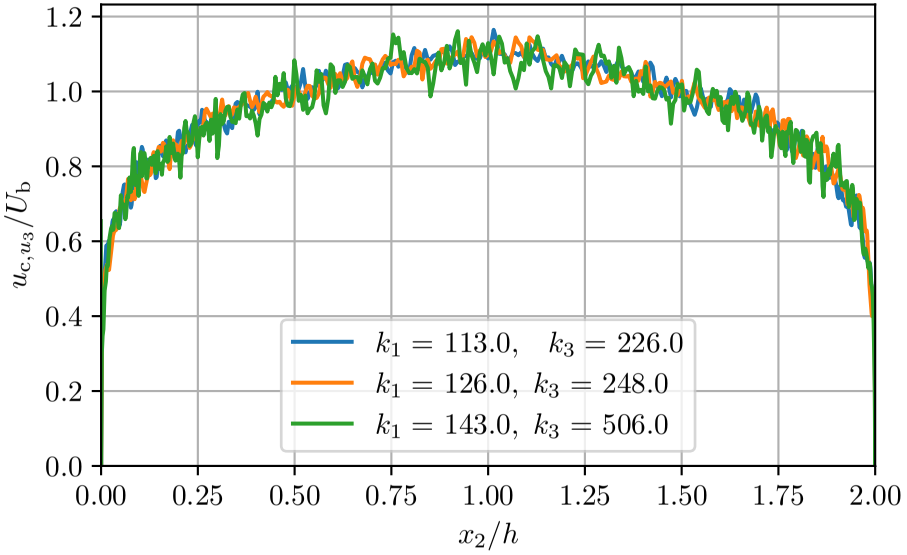

(d) Symmetry behaviour for case m1000

Figure D.47.: u_{c,u_3} symmetry behaviour with respect to wall distance

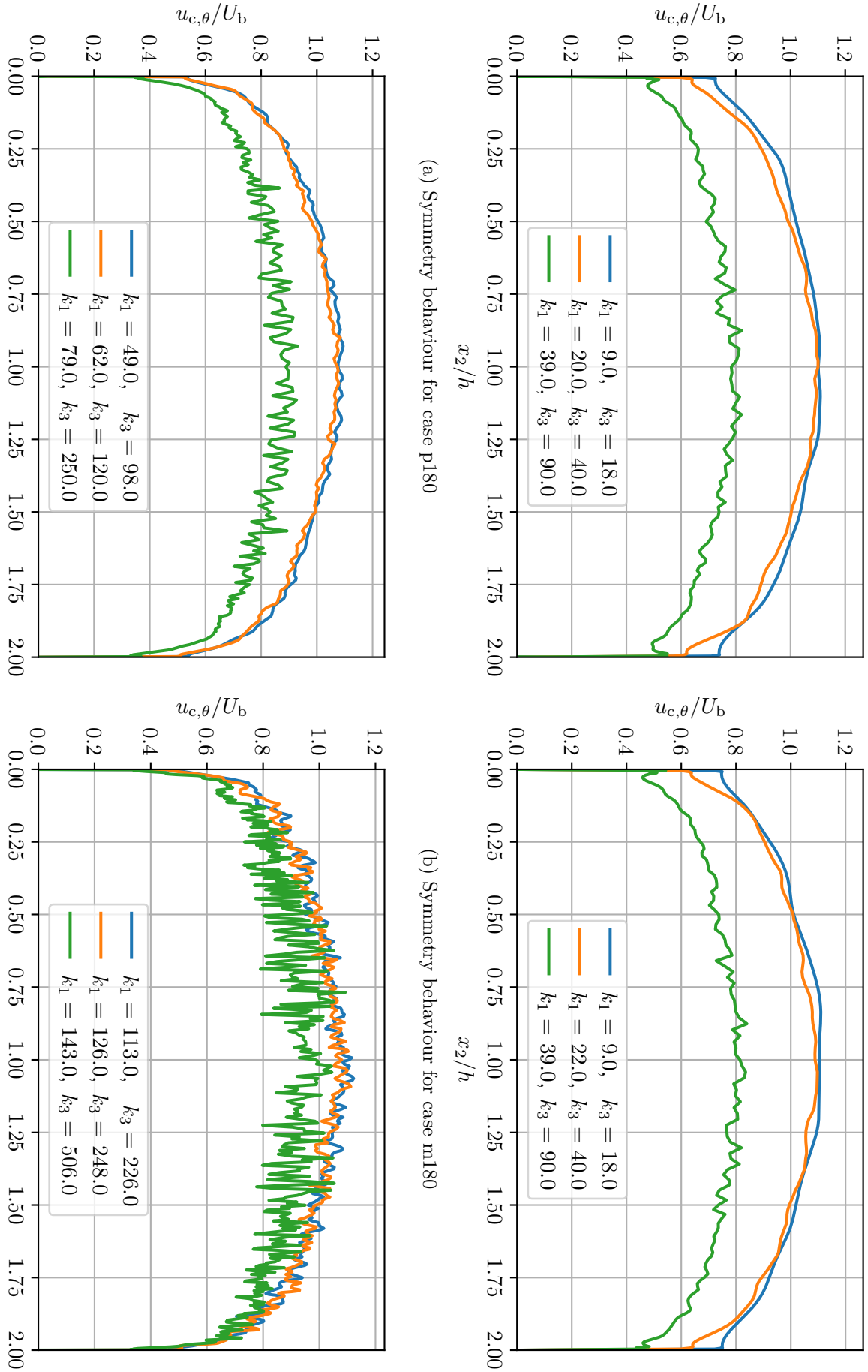

(a) Symmetry behaviour for case p180

(b) Symmetry behaviour for case m180

(c) Symmetry behaviour for case m500

(d) Symmetry behaviour for case m1000

Figure D.48.: $u_{c,\theta}$ symmetry behaviour with respect to wall distance for small Pr

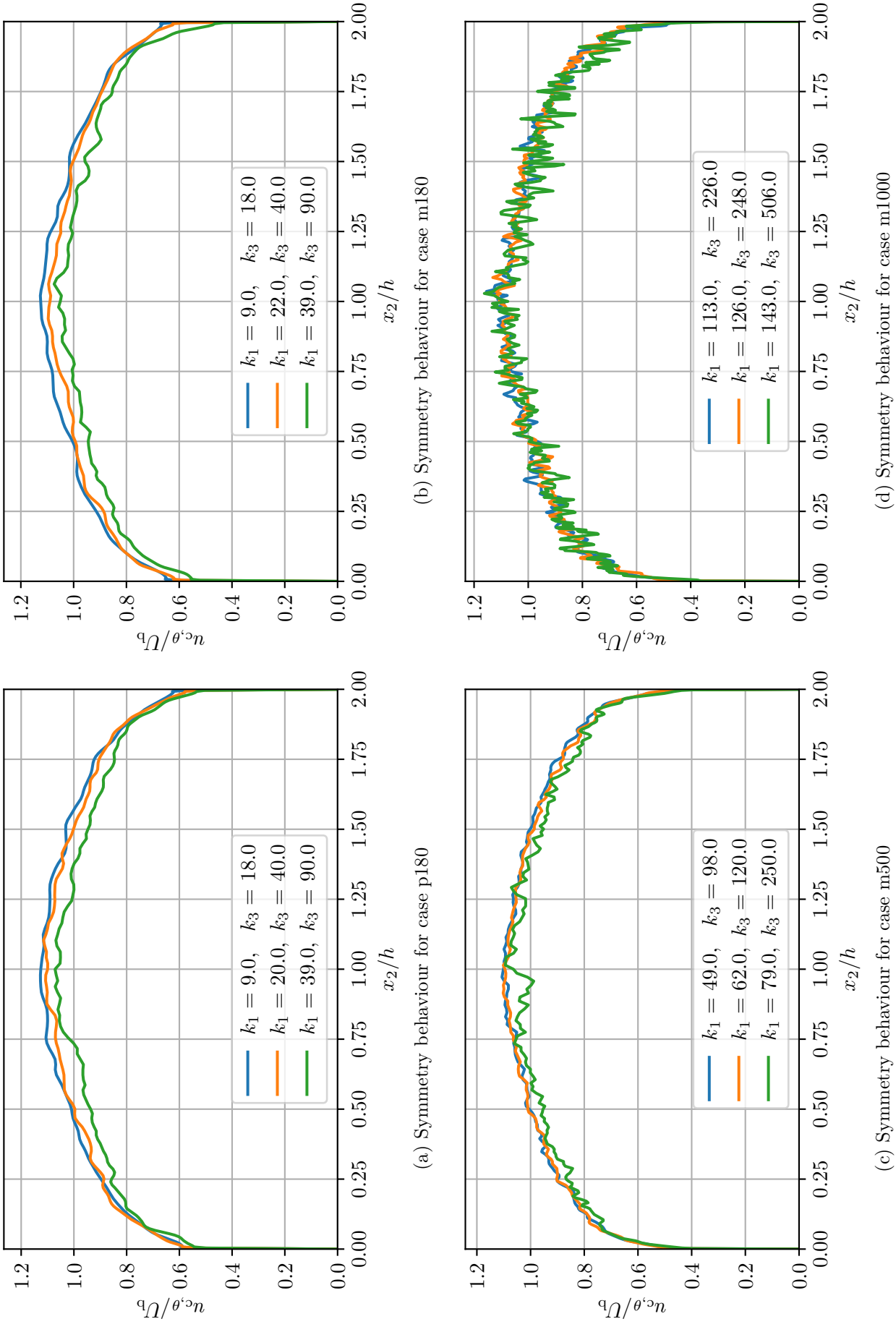

(a) Symmetry behaviour for case p180

(b) Symmetry behaviour for case m180

(c) Symmetry behaviour for case m500

(d) Symmetry behaviour for case m1000

Figure D.49.: $u_{c,\theta}$ symmetry behaviour with respect to wall distance for medium Pr

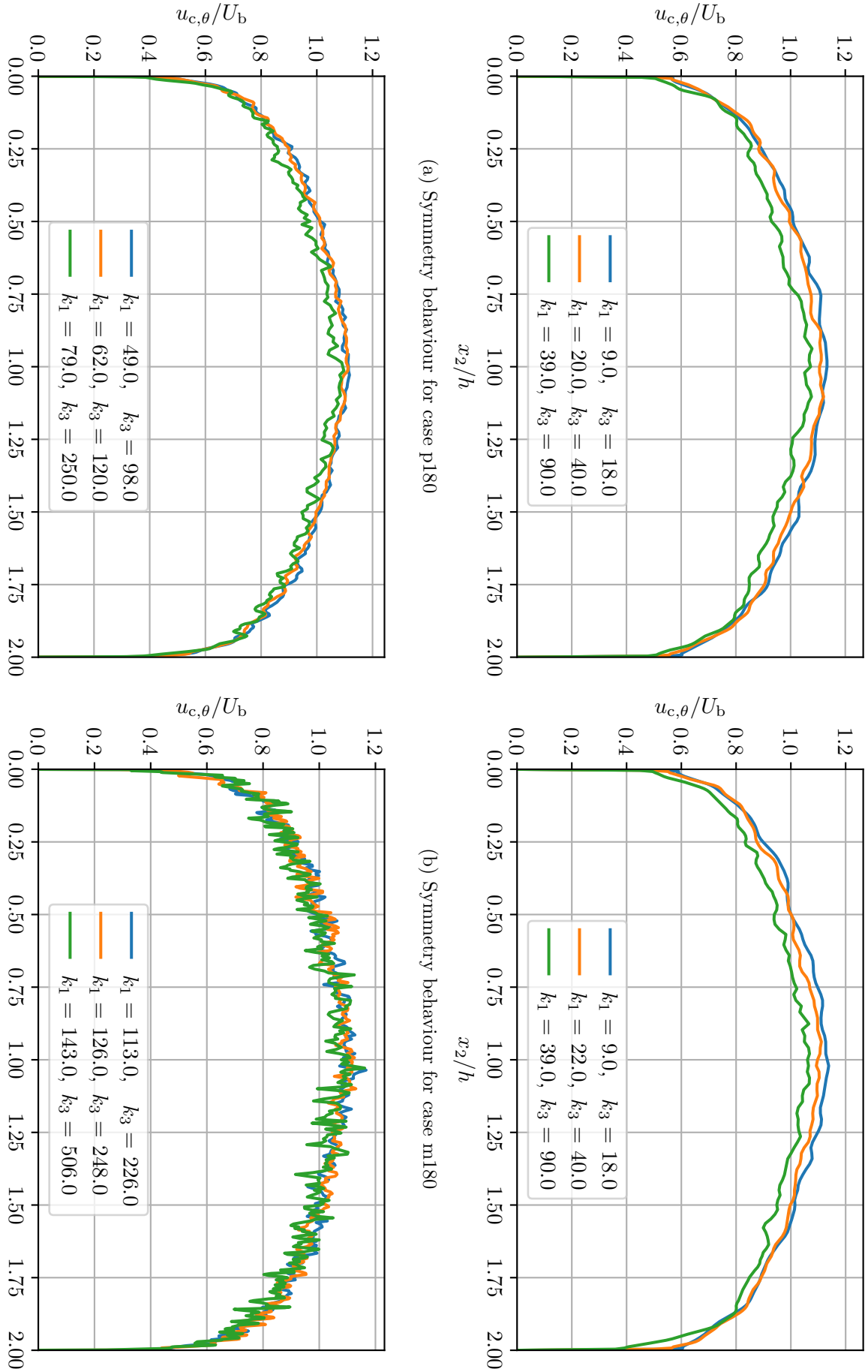

(a) Symmetry behaviour for case p180

(b) Symmetry behaviour for case m180

(c) Symmetry behaviour for case m500

(d) Symmetry behaviour for case m1000

Figure D.50.: $u_{c,\theta}$ symmetry behaviour with respect to wall distance for large Pr

D.2. Wavenumber-space symmetry

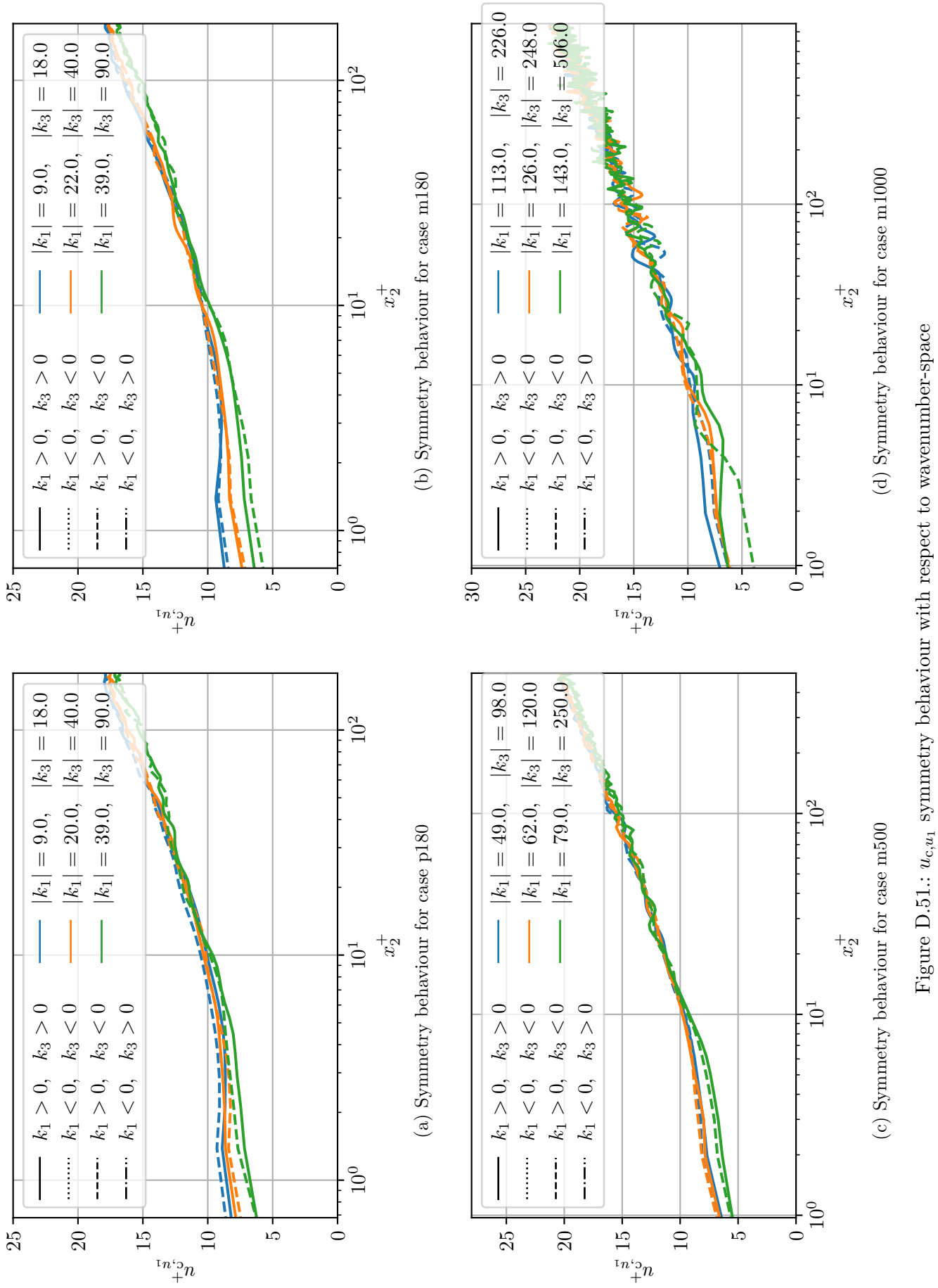

(a) Symmetry behaviour for case p180

(b) Symmetry behaviour for case m180

(c) Symmetry behaviour for case m500

(d) Symmetry behaviour for case m1000

Figure D.51.: u_{c,u_1} symmetry behaviour with respect to wavenumber-space

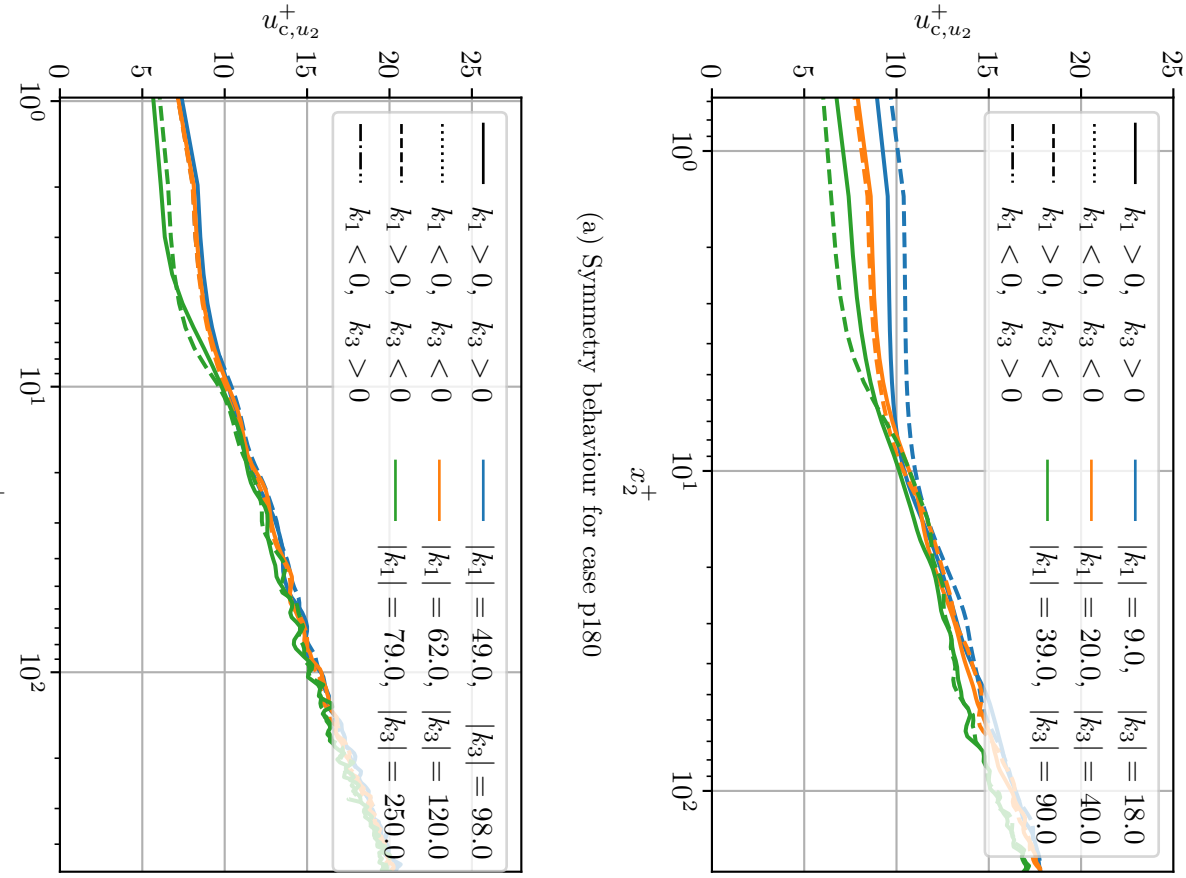

(a) Symmetry behaviour for case p180

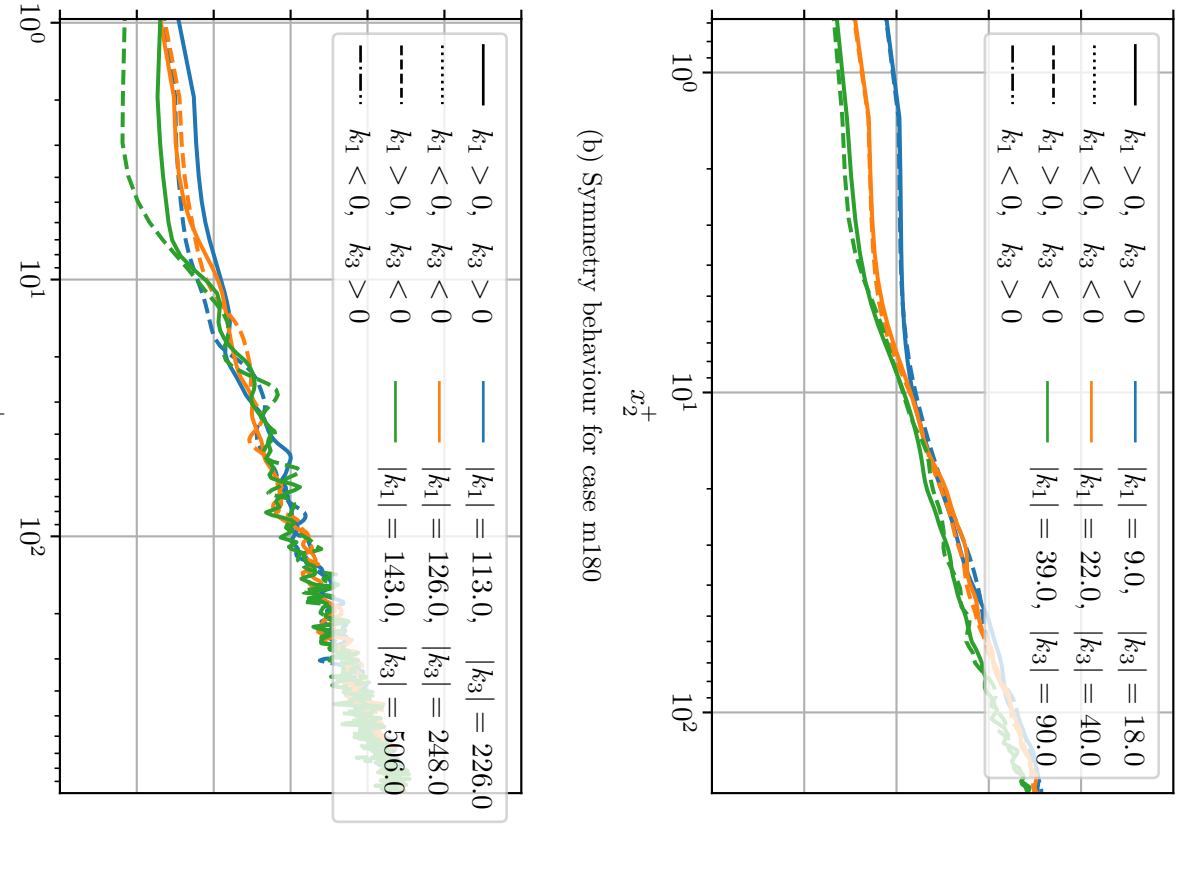

(b) Symmetry behaviour for case m180

(c) Symmetry behaviour for case m500

(d) Symmetry behaviour for case m1000

Figure D.52.: u_{c,u_2} symmetry behaviour with respect to wavenumber-space

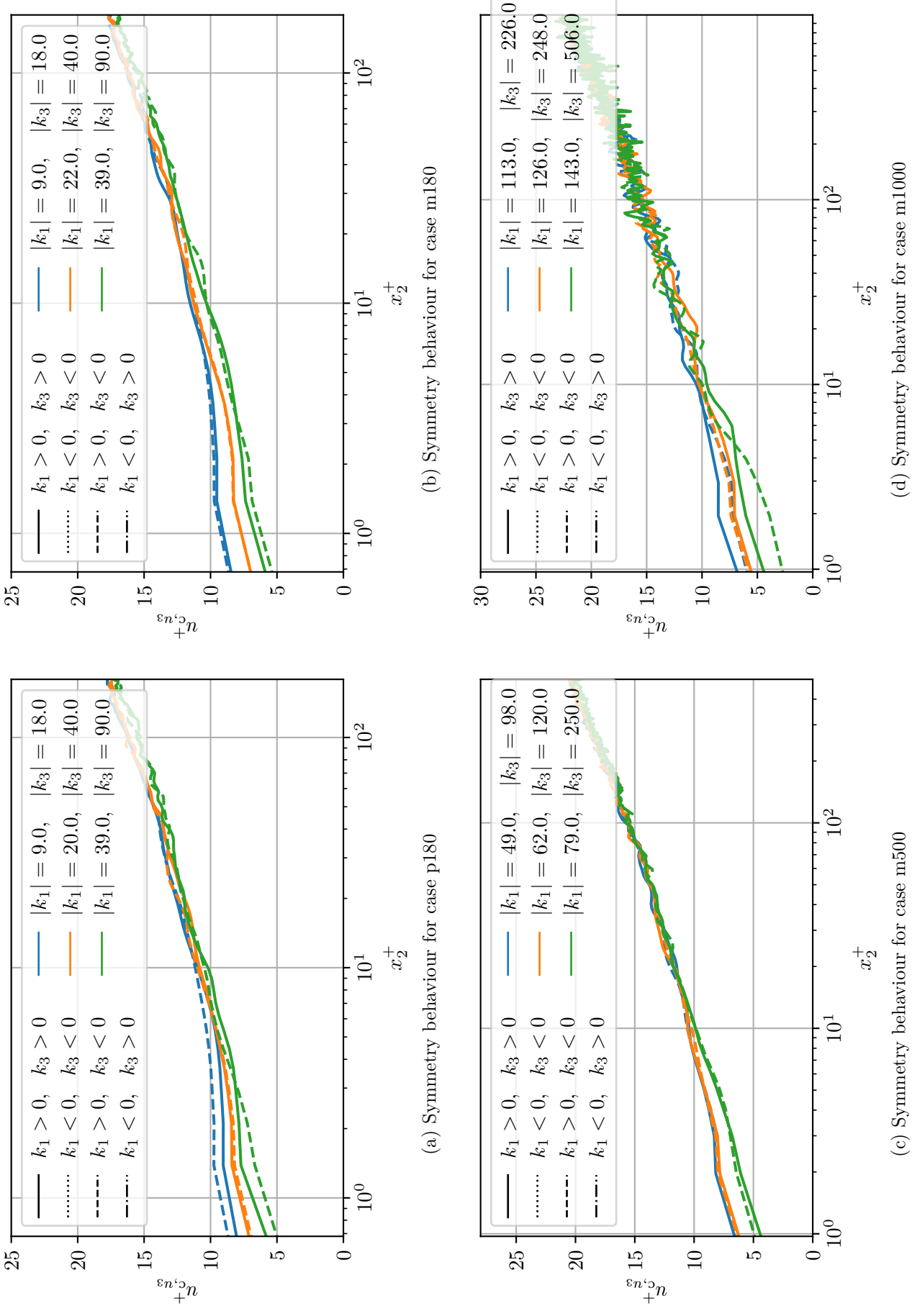

(a) Symmetry behaviour for case p180

(b) Symmetry behaviour for case m180

(c) Symmetry behaviour for case m500

(d) Symmetry behaviour for case m1000

Figure D.53.: u_{c,u_3} symmetry behaviour with respect to wavenumber-space

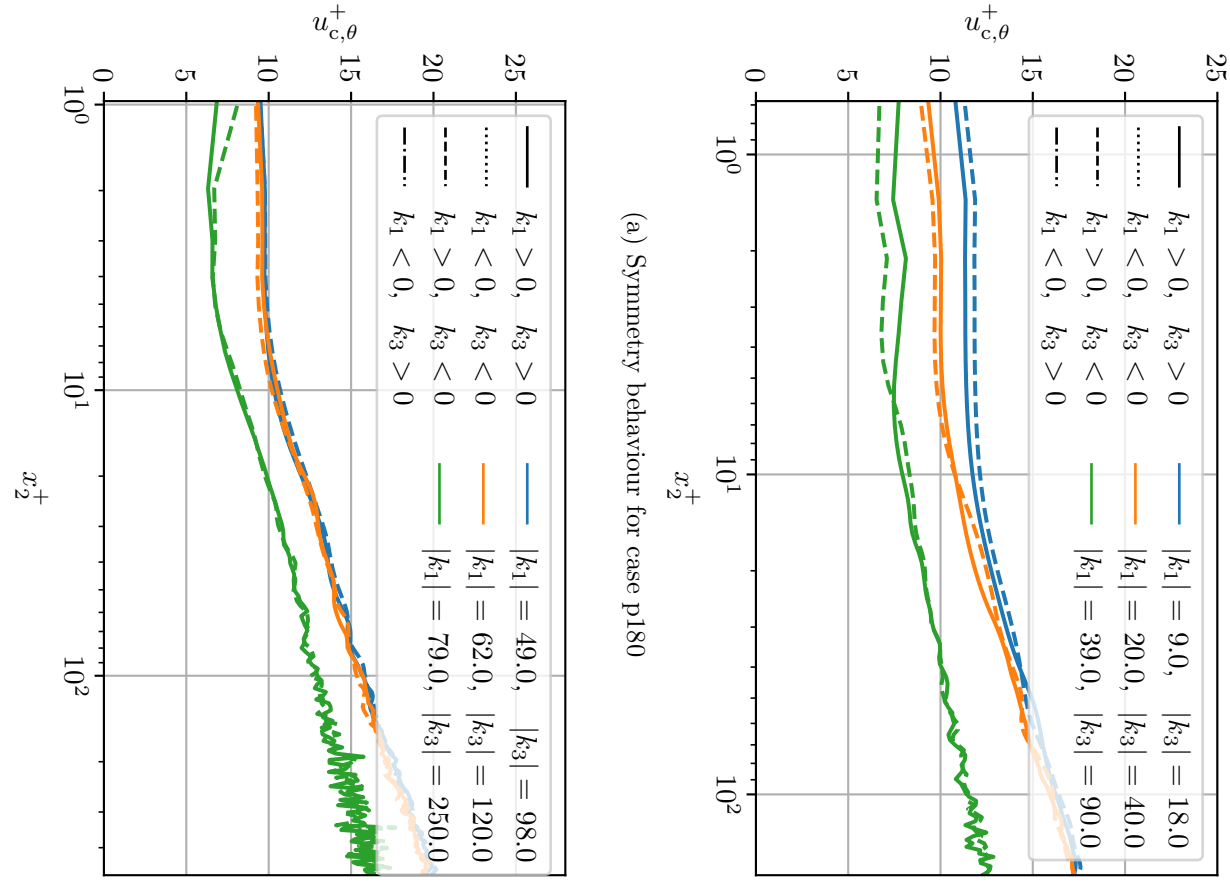

(a) Symmetry behaviour for case p180

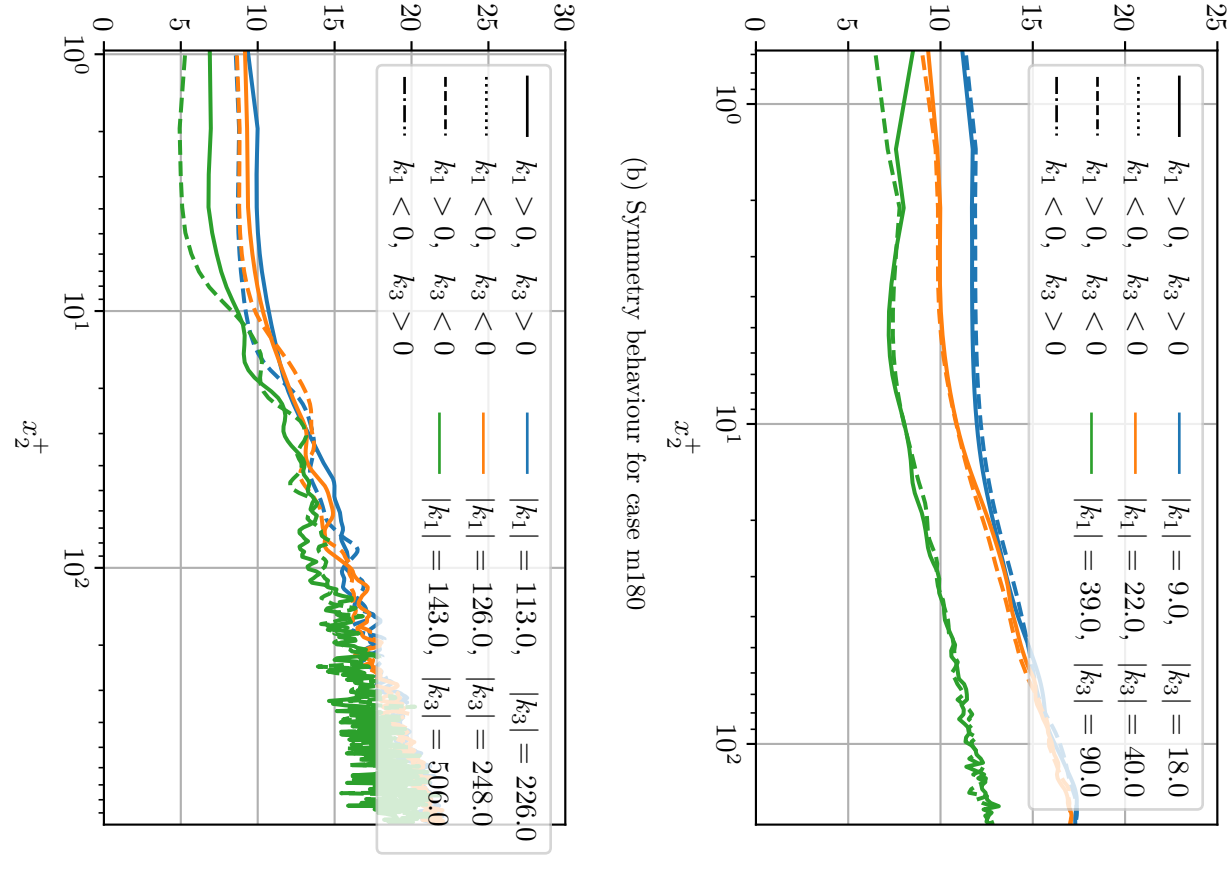

(b) Symmetry behaviour for case m180

(c) Symmetry behaviour for case m500

(d) Symmetry behaviour for case m1000

Figure D.54.: $u_{c,\theta}$ symmetry behaviour with respect to wavenumber-space for small Pr

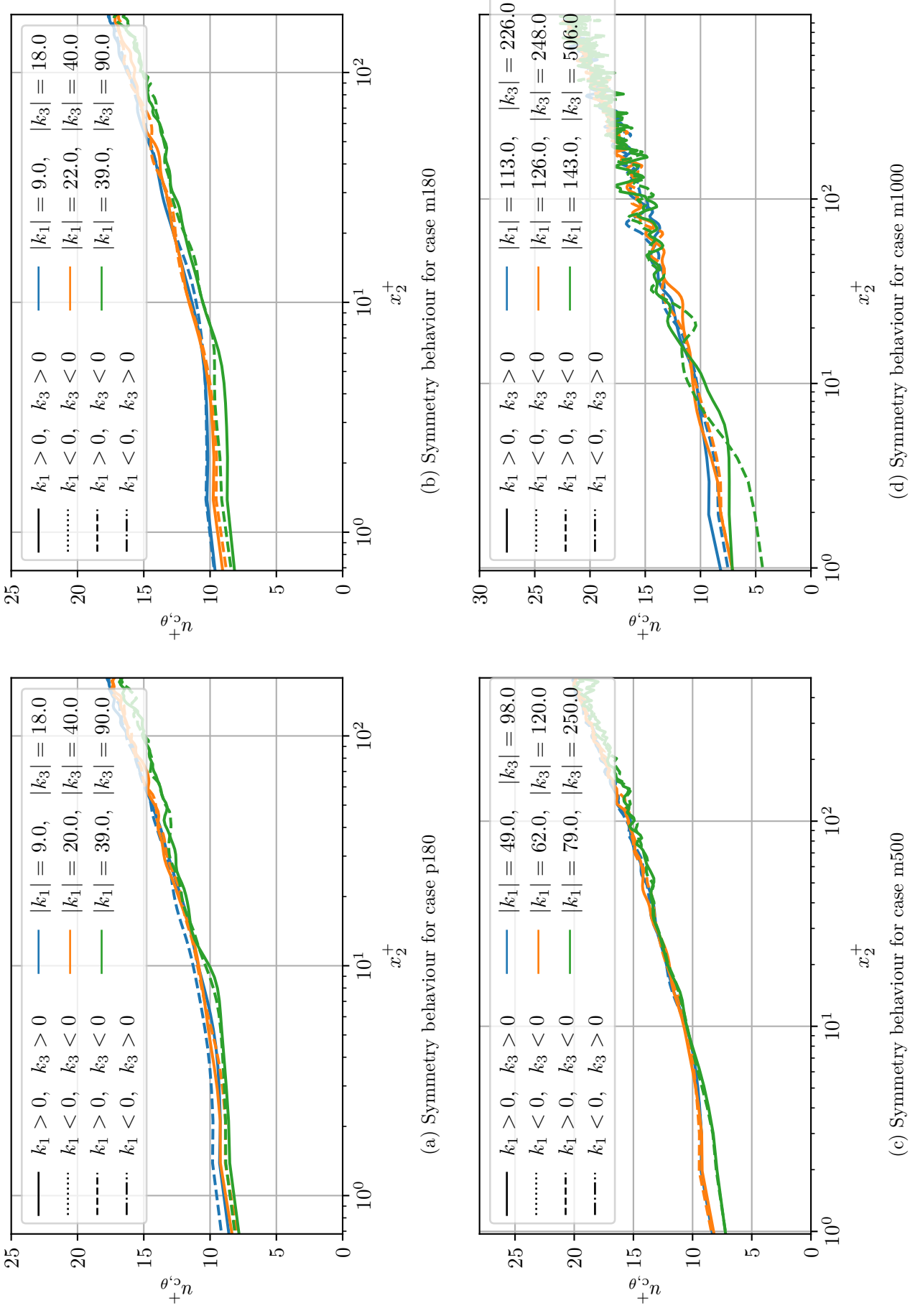

(a) Symmetry behaviour for case p180

(b) Symmetry behaviour for case m180

(c) Symmetry behaviour for case m500

(d) Symmetry behaviour for case m1000

Figure D.55.: $u_{c,\theta}$ symmetry behaviour with respect to wavenumber-space for medium Pr

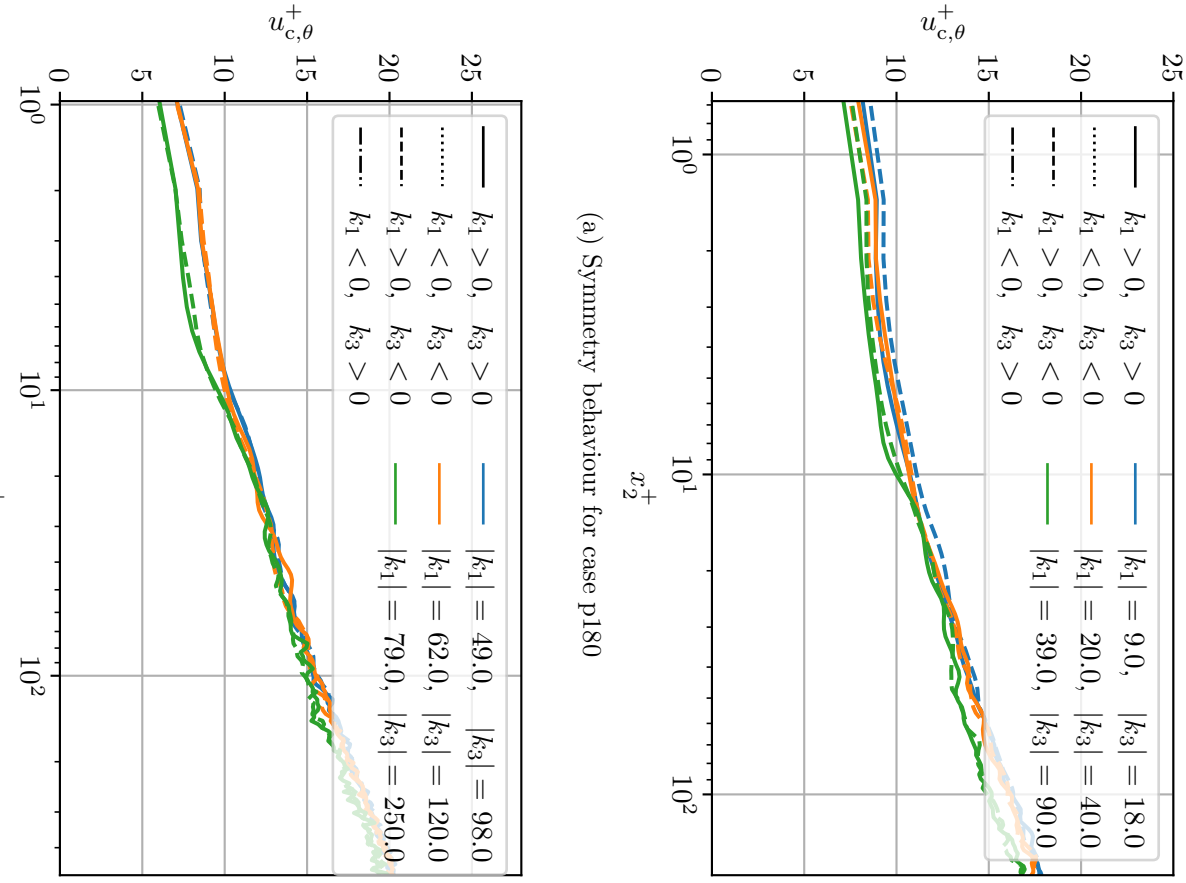

(a) Symmetry behaviour for case p180

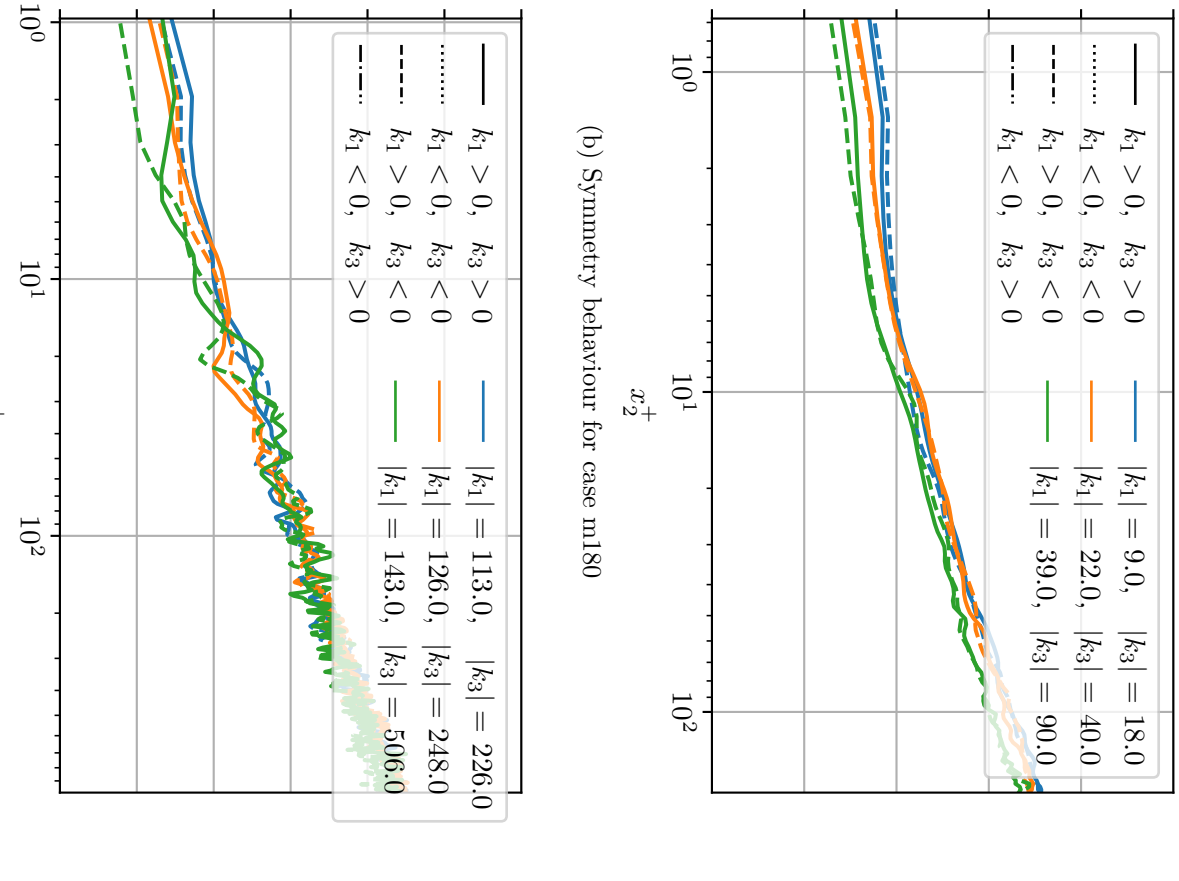

(b) Symmetry behaviour for case m180

(c) Symmetry behaviour for case m500

(d) Symmetry behaviour for case m1000

Figure D.56.: $u_{c,\theta}$ symmetry behaviour with respect to wavenumber-space for large Pr

D.3. Overall convection velocities

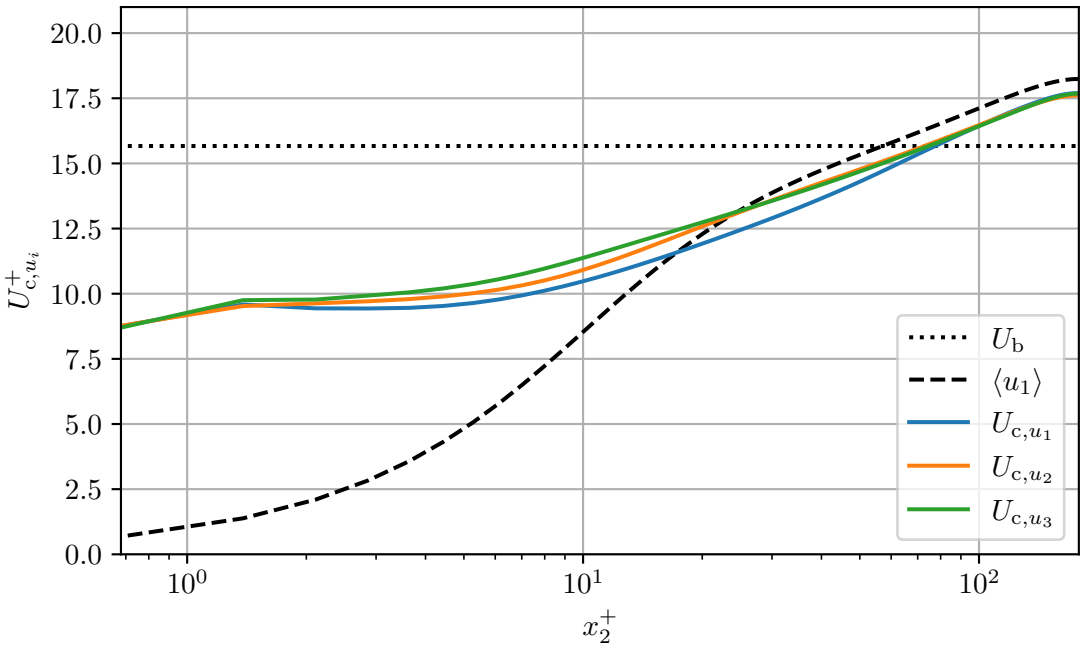

(a) Overall convection velocities of velocity structures

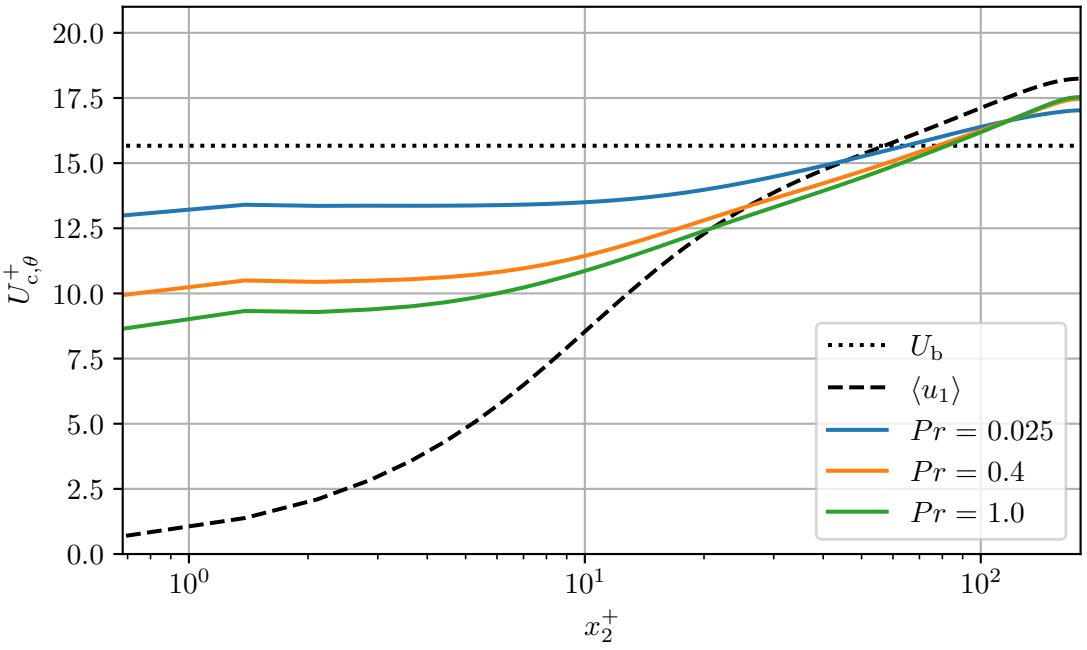

(b) Overall convection velocities of passive scalar structures

Figure D.57.: Overall convection velocities (case m180)

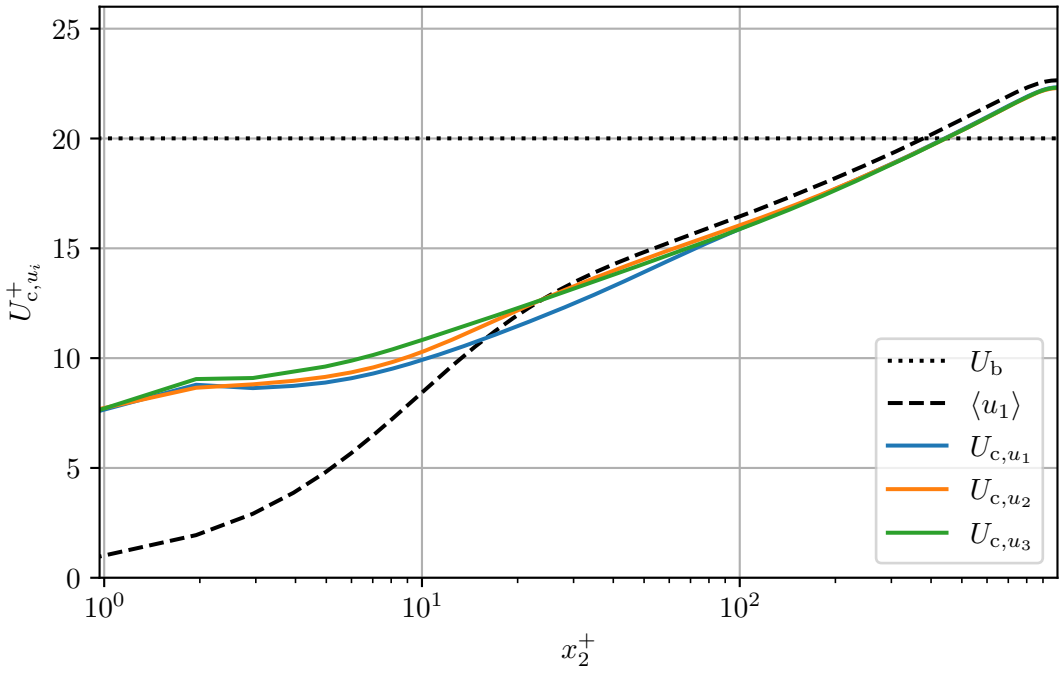

(a) Overall convection velocities of velocity structures

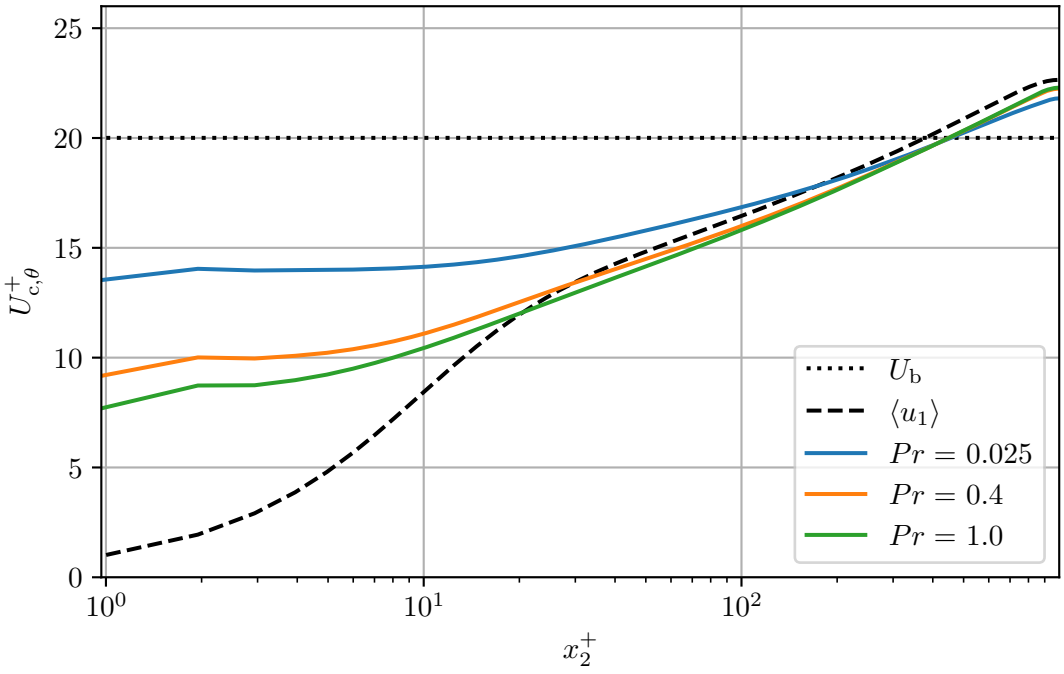

(b) Overall convection velocities of passive scalar structures

Figure D.58.: Overall convection velocities (case m1000)

D.4. Partitioned overall convection velocities

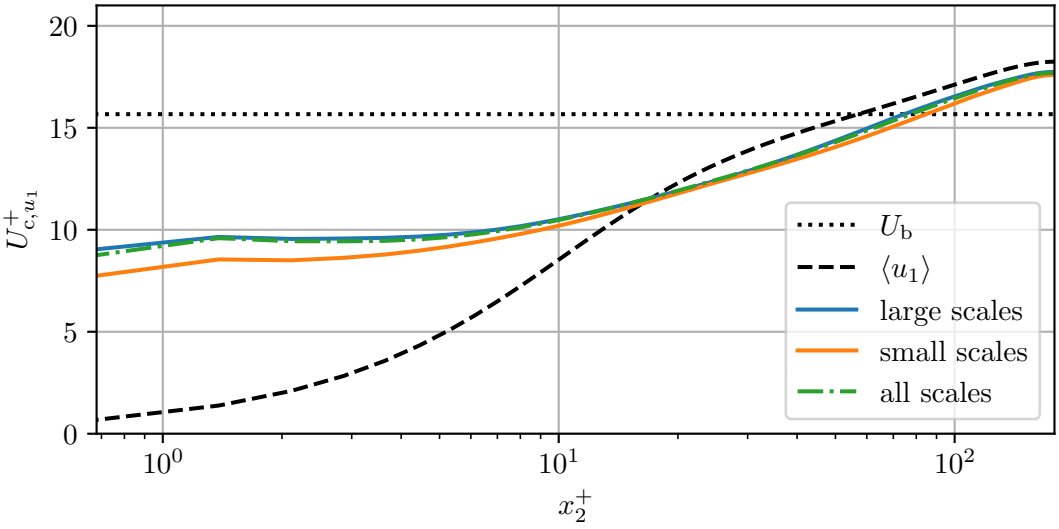

(a) Partitioned overall convection velocities of streamwise velocity structures

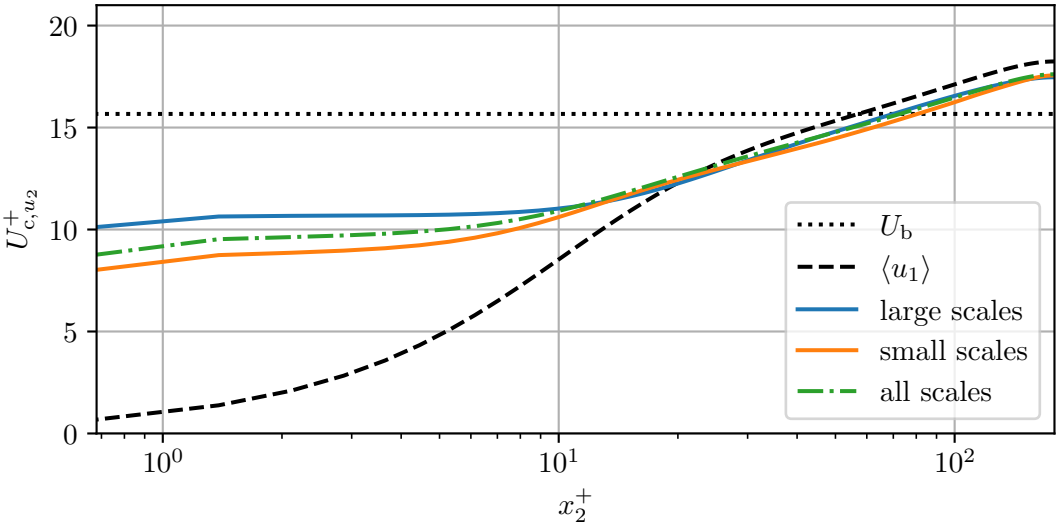

(b) Partitioned overall convection velocities of wall-normal velocity structures

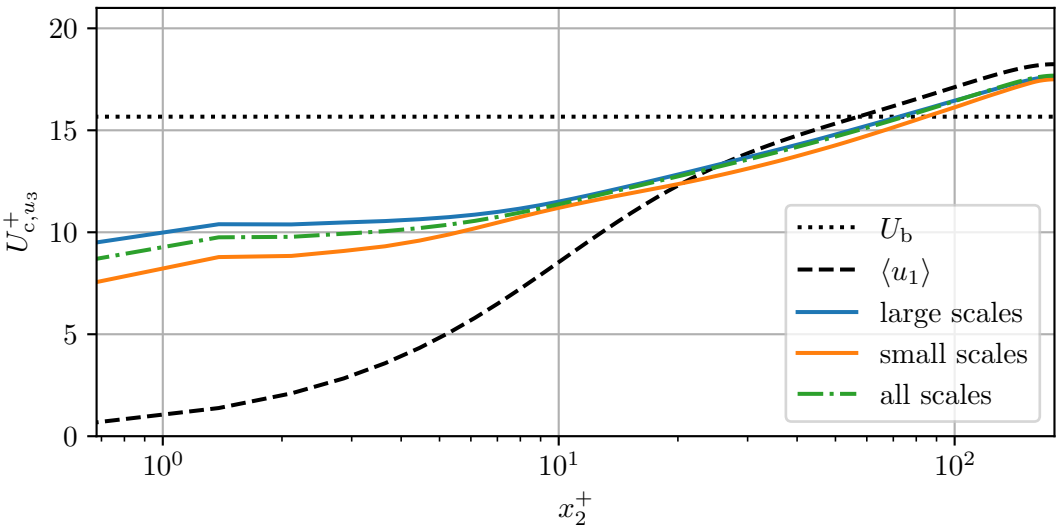

(c) Partitioned overall convection velocities of spanwise velocity structures

Figure D.59.: Partitioned overall convection velocities of velocity structures (case m180, cut-off at $(\lambda_1, \lambda_3) = (h, h/4)$)

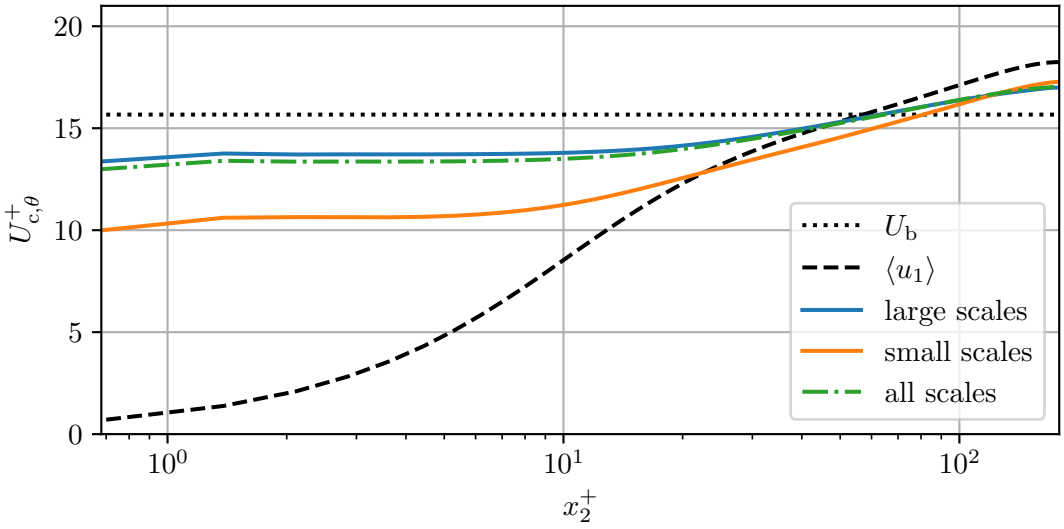

(a) Partitioned overall convection velocities with $Pr = 0.025$

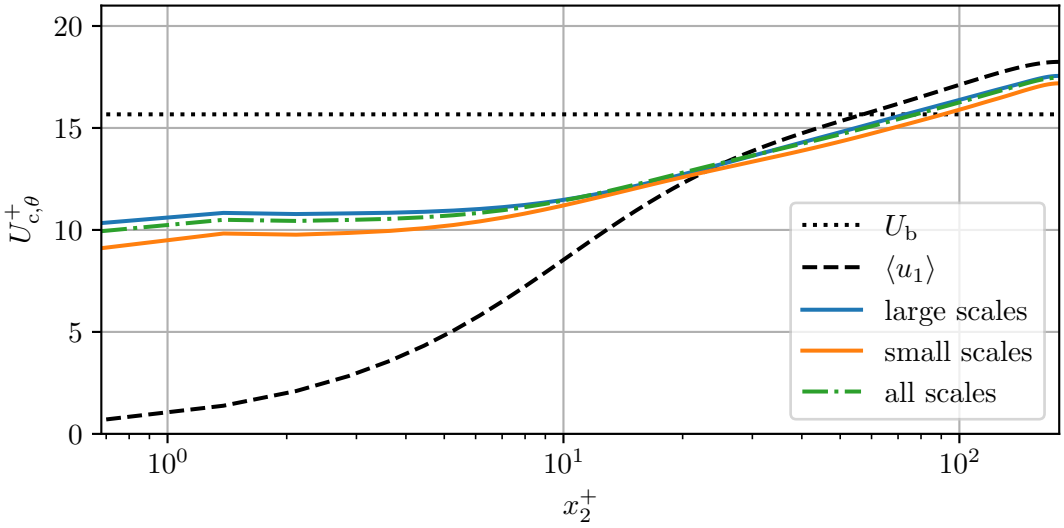

(b) Partitioned overall convection velocities with $Pr = 0.4$

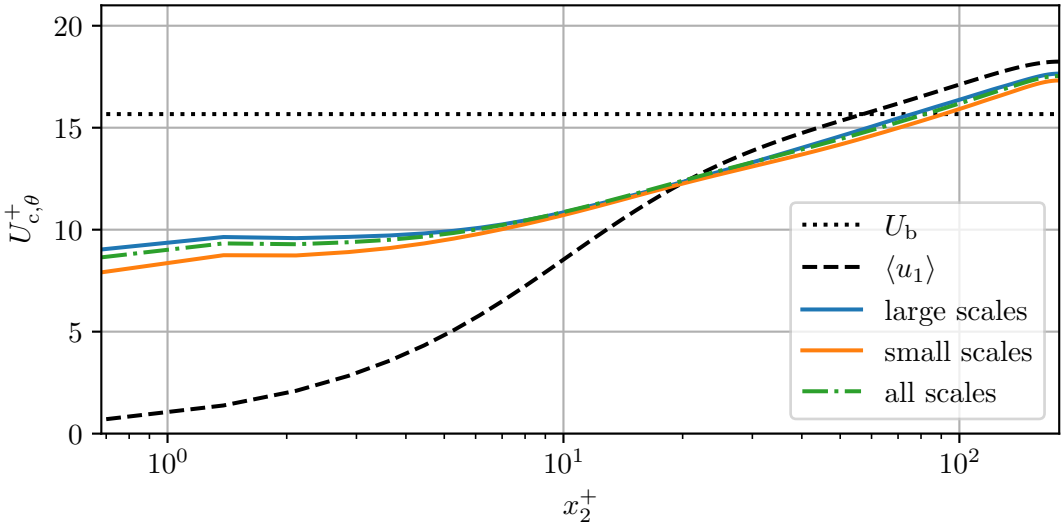

(c) Partitioned overall convection velocities with $Pr = 1$

Figure D.60.: Partitioned overall convection velocities of scalar structures (case m180, cut-off at $(\lambda_1, \lambda_3) = (h, h/4)$)

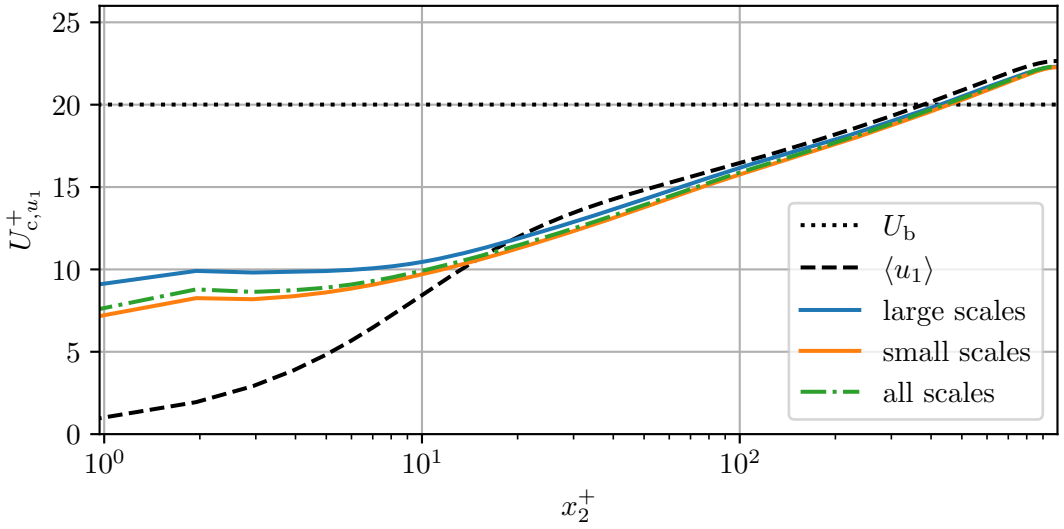

(a) Partitioned overall convection velocities of streamwise velocity structures

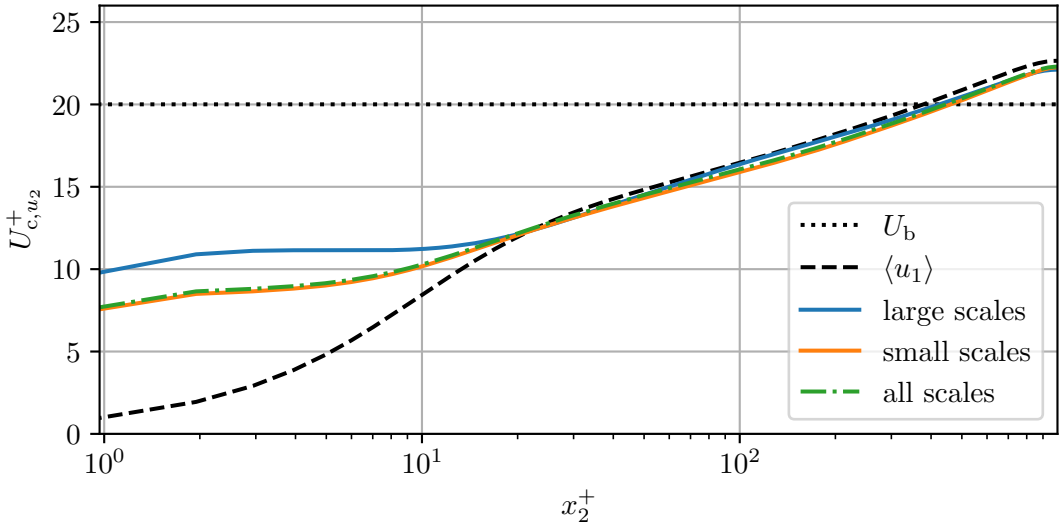

(b) Partitioned overall convection velocities of wall-normal velocity structures

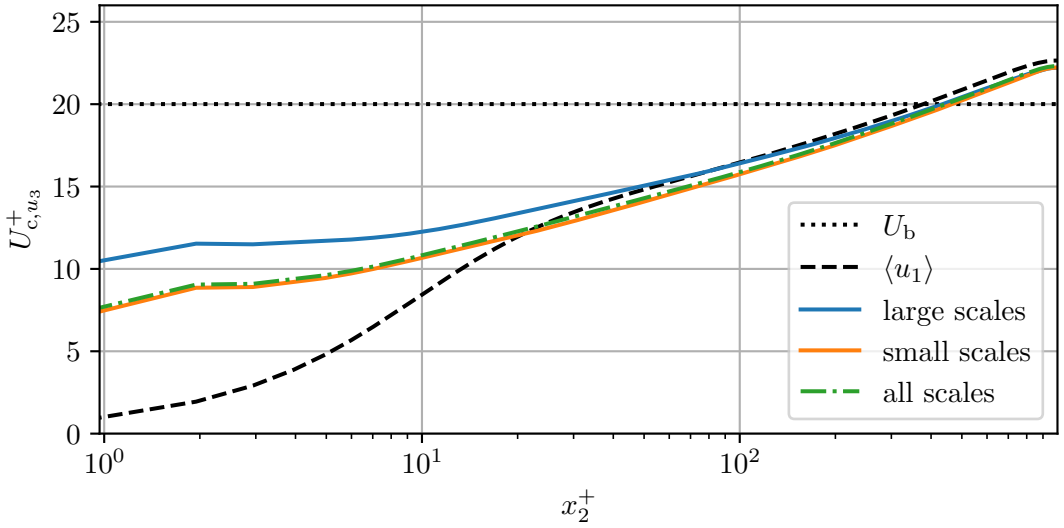

(c) Partitioned overall convection velocities of spanwise velocity structures

Figure D.61.: Partitioned overall convection velocities of velocity structures (case m1000, cut-off at $(\lambda_1, \lambda_3) = (h/2, h/8)$)

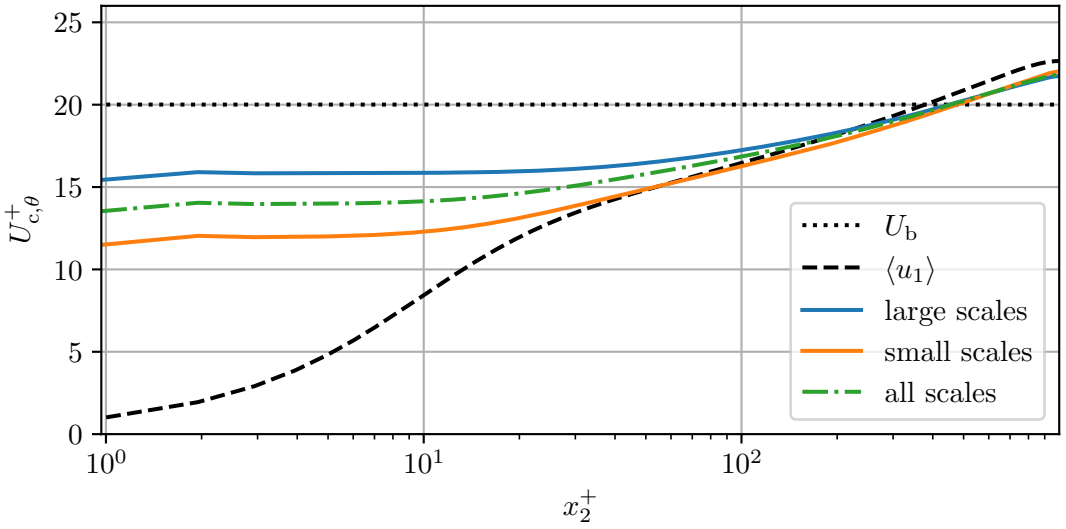

(a) Partitioned overall convection velocities with $Pr = 0.025$

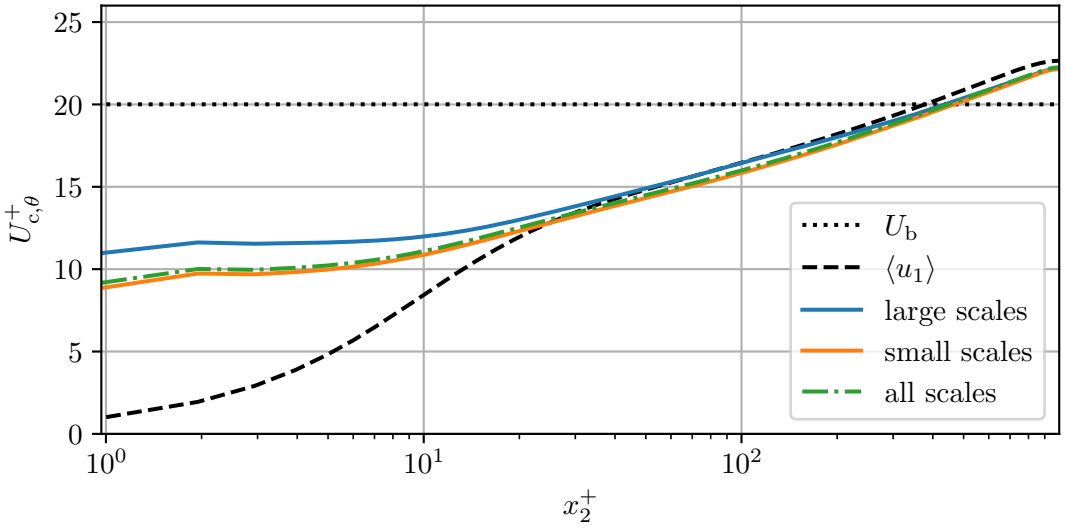

(b) Partitioned overall convection velocities with $Pr = 0.4$

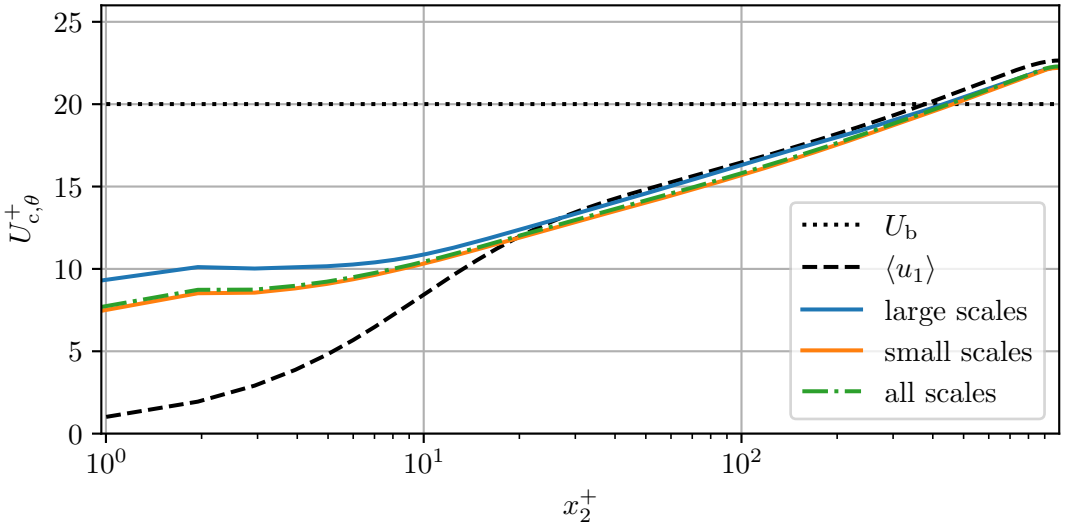

(c) Partitioned overall convection velocities with $Pr = 1$

Figure D.62.: Partitioned overall convection velocities of scalar structures (case m1000, cut-off at $(\lambda_1, \lambda_3) = (h/2, h/8)$)

D.5. Convection velocity contributions

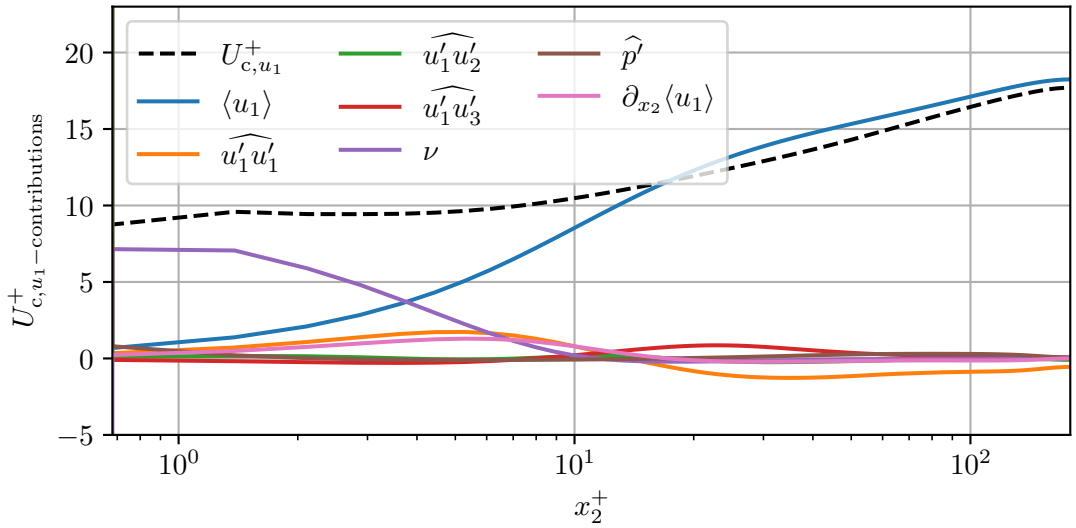

(a) Overall convection velocity contributions of streamwise velocity structures

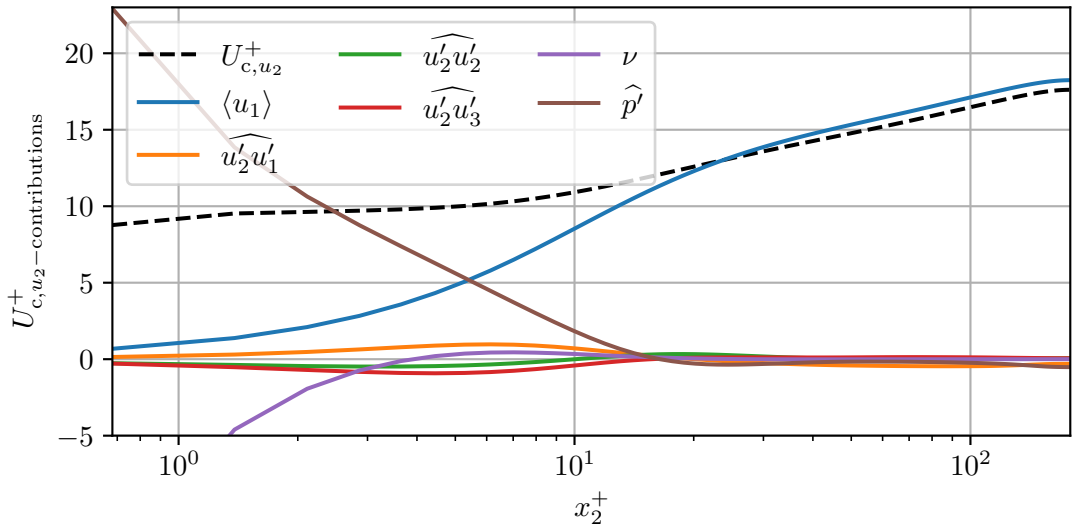

(b) Overall convection velocity contributions of wall-normal velocity structures

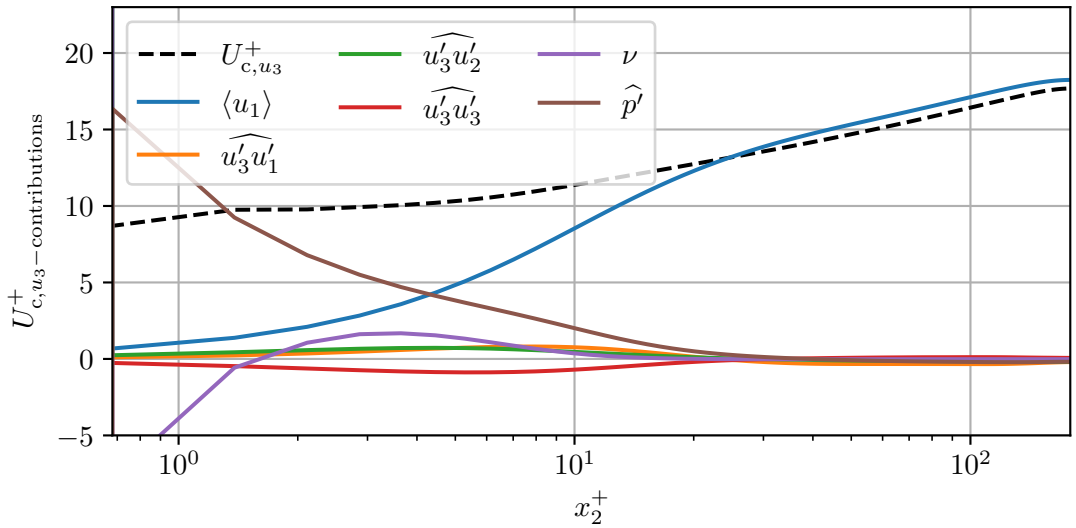

(c) Overall convection velocity contributions of spanwise velocity structures

Figure D.63.: Overall convection velocity contributions of velocity structures (case m180)

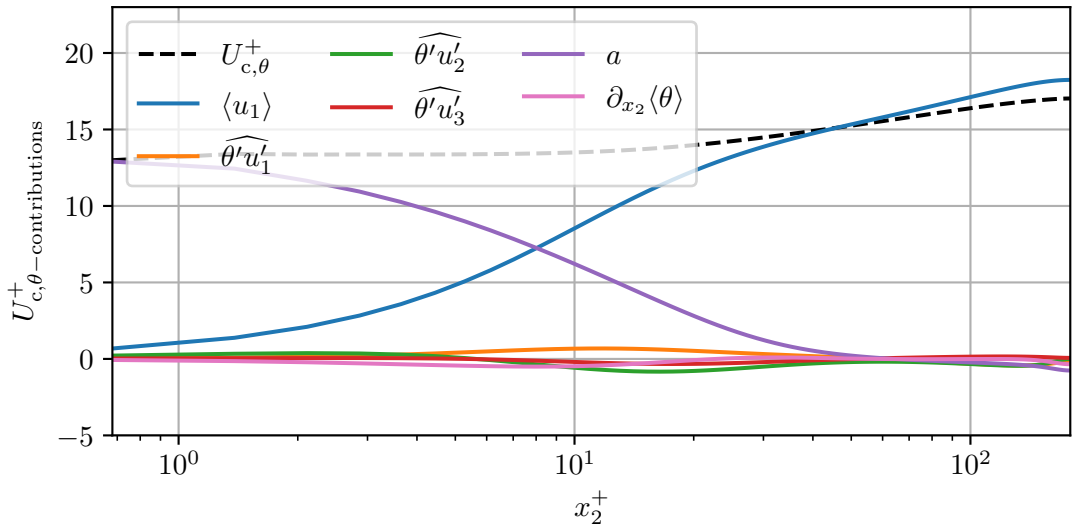

(a) Overall convection velocity contributions with $Pr = 0.025$

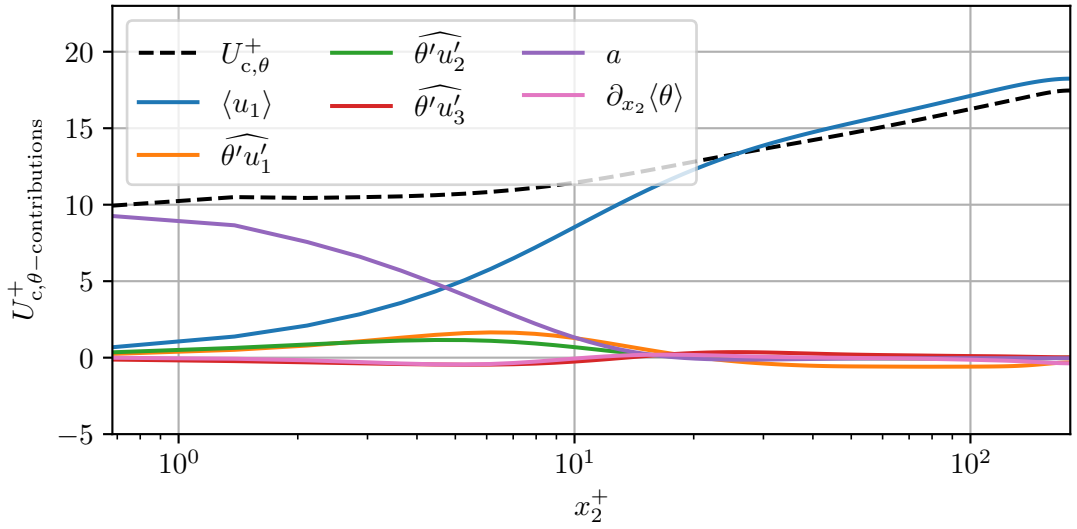

(b) Overall convection velocity contributions with $Pr = 0.4$

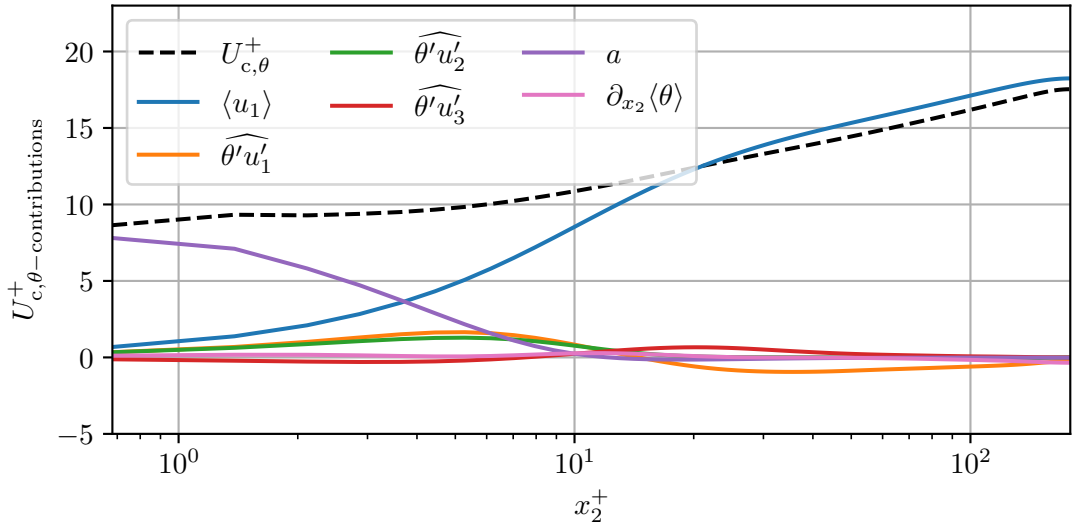

(c) Overall convection velocity contributions with $Pr = 1$

Figure D.64.: Overall convection velocity contributions of scalar structures (case m180)

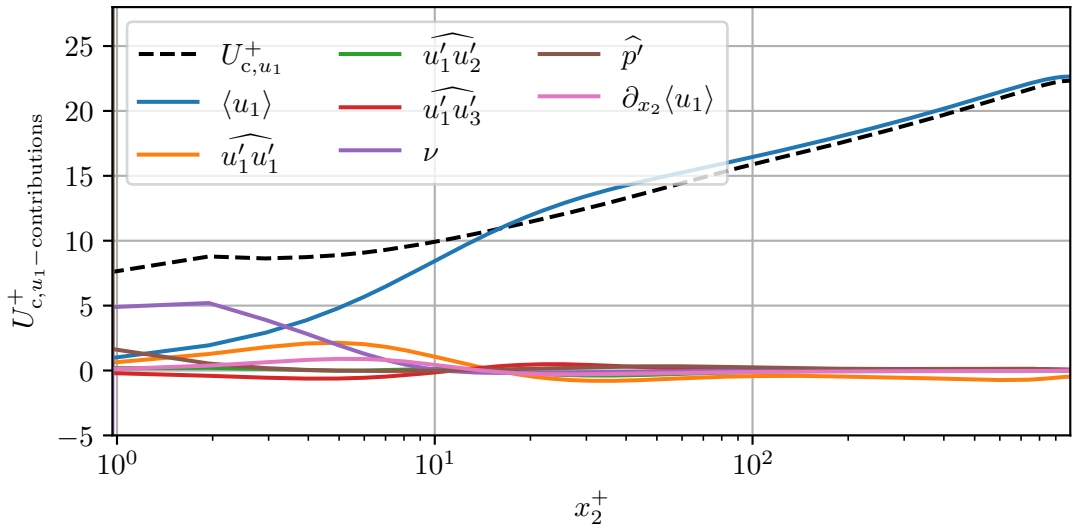

(a) Overall convection velocity contributions of streamwise velocity structures

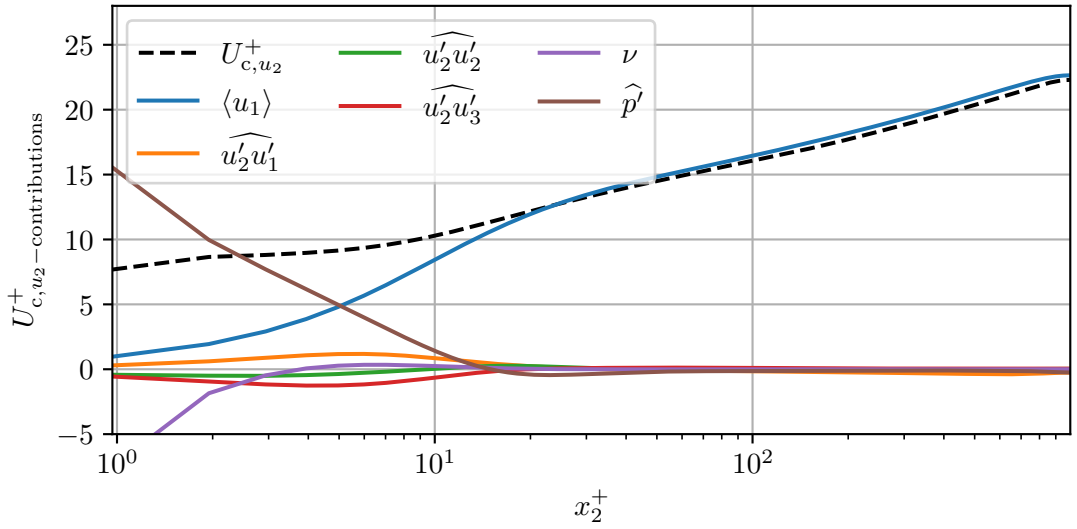

(b) Overall convection velocity contributions of wall-normal velocity structures

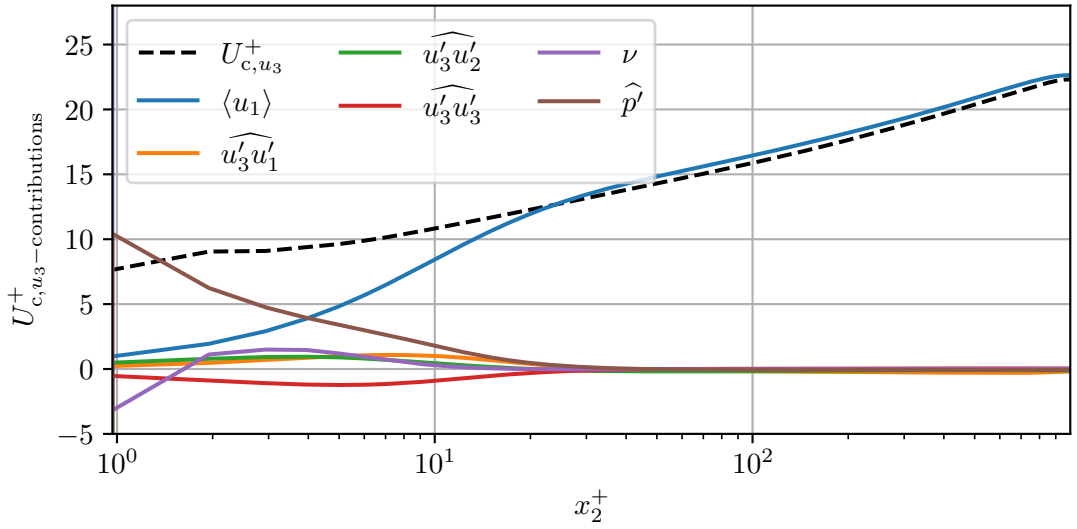

(c) Overall convection velocity contributions of spanwise velocity structures

Figure D.65.: Overall convection velocity contributions of velocity structures (case m1000)

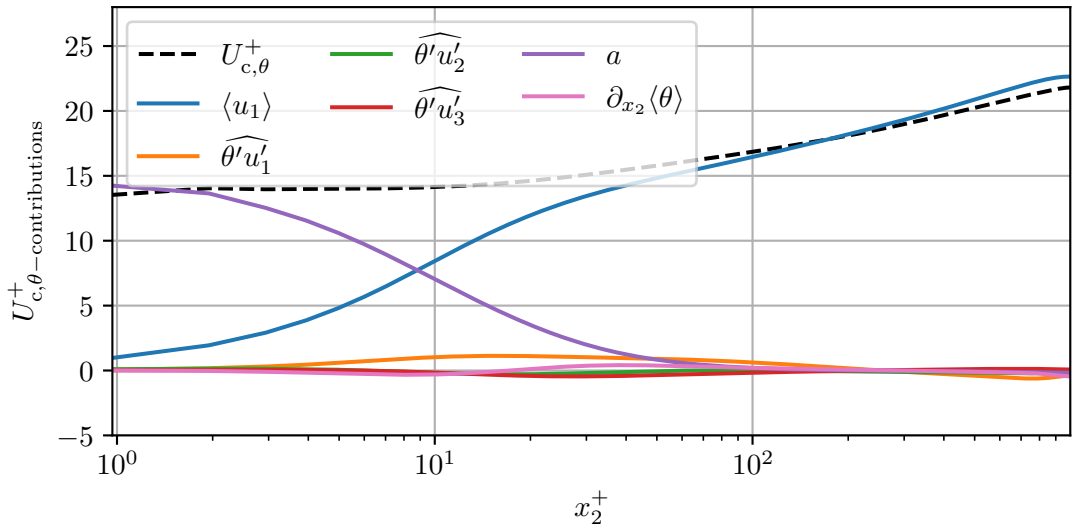

(a) Overall convection velocity contributions with $Pr = 0.025$

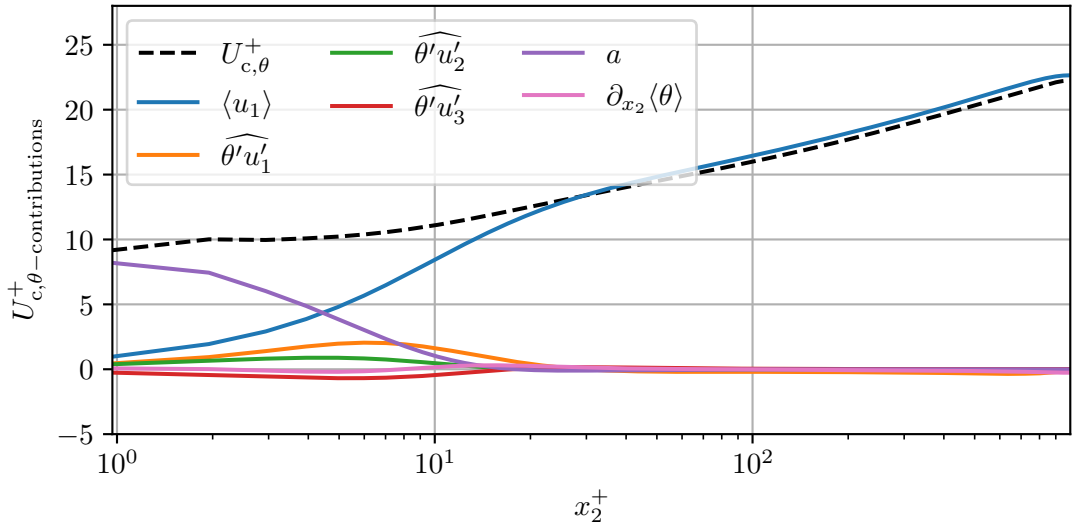

(b) Overall convection velocity contributions with $Pr = 0.4$

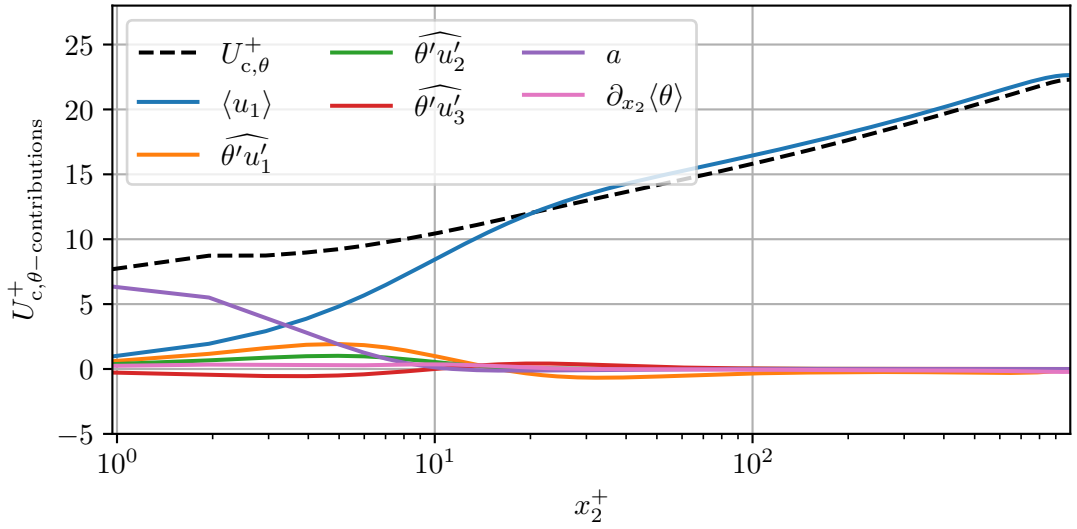

(c) Overall convection velocity contributions with $Pr = 1$

Figure D.66.: Overall convection velocity contributions of scalar structures (case m1000)

D.6. Spectral distributions

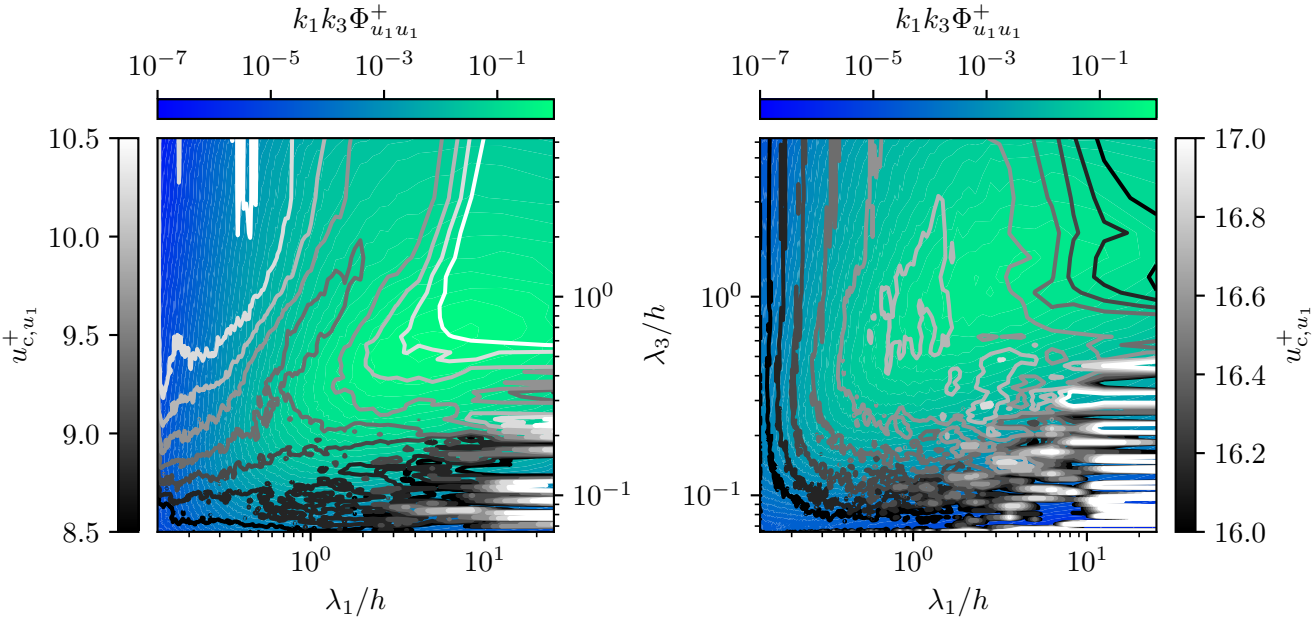

(a) Distribution at $x_2^+ \approx 5$ (b) Distribution at $x_2^+ \approx 105$

Figure D.67.: Spectral distributions of u_{c,u_1} (case m180)

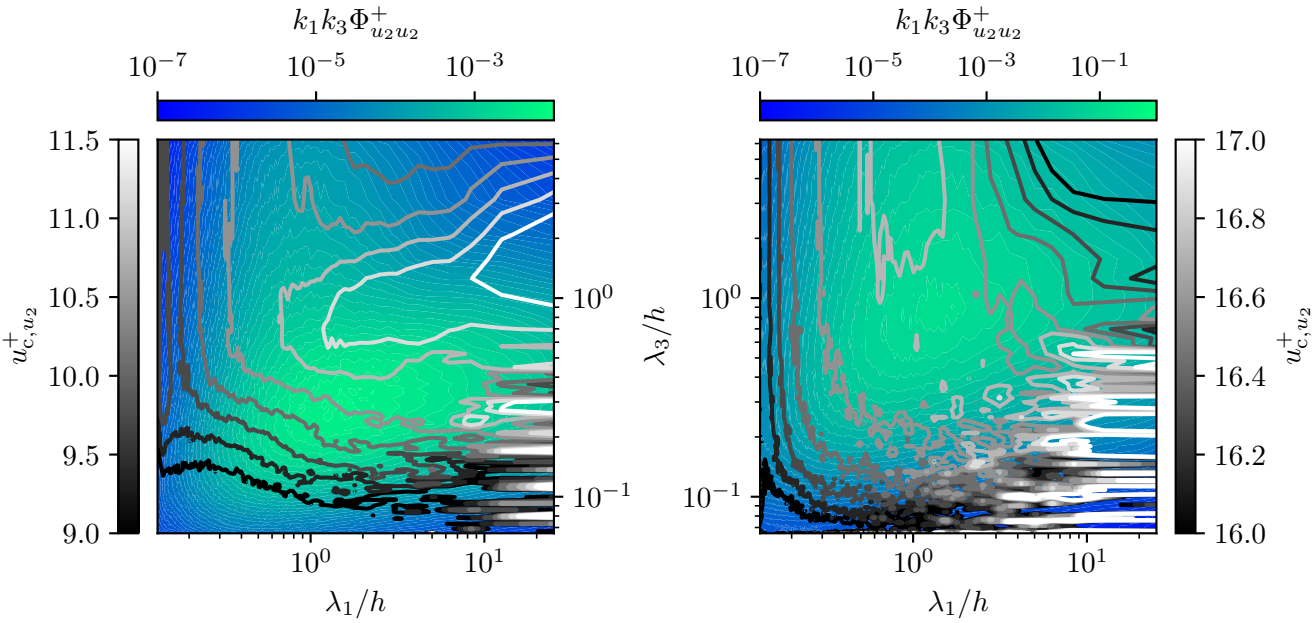

(a) Distribution at $x_2^+ \approx 5$ (b) Distribution at $x_2^+ \approx 105$

Figure D.68.: Spectral distributions of u_{c,u_2} (case m180)

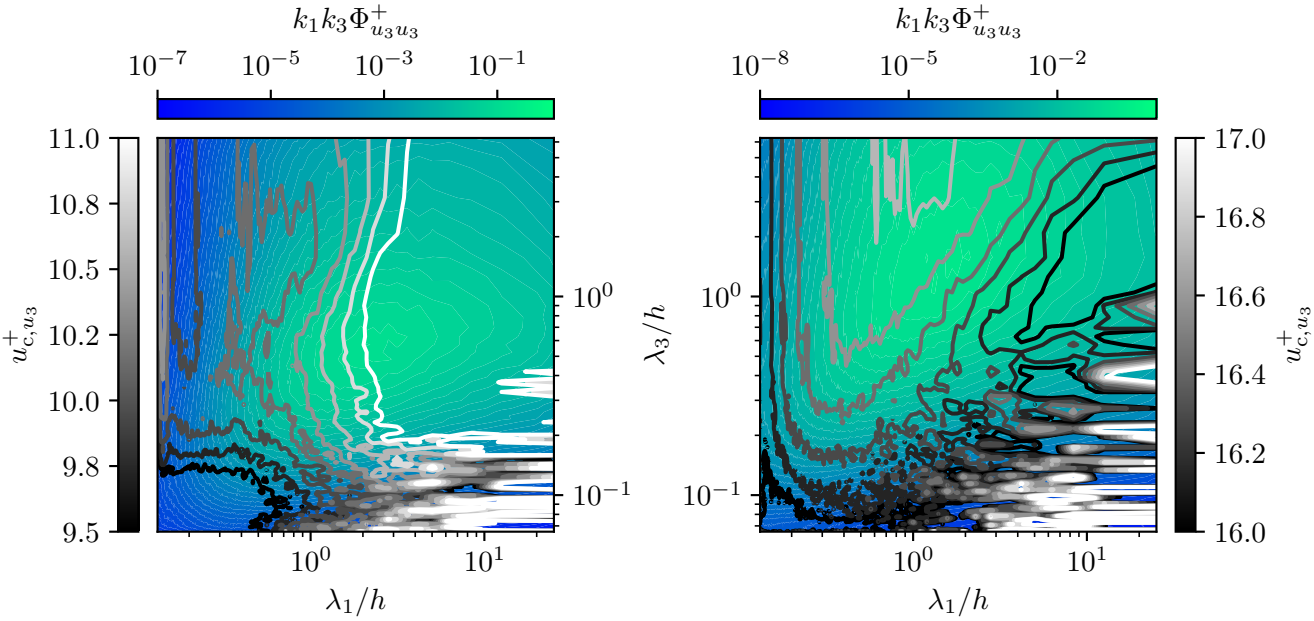

(a) Distribution at $x_2^+ \approx 5$ (b) Distribution at $x_2^+ \approx 105$

Figure D.69.: Spectral distributions of u_{c,u_3} (case m180)

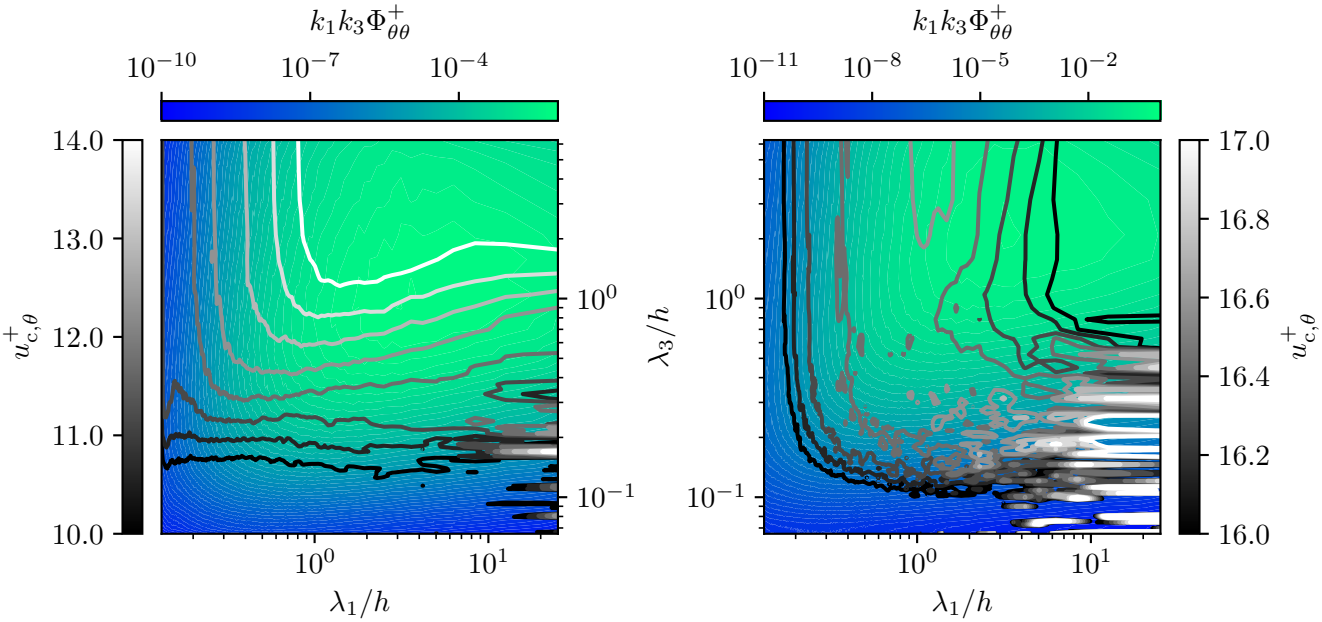

(a) Distribution at $x_2^+ \approx 5$ (b) Distribution at $x_2^+ \approx 105$

Figure D.70.: Spectral distributions of $u_{c,\theta}$ with $Pr = 0.025$ (case m180)

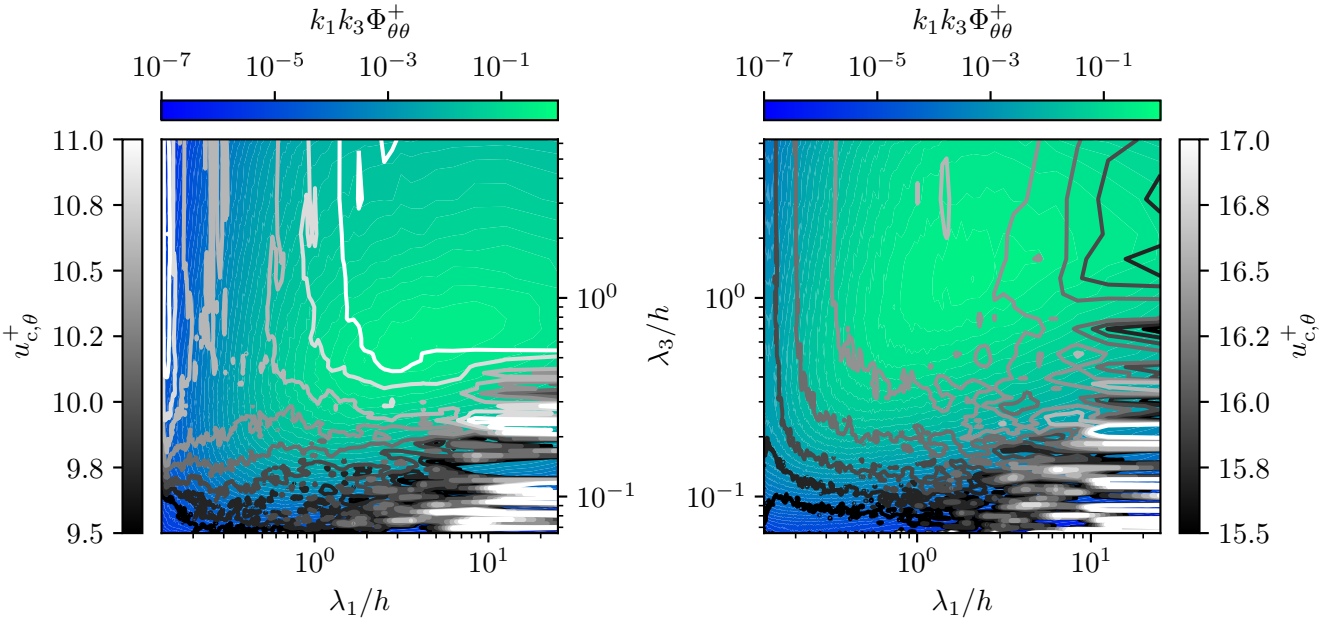

(a) Distribution at $x_2^+ \approx 5$ (b) Distribution at $x_2^+ \approx 105$

Figure D.71.: Spectral distributions of $u_{c,\theta}$ with $Pr = 0.4$ (case m180)

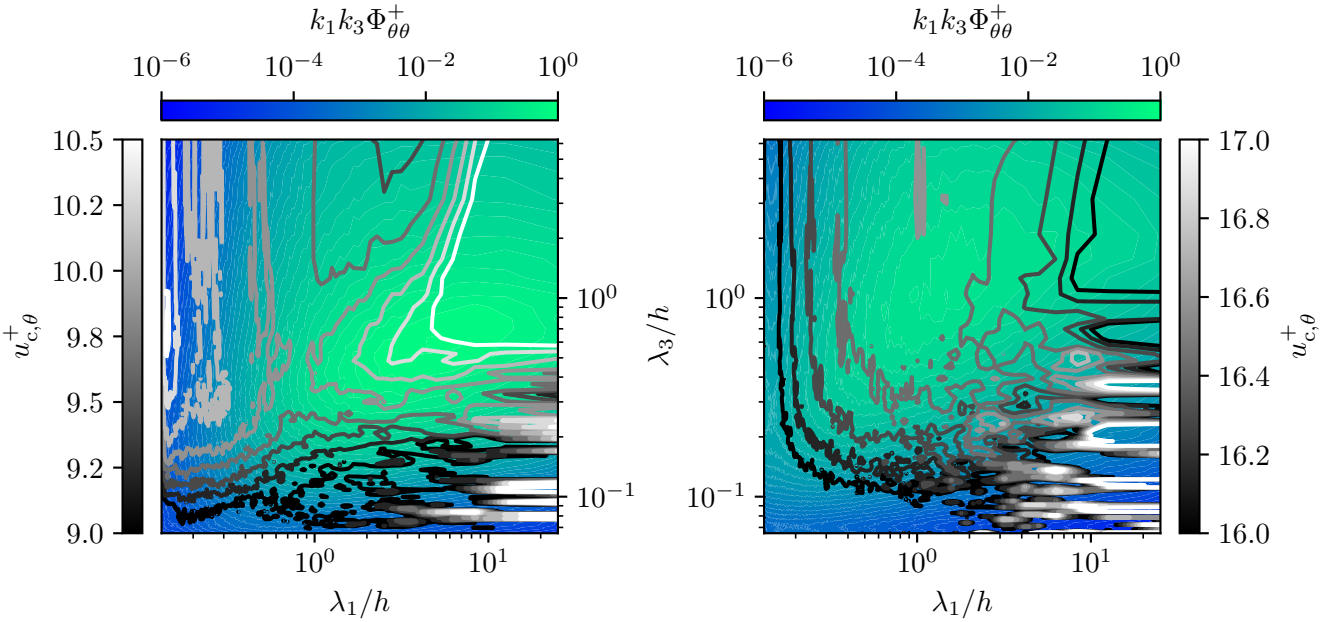

(a) Distribution at $x_2^+ \approx 5$ (b) Distribution at $x_2^+ \approx 105$

Figure D.72.: Spectral distributions of $u_{c,\theta}$ with $Pr = 1$ (case m180)

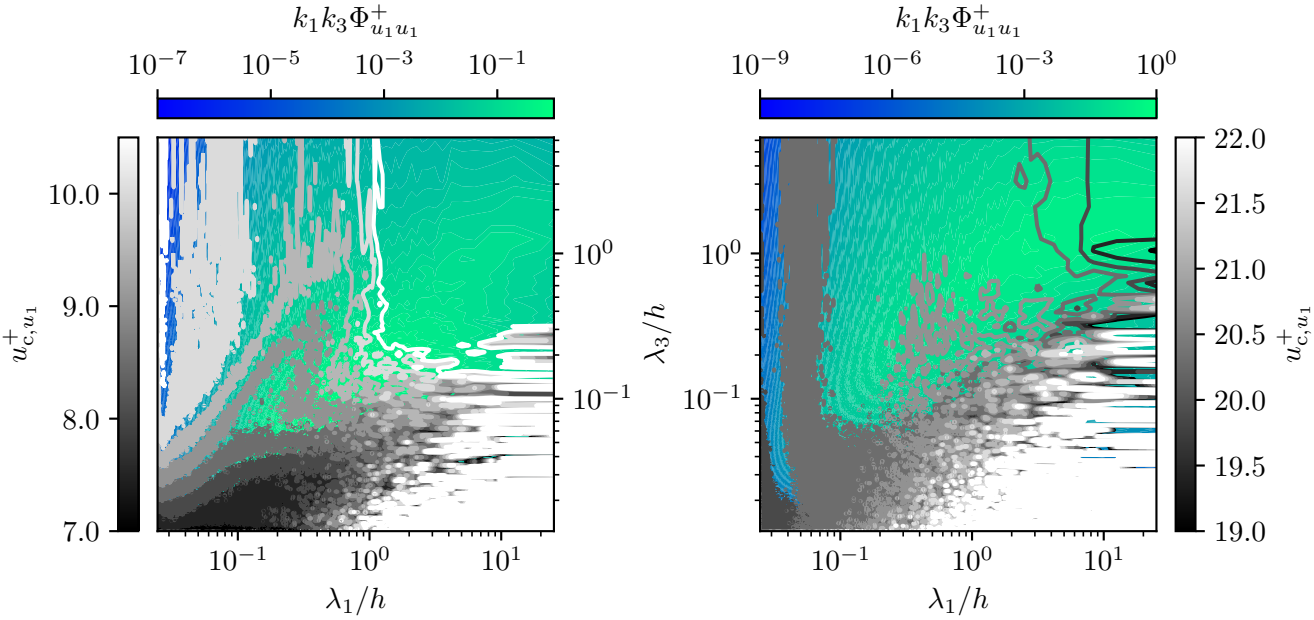

(a) Distribution at $x_2^+ \approx 5$ (b) Distribution at $x_2^+ \approx 515$

Figure D.73.: Spectral distributions of u_{c,u_1} (case m1000)

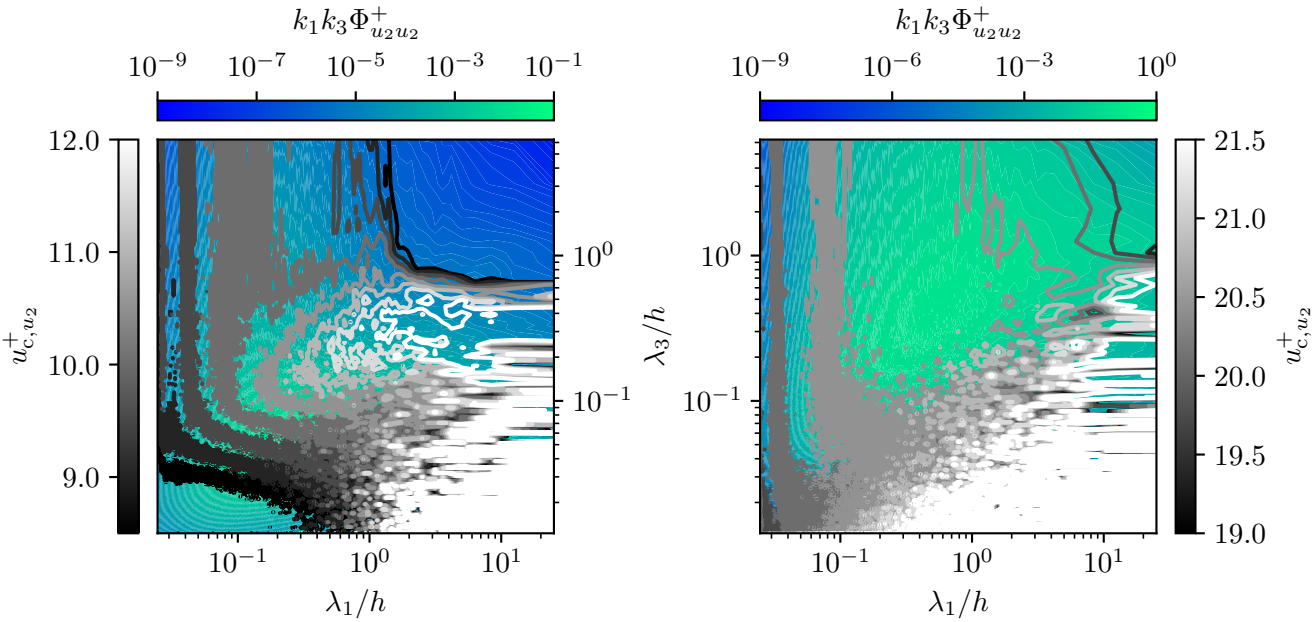

(a) Distribution at $x_2^+ \approx 5$ (b) Distribution at $x_2^+ \approx 515$

Figure D.74.: Spectral distributions of u_{c,u_2} (case m1000)

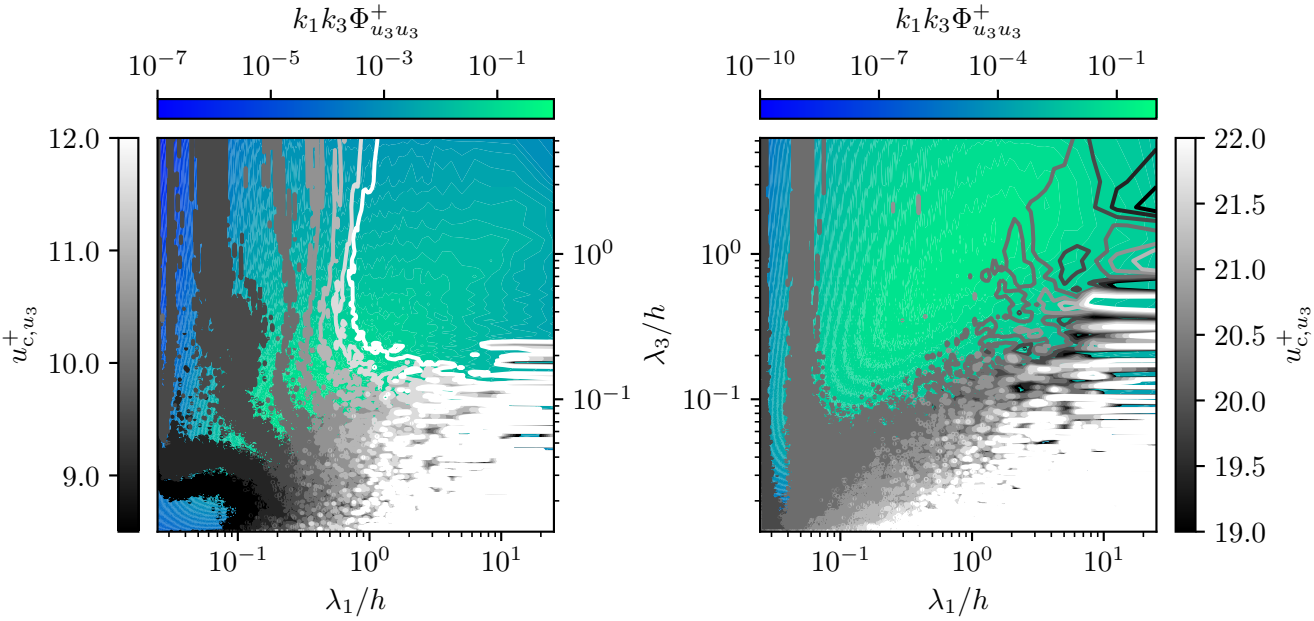

(a) Distribution at $x_2^+ \approx 5$ (b) Distribution at $x_2^+ \approx 515$

Figure D.75.: Spectral distributions of u_{c,u_3} (case m1000)

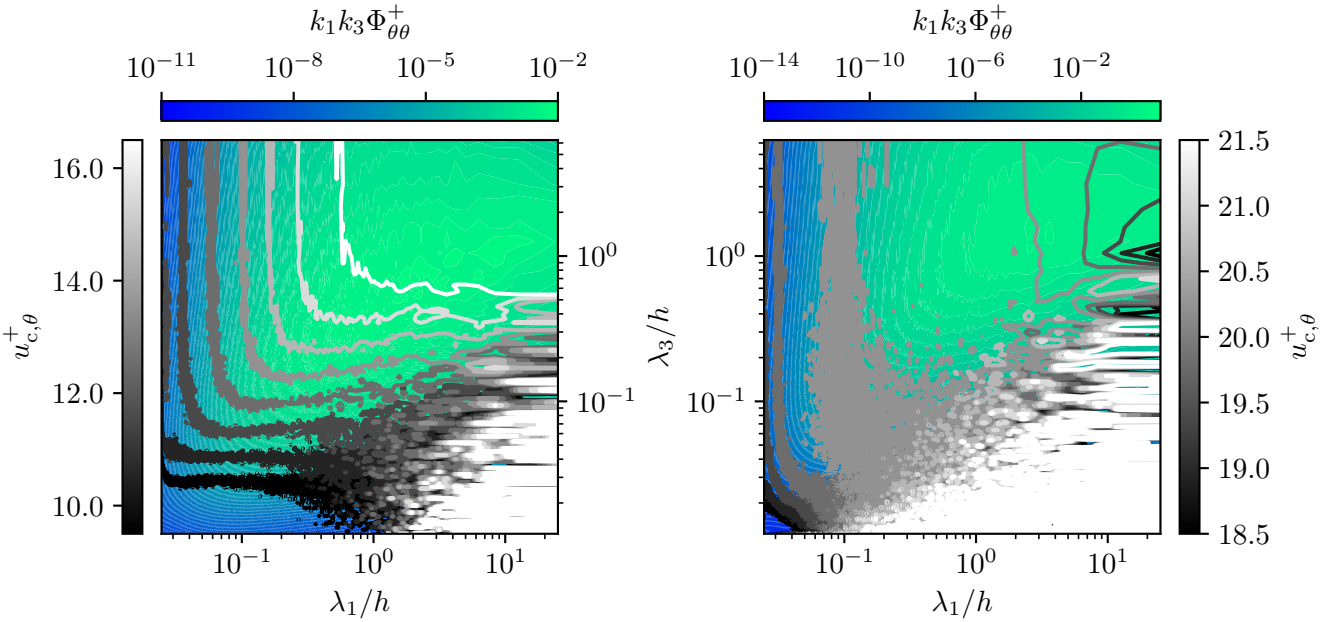

(a) Distribution at $x_2^+ \approx 5$ (b) Distribution at $x_2^+ \approx 515$

Figure D.76.: Spectral distributions of $u_{c,\theta}$ with $Pr = 0.025$ (case m1000)

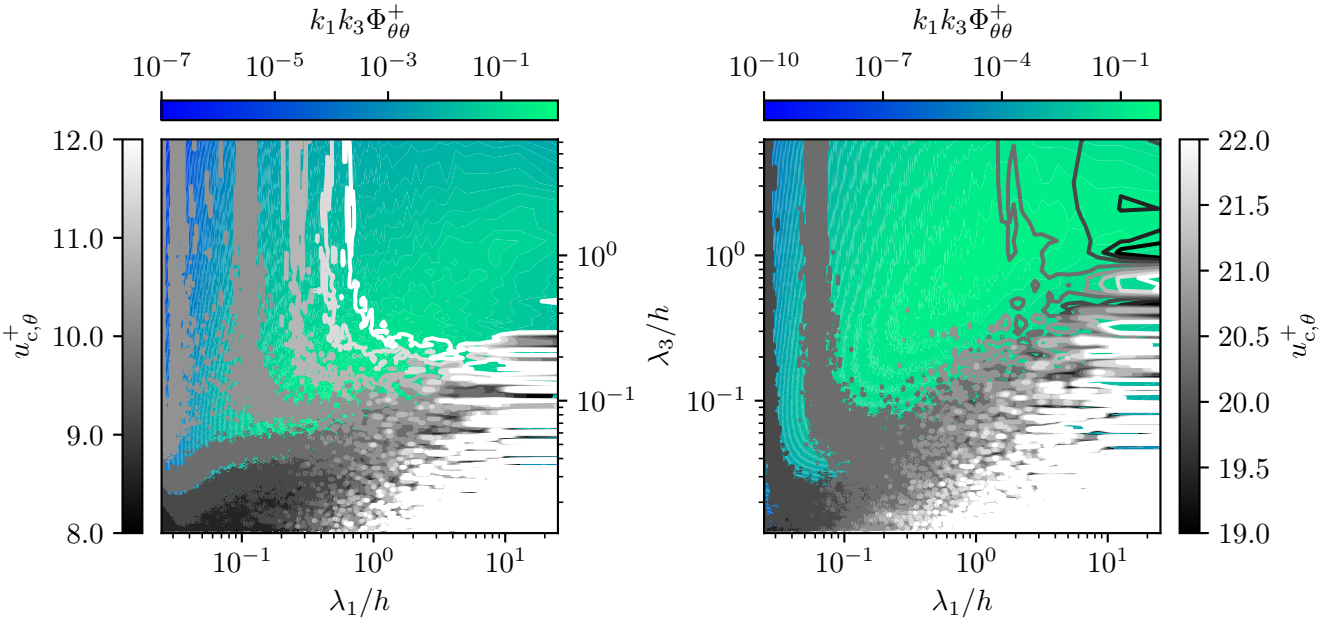

(a) Distribution at $x_2^+ \approx 5$ (b) Distribution at $x_2^+ \approx 515$

Figure D.77.: Spectral distributions of $u_{c,\theta}$ with $Pr = 0.4$ (case m1000)

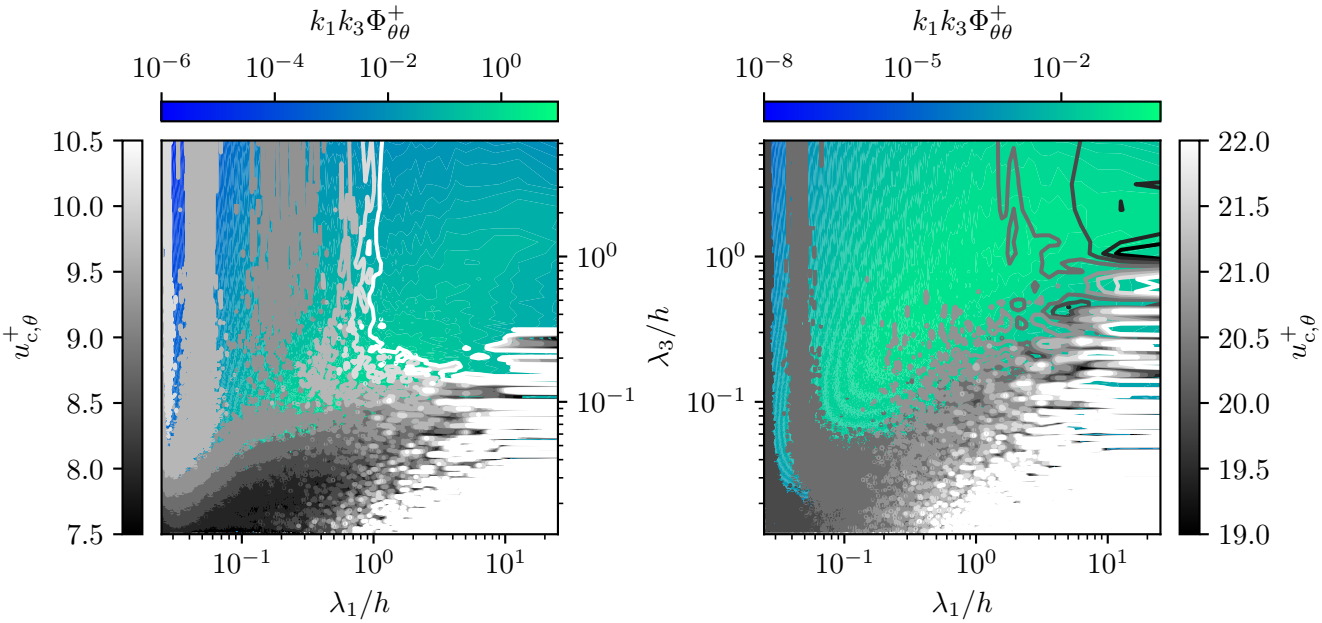

(a) Distribution at $x_2^+ \approx 5$ (b) Distribution at $x_2^+ \approx 515$

Figure D.78.: Spectral distributions of $u_{c,\theta}$ with $Pr = 1$ (case m1000)

E. Additional Reynolds number dependencies

E.1. Partitioned overall convection velocity comparisons

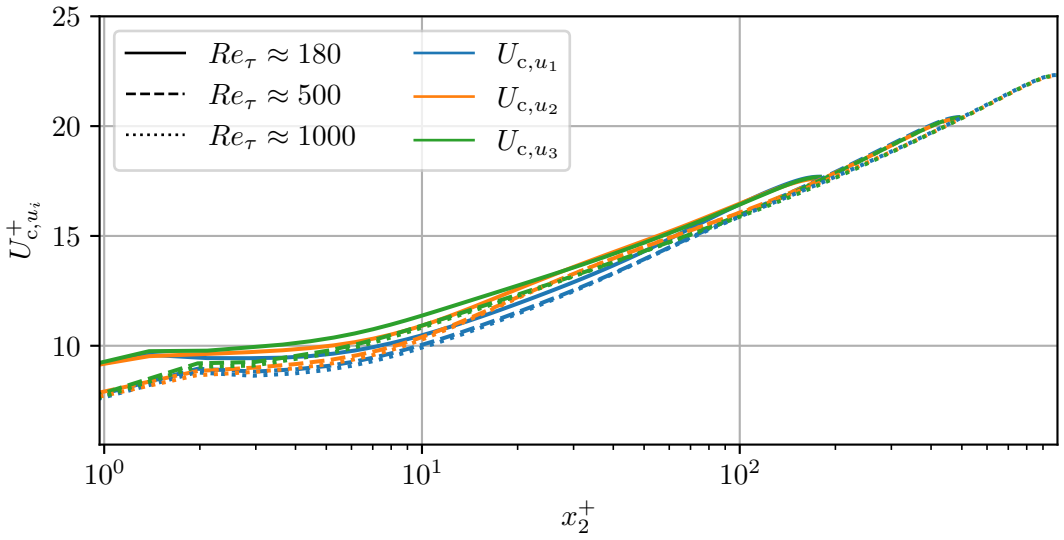

(a) Comparison of all-scale structures

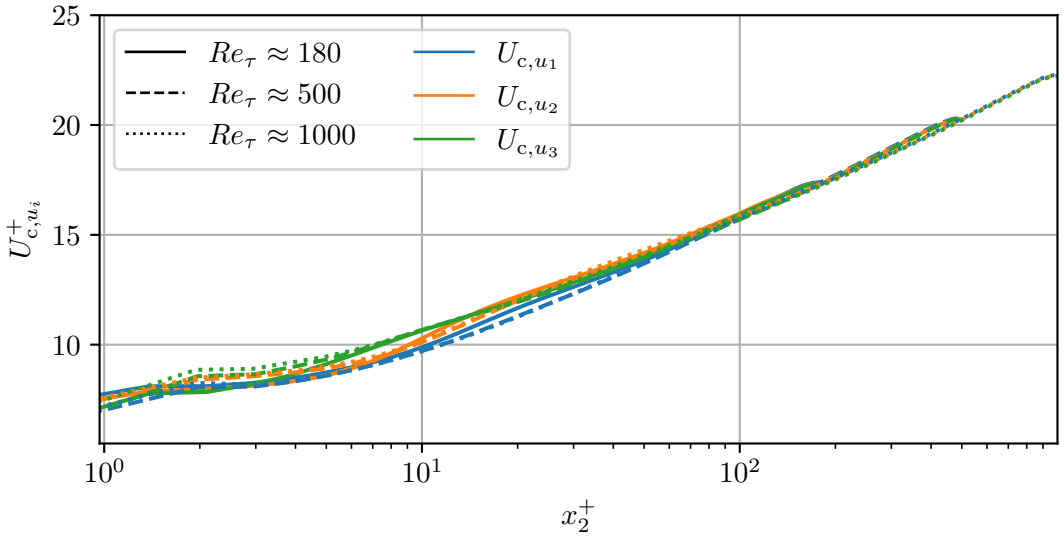

(b) Comparison of small-scale structures (cut-off at $(\lambda_1, \lambda_3) = (h/2, h/8)$)

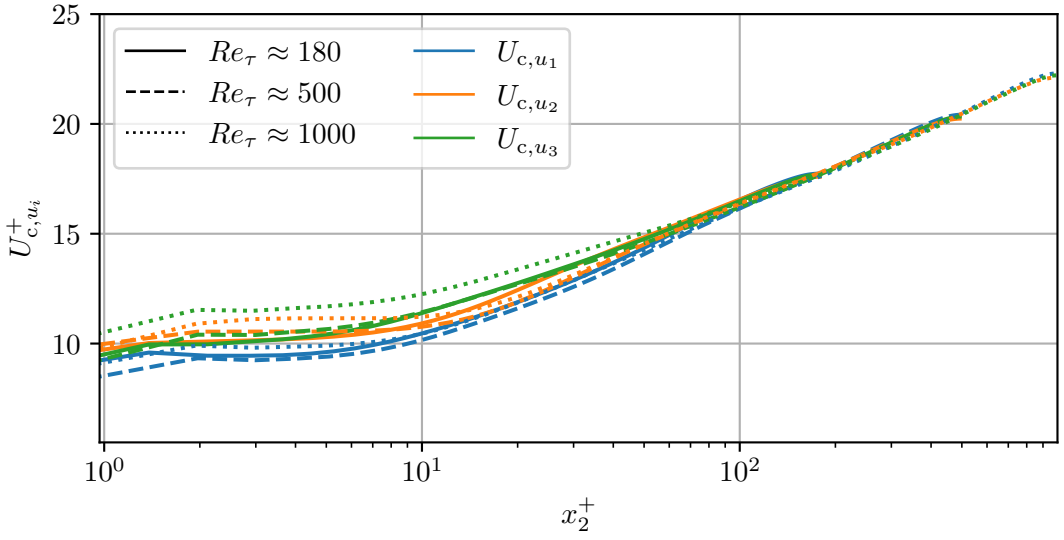

(c) Comparison of large-scale structures (cut-off at $(\lambda_1, \lambda_3) = (h/2, h/8)$)

Figure E.79.: Comparison of overall convection velocities of velocity structures

E.2. Convection velocity contributions comparison

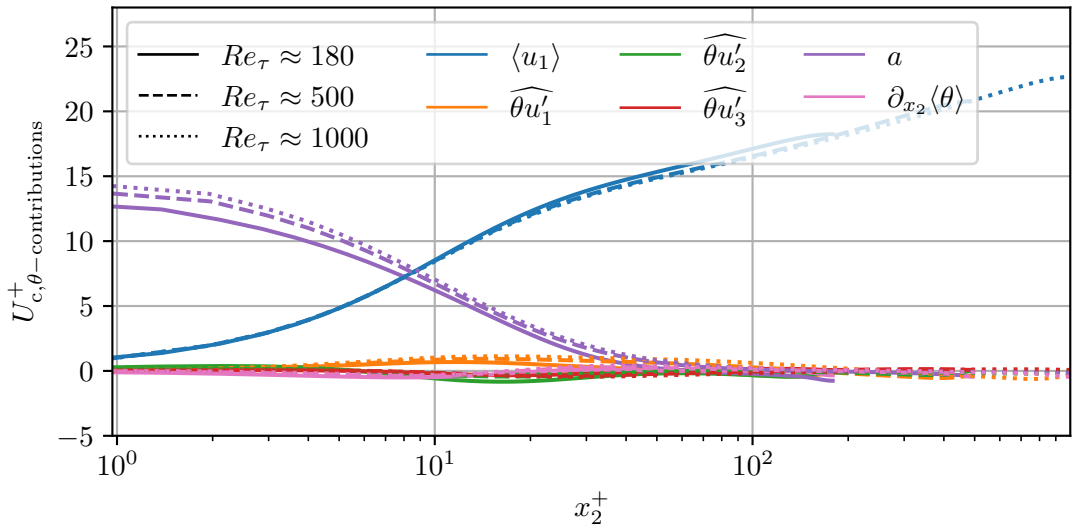

(a) Comparison of passive scalar structures with $Pr = 0.025$

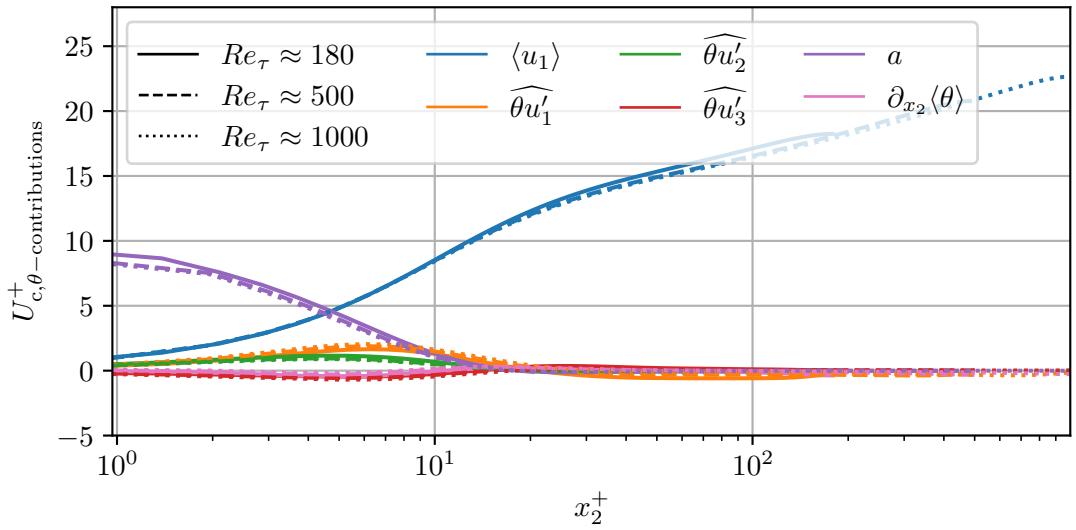

(b) Comparison of passive scalar structures with $Pr = 0.4$

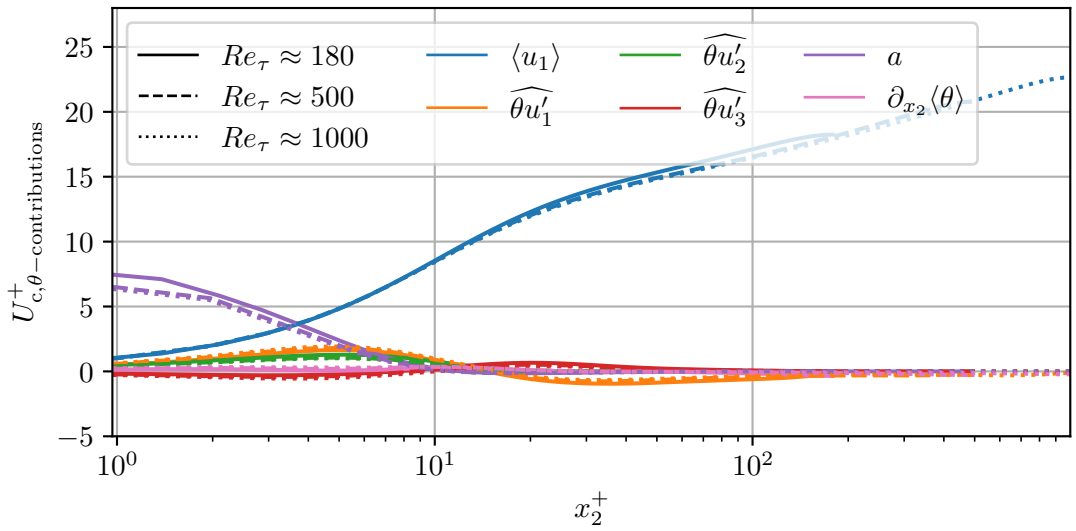

(c) Comparison of passive scalar structures with $Pr = 1$

Figure E.80.: Comparison of $U_{c,\theta}$ contributions

E.3. Spectral distributions comparison

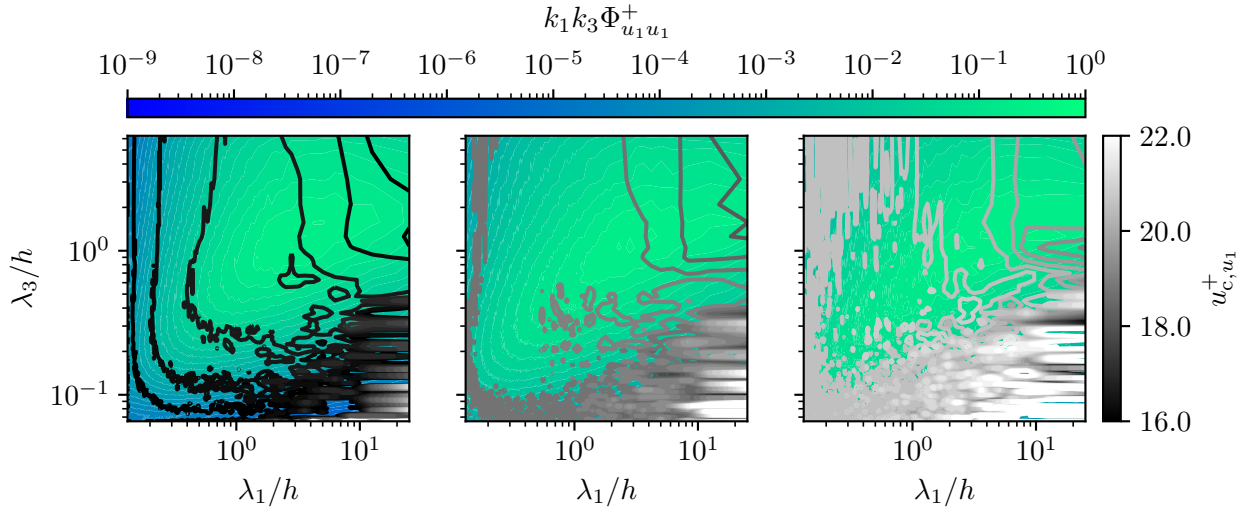

(a) $Re_\tau \approx 180$ (b) $Re_\tau \approx 500$ (c) $Re_\tau \approx 1000$

Figure E.81.: Comparison of spectral distributions of u_{c,u_1} in the log layer

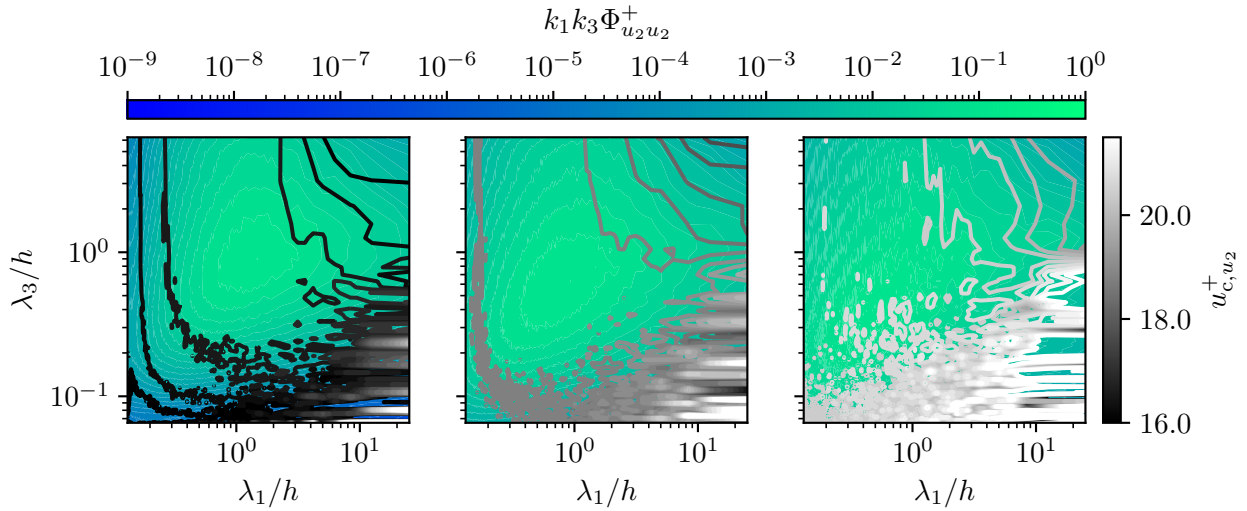

(a) $Re_\tau \approx 180$ (b) $Re_\tau \approx 500$ (c) $Re_\tau \approx 1000$

Figure E.82.: Comparison of spectral distributions of u_{c,u_2} in the log layer

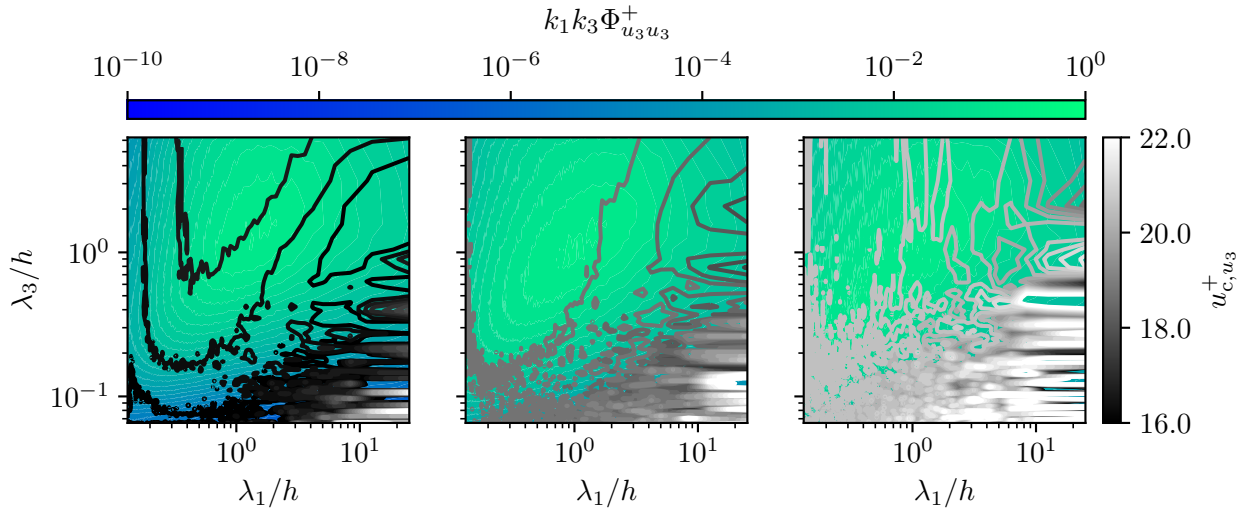

(a) $Re_\tau \approx 180$ (b) $Re_\tau \approx 500$ (c) $Re_\tau \approx 1000$

Figure E.83.: Comparison of spectral distributions of u_{c,u_3} in the log layer

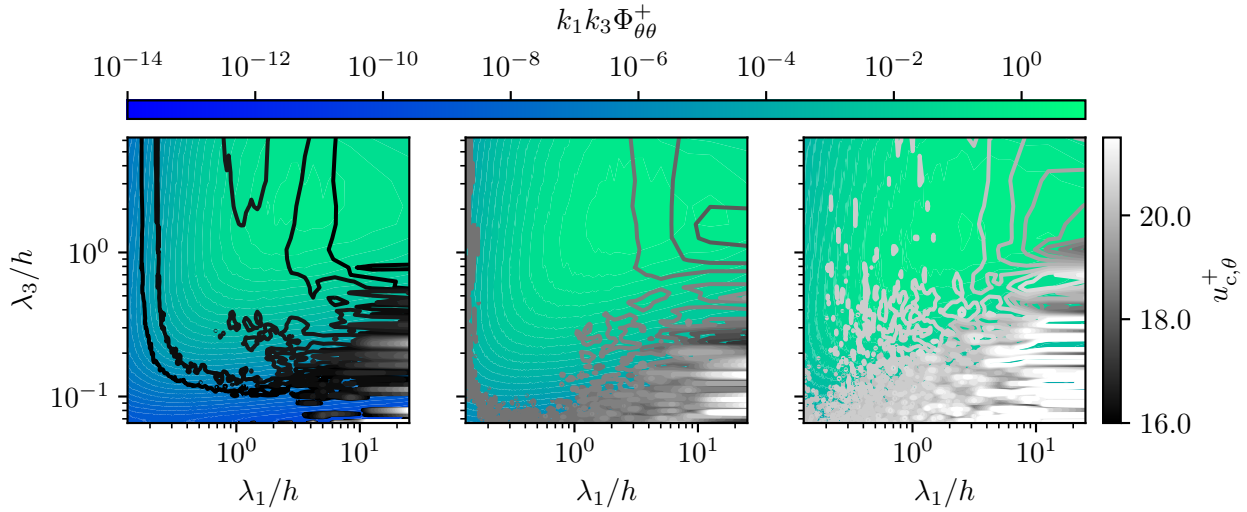

(a) $Re_\tau \approx 180$ (b) $Re_\tau \approx 500$ (c) $Re_\tau \approx 1000$

Figure E.84.: Comparison of spectral distributions of $u_{c,\theta}$ with $Pr = 0.025$ in the log layer

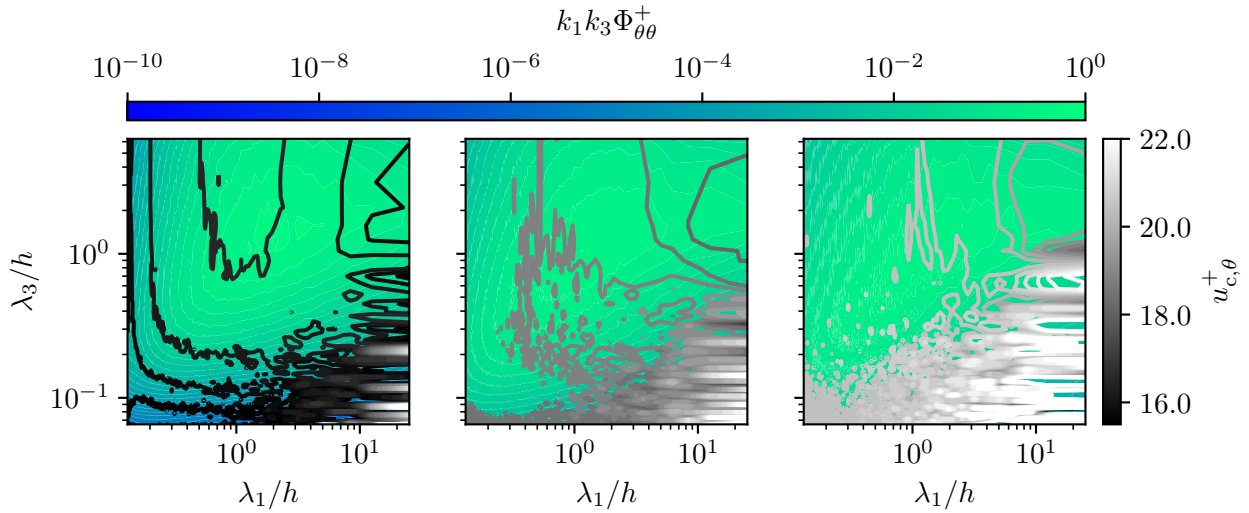

(a) $Re_\tau \approx 180$ (b) $Re_\tau \approx 500$ (c) $Re_\tau \approx 1000$

Figure E.85.: Comparison of spectral distributions of $u_{c,\theta}$ with $Pr = 0.4$ in the log layer

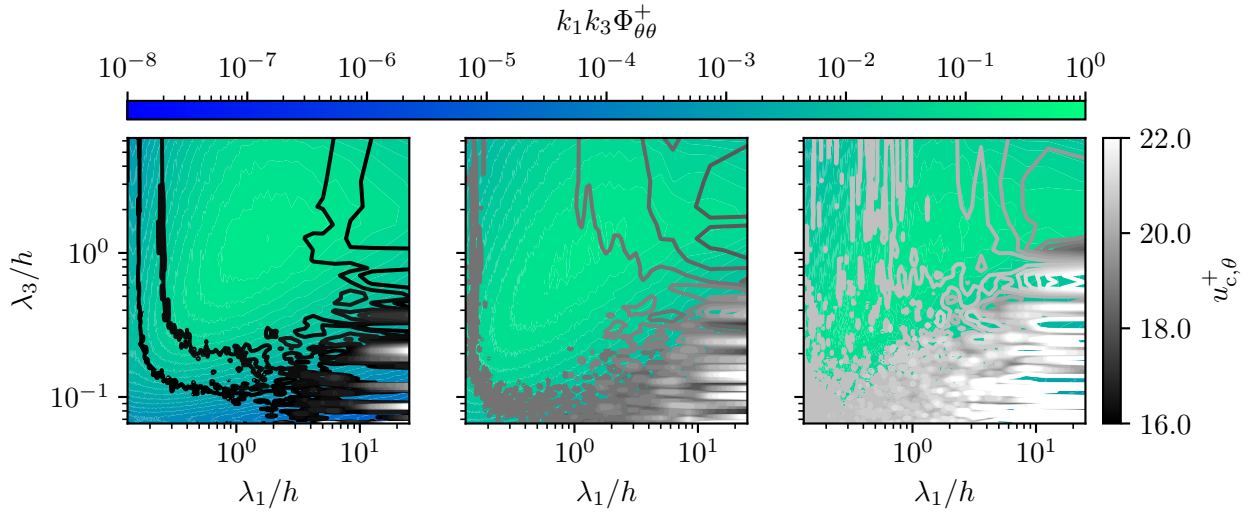

(a) $Re_\tau \approx 180$ (b) $Re_\tau \approx 500$ (c) $Re_\tau \approx 1000$

Figure E.86.: Comparison of spectral distributions of $u_{c,\theta}$ with $Pr = 1$ in the log layer